Wire Wrapped Fuel Pin Hexagonal Arrays for PWR Service

by

Peter Ray Diller

B.S Mechanical Engineering
Carnegie Mellon University, 2004

SUBMITTED TO THE DEPARTMENT OF NUCLEAR ENGINEERING IN PARTIAL FULFILLMENT OF THE REQUIREMENTS FOR THE DEGREE OF

MASTER OF SCIENCE IN NUCLEAR ENGINEERING
AT THE
MASSACHUSETTS INSTITUTE OF TECHNOLOGY

SEPTEMBER 2005

Signature of Author: _____
Department of Nuclear Engineering
September 9, 2005

Certified By: _____
Neil E. Todreas
KEPCO Professor of Nuclear Engineering, Professor of Mechanical Engineering
Thesis Supervisor

Read By: _____
Pavel Hejzlar
Principal Research Scientist
Thesis Reader

Accepted By: _____
Jeffrey A. Coderre
Chairman, Department Committee on Graduate Students

Wire Wrapped Fuel Pin Hexagonal Arrays for PWR Service

by
Peter Ray Diller

Submitted to the Department of Nuclear Engineering on September 9, 2004 in partial fulfillment of the requirements for the degree of Master of Science in Nuclear Engineering

Abstract

This work contributes to the Hydride Fuels Project, a collaborative effort between UC Berkeley and MIT aimed at investigating the potential benefits of hydride fuel use in light water reactors (LWRs). Core design is accomplished for both hydride and oxide-fueled cores over a range of geometries via steady-state and transient thermal hydraulic analyses, which yield the maximum power, and fuel performance and neutronics studies, which provide the achievable discharge burnup. The final optimization integrates the outputs from these separate studies into an economics model to identify geometries offering the lowest cost of electricity, and provide a fair basis for comparing the performance of hydride and oxide fuels.

This work focuses on the steady-state and transient thermal hydraulic as well as economic analyses for PWR cores utilizing wire wraps in a hexagonal array with $UZrH_{1.6}$ and UO_2. It was previously verified that square and hexagonal arrays with matching rod diameters and H/HM ratio have the same thermal hydraulic performance. In this work, this equivalence is extended to hexagonal wire wrap arrays, and verified by comparing the thermal hydraulic performance of a single hexagonal wire wrap core with its equivalent square array core with grid spacers. A separate neutronics equivalence is developed, based on the assumption that arrays with matching rod diameters and H/HM ratios will have identical neutronic performance.

Steady-state design limits were separated into hard limits, which must be satisfied, or soft limits, which serve to keep the design reasonable. Design limits were placed on the pressure drop, critical heat flux (CHF), vibrations, and fuel and cladding temperature. Vibrations limits on the wire wrap assemblies were imposed for flow induced vibrations (FIV) and thermal hydraulic vibrations (THV). An analysis of the fretting wear of wire wraps was performed, which outperformed the analogous fretting wear analysis for grid spacers. A CHF study found wire wraps to outperform grid spacers. LOCA and overpower transient analyses were performed for wire wraps. The overpower transient was analyzed over a range of geometries, and found to be more limiting than the steady-state analysis. The LOCA was analyzed for various powers at the reference geometry and another geometry of interest. Through all of these analyses, it was determined that the thermal hydraulic performance of $UZrH_{1.6}$ and UO_2 are very similar. The optimal wire wrap designs were found to have significantly higher maximum powers than the reference core, allowing for uprates up to ~54%. This is due to improved vibrations, pressure drop, and CHF.

The steady-state and transient analyses were combined with fuel performance and neutronic studies into an economics model that determines the optimal geometries for incorporation into existing PWR's. The model also provides a basis for comparing the performance of $UZrH_{1.6}$ to UO_2 for a range of core geometries. Results presented herein show cost savings for oxide fuel with wire wraps over grid spacers of at least 0.8 mils/kWe-hr, or 4%, due to power increases predicted by the thermal hydraulic analyses. Wire wrap $UZrH_{1.6}$ has a COE savings over UO_2 of 0.7 mils/kWe-hr, or 4%. Due to the large power uprates possible, a utility could achieve a cost savings of up to 10.9 mils/kWe-hr, or 40%, with a $UZrH_{1.6}$ wire wrap uprate instead of building a new core.

Thesis Supervisor: Neil E. Todreas
Title: KEPCO Professor of Nuclear Engineering, Professor of Mechanical Engineering

Thesis Reader: Pavel Hejzlar
Title: Principal Research Scientist

Acknowledgements

I am extremely grateful to Dr. Todreas for his help and guidance throughout my time at MIT. His instruction was invaluable, not only on the topic of Nuclear Engineering, but professional development in general. Thanks to him, I've learned much about engineering design this year. Pavel Hejzlar was invaluable in helping with the various programs used in this study. I'd also like to thank Dr. Greenspan and Francesco Ganda, whose patience and understanding helped me gain a basic understanding of neutronic issues.

Several previous and current MIT students have helped me gain understanding of previous work on the project, as well as providing programs that are written with a level of genius. Without them, this work would not have been possible. They are: Carter Shuffler, Chris Handwerk, Jarrod Trant, Sung Joong Kim, Jon Malen, Jacopo Saccheri and Stu Blair.

I'd also like to thank those professionals who took the time and effort to help give perspective and experimental data that were invaluable in determining the performance and relevant issues of wire wraps. These included personal communications with T. Shulz, H. Garkisch, R. Ballinger, X. Cheng, R. Baker, M. Carelli, G. Bogoslovskaia, R. Collingham and K. Rehme.

Finally, I'd like to thank those closest to me: my parents, Tom and Sharon, and of course Sarah. Your support and understanding has been invaluable, and I look forward to being closer to all of you in the future.

Table of Contents

List of Figures

List of Tables

Chapter 1: Introduction

1.1- Motivation

Hydride fuels have a hydrogen concentration comparable to liquid water. Hydrogen atoms moderate fast neutrons created by the fission process. These moderated neutrons then cause other fissions, maintaining the fission chain reaction. In contemporary PWR's, the only moderation is provided by the coolant. This means that there is a minimum water volume fraction to provide the necessary moderation. Since hydride fuels have moderation in the fuel, the moderation does not exclusively depend on the water volume fraction. This means that hydride-fueled cores can provide the needed moderation with a much smaller water volume fraction. This allows for increased fuel volume fraction, possibly enabling an increase in the achievable power for the same burnup and fuel cycle length of a reactor that uses hydride fuel.

To achieve a small water volume fraction, tight lattices are necessary. While grid spacers are used exclusively in current PWR's, there are other methods of achieving spacing between rods. Wire wrap spacers, an alternative to grid spacers, have been used extensively in LMFBR's **[6]**, and are considered superior for tight-lattice geometries, mainly due to the advantageous pressure drop of wire wrap spacers in tight lattices. Wire wrap spacers have also been considered for tight-lattice, high-conversion cores investigated in the 1990's **[17]**. Since the goal of this study is to investigate hydride fuels in a tight-lattice geometry, wire wraps are a natural design choice.

The goal of this study is to find the economic advantage, if any, of using wire wraps with hydride fuel in a PWR. To this end, a steady-state achievable power analysis will be performed over a range of pitch-to-diameter ratios (P/D) and diameters (D) to determine the steady-state benefits of wire wraps. A transient power analysis will also be done and the steady-state power will be reduced until the design constraints are satisfied. Finally, an economic analysis will quantify the economic benefits that wire-wrapped hydride fuel present.

The design created by this study could have one or more of the following advantages relative to contemporary PWR's.

- Increased core life, discharge burnup, total energy generated per fuel load, and capacity factor of LWR cores – anticipated outcomes are reduction in fuel cycle electricity costs along with improved resource utilization, reduction in the volume and hazard of high level waste, and increased proliferation resistance.
- Reduced core and pressure vessel volume per power output, or increased power level per core volume, thus reducing the cost of electricity.
- Increased capability of LWR's to recycle commercial plutonium and effectively dispose of military plutonium due to softer neutron spectrum and elimination of ^{238}U as a fertile fuel.
- Increased capability of LWR's to utilize thorium, even as compared with LWR's that use ThO_2 as the primary fertile fuel.
- Improved safety of LWR's, due to the inherent negative temperature coefficient of hydride fuel.

Candidate fuels include but are not limited to: $UZrH_{1.6}$, PuH_2-$ZrH_{1.6}$, PuH_2-ThH_2, $UZrH_{1.6}$-ThH_2, and PuH_2-$ZrH_{1.6}$-ThH_2. Note that fuels with thorium hydride have a higher heavy metal concentration than traditional oxide fuel. Combined with the higher power density offered by hydride fuels, they will allow achievement of higher energy generation per core loading. The expected outcome includes improvements in economics, resource utilization, proliferation resistance, safety, and waste reduction.

1.2 - Scope of this Study in the Larger NERI project

The participants in the study and their respective responsibilities include: (1) University of California, Berkeley, responsible for neutronics and materials compatibility; (2) MIT, responsible for thermal hydraulics, fuel performance, and economic optimization; and (3) Westinghouse, responsible for practical fuel and core design considerations. The role played by each analysis in the optimization study is briefly summarized below:

- Neutronics: The neutronics analysis seeks the maximum fuel burnup that maintains the critical nuclear reaction in the core, accounting for fuel depletion. It depends on fuel type, enrichment, and geometry. It also provides the range of geometries with acceptable fuel and moderator temperature and void coefficients.

- Fuel Performance: The fuel performance analysis seeks the maximum fuel burnup subject to design constraints that protect the integrity of the fuel pin during irradiation. Constraints are placed on: fission gas release and internal fuel pin pressure, clad strain, and clad oxidation. The fuel performance limited burnup depends on the fuel type, and the power in the core.

- Thermal Hydraulics: The thermal hydraulics analysis seeks the maximum power that can be safely sustained in the core subject to steady-state and transient design limits. Steady-state limits are placed on the minimum departure from nucleate boiling ratio (MDNBR), fuel bundle pressure drop, fuel temperature, and rod vibration and wear. Transient limits are derived by consideration of the loss of flow and loss of coolant accidents, and an overpower transient. The maximum power in the core depends on fuel type and geometry.

- Materials Compatibility: The materials compatibility study supports the neutronics, fuel performance, and thermal hydraulic analyses by specifying materials that are compatible for use with hydride fuels (i.e., cladding material, gap fill).

- Economic Optimization: An economics model uses the maximum burnup and power defined by the neutronics, fuel performance, and thermal hydraulic analyses to determine the cost of electricity (COE) as a function of fuel type, enrichment, and geometry. Both hydride and oxide fuels are considered, and designs are optimized for the cases of minor and major backfit by identifying the geometries where costs are minimized, and where hydride fuel use offers potential cost savings over oxide.

Figure 1.1 - Typical Wire-wrapped Assembly and Rod Configurations

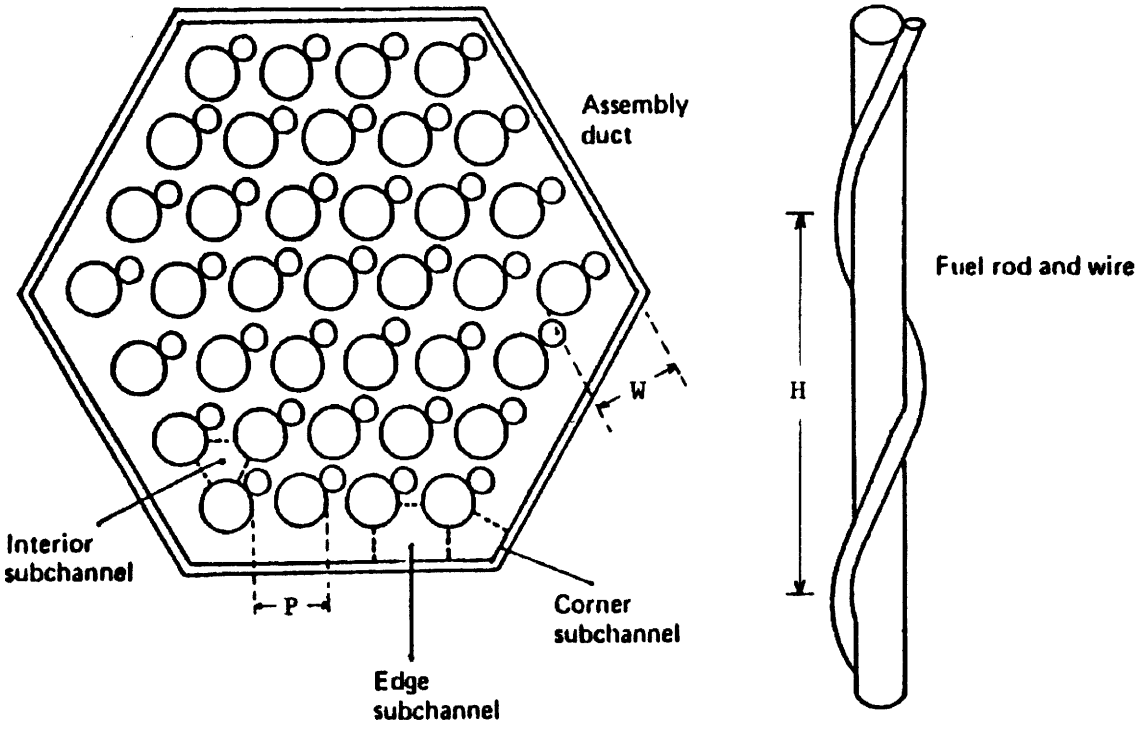

1.3 - Design Methodology

Figure 1.1 shows a typical 37-rod wire assembly, with relevant parameters illustrated. The wire-wrapped core design methodology presented in this work is applicable to the design of new reactors, as well as the backfit of current reactors with hydride fuels. The vessel size (diameter and height) is assumed to be constant for all of these designs.

1.3.1 - Major and Minor Backfits

Backfitting current reactors with hydride fuels can allow for power uprates, and possibly higher burnups. There are two types of modifications that allow for the uprate of PWR's using hydride fuel, as shown below. The implementation of a hexagonal wire wrap array in existing cores requires a major backfit, as the rod array is inherently different.

- A minor backfit seeks to limit the plant modifications required for the conversion to hydride fuel by maintaining the existing fuel assembly (pitch, diameter, and rod array). In this case, only the replacement of the steam generators and upgrades to the high pressure turbine will be required to accommodate higher powers.

- For a major backfit, the assembly envelope is not limited. The only constraint is that the design fit inside of the reactor vessel of the reference reactor considered, the South Texas Plant **[2]**. That is, any combination of geometry (pitch and diameter) that is practically feasible will be considered. Note that in addition to upgrades and modifications on the steam side of the plant, replacement of the reactor vessel head and core internals will also be necessary.

Wire-wrapped cores historically have been hexagonal, because a hexagonal arrangement allows for tighter rod packing, which was the goal of using wire wraps in the first place. Since almost all wire wrap experiments (pressure drop, CHF, mixing) have been performed using hexagonal arrays, only hexagonal arrays will be quantitatively considered in this study.

However, wire-wrapped bundles in a square array are perfectly feasible, and could offer some advantages. Specifically, for the same water volume fraction, the wires of a square array will be smaller, and thus less inhibitive to the flow. More importantly, using wire wraps in a square array would allow a minor backfit, A minor backfit requires a much smaller commitment to implement and would help prove the feasibility of wire wraps in PWR's before implementation in new cores or major backfits. Chapter 11 deals with square arrays as well as other design alternatives to the standard hexagonal wire wrap.

1.3.2 - Geometry of an Assembly

The geometry of a core design refers to the physical design parameters that characterize a core. For a grid spacer core, the important design parameters are the pitch (P), outer clad diameter (D), hydrogen to heavy metal ratio (H/HM), and number of rods in a fuel assembly. The pitch to diameter ratio (P/D) can be related to P, D, and H/HM. Thus, P/D and D are respectively the abscissa and ordinate of "power maps", 3-D maps that characterize the achievable power for a given geometry. Other aspects of the geometry are the clad and gap thickness, but these are assumed to be solely dependent on the outer clad diameter, according to the relationships given in Appendix B.3.

For wire-wrapped cores, an additional design parameter is introduced. It is the axial pitch (or lead length), H or H_{wire}, the axial distance over which the wire completely wraps around the rod. The axial pitch to diameter ratio (H/D) is a useful form of representing this design parameter. While it is impractical to iterate all geometries over a range of H/D, it is possible to find the optimal H/D for each geometry.

It should be noted that there is also an axial pitch for grid spacer assemblies, H_{grid}, defined as the distance between grid spacers in the assembly. However, for this project, the grid spacer configuration was not varied from the reference grid spacer configuration.

Power maps are not intuitive, especially for thermal-hydraulic designers who are more used to describing the geometry in terms of P and D, instead of P/D and D. While both fully describe the geometry, the relationship between the two methods is not immediately clear. Obviously, P can be related to P/D and D through

$$P = \left(P/D\right)D \qquad [1.1]$$

For the power maps, D is plotted against P/D. Lines of constant pitch can be drawn. For these lines of constant pitch (P_{const}), D is a function of P/D, as follows

$$D = \frac{P_{const}}{\left(P/D\right)} \qquad [1.2]$$

So the relationship for a line of constant pitch is hyperbolic on a power map, as shown in Figure 1.2. The range of geometries shown here is the range considered throughout this work. The details of the range considered will be developed in Section 4.4.2, but are based on where the power is highest and what is reasonable.

Figure 1.2 - Lines of Constant Pitch on a Power Map

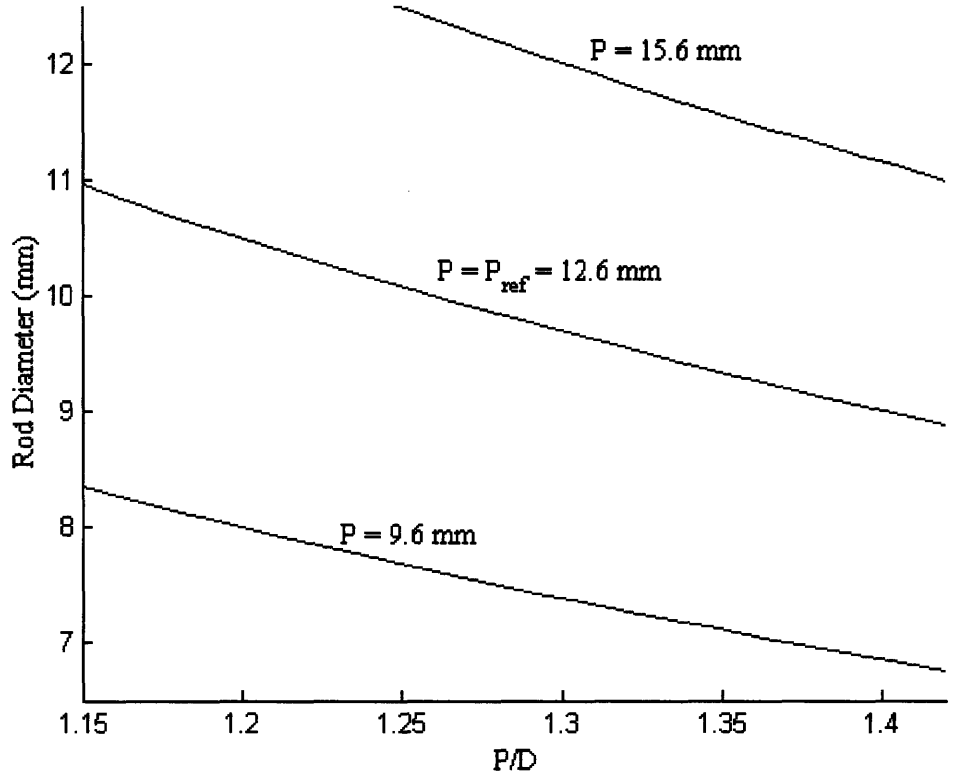

1.3 - Reference Geometry

The hydride fuel is being investigated as a potential backfit to operating LWR plants as well as new plants. The South Texas Plant has been selected as the reference PWR. The water properties used in the hand calculations throughout this report are taken at saturation for the system pressure (2250 psia). The key parameters of this plant used in this study are listed in Table 1.1.

Geometry	*Symbol*	*Value*
Pitch	P_{ref}	*12.6 mm*
Diameter	D_{ref}	*9.5 mm*
Number of Fuel Rods	N_{ref}	*50956*
Cross-Sectional Area for Heated Channels	A_{core}	*8.089 m^2*
Reactor Vessel Inner Radius	R_{core}	*1.83 m*
Active Fuel Length	L	*4.26 m*

Grid Spacer Thickness	t	*0.5 mm*
Operating Conditions		
Thermal Power	Q_{ref}	*3800 MW*
Core Enthalpy Rise	Δh	*204 kJ/kg*
Inlet Temperature	T_{in}	*294 C*
System Pressure	p	*15.5 MPa*
Fluid Properties		
Viscosity	μ	$9.274 \cdot 10^{-7}$ *N·s/m²*
Density	ρ	*749.3 kg/m³*

Table 1.1 - Reference South Texas Core

1.4 - Organization of this Report

Chapter 2 is an overview of the steady-state thermal-hydraulic analysis performed. It includes a list of the steady-state constraints, as well as the design methodology used in choosing design parameters. Chapters 3-6 evaluate the steady-state performance of wire wraps, and compare it to the steady-state performance of grid spacers. Chapter 7 establishes a wire wrap equivalence, which allows square input decks for VIPRE to be modified to represent hexagonal wire wrap cores. Chapter 8 presents the specific design methodology, and the steady-state achievable power for cores of wire-wrapped hydride and oxide fuel pins. Chapter 9 evaluates the transient performance of the wire wrap cores under LOCA, LOFA and overpower transients. Chapter 10 determines the economic advantages of wire-wrapped hydride cores. Chapter 11 identifies alternative wire wrap orientations that can be used, and Chapter 12 summarizes conclusions and recommendations for future work.

Chapter 2: Steady-State Thermal Hydraulic Analysis

2.1 - Steady-State Methodology

The steady-state thermal hydraulic analysis determines the maximum achievable power for a given geometry that does not exceed safety and performance limits. Since the economic performance of a nuclear power plant is mainly determined by its achievable steady-state power, this is an extremely important design point.

2.1.1 - Maximum Power Methodology

A recent MIT graduate, Jon Malen (2003), performed a parametric study to determine the steady-state maximum achievable power for square array PWR geometries with design limits placed on MDNBR, fuel bundle pressure drop, fuel temperature, and rod vibration **[1]**. The steady-state power presented in these results is only limited by these constraints. The performance of new designs with respect to the limits was determined by VIPRE, a sub-channel thermal-hydraulic analysis code used for steady-state performance analysis of a given core at a given power. VIPRE was cleverly linked to a series of student written MATLAB scripts to iteratively determine the maximum power for a user defined range of geometries, subject to the constraints. The maximum power is defined as the largest power that will not exceed any of the constraints. Carter Shuffler expanded on Jon Malen's work, and introduced a more extensive vibrations limit, as well as a cost-of-electricity determination model **[2]**.

The analysis performs the following steps to create a power map of maximum powers:

1. Design performance constraints are established.
2. The user specifies a range of geometries (D and P/D) to be investigated.
3. For each geometry, MATLAB constructs a full core VIRPE input deck, and supplies an initial guess for the power.
4. VIPRE is run for the given power, and the values of the performance constraints (MDNBR, pressure drop, axial velocity and temperature) are returned for that power.
5. If any of the constraints exceed the established limits, the power is reduced, and the input deck is modified accordingly.
6. If no constraint exceeds its limit, the power is increased.

7. This process converges iteratively on the maximum power. The maximum power is reached when the difference between one of the constraints and the constraint limit is less than 1% without any constraint exceeding their limits. For example, if the pressure drop limit is 60 psia and the pressure drop of the current power is 59.9 psia, with none of the other constraints exceeding their limits, the maximum power has been reached.

2.1.2 - Hard and Soft Constraints

Most of the performance constraints considered are hard constraints. For safety reasons, the hard constraints cannot be exceeded under any circumstances. Soft constraints serve to keep the design reasonable, and thus the constraints themselves are simply based on a judgment of what is reasonable. Soft constraints exist for manufacturing, monetary, and performance reasons. As a result, soft constraints generally have a range of acceptable values, while hard constraints are single values that cannot be violated. The acceptable values for hard and soft constraints are listed in Table 2.1.

Hard Constraint	*Acceptable Values*	*Soft Constraint*	*Limit Range*
CHF	MDNBR>$MDNBR_{ref}$	Pressure Drop	30 - 120 psia
Axial Velocity	$V < V_{ref}$	Axial Pitch	0.5_H_{grid} - H_{grid}
Fuel Temp.	$T_{CL} < 750$ °C	H/D	H/D < 50
Clad Temp.	$T_{Clad} < 400$ °C	Diameter	D > 6.5 mm
		P/D	P/D < 1.42

Table 2.1 - Hard and Soft Constraints used in the Steady-State Analysis

The soft limits are determined through a study of their effect on the performance, and specific values are chosen for the Achievable and Stretch Cases.

2.1.3 - Achievable and Stretch Case with Hydride Fuel

Experimental data and associated correlations for the operating parameters and performance of wire wrap required to develop limits are scarce. In addition, assumptions were made concerning the future achievable pressure drop and manufacturability of small-diameter rods. For example, the pressure drop constraint has a limit range of 30-120 psia. For the Achievable Case, the pressure drop *limit* is 60 psia (within the range of

30-120 psia), so the pressure drop is not allowed to exceed 60 psia. Different values of the soft limits are explored to find a reasonable value that also gives a high achievable power. This naturally has led to the generation of 2 hydride (and the comparative oxide) core design cases:

1. Achievable Case – this power map shows the power increases when making conservative assumptions throughout. Specifically, this map is developed using the following values and correlations or methods for the hard and soft constraints:

Hard Constraint	*Acceptable Values*	*Calculated using*
CHF	MDNBR>MDNBR$_{ref}$	W-3L correlation
Axial Velocity	$V < V_{ref}$	Connors analysis
Fuel Temp.	$T_{CL} < 750$ °C	VIPRE
Clad Temp.	$T_{Clad} < 400$ °C	VIPRE

Table 2.2 - Hard Constraints for Achievable Case

Soft Constraint	*Acceptable Values*
Pressure Drop	< 60 psia
Axial Pitch	H_{grid}
H/D	H/D < 50
Diameter	D > 6.5 mm
P/D	P/D < 1.42

Table 2.3 - Soft Constraints for Achievable Case

2. Stretch Case – this power map shows the potential advantages of wire wraps. Generally, it has higher achievable powers, but is farther outside the range of correlations and experience. This map is developed using the following values and correlations or methods for the hard and soft constraints:

Hard Constraint	*Acceptable Values*	*Calculated using*
CHF	MDNBR>MDNBR$_{ref}$	Dalle Donne
Axial Velocity	$V < V_{ref}$	Connors analysis
Fuel Temp.	$T_{CL} < 750$ °C	VIPRE
Clad Temp.	$T_{Clad} < 400$ °C	VIPRE

Table 2.4 - Hard Constraints for Stretch Case

Soft Constraint	*Acceptable Values*
Pressure Drop	< 90 psia
Axial Pitch	$0.75 \cdot H_{grid}$
H/D	H/D < 50
Diameter	D > 6.5 mm
P/D	P/D < 1.42

Table 2.5 - Soft Constraints for Stretch Case

The oxide constraints differ only in the temperature limits, as established in Section 2.2.2.

2.2 - Steady-State Hard Constraints

2.2.1 - Axial Velocity Constraint

Spacers, whether grid spacers or wire wrap spacers, provide support to the fuel rods within the bundle. While their primary function is to keep the rods from contacting each other, they also keep the rods from vibrating. However, due to the spacers' loss of ductility with irradiation, this will occur to some extent regardless. If the vibrations are extreme enough, the spacers will rub against the rods, removing the oxide film on the Zr cladding. This allows oxidation of the base metal and hence reduction of its effective thickness. This process of Zr removal is called fretting wear, and if it continues, the effective clad thickness can be reduced below design requirements.

Jon Malen's design approach to avoiding this fretting wear was an axial velocity limit. This is a limit on the average axial velocity in any of the subchannels in the core, and is determined through experience. An analogous axial velocity limit will be derived for wire wraps using Connors' analysis. Since the vibrations characteristics will vary with varying geometry, an axial velocity limit will be computed for each geometry.

- Flow-Induced Vibration (FIV) - this is the type of vibration that affects grid spacer assemblies. Generally, FIV is vibration caused solely by the fluid flow. An analysis analogous to Carter Shuffler's will be performed, to determine the relative performance of wire-wrapped rods compared to grid spacers.

- Thermohydraulic Vibration (THV) - this is an additional type of vibration that affects wire wrap assemblies. While it is not clear what mechanism causes this, there is feedback between the heat flux and fluid flow that can cause low frequency vibrations. The effect of this is a shifting of the entire bundle, causing larger scale, slower vibrations.

It is difficult to predict fretting wear, and it is a problem with current grid spacer fuel designs. So as with the rest of the imposed design limits, this work will attempt to prove that the wire wrap spacers will experience less FIV than the reference core grid spacers. In addition, there is some flow test experience with wire wraps, showing them to be more resistant to FIV than grid spacers. Regardless, flow testing will be necessary to evaluate the fretting wear performance of the chosen wire wrap design.

2.2.2 - Temperature Limits

- Cladding Oxidation. Zirconium oxide forms on the cladding of both the oxide and hydride fuels, reducing the structural integrity of the cladding. An oxidation layer is formed over time at a certain rate. The rate of formation is very temperature-dependent, and for the purposes of this study, the cladding temperature is the only factor affecting the formation rate. While a complicated analysis is necessary to determine the exact oxidation thickness, the recommended steady-state cladding temperature limit is 400°C **[3]**. Over the extensive number of runs performed in this study, the maximum cladding temperature was found to be extremely insensitive to anything. The value was found to be within a few degrees of 350°C for all runs performed. Since this is substantially lower than the cladding temperature limit of 400°C, there was no active constraint placed on the cladding temperature and it is anticipated that oxidation levels will be no worse than that of the reference core.

- Fission Gas Release. For hydride fuels the maximum centerline fuel pellet temperature under steady-state operation has been selected to be 750°C **[3]**. This limit was derived from TRIGA experience, and is based on mitigation of hydrogen (and other fission gas) release from the fuel. The analogous oxide

temperature limit for the prevention of excessive fission gas release (more than 5%) is a maximum average temperature of 1400°C. This gas release from the fuel causes internal pressurization of the fuel rod.

- Fuel Melting. For hydride fuels, hydrogen gas release is the constraining temperature-dependent failure of the fuel. However, the melting of oxide fuels can be a problem. As a result, a centerline fuel temperature constraint of 2800°C (the melting temperature of UO_2) has been imposed on oxide fuels. The melting temperature is much higher than the fission gas release temperature, but can still be constraining, since the centerline temperature can be much higher than the average temperature, especially since UO_2 has a low thermal conductivity.

2.2.3 - MDNBR

Departure from nucleate boiling (DNB) is the most limiting constraint on power for commercial PWRs. DNB occurs at the critical heat flux, which is a function of the geometry and operating conditions in the core. It is characterized by a sharp decline in the heat transfer coefficient at the coolant/cladding interface, as an insulating layer of vapor blankets the fuel rod. Since the heat flux is unchanged (fissions are still occurring and generating heat), the result of DNB is a large temperature increase of the fuel and cladding, which can damage the fuel and/or cause a cladding breach.

The minimum departure from nucleate boiling (MDNBR) is the minimum ratio of the critical heat flux to the actual heat flux found in the core. Since DNB causes fuel damage, significant margin relative to damage limits exists in commercial designs of PWR's. This accounts for core anomalies (blockages, coolant temperature variation, etc.), measurement uncertainty, and correlation uncertainty. It is nearly impossible to analytically derive these uncertainties, and even harder to validate the derivations. In lieu of this, VIPRE was run using the reference geometry with the reference power, and an MDNBR value (~2.17) was obtained for the operating conditions. This was set as the minimum MDNBR for the entire power map, under the premise that any design created by the power map would be at least as safe as the reference core.

As with all other characteristics, wire wraps have a different CHF than grid spacers. Wire wrap mixing is more axially uniform and there is also a swirl effect, increasing the mixing, which increases the CHF performance. The DNB mechanism is also different for wire wraps, as the bubbles and bubble layer form differently in the presence of the wire. In addition, the axial pitch has a strong effect on the CHF, mainly due to its effect on the swirl.

The end result is that the CHF in wire-wrapped arrays has to be determined experimentally. This testing is necessary for new grid spacer designs as well as any specific wire wrap design. Some CHF experiments comparing wire wraps to grid spacers have been performed but only over a limited range of geometries. All of this experimental data suggests that the CHF is higher (better) with wire wraps. It is therefore a conservative assumption for the Achievable Case that the CHF of wire wraps is equal to that of grid spacers over the entire geometry range. For the Stretch Case, a correlation created by Dalle Donne **[4]** is used to quantify the predicted CHF benefit of wire wraps, although this CHF prediction is somewhat outside of the range of the correlation.

2.3 - Steady-State Soft Constraints

2.3.1 - Pressure Drop

Previously in the project, the pressure drop was treated as a hard constraint. During the course of this work, pressure drop has been deemed a soft constraint. Unlike the hard limits placed on the design, the pressure drop limit is essentially an economic concern. The pressure drop in the core is a part of the system head, which has to be compensated for with a pump. If the pressure drop of the core design is higher than the reference pressure drop, the only consequence is that a higher head pump has to be installed. While the pump has to compensate for the entire system head, the pressure drop across the core will vary most with different geometries, and thus is the pressure drop considered for the limit.

PWR commercial designers have confirmed that using a larger pump that provides a higher head is technically feasible. The only restriction cited on the achievable pressure drop is convincing utilities that the risk of a bigger pump is not significant. The approach

currently used is to keep size increases small, and gain experience before moving to an even larger pump. It was recommended **[5]** that a size increase of 2 to 4 is reasonable. The pressure drop of the reference core, as calculated by VIPRE for the reference core, is ~29.0 psia. If the pressure drop limit is taken in the range of 2 to 4 times the reference core pressure drop, an acceptable pressure drop limit ranging from 60 _ 120 psia results.

After a study of the effect of different pressure drop limits on the power map, the pressure drop limits of 60 psia and 90 psia were chosen for the Achievable and Stretch Case, respectively. However, the pressure was never constraining for the Stretch Case, and the maximum power geometry has a pressure drop of 76.5 psia.

An additional concern associated with pressure drop is fuel assembly liftoff. Assembly liftoff occurs when the friction drag on the assembly by the flow is large enough to overcome the force holding the assembly in place. This will not be a problem for designs that fall within the reference core pressure drop, since the friction drag will not exceed that of the reference core. For higher pressure drops, mechanical hold downs may be necessary to prevent assembly liftoff. However, this is not addressed extensively since hold downs can be installed as needed.

2.3.2 - Axial Pitch

The axial pitch is an extremely important design parameter. Holding everything else constant, tighter axial pitch results in more support points for fuel pins within the bundle, increased swirl velocity, and increased friction coefficient. As a result, a tighter axial pitch leads to improved CHF and a larger axial velocity limit, but also a higher pressure drop. A constant axial pitch was chosen to be used over the power map. The specific value was chosen after several iterations, so that the pressure drop and axial velocity limits established to accommodate FIV concerns were reasonable.

2.3.3 - H/D

H/D is the axial pitch to diameter ratio. It is the parameter used in the Cheng/Todreas pressure drop correlation and the Dalle Donne CHF correlation, and these correlations are only both valid for $13.6 < H/D < 50$. Using the constant axial pitch from Section 2.3.2,

no values of H/D < 13.6 occur, but values of H/D > 50 do occur for small diameters. For any H/D > 50, the axial pitch is reset to be H = 50·D, so that the correlations used are valid. As a result, the axial pitch is not truly constant over the entire power map.

2.3.4 - D and P/D

The rod diameter and the pitch-to-diameter ratio ranges define the ordinate and abscissa, respectively, of the axes of the power maps. The rod diameter range is 6.5 mm _ 12.5 mm, and was selected using industry guidance to be manufacturable. The P/D range was originally the equivalent P/D of the entire range of geometries considered for the grid case, $1.07 < P/D_{sq} < 1.54$, equivalent to $1.15 < P/D_{hex} < 1.65$, where P/D_{sq} and P/D_{hex} are the pitch-to-diameter ratios of square and hexagonal arrays respectively (see Chapter 7 for discussion of equivalence). However, the current range was restricted to $1.15 < P/D_{hex} < 1.42$, equivalent to $1.07 < P/D_{sq} < 1.32$, effectively only considering the left half of the original power map. The new upper limit of 1.42 was chosen because no wire wrap pin assembly pressure drop experiments have been performed for $P/D_{hex} > 1.42$.

$P/D_{hex} = 1.42$ is also equivalent to the reference geometry, so only geometries with a higher fuel volume fraction than the reference geometry are considered. The fuel volume fraction can be approximated using Figure 2.1, where the outer rod diameter is used but for simplicity the cladding and gap are neglected.

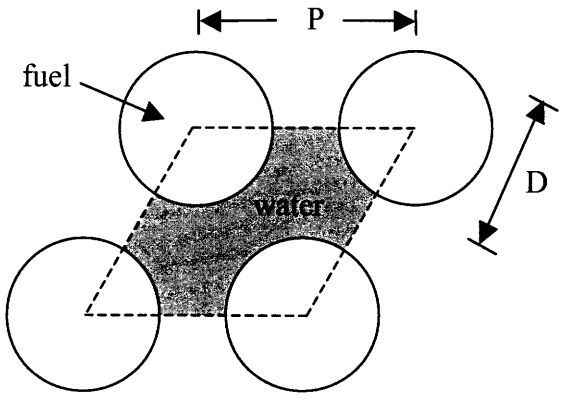

Figure 2.1 - Hexagonal Array

From Figure 2.1, the fuel volume can be calculated using Equation 2.1.

$$Fuel\ Vol.\ Fraction = \frac{\frac{\pi}{4}D^2}{\frac{\sqrt{3}}{2}P^2} \propto \frac{D^2}{P^2} \propto \frac{1}{\left(P/D\right)^2} \qquad [2.1]$$

A higher fuel volume fraction allows more net fuel volume to be loaded in the core, as more of the cross-sectional area of the core is occupied by fuel. This allows for a fuel with a lower enrichment to be used, which requires less poison at beginning of life (BOL), resulting in better neutronic performance. A higher fuel volume fraction also results in a smaller moderator temperature coefficient, which can become positive for hydride fuels with small fuel volume fractions.

In addition, setting the upper limit to 1.42 pushes the fuel pin diameter of the optimum geometry to around 8.5 mm, which is much more feasible from a manufacturing standpoint than 6.5 mm.

Chapter 3: Vibrations Analysis

There are two types of vibrations that are relevant to PWR design: thermal-hydraulic vibrations (THV), and flow-induced vibrations (FIV). THV are low frequency vibrations caused by feedback between the fluid flow and rod bow, due to thermal expansion in the fuel rods. FIV are high frequency vibrations caused by the local pressure variations due to the nature of the turbulent flow. These two types are fundamentally different, and result in different design constraints. As a consequence, they will be treated separately. In addition, a preliminary fretting wear analysis will be performed to compare the fretting wear of wire wraps and grid spacers.

3.1 - Thermal-Hydraulic Vibrations (THV)

For manufacturing reasons and to accommodate fuel swelling, wire-wrapped bundles have porosity, e.g. extra space between the edge of the bundle and the bundle wall as defined in Figure 3.1. This porosity can allow some movement of the bundle as a whole inside of the assembly walls, and even movement of individual rods.

Figure 3.1 - Illustration of Porosity in a Wire-Wrapped Bundle [6]

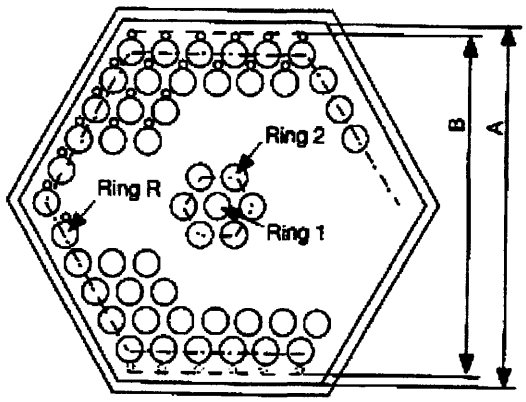

Porosity = A - B Porosity / Ring = (A - B) / R

A : Distance betweem two wrapper tube walls

$B = 2(R - 1)(D + d_w)\cos 30^\circ + D + 2d_w$

D : Fuel pin diameter

d_w: Spacer wire diameter

Wear marks (the precursor to cladding failure) have been observed on irradiated wire-wrapped fuel bundles from fast reactors. Otsubo et al. **[6]** studied the causes of these

wear marks, and found that the cause was thermal-hydraulic vibration (THV). This section analyses the potential problem with THV for wire wraps in PWR's.

THV is caused by temperature differences that develop due to flow differences across the rods at the edge of the bundles. Hence, the temperature of the side of the rod facing the wall is different from the temperature of the side of the rod facing the interior of the bundle. Due to differential thermal expansion caused by this temperature difference across the edge rods, and the space provided by the porosity, the edge rods will tend to bow. Since there is a power distribution gradient across the core, the rods on one side of the bundle will heat up more, and consequently bow more.

If the difference in bowing is substantial enough, the entire rod bundle will shift to one side. This shift causes changes in the flow, which tend to reverse the shift. This negative feedback loop can create a low frequency, but large scale vibration, dubbed thermal-hydraulic vibration. THV is low frequency, since the rods have to heat up and cool down for the shift to occur. However, since the entire bundle shifts, the movement is substantial and the rods rub against adjacent wires in the process, which can eventually cause wear marks.

Otsubo created a model of THV, which he used to correlate the occurrence of wear marks. To insure against THV, Otsubo concluded that the relevant parameters are as follows:

$$P_o / R \frac{\Delta T}{L} \frac{(H/D) D}{P/D - 1} \leq 2050 mm \cdot {}^{\circ} C \qquad \textbf{[3.1]}$$

where P_o is the porosity in mm, R is the number of rings in the bundle, $\_T$ is the temperature drop across the bundle in °C, P/D is the pitch to diameter ratio, D is the rod diameter, H is the axial pitch, and L is the length of the assembly. The THV constraint is plotted as the dotted line in Figure 3.2, as well as the relevant data on THV-induced wear. It is important to note that Equation 3.1 is dimensional and has been developed exclusively from sodium cooled fast reactor data.

Figure 3.2 - THV-induced Wear Data with Otsubo's Wear Constraint [6], [7]

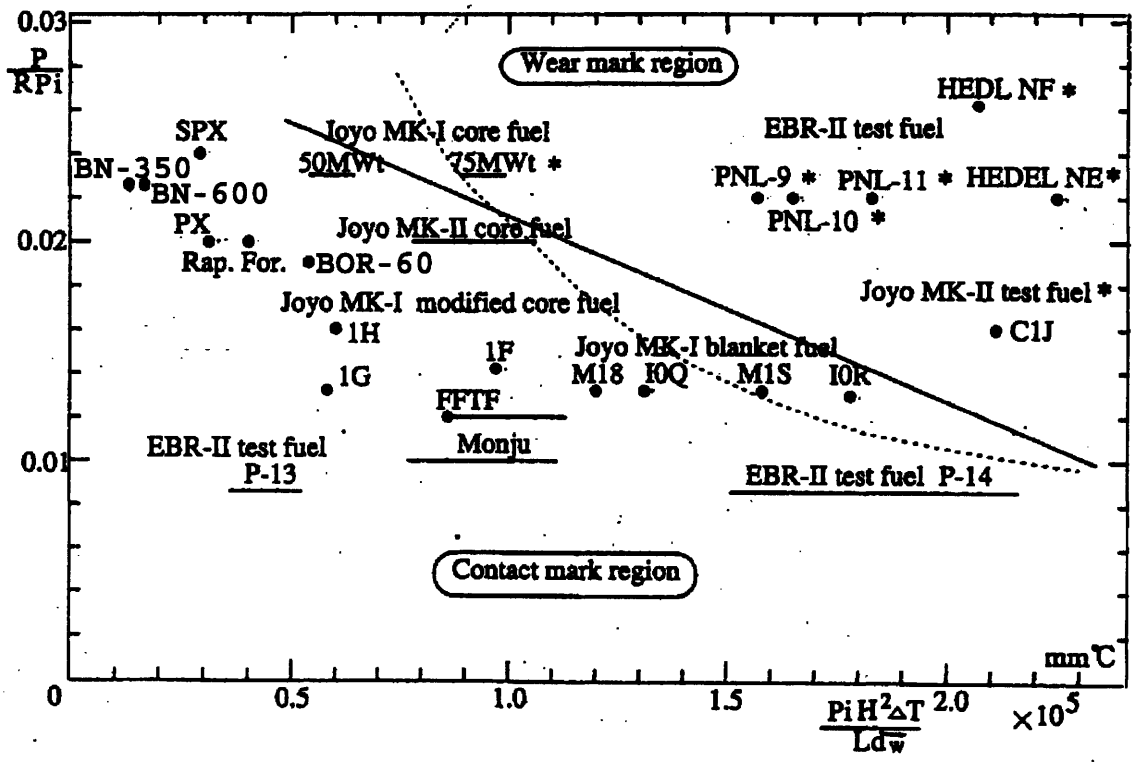

The dotted line in Figure 3.2 is a plot of Equation 3.1. However, the notation used in Figure 3.2 is inconsistent with the notation used in Equation 3.1. *As Figure 3.2 defines the parameters*, P_i is the pitch, P is the porosity, and d_w is the wire diameter. The notation in Equation 3.1 will be exclusively used in this study. The region above this line (labeled wear mark region) is the region where Otsubo's constraint predicts that wear will occur. In the region below the dotted line, Otsubo's constraint predicts that no significant wear will occur. The points marked with a _ represent reactors in which no wear has been observed, while the points marked with a * represent reactors in which wear marks occurred. The horizontal lines identify the range over which the subject fuel tests were conducted. The red dots, _, used for BN-350, BN-600, and BOR-60, represent Russian fast reactor data not used by Otsubo. These points were obtained through Alexander Sorokin [7], who confirmed that the fast reactors had never experienced wear marks. These data points are a confirmation of the validity of Otsubo's constraint.

Conveniently, $\_T$ and L are fixed for the design. P_o/R is dependent on the final bundle specifications, set by mechanical assembly constraints. A representative value of P_o/R = 0.175 mm is used for the following calculation, with the anticipation that this porosity can be achieved as needed. This value is typical for the fast reactors that Ostubo used when creating his constraint.

Otsubo's calculation was carried out using the reference core PWR values of $\_T$ = 39.6 °C and L = 4.27 m and H = 522 mm, all of the design space was found to be well within the limit, as proposed by Otsubo. These results are indicative that wire wraps will be relatively immune to THV under PWR service conditions. Figure 3.3 is a plot of the ratio of the left side to the right side of Equation 3.1 for the Achievable Case, and is conservative for the Stretch Case since the axial pitch of the Stretch Case is less. The wear term is the left side of Equation 3.1, and the critical wear term is the right side.

Figure 3.3 - Wear Term/Critical Term (margin to THV)

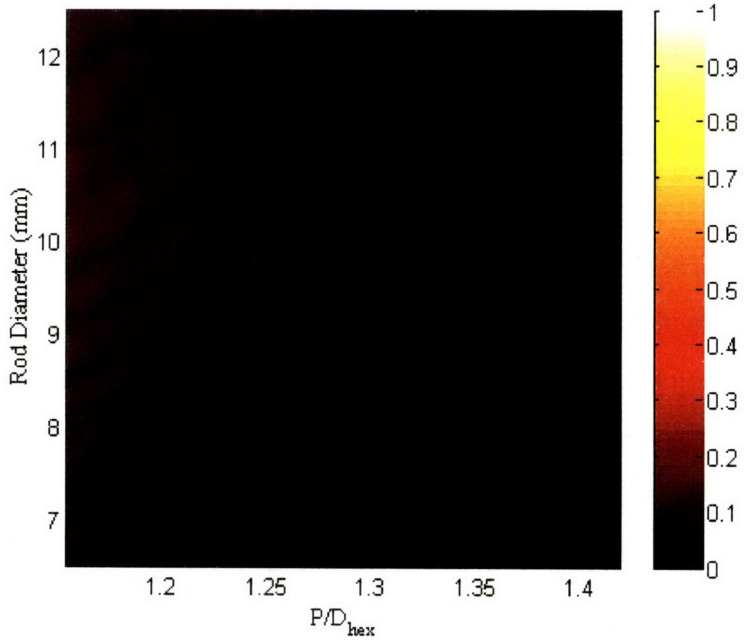

The left side of Equation 3.1 is no more than 20% of the right side for any geometry considered. This huge margin to THV is largely due to the combined effect of a relatively small temperature drop across the core and relatively large length of the bundle.

Otsubo predicts that the occurrence of wear is linear with respect to ΔT and L. However, it is not clear if the relationship is that strong. It seems unlikely that cutting the temperature difference in half would result in halving the wear experienced.

To insure that wire wraps in PWR's will not experience THV, the beneficial effect of ΔT and L were removed, and the analysis was repeated. Instead of the reference core values, $\Delta T = 80$ ℃ and $L = 0.6$ m were chosen from JOYO, the plant most extensively studied by Otsubo, while $H/D = 50$, as before. The highlighted areas in Table 3.1 show the values used in the following analysis.

	L	*ΔT*	*ΔT/L*	*H/D*
PWR	3.66 *m*	40 *°C*	10.9 *°C/m*	50
Fast Reactor (Joyo Mark-1 50 MWt)	0.6 *m*	80 *°C*	133.3 *°C/m*	41.6
Phenix	0.85 m	175 *°C*	205.9 *°C/m*	22.9

Table 3.1 - THV Parameters (highlighted values used in the following analysis)

The analysis using the highlighted parameters in Table 3.1 did show wear impacted regions of the power map. These geometries are shown in Figure 3.4. Even with the L and ΔT values from the fast reactor, most of the power map is predicted to be wear free. From this analysis, it is highly unlikely that THV will be a problem for wire wraps in PWR's, especially for the maximum power geometries, as will be shown later to have exclusively large P/D values. If THV turns out to be a problem, it is anticipated that the porosity can simply be decreased, the solution used successfully on all previous THV-impacted fast reactors. Since even the very conservative analysis in Figure 3.4 shows that THV will not be a problem for the geometries of interest (high P/D), no THV constraint will be used for this design and THV is not anticipated to be a problem for PWR's in general.

Figure 3.4 - Occurrence of Wear (black indicates wear impacted areas) with Conservative *L* and _*T* Values

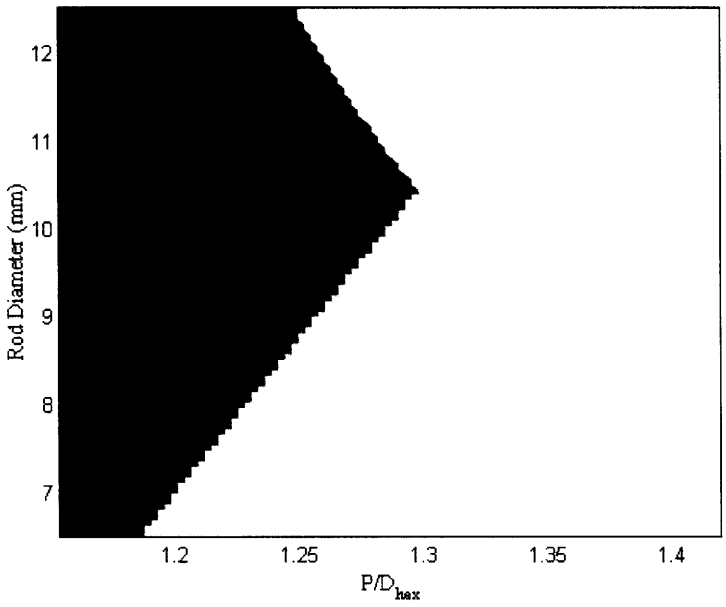

3.2 - Flow-Induced Vibrations (FIV)

Flow induced vibrations in a fuel bundle can be classified into two types:

1. Turbulent buffeting is the vibration caused by random pressure field fluctuations experienced during turbulent flow. Turbulent buffeting can be considered to be the effect of turbulent eddies impacting the rod. The flows that are considered for this design are exclusively turbulent, so turbulent buffeting will occur in the final design. However, this effect is generally not constraining.
2. Fluid-elastic instabilities are caused by the motion of the rod in cross-flow, which creates a positive feedback loop between structural vibrations and fluid forces. This creates an increase in vibration amplitude, and can lead to rods impacting each other. This progression of events is analogous to the famous collapse of the Tacoma Narrows Bridge. Fluid-elastic instabilities are the most constraining, and will be considered here.

An argument will be made for the structural stability of wire wraps against FIV. However, this does not mean that there will not be any wear on the bundle. Turbulent buffeting will exist at all flow velocities, and wear will occur as a result. So as with

many of the other limits established, the stability of wire wraps will be shown to be at least as good as the stability of the reference grid spacers. This improved stability will allow wire wrap designs with higher axial velocity limits than grid spacers.

3.2.1 - Fluid-Elastic Instability

Vortex shedding is the periodic alternation of pressure forces across a rod in cross-flow. If unconstrained, the rod will oscillate under vortex shedding. For rods under cross-flow, the frequency of the vortex shedding increases with flow velocity. When this frequency reaches the natural frequency of vibration for the rod, fluid-elastic instability occurs. This occurs at the critical cross-flow velocity. The motion of the rods amplifies the vortex shedding, creating a positive feedback loop that only ends when one of the following happens:

- Tube-to-tube impaction causes impact wear at the midpoint of a span length. Within a few days, or even hours in the most extreme cases, enough material can be removed from the cladding surface to burst the fuel rod.

- Cladding failure occurs when stress in the fuel rod exceeds the endurance limit for the cladding material. The fuel rod cladding will crack at the location where the stress is highest, often at the grid supports.

- Accelerated fretting wear rates accompanying the large vibration amplitudes can quickly wear through the cladding surface at contact points.

3.2.2 - Assumptions for Connors' Analysis

The flow dynamics of fluid-elastic instability of rod bundles (of interest in this study) are different than those of a single rod, but the principles remain the same. Connors, who first discovered the phenomenon of fluid-elastic instability **[8]**, derived an empirical equation for the critical cross-flow velocity of a rod bundle pinned at both ends, which will be referred to as a Connors bundle. Connors' analysis is still recommended in the 1998 version of the ASME Boiler Code. There are a number of assumptions in applying Connors' analysis to the rod bundles considered in this study as follows:

- *The support provided by grid spacers is pinned.* In reality, the rods are supported by springs on the grid spacers and lateral movement is allowed between the grids and the rods. The natural frequency of the actual bundle will be somewhat lower than that of a Connors bundle, making the vibrations performance worse than predicted by Connors' analysis. However, the rods are not allowed much movement at the grid spacers, so the assumption of pinned supports is a good approximation.

- *The wire-wrapped bundle has pinned supports at every axial pitch (H).* Rod bundles with wire-wrapped spacers are fundamentally different from Connors bundles as well. The contact points with wire wraps are the wires themselves, which are not springs and theoretically provide a pinned support for the rod, as is valid for Connors' analysis. But in practice the dynamics of a wire wrap rod bundle are different than a Connors bundle. This is due to the porosity of wire-wrapped bundles, as discussed in the Section 3.1. The porosity allows some movement of the bundle as a whole, and the presence of additional space can allow individual rods to move away from each other, making the gap larger than the wire and accommodating limited movement of individual fuel rods.

The porosity of the bundle is increased at beginning of life (BOL), when the bundle is exposed to highly pressurized water, causing the cladding to creep down on the fuel pellet. This creep essentially decreases the outer diameter of the rod, increasing the size of the gap and hence the porosity, allowing limited movement of the fuel rods. Creep is a problem also currently experienced with grid spacers, and in and of itself is not responsible for fretting wear.

As a consequence of irradiation, fuel swelling is experienced, causing strain on the cladding and increasing the effective outer diameter of the rod. The BOL enhancement of porosity from creep is mitigated, and eventually the fuel will swell enough to eliminate all porosity in the bundle. At this point, the bundle can be considered to be a Connors bundle.

Additionally, wire-wrapped bundles provide support that is inherently three dimensional. The support provided by wires occurs at different axial, as well as radial locations, but is only one dimensional at any given contact point. This can be viewed as regular, directional support points, 6 of which occur along the length of the axial pitch. This support can be considered to be comparable to a Connors bundle with pinned support at each end of the axial pitch. Since the support provided by the wire-wrapped bundle occurs regularly along the length, the natural frequency of the system will be higher, and the wire-wrapped bundle will perform better. For this analysis, the Connors bundle with support pinned at each end of the axial pitch will be used, and the result will be conservative.

- *The damping ratio used for the bundles is the conservative value for tightly supported bundles.* While the supports of both bundles are looser than pinned supports, the damping ratios, and associated critical cross-flow velocities for loosely supported bundles are higher than those for tightly pinned bundles. The damping ratios for tightly pinned bundles will be used, and the results will be conservative.

- *The effect of the fuel is ignored, only the cladding and fluid are considered.* In reality, the fuel will add some additional stiffness and improve the critical cross-flow velocity. However, there is a gap between the fuel and cladding, so relative motion of the fuel and cladding is allowed. Since it is not clear what stiffening effect the fuel will have, its presence is ignored, and the result will be conservative.

- *Only the first vibration mode is considered.* The first vibration mode (fundamental mode) typically has the largest impact on rod vibration. With regard to vortex shedding lock-in and fluid-elastic instability, the use of the first mode typically yields the most conservative design margin. Furthermore, several correlations used in place of FEA (finite element analysis) codes for modeling turbulence-induced vibration response are only applicable for the fundamental mode.

3.2.3 - Comparison of Connors' Analysis for Wire Wraps and Grid Spacers

Connors' analysis of the wire-wrapped bundle will result in a critical cross-flow velocity, which can then be used to approximate an axial velocity limit. Equation 3.2 is Connors' equation for the critical velocity, V_c, of a tube bundle **[8]**.

$$V_c = \beta \cdot f_n \cdot \sqrt{\frac{2\pi \cdot m_n \cdot \zeta_n}{\rho}} \qquad \textbf{[3.2]}$$

where _ is the Connors' constant, f_n is the natural frequency, _ is the fluid density, m_n is the linear mass of the system (clad and fluid) and $\__n$ is the damping ratio. They can be calculated as follows:

$$\beta = 4.76\left(P/D - 1\right) + 0.76 \qquad \textbf{[3.3]}$$

$$f_n = (n \cdot \pi)^2 \frac{1}{2\pi (H)^2} \sqrt{\frac{EI}{m_T}} \qquad \textbf{[3.4]}$$

$$M_{CL} = \rho_{CL} A_{CL} = \rho_{CL} \frac{\pi}{4}\left(D^2_{CLAD-OUT} - D^2_{CLAD-IN}\right) \qquad \textbf{[3.5]}$$

$$M_{FL} = C_M \rho_{FL} \frac{\pi}{4} D^2_{CLAD-OUT} \qquad \textbf{[3.6]}$$

$$m_T = M_{CL} + M_{FL} \qquad \textbf{[3.7]}$$

H is the span length (axial pitch in the case of wire wraps), n is the modal number, and C_M is the added mass coefficient.

	Tightly Supported Bundle	Loosely Supported Bundle
Mean Value	0.015	0.04
Conservative Value	0.01	0.03

Table 3.2 - Connors' Recommended Damping Ratio Values (ζ_n)

To solve Equations 3.2 through 3.7, it is necessary to calculate the area moment of inertia of the clad and the added mass coefficient, C_M.

$$I_{CL} = \frac{\pi}{64}\left(D_{CLAD-OUT}^4 - D_{CLAD-IN}^4\right) \quad \textbf{[3.8]}$$

$$C_M = \frac{D_*^2 + 1}{D_*^2 - 1} \quad \textbf{[3.9]}$$

$$D_* = \left(1 + 0.5 \cdot \left(P/D\right)\right) * \left(P/D\right) \quad \textbf{[3.10]}$$

The critical cross-flow velocity is dependent on the geometry, so a single axial velocity limit cannot be derived. The following calculation is carried out for wire wraps at the geometry of maximum power for the Achievable Case (D = 8.39 mm, P/D = 1.42, H = 420 mm). This geometry was consistently close to the maximum power (see Chapter 8 on Core Performance Results). The same calculation will be used to determine the axial velocity limit for each geometry.

Table 3.3 - Calculation of Critical Cross-flow Velocity for Achievable Case Maximum Power Geometry (D = 8.39 mm, P/D = 1.42, H = 420 mm)

Material Properties			
Cladding inside temp.	T_{CL}	410	^oC
Cladding density	ρ_C	8470	kg/m^3
Cladding Young's modulus	E	9.91e10	N/m^2
Linear Mass			
Geometry			
Clad inner diameter	$D_{CLAD\text{-}IN}$	7.38	mm
Clad outer diameter	$D_{CLAD\text{-}OUT}$	8.39	mm
Pitch	P	11.92	mm
P/D ratio	P/D	1.42	-
Cladding			
Cladding density	ρ_{CL}	8470	kg/m^3
Cladding linear mass	M_{CL}	0.106	kg/m
Fluid			
Non-dimensional diameter	D^*	2.428	-
Added mass coefficient	C_M	1.408	-
Fluid temperature	T_{FL}	292	^oC
Fluid density	ρ_{FL}	740	kg/m^3
Fluid linear mass	M_{FL}	0.058	kg/m
Total linear mass (fluid and clad)	m_T	0.164	kg/m
Moment of Inertia			
Cladding moment of inertia	I_{CL}	9.78e-11	m^4
Natural Frequency			
H/D ratio	H/D	50	-
Axial pitch	H	0.420	m

modal number (n)	Frequency (f_n)
1	68.65 /s
2	274.40 /s
3	617.40 /s
4	1097.61 /s

Critical Cross-flow Velocity Calculation			
Conner's Beta constant	β	2.759	-
Natural frequency (1st mode)	f_n	68.59	$/s$
Damping ratio (conservative)	ζ_n	0.01	-
Total linear mass	m_T	0.164	kg/m
Fluid density	ρ_{FL}	740	kg/m^3
Critical cross-flow velocity	V_c	0.706	m/s

Atomic International's 217 pin tests **[9]** show that for large size bundles, the transverse velocity component is the same as that predicted by the wire wrap angle. The design put forth in this work will have a bundle size comparable to the bundle size used in PWR's, so the cross-flow velocity can be predicted by the wire wrap angle.

Figure 3.5 - Illustration of Wire Wrap Angle

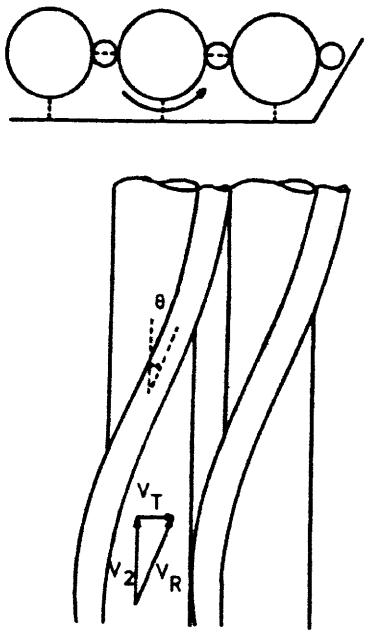

Figure 3.5 shows the wire wrap angle that can be used to calculate the cross-flow velocity given the axial velocity and flow angle. V_T is the cross-flow velocity, and V_2 is the axial velocity. Inversely, the axial velocity can be calculated given the cross-flow velocity. An axial velocity limit can be determined by calculating the axial velocity that corresponds to the critical cross-flow velocity found by Conners' analysis. The axial velocity is calculated from the cross-flow velocity by

$$V_2 = V_T \cot\theta \qquad \cot\theta = \frac{\left(H/D\right)}{\pi} \qquad \textbf{[3.11]}$$

For the maximum power geometry, H/D = 50, giving a contact angle of 4.6°. Calculating the axial velocity corresponding to the critical cross-flow velocity by setting $V_T = V_c$,

$$V_{max} = V_c \cot\theta = V_c \frac{\left(H/D\right)}{\pi} = 0.706 m/s \frac{(50)}{\pi} = 11.23 m/s \qquad \textbf{[3.12]}$$

where V_{max} is the maximum allowable axial velocity. Thus, using Connors' analysis, the axial velocity limit for the Achievable Case maximum power geometry is 11.23 m/s. The axial velocity limit turns out to be an active constraint for this geometry, as well as a large portion of the rest of the power map, as reported in Chapter 8. Connors' analysis can also be carried out for the reference geometry. Recall that the reference geometry is a square array with grid spacers and D = 9.5 mm, P/D = 1.326. The equivalent wire wrap geometry is D = 9.5 mm, P/D = 1.424, and H/D = 50. Table 3.4 compares the reference geometry with grid spacers, the equivalent geometry with wire wraps, and the maximum power geometry.

The equivalent wire-wrap geometry gives a 31% higher critical cross-flow velocity than the reference geometry, and the corresponding axial velocity limit for the equivalent wire-wrap geometry is 11.2 m/s. Due to the much higher critical cross-flow velocity, the wire-wrap geometry should be more resistant to fluid-elastic instability.

While Connors' analysis is only applicable to fluid-elastic instability, it highlights the vibrations benefits offered by wire wraps. In particular, Connors' analysis shows wire wraps to be stiffer (higher natural frequencies) than grids. In addition, the analysis actually under-predicts the stiffness of the wire-wrapped geometries, because the span length is taken to be the axial pitch. In reality, there are 6 different contact points over the axial pitch.

This increased stiffness results not only in improved resistance to fluid-elastic instability, but also improved FIV performance in general. The axial velocity limit for wire wraps should accordingly be higher than the axial velocity limit for grid spacers. According to industry expertise, the current PWR designs encounter problems when the flow is greater than 7 m/s. The axial velocity limit assumed by Jon Malen for PWR's with grid spacers is 8 m/s, with the anticipation that additional spacers will be added if deemed necessary by the flow-induced vibrations analysis.

Table 3.4 Comparison of Critical Cross-flow Velocities for Reference Core, Wire Wrap Equivalence, and Achievable Case Maximum Power Geometry

			Reference Geometry	Equivalent Reference Wire Wrap Geometry	Maximum Power Geometry
Fuel Type			UO_2	$UZrH_{1.6}$	$UZrH_{1.6}$
Clad inner diameter	$D_{CLAD\text{-}IN}$	*cm*	0.8379	0.8379	0.738
Clad outer diameter	$D_{CLAD\text{-}OUT}$	*cm*	0.95	0.95	0.839
Lattice Pitch	P	*cm*	1.2597	1.3528	1.192
P/D ratio	P/D	-	1.326	1.424	1.42
Cladding density	$\_{CL}$	kg/m^3	8470	8470	8470
Cladding Young's modulus	E		9.91E+10	9.91E+10	9.91E+10
Cladding linear mass	M_{CL}	*kg/m*	0.133	0.133	0.106
Added mass coefficient	C_M	-	1.518	1.405	1.408
Fluid density	$\_{FL}$	kg/m^3	740	740	740
Non-dimensional diameter	$D*$	-	2.205	2.438	2.428
Fluid linear mass	M_{FL}	*kg/m*	0.080	0.074	0.058
(Clad) + (fluid) linear mass	m_T	*kg/m*	0.213	0.207	0.164
Cladding moment of Inertia	I	m^4	1.58E-10	1.58E-10	0.978E-10
H/D ratio	H/D	-	54.9	50	50
Axial Pitch	H	*m*	0.522	0.475	0.420
Frequency, mode 1	f_1	*1/s*	49.40	60.51	68.65
Frequency, mode 2	f_2	*1/s*	197.61	242.05	274.40
Frequency, mode 3	f_3	*1/s*	444.62	544.60	617.40
Frequency, mode 4	f_4	*1/s*	790.43	968.19	1097.61
Connors' _ constant	_	-	2.312	2.778	2.759
Damping ratio	_	-	0.01	0.01	0.01
Cross-flow critical velocity	V_C	*m/s*	0.486	0.705	0.706
Axial flow critical velocity	$V_{2,crit}$	*m/s*	8.0 (assumed)	11.217	11.232

3.2.4 - Effect of Axial Pitch on Velocity Limit

The axial pitch effect on the velocity limit is an extremely important design point. A smaller axial pitch increases the number of support points, increasing the natural frequency of the vibrations, and improving the axial velocity limit. However, a smaller axial pitch also results in a higher cross-flow velocity, due to the change in the wire wrap angle. Rewriting the key equations for the calculation of the maximum axial velocity, and noting that $\left(L/k\right) = H$,

$$V_c = \beta \cdot f_n \cdot \sqrt{\frac{2\pi \cdot m_n \cdot \zeta_n}{\rho}} \qquad [3.2]$$

$$f_n = (n \cdot \pi)^2 \frac{1}{2\pi (H)^2} \sqrt{\frac{EI}{m_T}} \qquad [3.4]$$

$$V_{max} = V_c \frac{\left(H/D\right)}{\pi} \qquad [3.12]$$

Solving for the relationship between V_{max} and H,

$$V_2 \propto \frac{1}{H} \qquad [3.13]$$

The change in natural frequency due to a change in H is quadratic, while the change in cross-flow velocity is linear. As a result, the natural frequency effect dominates, and the axial velocity limit is improved with smaller H. Figure 3.6 shows the effect of H on the axial velocity limit for the equivalent reference geometry (P/D_{hex} = 1.425, D = 9.5 mm), consistent with Equation 3.13.

Figure 3.6 - Axial Velocity Limit v. Axial Pitch for Equivalent Reference Geometry

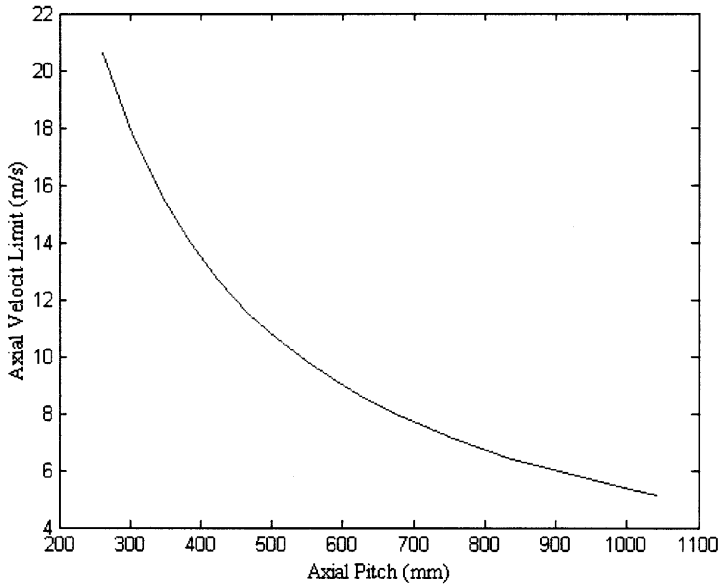

3.2.5 - Experimental confirmation of wire wrap vibrations performance

Flow experiments have been performed for wire wraps, and some have been performed using water as a working fluid. Collingham et al **[10]** performed a wire wrap mixing experiment, with an axial velocity of 8.95 m/s. While this was not an FIV experiment, the bundle did not experience significant FIV, proving that the axial velocity limit is at least 8.95 m/s for the given geometry. Table 3.5 shows the geometry of the test assembly, and the maximum axial velocity used in the experiment. Table 3.6 shows Connors' analysis for the test assembly, and the resultant critical axial velocity.

Table 3.5 - Collingham's Geometry and Axial Velocity

Number of pins	N	217
Rod diameter	D	5.842 *mm*
Wire diameter	d_w	1.422 *mm*
Pitch	P	7.274
Pitch to diameter ratio	P/D	1.243
Axial pitch	H	302 *mm*
Axial pitch to diameter ratio	H/D	51.7
Axial Velocity	V_2	8.95 *m/s*

Table 3.6 - Connors' Analysis for Collingham's [10] Test Assembly

Cladding Type			Stainless Steel
Clad inner diameter	$D_{CLAD\text{-}IN}$	*cm*	0.4763
Clad outer diameter	$D_{CLAD\text{-}OUT}$	*cm*	0.5842
Lattice Pitch	P	*cm*	0.7264
P/D ratio	P/D	-	1.243
Cladding density	$\_{CL}$	kg/m^3	7920
Cladding Young's modulus	E		1.9E+11
Cladding linear mass	M_{CL}	*kg/m*	0.071
Added mass coefficient	C_M	-	1.652
Fluid density	$\_{FL}$	kg/m^3	740
Non-dimensional diameter	D_*	-	2.205
Fluid linear mass	M_{FL}	*kg/m*	0.033
(Clad) + (fluid) linear mass	m_T	*kg/m*	0.104
Cladding moment of Inertia	I	m^4	3.19E-11
H/D ratio	H/D	-	51.7
Axial Pitch	H	*m*	0.3023
Frequency, mode 1	f_1	*1/s*	131.3
Connors' _ constant	_	-	1.919
Damping ratio	_	-	0.01
Cross-flow critical velocity	V_C	*m/s*	0.749
Axial flow critical velocity	$V_{2,crit}$	*m/s*	12.33

The maximum axial velocity is 27% less than the critical axial velocity for Collingham's test assembly. This is consistent with Collingham's experimental results, in which significant FIV was not experienced.

Westinghouse and Hanford performed many flow tests of wire-wrapped bundles in water, some of which exceeded the axial velocity limit and were instrumented to measure vibrations. Hans Garkisch **[11]** confirmed that in none of those tests "significant" FIV or wear marks occurred.

According to Mario Carelli **[12]**, the axial velocity limit for the Clinch River reactor was 9.1 m/s. The axial velocity limit used for the FFTF test reactor was 9 m/s. Both of these limits are for liquid sodium as the working fluid, but Connors' analysis predicts that water will have a slightly higher axial velocity limit than liquid sodium. No Connors' analysis was performed for the Westinghouse and Hanford flow tests, as data on the geometries tested is not available. Regardless, it is clear that the axial velocity limit for wire wraps should be higher than that for grid spacers.

3.2.6 - Axial velocity limit used for steady-state power maps

The axial velocity limit for wire wraps is calculated for each geometry using Connors' analysis, as a function of P/D, D and H of the given geometry. The only difference applicable to the axial velocity limit between the velocity limits of the two cases is the axial pitch used. A constant axial pitch is used in both cases, except when H/D > 50 (this is a soft limit), in which case axial pitch is reset so that H/D = 50. The resulting axial pitch and axial velocity limits for both cases are shown in Figures 3.7 and 3.8.

Figure 3.7 - Axial pitch and velocity limit for Achievable Case

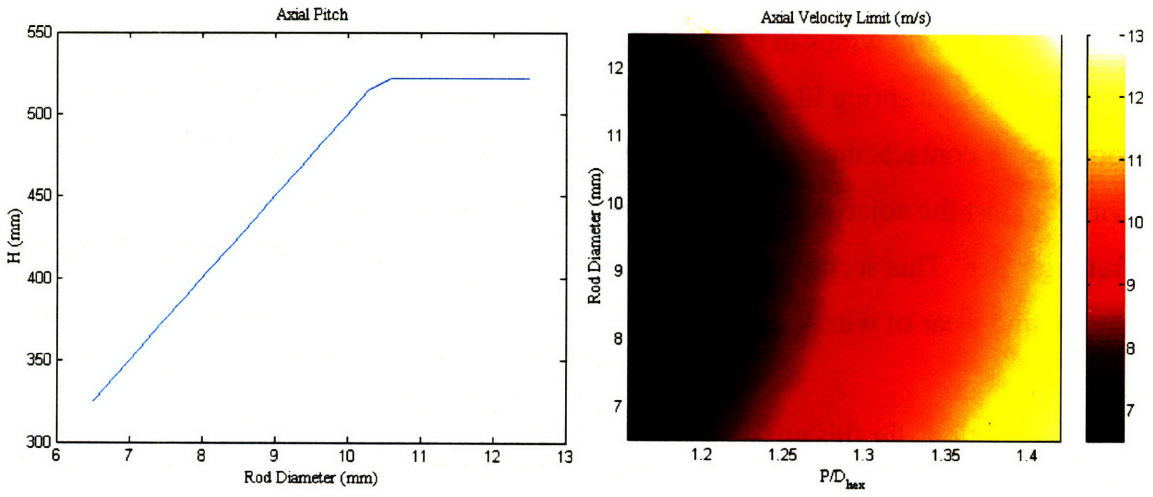

Figure 3.8 - Axial pitch and velocity limit for Stretch Case

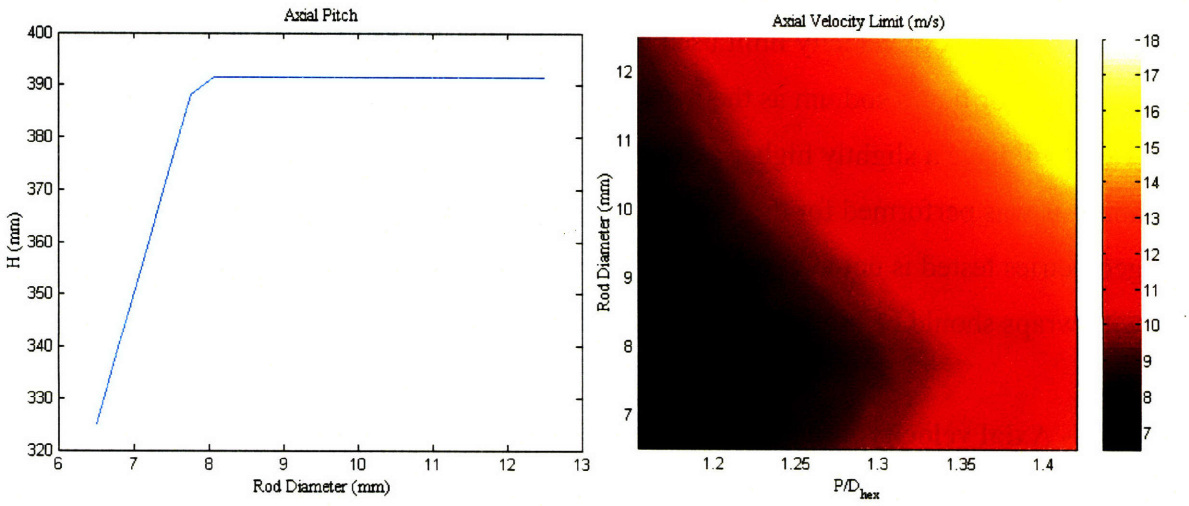

3.3 - Fretting Wear of Wire Wraps

3.3.1 - Methodology

Fretting wear is the most common wear mechanism, and historically the most costly flow-induced vibration problem in the nuclear industry. Fretting results from combined rubbing and impaction between the fuel rod support and the cladding surface. The fretting wear of wire wraps is a foremost concern to core designers considering implementing wire wraps in PWR's. While in current designs, the rod rests on the intermediate and spring like grid spacers, in a wire-wrapped assembly, the wire of one rod directly contacts the adjacent rod. The current thinking anticipates that the rubbing of wires against the adjacent rods due to their relative motion causes prohibitive amounts of fretting wear. This section will attempt a preliminary fretting wear analysis to determine the fretting wear of wire-wrapped rods.

The assumptions for this analysis are the same as the assumptions for Connors' analysis, as laid out in Section 3.2.2. This fretting wear analysis mirrors that of Shuffler **[2]**, and Shuffler should be referred to for additional details of the analysis. The goal of this analysis is to compare the fretting wear rate of wire wraps and grid spacers. To do this, a wear rate analysis will be performed at the reference geometry (D = 9.5 mm,

$P/D_{sq} = 1.326$) for wire wraps and grid spacers, and the results will be compared. Yetisir et al. **[13]** suggested that the fretting wear rate can be approximated as the power dissipated by the vibrating rod. The power dissipation depends on the structural properties of the rod and the RMS response from flow-induced vibration. The power dissipation, or fretting wear rate, for the first vibration mode is given by:

$$W_{fretting} = 32 \cdot \pi^3 \cdot \zeta_1 \cdot f_1^3 \cdot L_s \cdot m_t \cdot y_{rms}^2 \qquad \textbf{[3.14]}$$

where $\__1, f_1, L_s$[1], and m_t are the damping ratio, first mode natural frequency, span length, and total mass of the system, as defined in Section 3.2.3. y_{rms} is the amplitude of the RMS rod reponse, and is calculated as the sum of the RMS rod response due to cross-flow and axial-flow.

$$y_{rms} = y_{rms-axial} + y_{rms-cross} \qquad \textbf{[3.15]}$$

Assuming the vibrations modes of the rod are well-separated, Au-Yang recommends the following relationship for estimating the RMS rod response from cross-flow turbulence. In this analysis, only the first mode is considered.

$$y_{rms-cross} = \sqrt{\frac{2 \cdot n_s \cdot G_F}{64 \cdot \pi^3 \cdot m_t^2 \cdot f_1^3 \cdot \zeta_1} J_{11}} \qquad \textbf{[3.16]}$$

$$G_F = \left\{ C_R \cdot D \cdot \left(\frac{1}{2} \cdot \rho_{fl} \cdot V_{cross}^2 \right) \right\}^2 \qquad \textbf{[3.17]}$$

$$C_R = \sqrt{\frac{D}{V_{cross}} \cdot \overline{G}_p} \qquad \textbf{[3.18]}$$

$$\overline{G}_p = \begin{cases} 0.01 & \text{for } F < 0.1 \\ 0.2 & \text{for } 0.1 < F < 0.4 \\ 5.3e^{-4}/F^{7/2} & \text{for } F > 0.4 \end{cases} \qquad F = \frac{f_n \cdot D}{V_{cross}} \qquad \textbf{[3.19]}$$

$$J_{11} = 0.64 \text{ for simply supported tube} \qquad \textbf{[3.20]}$$

[1] The span length is the axial pitch for grid spacers, and is assumed to be the axial pitch for wire wraps.

where n_s is the number of spans, V_{cross} is the cross-flow velocity as calculated by Equation 3.11, G_F is the random force power spectral density (PSD), and J_{11} is the joint acceptance for the first mode.

Paidoussis **[13]** developed the following correlation to estimate the upper bound maximum rod response from axial-flow turbulence.

$$y_{max-axial} = 5e^{-5} \cdot D \cdot K \cdot \alpha^{-4} \cdot \left(\frac{u^{1.6} \cdot \varepsilon^{1.8} \cdot Re^{0.25}}{1+u^2} \right) \cdot \left(\frac{D_h}{D} \right)^{0.4} \cdot \left(\frac{\beta^{0.67}}{1+4 \cdot \beta} \right) \quad \textbf{[3.21]}$$

$$K = 0.5 \text{ for turbulent flow} \quad \textbf{[3.22]}$$

$$\alpha = \pi \text{ for simply supported rod} \quad \textbf{[3.23]}$$

$$u = V_{axial} \cdot L_s \sqrt{\frac{\rho_{fl}\left(\frac{\pi}{4}D^2\right)}{E_{cl} \cdot I_{cl}}} \quad \textbf{[3.24]}$$

$$\varepsilon = \frac{L_s}{D} \quad \textbf{[3.25]}$$

$$\beta = \frac{\rho_{fl}\left(\frac{\pi}{4}D^2\right)}{m_t} \quad \textbf{[3.26]}$$

where Re is the Reynolds number and V_{axial} is the axial flow velocity. Assuming the rod response follows a normal distribution, the RMS response is given by Equation 3.27.

$$y_{rms-axial} = \frac{y_{max-axial}}{3} \quad \textbf{[3.27]}$$

3.3.2 - Results

This analysis was performed at reference power for the reference core geometry for both wire wraps and grid spacers, as shown in Table 3.7. The mass flow rate and H/HM ratio is the same for the wire wrap and grid spacer cases, as developed in Chapter 7 on Wire Wrap Equivalence. Since the wire wrap geometry has a slightly smaller flow area, the wire wrap axial velocity is somewhat higher. Table 3.7 also shows the results of the fretting wear analysis for both grid spacers and wire wraps.

Inputs	*Wire Wraps*	*Grid Spacers*
Power	3800 MWth	3800 MWth
D	9.5 mm	9.5 mm
P/D_{sq}	1.326	1.326
Pressure Drop	23.6 psia	29.0 psia
Axial Velocity	6.7 m/s	5.75 m/s
H, or L_s	475 mm	522 mm
D_h	7.05 mm	11.77 mm

Results	*Wire Wraps*	*Grid Spacers*
f_1	66.40 Hz	56.45 Hz
D_h	7.05 mm	11.76 mm
V_{cross}	0.496 m/s	0.064 m/s
$y_{rms\text{-}cross}$	4.610_10^{-6} m	9.958_10^{-9} m
$y_{rms\text{-}axial}$	3.478_10^{-5} m	5.037_10^{-5} m
y_{rms}	3.939_10^{-5} m	5.038_10^{-5} m
$W_{fretting}$	3.74_10^{-4} W	4.17_10^{-4} W

Table 3.7 - Inputs and Results for Fretting Wear Analysis

This analysis predicts that the fretting wear of wire wraps is 10.4% lower with wire wraps than grid spacers. The largest difference between the wire wraps and grid spacers was a slightly smaller span length for wire wraps, as the soft constraint limits H/D to be less than 50. However, this is realistic, as reducing the span length of wire wraps carries a much smaller penalty to pressure drop than grid spacers. The wear rate is proportional to the span length (Equation 3.14). However, the span length also affects $y_{rms\text{-}axial}$ (Equation 3.21) and the natural frequency, f_1 (Equation 3.4). While the relationship between wear rate and span length is complicated, the net effect is a decrease in the wear rate with a decrease in the axial pitch.

The maximum cross-flow velocity of the wire wraps is higher than grid spacers, although this difference reported in Table 3.6 is likely overstated. The cross-flow velocity of wire wraps was computed using the swirl angle as per Equation 3.11, and the cross-flow velocity of grid spacers was computed by VIPRE, and the large difference between the two is not likely to be reflected in reality. While the value of $y_{rms\text{-}cross}$ is much larger for wire wraps than grid spacers, it still has little effect on y_{rms}.

3.3.3 - Conclusions

This analysis predicts that wire wraps will have a lower fretting wear rate than grid spacers. The assumptions necessary for this analysis could create a discrepancy between these results and reality, however. As always, testing will need to be done to confirm the results. But this analysis shows that wire wraps have the potential for good fretting wear performance, and should not be discarded offhand due to fretting wear concerns.

The fretting wear performance of wire wraps versus grid spacers can also be assessed qualitatively. One of the largest differences between the two is the increased number of support points achieved with wire wrap. Wire-wrapped assemblies have six contact points at three axial locations over the axial pitch. It is anticipated that this will increase the effective stiffness of the rod, increasing the natural frequency and decreasing the turbulence induced vibration. The net effect of this is to decrease the fretting wear rate. It is also possible to decrease the axial pitch of wire wraps without a prohibitive pressure drop increase, additionally increasing the stiffness of the rod.

It is generally held that grid spacers provide a limited amount of room for movement, but, due to the porosity, wire wraps will have more room for movement, possibly allowing impaction between rods, increasing the fretting wear. However, for the large bundles considered here, the average porosity per rod would be very low, creating very little room for movement. There is also some freedom of movement for grid spacers caused by the embrittlement of the grids due to irradiation. Generally, it is likely that the wire-wrapped bundles will not have substantially more freedom of movement than grid spacers. If the porosity stays at the edge of the bundle, the center rods will have no freedom of movement. With no freedom of movement at the contact points, the rods will not slide against each other and wear cannot occur. In addition, as discussed in Section 3.1, the uneven power distribution across the core will cause rod bow, and the porosity of a wire-wrapped bundle will accumulate at one side. Provided that THV is not experienced, none of the rods will have freedom of movement, and fretting wear will not occur.

The combination of this analysis and qualitative assessment suggest that wire wraps will likely experience less fretting wear than grid spacers.

Chapter 4 : Pressure Drop

4.1 - Pressure Drop Comparison of Wire Wraps and Grid Spacers

4.1.1 - Comparison at Reference Geometry

Pressure drop proved to be limiting over a large range of grid spacer geometries [1], so an improvement in the pressure drop can give substantial power increases. The pressure drop is not considered to be a hard constraint in this work, but a limit will still be imposed. An improved pressure drop performance will allow higher achievable powers before the limit is reached. While the friction pressure loss of wire wrap arrays is larger than that of bare rods due to the presence of the wire, the lack of grid spacers in wire wrapped bundles removes the associated form losses within the bundle. The net result is a better pressure drop performance of wire wraps over grid spacers for nearly every geometry considered. The pressure drop is the one design constraint based on extensive experimental data, so the improved pressure drop is quantitatively verifiable.

_P advantages of wire wrap	_P disadvantages of wire wrap
No bundle form losses	Larger P_w
	Smaller A_{flow}

Table 4.1 - _P differences of wire wraps and grid spacers

To illustrate the potential pressure drop improvement of wire wraps, the total pressure drop of wire wraps and grid spacers can be compared. The total pressure drop is computed as a sum of component pressure losses.

$$\Delta P_{total} = \Delta P_{fric} + \Delta P_{grav} + \Delta P_{ent/exit} + \Delta P_{spacer} \qquad [4.1]$$

This total pressure drop was computed for the reference core with grid spacers by Trant [2]. An analogous wire-wrapped core with the same H/HM ratio can be constructed using the thermal-hydraulic wire wrap equivalence of Section 7.2.2. The only difference between the equivalent square and hexagonal cores is that $P/D_{hex} = 1.0746*P/D_{sq}$. Table 5.2 compares these equivalent wire wrap and grid spacer geometries. The wire wraps

have an axial pitch to diameter ratio of $\left(H/D\right) = 50$, the chosen value for the Achievable Case at the reference geometry.

	array	H/HM	P/D	D (mm)	D_e (mm)	A_{flow} (mm^2)	H/D	L (m)
Grids	sq.	12.99	1.326	9.5	11.77	87.8	54.9	4.27
Wire wraps	hex.	12.99	1.425	9.5	7.05	75.0	50	4.27

Table 4.2 - Comparison of reference geometry to equivalent wire wrap geometry

Applying the reference power (3800 MWth) allows a direct comparison of the pressure drop performance of grid spacer bundles and wire wrap bundles over the PWR core length. Table 5.3 summarizes the results and shows the substantially superior pressure drop performance of wire wraps. Acceleration pressure losses across the core will not change appreciably between grid spacers and wire wraps, and are not considered here.

	Grids	Wire wraps
Friction losses (ΔP_{fric})	8.66 psia	19.00 psia
Spacer losses (ΔP_{spacer})	15.44 psia	--
Gravity losses (ΔP_{grav})	4.55 psia	4.55 psia
Entrance/Exit losses ($\Delta P_{ent/exit}$)	2.25 psia	1.51 psia
Total pressure loss (ΔP_{totalt})	30.9 psia	25.1 psia

Table 4.3 - Comparison of component pressure drops for reference power

The pressure drops calculated here are an analytical solution, assuming constant mass flux across the core. The total predicted core pressure drop for wire wraps is 5.8 psia, or 19%, lower than the pressure drop for grid spacers. VIPRE's calculation of pressure drop, using the same pressure drop correlations, is consistent with this analytical solution, and predicts that wire wraps have an 18% lower pressure drop. The results from VIPRE are slightly different because of the communication allowed between the subchannels. VIPRE also accounts for temperature dependent property changes.

4.1.2 - Comparison over Geometry Ranges

This improved pressure drop performance allows increased power with wire wraps without exceeding the pressure drop limit. Since the pressure drop improvement is substantial, this can result in substantial power increases for wire wrapped over grid spacer bundles of the same H/HM ratio when the pressure drop is limiting.

Using VIPRE, it is possible to compare the pressure drop of grid spacers and wire wraps over a range of geometries at reference power. The results of this comparison are in Figure 4.1, which shows the pressure drop difference between wire wraps and grid spacers. For tight geometries, wire wraps are vastly superior to grid spacers. However, as P/D increases, the grid spacer performance approaches, and eventually exceeds, the wire wrap performance.

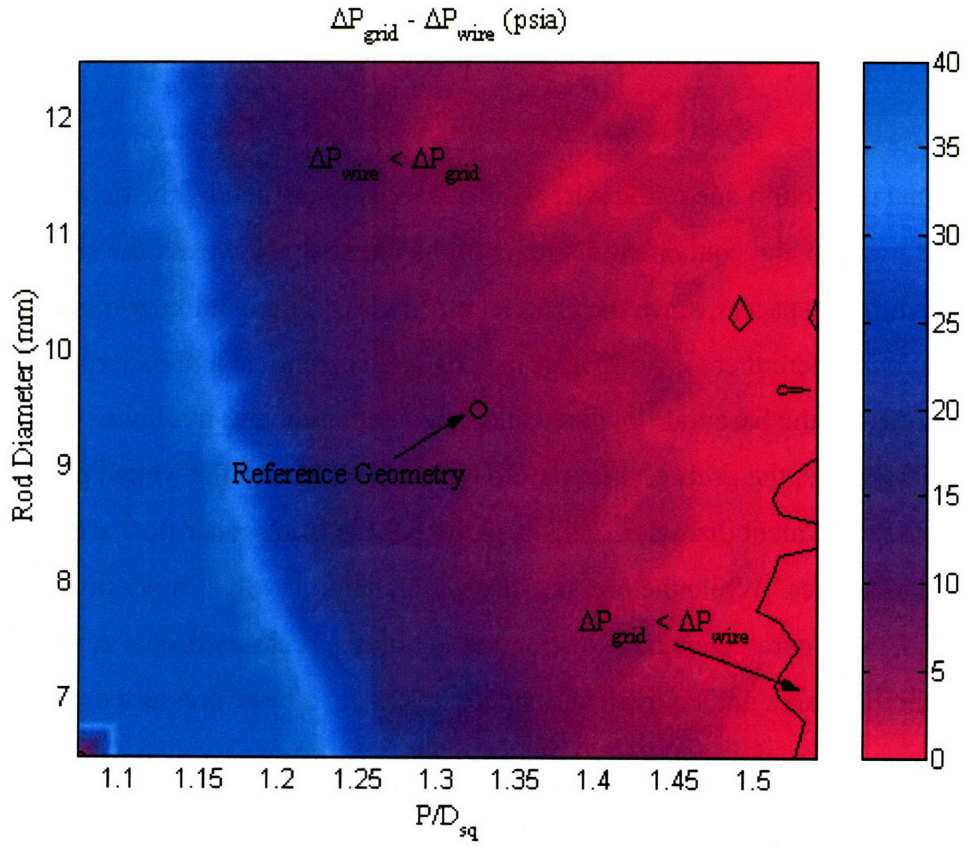

Figure 4.1 - Comparison of Wire Wrap and Grid Spacer Pressure Drop at Reference Power Over a Standard Range of Geometries

The grid spacers are a constant thickness, regardless of D or P/D, while the wire size depends on both. Qualitatively, the wire wraps have better performance at tight geometries because the grid spacer strap thickness become more restrictive as the rod gap decreases, while for wire wraps, the wire simply becomes smaller and generally less restrictive. Alternatively, for high P/D the wires become very large and obstructive (to fill the increasingly large gap between the rods), and eventually the wire wrap pressure drop exceeds the grid spacer pressure drop.

The flow area and equivalent diameter are calculated for the reference pitch, and plotted as a function of P/D_{sq} in Figures 4.2 and 4.3. Physically, holding the reference pitch constant and varying P/D_{sq} is effectively the same as changing the rod diameter, as shown in Equation 4.2.

$$D = \frac{P}{\left(P/D\right)} \qquad [4.2]$$

The channel restriction due to the wire wrap spacer is illustrated by the decrease in the resultant flow area and equivalent diameter of the channel. However, the situation is not as simple for grid spacers, since the channel profile is different at the grid spacers. At axial locations where there is no spacer, the channel is identical to a bare rod channel. This is plotted as the bare rod flow area and equivalent diameter in Figures 4.2 and 4.3. At the grid spacers, the grids restrict the flow area and increase the wetted perimeter, reducing the equivalent diameter. This is plotted as the grid spacer flow area and equivalent diameter. While the pressure drop calculation involves more than these parameters, these parameters have a strong effect on the pressure drop. A small value for both the flow area and equivalent diameter results in a large pressure drop.

Figure 4.2 - Flow Area as a Function of P/D_{sq} for Reference Pitch (12.6 mm)

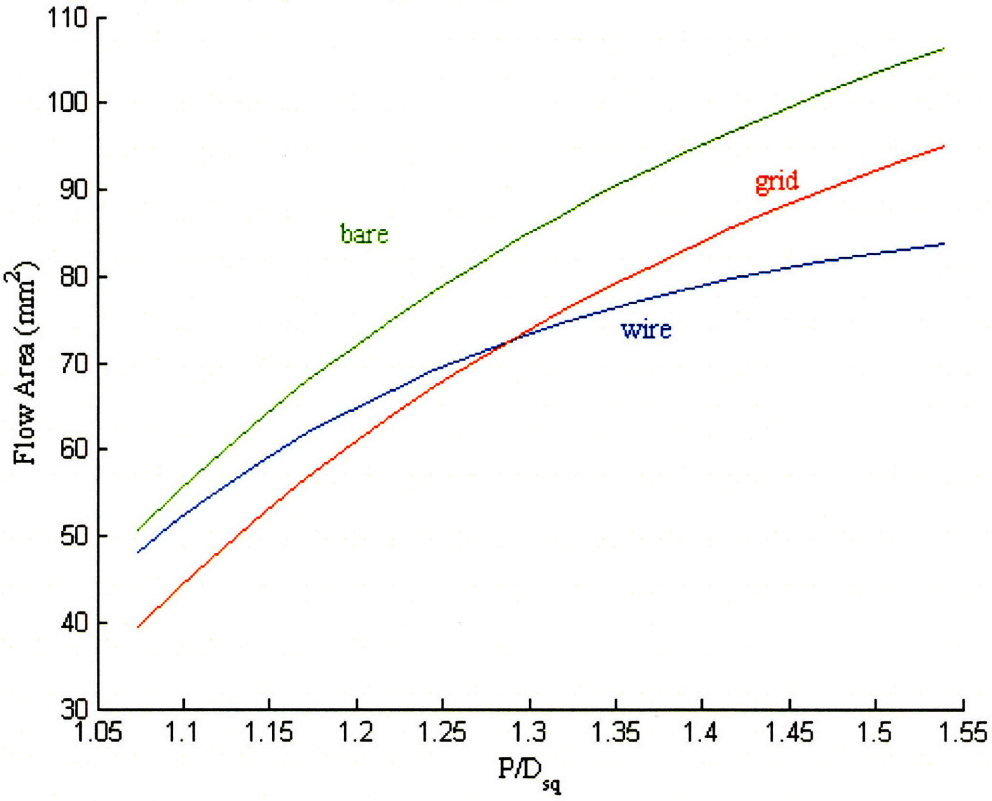

Figure 4.3 - Equivalent Diameter as a Function of P/D_{sq} for Reference Pitch (12.6 mm)

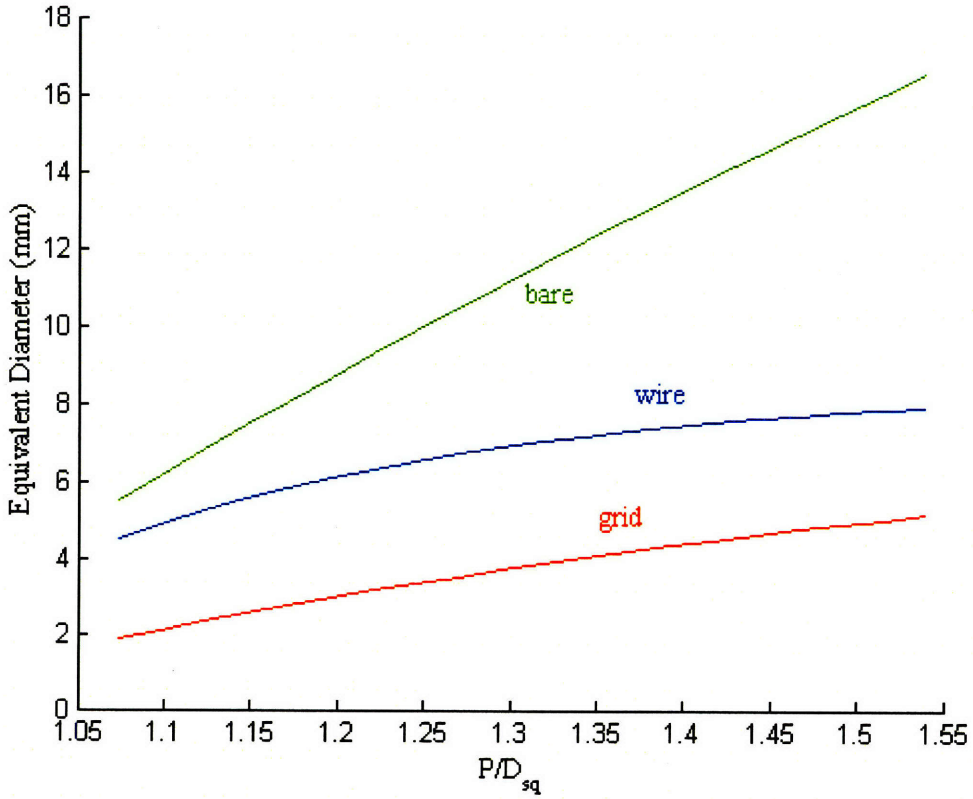

The wire wrap flow area and equivalent diameter approach bare rod values for small P/D, and will actually converge for P/D = 1. As P/D increases, the flow area and equivalent diameter deviate substantially, resulting worse pressure drop performance of wire wraps compared to bare rods. Physically, worse pressure drop performance of wire wraps at large P/D values is because of the large size of the wires compared to the size of the rods, which tend to block the channel.

Regardless, the wire wrap pressure drop is superior for the vast majority of geometries, and superior for all of the geometries of interest, as found later on in this study (see Section 8). This is mainly due to the removal of the grid spacers, which represent very substantial form losses resulting from the sudden geometry change and imposition of the grid spacers on the fully-developed flow at the center of the channel.

4.2 - Bare Rod Pressure Drop Correlation, Cheng/Todreas

Cheng and Todreas **[14]** created a pressure drop correlation for the different subchannel types (interior, edge and corner) of bare rods in square and hexagonal assemblies. The bare rod friction pressure drop is calculated by Equation 4.3.

$$\Delta P_{fric,bare} = f \frac{L}{D} \frac{G^2}{2\rho} \qquad \textbf{[4.3]}$$

Since there are by far more interior channels than other channel types in PWR core bundles, using the interior channel correlation gives a good approximation of the overall pressure drop. Since the grid spacer assemblies considered are square arrays, the square array interior correlation is used. For turbulent flow, the friction factor f is calculated by Equation 4.4.

$$f = \frac{C_{ft}}{Re^{0.18}} \qquad \textbf{[4.4]}$$

$$C_{ft} = 0.09423 + 0.5806\left[\left(P/D\right)_{sq} - 1\right] - 1.239\left[\left(P/D\right)_{sq} - 1\right]^2 \qquad 1.0 \le \left(P/D\right)_{sq} \le 1.1 \qquad \textbf{[4.5]}$$

$$C_{fT} = 0.1339 + 0.09059\left[\left(P/D\right)_{sq} - 1\right] - 0.09926\left[\left(P/D\right)_{sq} - 1\right]^2 \qquad 1.1 \le \left(P/D\right)_{sq} \le 1.5 \quad \textbf{[4.6]}$$

4.3 - Grid Spacer Pressure Loss Correlation, In et al.

Grid spacers are relatively short structures that essentially act as an obstruction to the flow. As such, it is natural to model them as a form loss. That is,

$$\Delta P_{spacer} = C_d \frac{G^2}{2\rho} \qquad \textbf{[4.7]}$$

In et al. **[15]** created the most recent empirical correlation for grid spacers in PWR's. The resulting equation for C_d is a sum of four components - form loss from the grid (term A in Equation 4.8), friction loss from the grid (term B), friction loss from the rod in the spacer region (term C), and form loss from the mixing vane (term D). Term D is only included for mixing vanes. A_v is the bare rod flow area, A_{grid} is the wetted area of the grid spacer, and A_{mv} is the wetted area of the mixing vane, and H is the grid spacer strap height.

$$C_d = \left[C_{d,form}\frac{\varepsilon}{(1-\varepsilon)^2}\right]_A + \left[C_{fric,grid}\frac{A_{grid}}{A_v}\frac{1}{(1-\varepsilon)^2}\right]_B + \left[C_{fric,rod}\frac{A_{grid}}{A_v}\frac{1}{(1-\varepsilon)^2}\right]_C + \left[C_{d,mv}\frac{\varepsilon_{mv}}{(1-\varepsilon_{mv})^2}\right]_D \qquad \textbf{[4.8]}$$

$$\varepsilon = \frac{A_s}{A_v} \qquad \varepsilon_{mv} = \frac{A_{mv}}{A_v} \qquad \textbf{[4.9]}$$

$$C_{d,form} = 2.75 - 0.27\log_{10}(Re_v) \qquad Re_v = \frac{GD_e}{\mu} \qquad D_e = \frac{4A_v}{\pi D} \qquad \textbf{[4.10]}$$

$$C_{fric,grid} = C_{fric,lam}\frac{L_t}{H} + C_{fric,turb}\frac{H - L_t}{H} \qquad L_t = \frac{30{,}000 \cdot \mu}{G} \qquad \textbf{[4.11]}$$

$$C_{fric,lam} = 1.327 \cdot Re_L^{-0.5} \qquad C_{fric,turb} = \frac{0.523}{ln^2(0.06 \cdot Re_L)} \qquad Re_L = \frac{G(H - L_T)}{\mu} \qquad \textbf{[4.12]}$$

$$C_{fric,rod} = f\frac{H}{D_e} \qquad f = \frac{0.184}{Re_v^{0.2}} \qquad \textbf{[4.13]}$$

$C_{d.mv}$ is an empirical constant between 0.6 and 0.8, with a recommended value of 0.72.

4.4 - Wire Wrap Pressure Drop Correlations

While grid spacers are treated as a form loss, wire wrap spacers are inherently different, since there is a pressure loss due to the wires along the entire length of the bundle. The experimental results were consistent with this distributed pressure loss from the wire, and consequently the pressure drop effect of the wire is treated as a modification to the friction factor. From the pressure drop calculation in Section 4.1, the gravity loss is constant, and the entrance/exit losses of the wire-wrapped bundle are insignificant, so the pressure drop can be characterized by the friction loss across the bundle. The friction loss is computed using the Darcy friction factor as follows,

$$\Delta P_{fric} = f\frac{L}{D_e}\frac{G^2}{2\rho} \qquad \textbf{[4.14]}$$

D_e is the equivalent diameter of the wire-wrapped bundle, computed as

$$D_e = \frac{4A}{P_w} \qquad \textbf{[4.15]}$$

A is the flow cross-sectional area and P_w is the wetted perimeter of the subchannel. Both include the effect of the wire wrap. The friction factor f is empirically fitted to extensive experimental data.

4.4.1 - Cheng/Todreas Friction Factor Correlation

Using an experimental database of 137 different geometries, Cheng and Todreas **[11]** created two correlations for the wire wrap friction factor. The first is a more exact method (the original method), based on finding the friction coefficient of individual

channels and calculating flow splits. After empirically fitting a simpler correlation to the first method, Cheng and Todreas found that the number of pins had little effect on the friction factor. The resulting empirical correlation (the simple correlation) is independent of the number of pins, and is much more convenient to use. As a result Equations 4.16 and 4.17 comprise the simple correlation used in this study.

$$f = \frac{C_{fbT}}{Re^{0.18}} \quad \textbf{[4.16]}$$

where

$$C_{fbT} = \left(0.8063 - 0.9022\left(\log\left(H/D\right)\right) + 0.3526\left(\log\left(H/D\right)\right)^2\right) \cdot \left(P/D\right)_{hex}^{8.7} \cdot \left(H/D\right)^{7.8-2.0\left(P/D\right)_{hex}} \quad \textbf{[4.17]}$$

This correlation is valid for

$$1.025 \le \left(P/D\right)_{hex} \le 1.42 \quad \textbf{[4.18]}$$

$$8.0 \le \left(H/D\right) \le 50.0 \quad \textbf{[4.19]}$$

Figure 4.4 shows some of the experimental data used to create the correlation. This study has determined the geometries of highest power have large P/D_{hex} values. The maximum P/D_{hex} covered by the correlation is 1.42, which is the maximum P/D_{hex} for which there is experimental data. As a result, the maximum P/D_{hex} considered in the power maps will be 1.42. From Table 5.2, the P/D_{hex} value equivalent to the reference geometry is 1.425. As a result, the H/HM values considered for wire wraps will approach, but always be less than the reference geometry H/HM value. In addition, for hydride fuels $P/D_{hex} < 1.42$ has better neutronic performance than $P/D_{hex} > 1.42$, and restricting the geometries to this range results in a larger D at the maximum power, which is much more feasible from a manufacturing perspective. For all these reasons, the geometry range will be restricted to $P/D_{hex} < 1.42$.

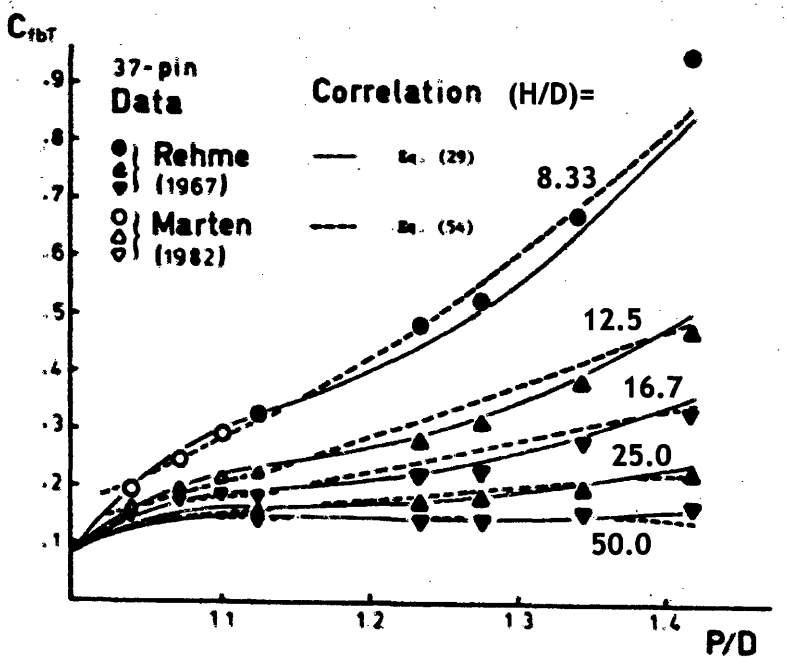

Figure 4.4 - Experimental results with Cheng/Todreas correlation predictions

The solid line corresponds to the first, more exact method. The dotted line (labeled Eq. 54 in the diagram) corresponds to the simple correlation (Equation 4.17), the correlation used in the final results. As mentioned before, the database for this correlation consisted of 137 geometries. To get an idea of the applicability of the correlation to our situation, Figure 4.5 shows the D and P/D values for which data is available.

In 2001, Chun et al. **[16]** performed pressure drop experiments of wire wrap bundles, and compared the results to the predictions of 4 correlations. Chun concluded that both the original and simple Cheng and Todreas correlations give the best agreement with experimental data for all flow regions. The geometries used by Chun are also plotted in Figure 4.5, and are confirmation that the Cheng/Todreas correlation is valid for those geometries.

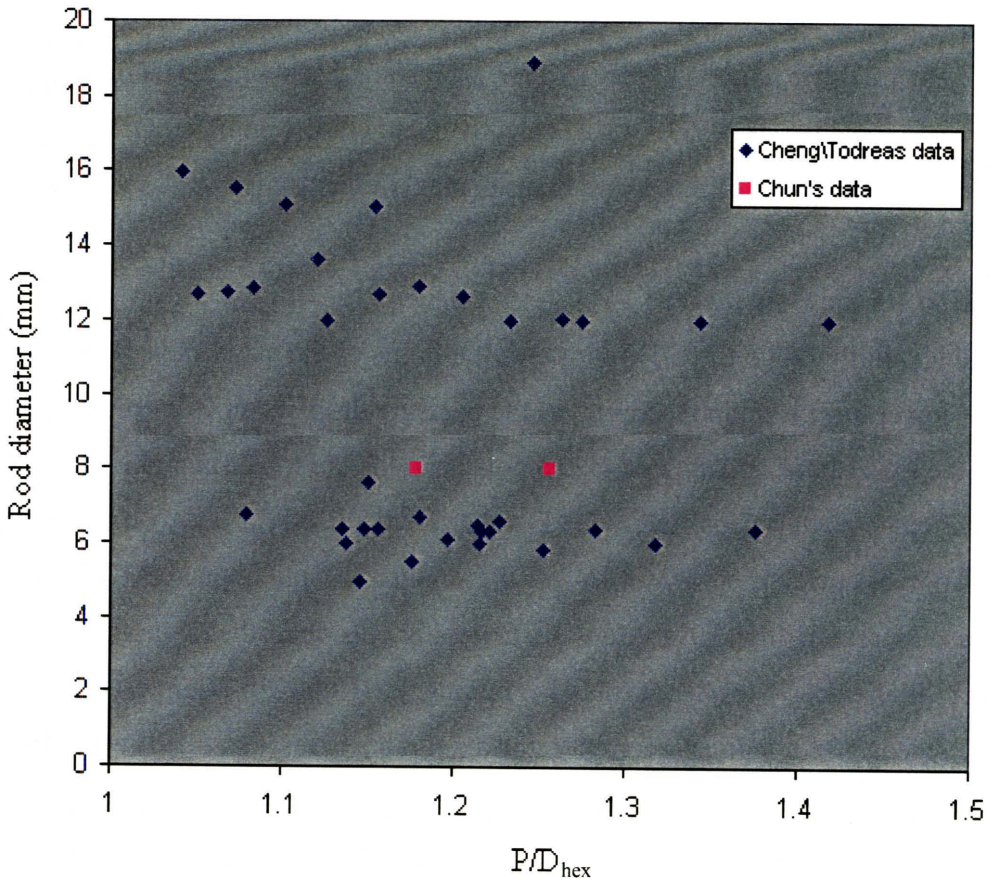

Figure 4.5 - Geometries of Experimental Friction Factor Data used in the Creation of Cheng/Todreas Average Bundle Friction Factor Correlation

Figure 4.5 shows that the range of geometries considered in this work (6.5 mm _ 12.5 mm) are relatively covered. There appears to be somewhat of a gap in the middle of the range of interest (8 mm _ 11 mm). However, since the extremes of the range are known, it is reasonable to assume that the intermediate diameters are well-behaved. In addition, the rod diameter only affects the equivalent diameter in the pressure drop calculation, and the behavior of pressure drop with equivalent diameter is well known.

4.4.2 - P/D Range Considered

A more serious problem is the P/D ratio. The lower limit is not of immediate concern, as low P/D geometries do not deliver high powers. As suggested by the limits of the correlation, there is no data for P/D > 1.42. However, the correlation appears to cover P/D < 1.42 very well. As a result, the range of geometries considered in this study is restricted to P/D < 1.42. While it is reasonable to extend the correlation past 1.42, there

is no experimental data to verify the pressure drop results calculated by VIPRE for P/D > 1.42. There are other reasons to restrict P/D, which are discussed in Chapter 7 (Core Performance Results), and P/D = 1.42 is a convenient cut-off point, so P/D = 1.42 is the upper limit of P/D on all of the power maps created in this study.

4.4.3 - H/D Range Considered

Again, the validity range for H/D represents the limits of the experimental data. As for P/D, the lower limit is not concerning, as the pressure drop becomes extremely high around the lower limit and the associated powers are low. A constant H is adopted for the steady-state power maps, and the H/D value is calculated for use with the simple Cheng/Todreas correlation. However, for the smaller fuel pin diameters, H/D can exceed 50. These extremely high H/D values are generally outside of the range of experience, not just pressure drop experience, but also mixing, CHF and vibration tests. As a result, if H/D exceeds 50 for a given geometry, the axial pitch is reset so that H = 50*D and H/D is never more than 50.

4.5 - Effect of P/D on Pressure Drop

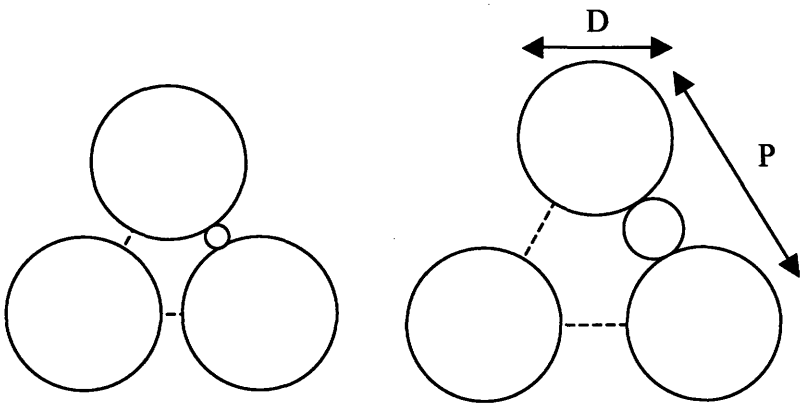

Figure 4.6 - Illustration of Variance of P/D

The Pitch to Diameter ratio (P/D) has a profound effect on pressure drop, both for grid spacers and wire wraps. Geometries with a small P/D have a small flow area. This decreases D_e and increases G (to hold the mass flow rate, and thus power constant), both of which substantially increase the pressure drop. This gives high P/D values a much

improved pressure drop performance, and is the fundamental reason that high P/D values give much higher achievable power.

Figure 4.6 gives an illustration of the effect on the subchannel geometry of changing P/D while holding D constant. While the flow area is larger with the large P/D, the wire is also larger. Figure 4.7 shows the effect that changing P/D has on pressure drop. This is for the reference pin diameter at reference power. As shown before, there is a substantially smaller wire wrap pressure drop for geometries with small P/D values, but the two pressure drops converge with increased P/D. The curves cross at the highest P/D value, so for P/D > 1.55, the grid spacer pressure drop is better. However, for both wire wraps and grid spacers, there are clearly large pressure drop benefits of moving to high P/D values. This is turn can allow higher powers without violating the pressure drop constraint.

Figure 4.7 - Pressure Drop Comparison at Reference Power and Pin Diameter

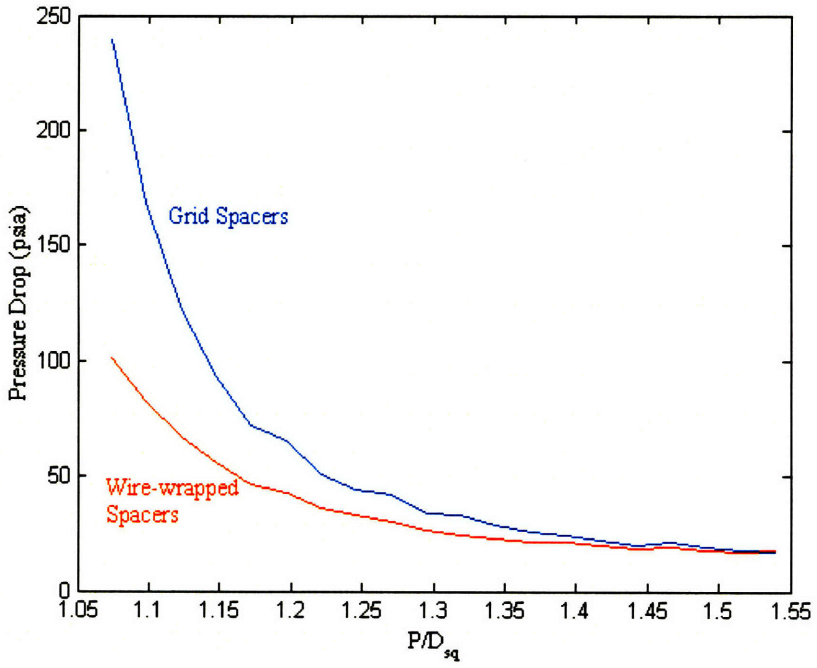

Chapter 5: Turbulent Mixing

For the majority of this study, subchannels are dealt with on an individual basis, and the effect of adjacent subchannels is ignored. While this is generally a good approximation, in reality, adjacent subchannels can exchange mass, momentum, and energy, leading to a CHF benefit for wire wraps in particular.

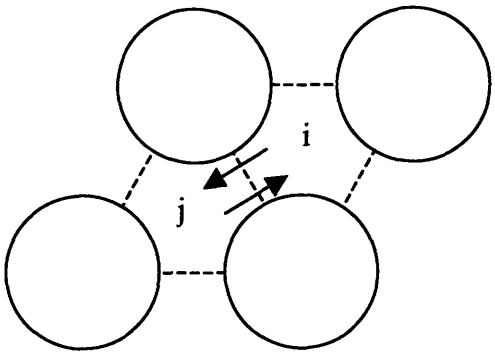

Figure 5.1 - Adjacent subchannels

5.1 - Mixing Mechanisms

The most important effect of the mass interchange is the effect on the enthalpy distribution across the bundle. The linear power is different for different rods, due to the neutronics of the bundle. The power density varies across the core as a result of the neutron leakage, difference in fuel assemblies' composition, and location of control rods. The highest linear power is, typically, near the center of the core. The hot channel is the channel with the highest heat output. This effect is captured by the radial peaking power, as defined in Equation 5.1.

$$F_p = \frac{q'_{hot}}{q'_{ave}} \qquad [5.1]$$

The average core-wide enthalpy rise is fixed as 204 kJ/kg, consistent with the reference core enthalpy rise. However, the enthalpy rise of individual subchannels will be different than the average core-wide enthalpy rise. The enthalpy of a given channel is dependent on the linear heat rate of the rods that surround it, as well as the interchange of mass and

energy between subchannels. There are two mechanisms that cause mixing: diversion cross flow due to pressure gradients, and turbulent interchange due to fluctuations in the axial flow.

5.1.1 - Diversion Cross Flow

Diversion cross flow can be thought of as a macroscopic phenomenon. This occurs when the fluid in one channel is hotter than the other channel, causing a density variation. The density difference causes a pressure differential between the two subchannels, and fluid from the hot channel moves to the cold channel. The density difference and associated pressure drop can be substantial in the presence of phase change, as in BWR's. Since diversion cross flow moves coolant away from the hot channel, the fluid exiting the hot channel will have a higher enthalpy than it would without diversion cross flow.

5.1.2 - Turbulent Interchange

However, diversion cross flow is not dominant in the PWR since the fluid is single phase, making the density difference between the channels negligible. The predominant subchannel mixing in a PWR occurs due to turbulent interchange. Turbulent interchange is random movement of mass in the form of eddies due to the turbulence of the flow. This effect can be substantial for the extremely turbulent flow in the core.

Since turbulent interchange is the exchange of mass between subchannels, it serves to bring the enthalpies of the two subchannels closer to each other. This effect occurs across the entire bundle, and makes the enthalpy distribution flatter. Most importantly, this helps to cool the hot channel, improving its CHF performance and thus the CHF performance of the bundle.

However, in practice, mixing does not noticeably impact the performance of a PWR. This is due to two reasons:

1. *The enthalpy distribution in the hot bundle is already flat.* For this study, a polynomial distribution is assumed across the core, and the hot bundle is close to the center of the core. The power for this distribution is relatively flat near the

center of the core, and since all derivatives of the distribution are continuous, the power distribution of the hot channel (at the distribution's maximum) must be flat. The governing equation of the radial power distribution is given by Equation 7.2, where r is the distance from the center of the core.

$$F_p = 8.8628 \cdot 10^{-6} \cdot r^3 - 8.6337 \cdot 10^{-4} \cdot r^2 + 5.7179 \cdot 10^{-3} \cdot r + 1.6402 \qquad \textbf{[5.2]}$$

To illustrate this graphically,

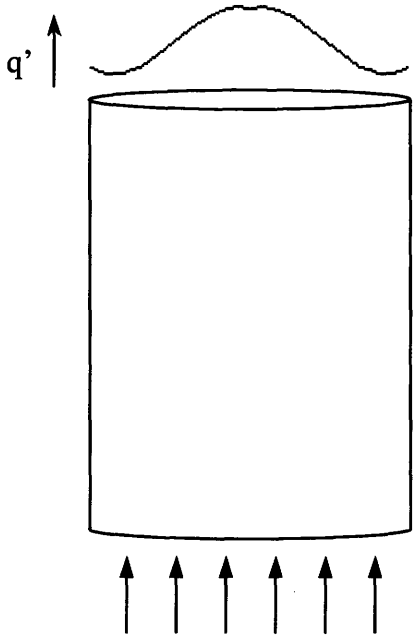

Figure 5.2 - Radial Power Distribution Across the Core

Since the exit enthalpy distribution roughly follows the power distribution, the flat power distribution at the center of the core results in a flat enthalpy distribution. This flat enthalpy distribution near the center of the core means that the effect of turbulent mixing will not improve the CHF of the hot channel, and therefore will not affect the steady state achievable power of the core.

2. *Turbulent interchange is not effective enough to directly affect the enthalpy distribution across a bundle.* This conclusion was reached by Collingham et al.**[10]**, after performing a mixing experiment on a 217-pin wire-wrapped bundle.

In particular, Collingham concluded that the mixing is insufficient to affect the temperature differences between the walls of the assembly.

Collingham **[10]** reached this conclusion even though the average interior cross flow was 20% of the channel flow per inch. This is a very substantial cross flow, but for the mixing to temper the enthalpy difference across a bundle, cool fluid has to travel across multiple channels to cool a hot channel. From Figure 5.3, for flow from channel 1 to reach channel 3, it has to go through channel 2. 20% of the flow from channel 1 reaches channel 2, and approximately 20% of that reaches channel 3. This means that only 4% of the flow from channel 1 reaches channel 3. Thus, the effect of turbulent interchange decreases approximately exponentially with the number of rows of channels considered, and turbulent interchange over a large number of rods quickly becomes insubstantial. This conclusion is consistent with Collingham's results, that the enthalpy distribution across a large bundle is unaffected by turbulent interchange.

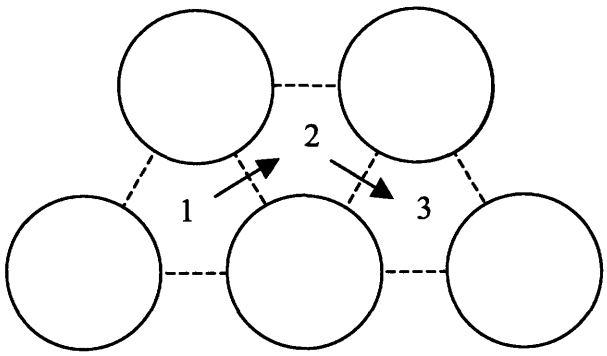

Figure 5.3 - Multiple Channel Turbulent Interchange

5.2 - Turbulent Mixing

5.2.1 - Turbulent Interchange Correlations

For subchannel analysis codes such as VIPRE, mass and momentum exchange due to the turbulent interchange can be quantified. The most common form of expressing the turbulent interchange between subchannels i and j is through the turbulent crossflow (w')

$$w' = \beta \cdot S \cdot \overline{G} \qquad \textbf{[5.1]}$$

where _ is the mixing coefficient, S is the gap width, and $\overline{G}$ is the average mass flux of the two subchannels.

$$\overline{G} = 0.5 \cdot (G_i + G_j) \qquad [5.3]$$

_ is unitless, S has units of length, and $\overline{G}$ has units of mass flow per area. As a result, w' has units of mass flow per unit length. Physically, w' is the mass flow rate from subchannel i to j across the gap separating the two per unit axial length.

5.2.2 - Mixing Coefficient

The mixing coefficient (_) is the only unknown in solving for w'. Cheng and Todreas **[14]** correlated _ for wire-wrapped bundles, according to the following set of equations.

$$\beta = C_{mT} \sqrt{\frac{A_{r1}}{A_1'}} \left(\frac{\pi}{H/D} \right) \qquad [5.4]$$

$$C_{mT} = 0.14 \cdot \left(P/D \right)_{wire} - 1 \Big)^{0.5} \qquad [5.5]$$

$$A_{r1} = \pi (D + d_w) d_w / 6 = \frac{\pi D^2}{6} \left(P/D \right)_{wire} \left(P/D \right)_{wire} - 1 \Big) \qquad [5.6]$$

$$A_1' = D^2 \left[\frac{\sqrt{3}}{4} \left(P/D \right)_{wire} - \frac{\pi}{8} \right] \qquad [5.7]$$

This correlation is the correlation implemented for use in VIPRE in determining the steady-state achievable power.

5.2.3 - Effect of Mixing Coefficient on Steady-State Power

After running scenarios with different mixing coefficients (_), it was noticed that _ has very little effect on the achievable steady-state power. See Chapter 8 for a detailed

discussion of the steady-state Achievable Case used for this illustration. A standard MATLAB/VIPRE run was performed using the _ correlation above. An identical run was also performed with the mixing coefficients all set at zero. Thus, the first run had turbulent interchange, while the second run had no turbulent interchange (the subchannels did not communicate at all).

The steady-state achievable power results (with and without subchannel mixing) are shown in Figures 5.4 and 5.5. If the two figures look similar, it is because they are. The maximum achievable power was different by 2.3%. The two maps are superimposed in Figure 5.7 to give the percentage power increase offered by mixing. For almost the entire power map, the power increase with mixing is less than 5%. However, there is a small portion of the power map that predicts upwards of a 25% increase in the achievable power with mixing. It is not apparent why only a small fraction of the geometries have substantially increased power with mixing. Figure 5.6 shows the wire wrap mixing coefficients used. The difference in mixing coefficients across the power map cannot explain the region of increased power with mixing, as the trends do not match. It is more likely that the increased mixing coefficient affects regions of the power map differently, depending on what parameter is constraining the power. The small region that has substantial power increases is exclusively in the CHF-limited region (see Chapter 8 for details of the parameter-limited regions), but different areas of the CHF-limited region have different power increases.

The mixing coefficient was taken into account in the final steady-state power analyses, but for reasons that will be discussed in Chapter 7 (Equivalence), the turbulent interchange calculated by VIPRE is not exactly correct. In Chapter 7 it will be illustrated that the mixing calculated by VIPRE is conservative, resulting in a conservative achievable power reported by VIRPE.

Due to the VIPRE modeling approach, for this analysis it was not possible to take into account the effect of the canned bundles necessary for wire-wrapped assemblies. The mixing coefficient between bundles should be zero. This will have an effect on the core-wide enthalpy distribution, and orificing will be necessary for wire wrap implementation.

Figure 5.4 - Core Power (GWth) with mixing

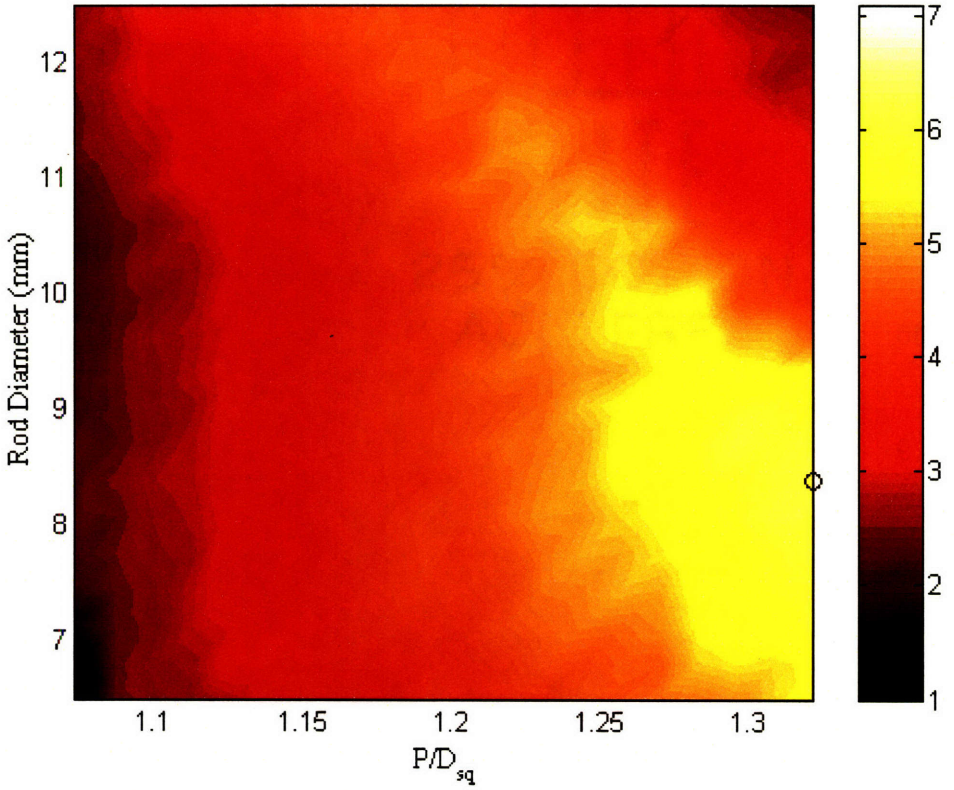

Figure 5.5 - Core Power without mixing

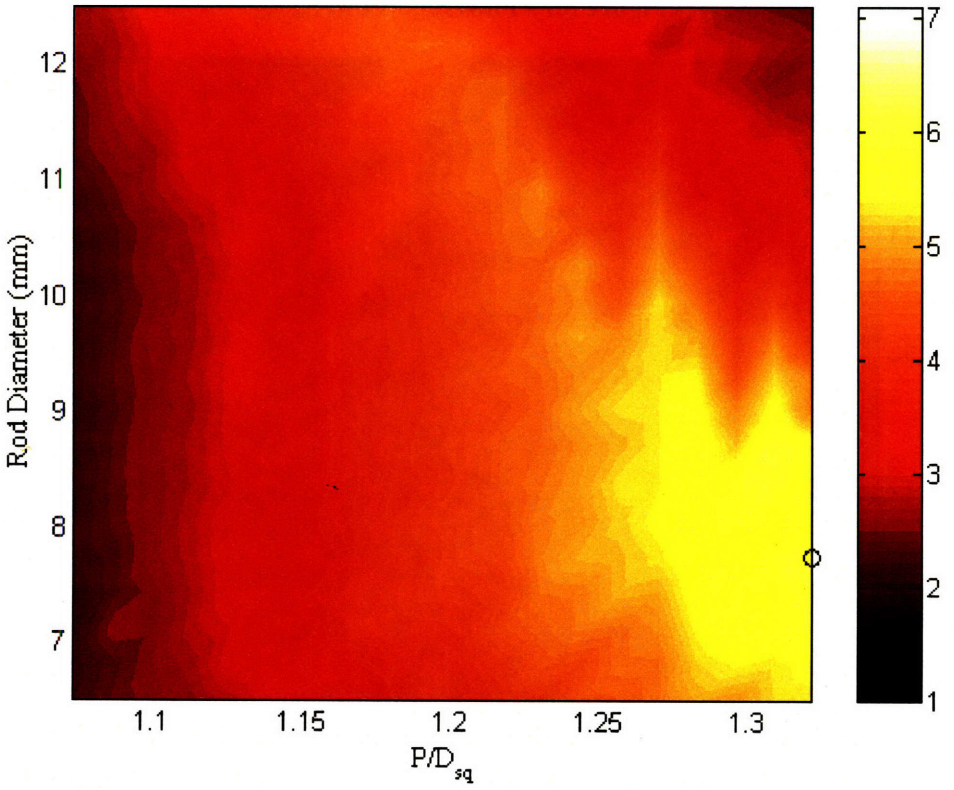

Figure 5.6 - Wire Wrap Mixing Coefficient, _

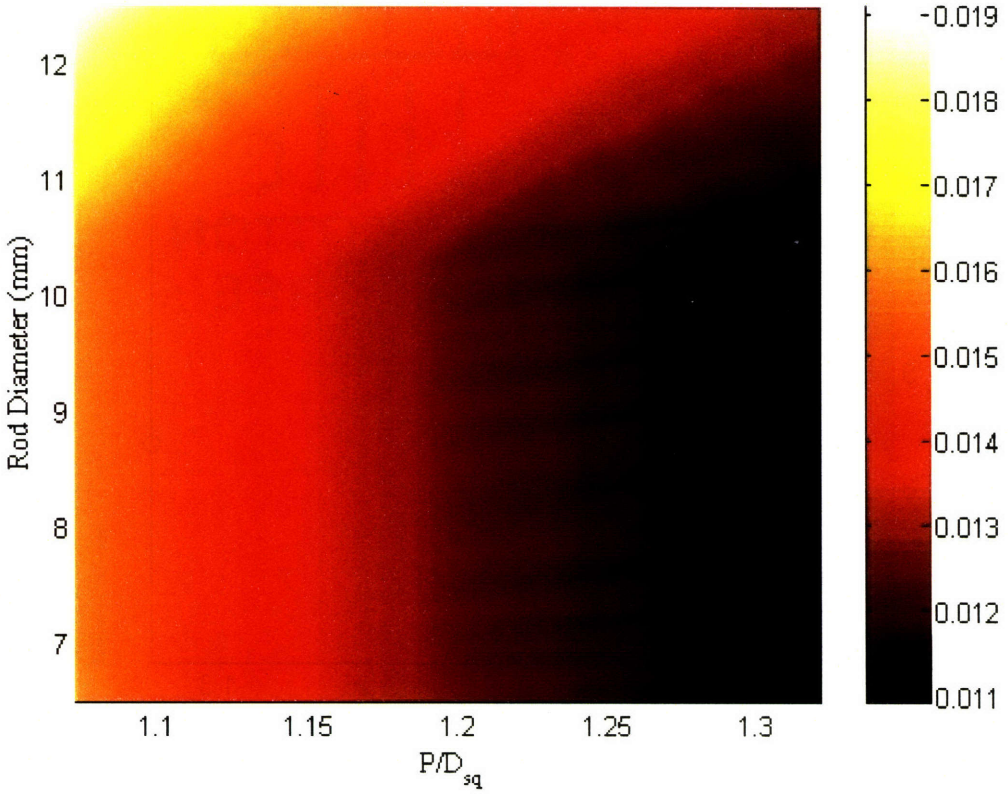

Figure 5.7 - Power$_{mix}$ / Power$_{no_mix}$

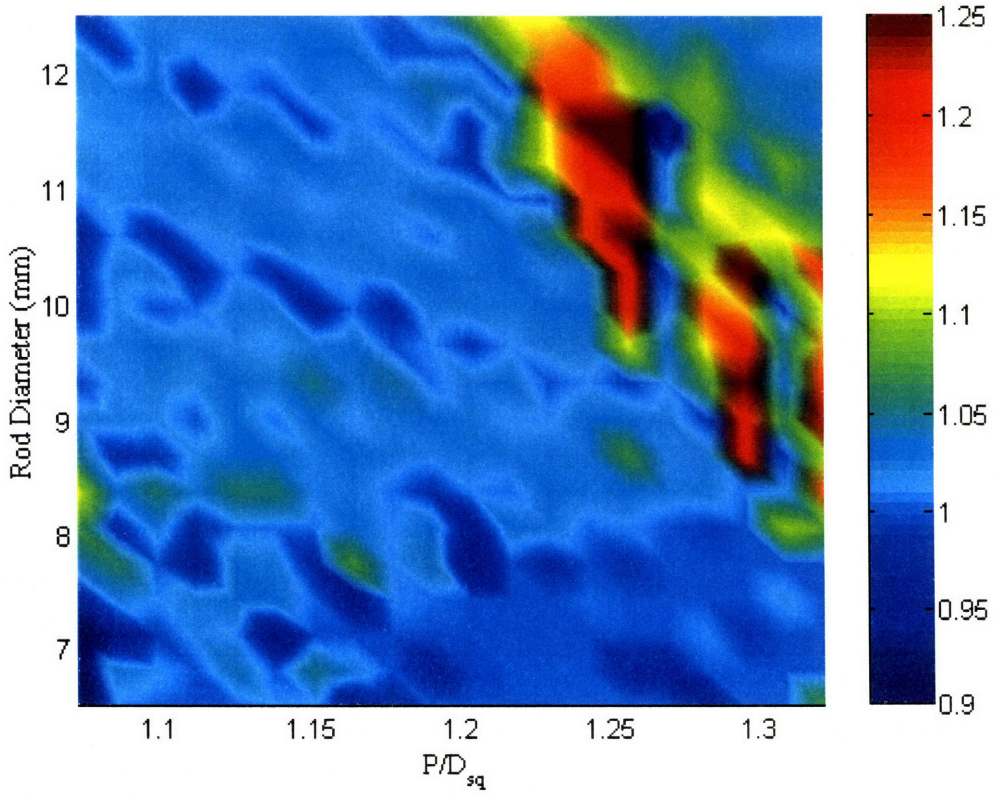

Chapter 6: Critical Heat Flux

6.1 - W-3L Correlation

The W-3 correlation is one of the most widely used CHF correlations for commercial PWR's. Grid spacers provide improved mixing and turbulence locally downstream, improving the CHF of the bundle. The W-3L correlation is a modified form of the W-3 correlation with a correction for L-grid spacers, a type of grid spacer with a mixing vane. This is the correlation used previously in the project for the calculation of the MDNBR.

As with other parameters, the design constraint on the MDNBR is that the predicted CHF performance of a given geometry is at least that of the reference core. Jon Malen used VIPRE to predict the MDNBR of the reference core at reference power. The resulting MDNBR is 2.17, which was set as the MDNBR limit. That is, the MDNBR predicted by the W-3L correlation for any design must be at least 2.17.

6.2 - Qualitative CHF Comparison of Grid Spacers and Wire Wraps

The effect of mixing on the enthalpy distribution across the bundle was shown to have little effect on the steady-state achievable power. But mass communication between subchannels is not the only effect that mixing has on the achievable power.

Increased mixing generally increases the turbulence of the flow within a subchannel. The increased turbulence tends to break up the bubble layer that can lead to CHF and helps feed cooler water to the liquid sublayer adjacent to the rod. As a consequence, improved mixing leads to higher MDNBR, and is of substantial interest to PWR designers. The widespread use of mixing vanes on grid spacers is exactly for this reason.

The CHF of a bundle is a strong function of a myriad of factors, including the physical characteristics of the bundle. In conventional PWR designs, the grids strongly improve the local CHF, as they increase the turbulent mixing of the fluid. As a result, the CHF of the flow directly downstream of grid spacers is very high, but reduces to a bare rod CHF as the flow once again becomes steady.

Analogously, in a wire-wrapped bundle, there are certain axial locations at which the subchannel mixing is substantially higher due to the swirl effect. At these locations, the cross-flow coming off of the wires is directed at the center of the subchannel. Figure 6.1 illustrates the cross-flow effect on the mixing of the channel. The arrows indicate cross-flow caused by the dotted wire.

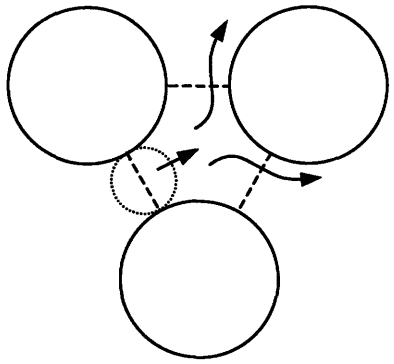

Figure 6.1 - Effect of Wire Wraps on Subchannel Mixing

This cross-flow occurs 6 times every axial pitch, once each time a wire sweeps across a dotted line. For the reference geometry with H/D = 50, there are about as many axial leads as grid spacers. Thus, for each axial location of improved mixing due to grid spacers, there are six analogous wire wrap locations. Since there are many more locations of improved turbulent mixing, the flow in a wire-wrapped bundle will have less of a chance to stabilize before encountering more cross-flow. The result is improved turbulent mixing, and thus CHF, of wire-wrapped bundles.

Figure 6.2 shows this graphically. The dotted lines represent the bare rod CHF, that is if there were no spacers in the bundle. Due to the relatively large gaps between the grid spacers, the CHF is allowed to approach the bare rod CHF. The rods are drawn to scale axially, representing the locations of grid spacers and wire wraps along the length of the rod. However, the CHF curves are not real CHF curves, but are simply drawn to illustrate the effect of more axial locations of increased mixing on the overall CHF.

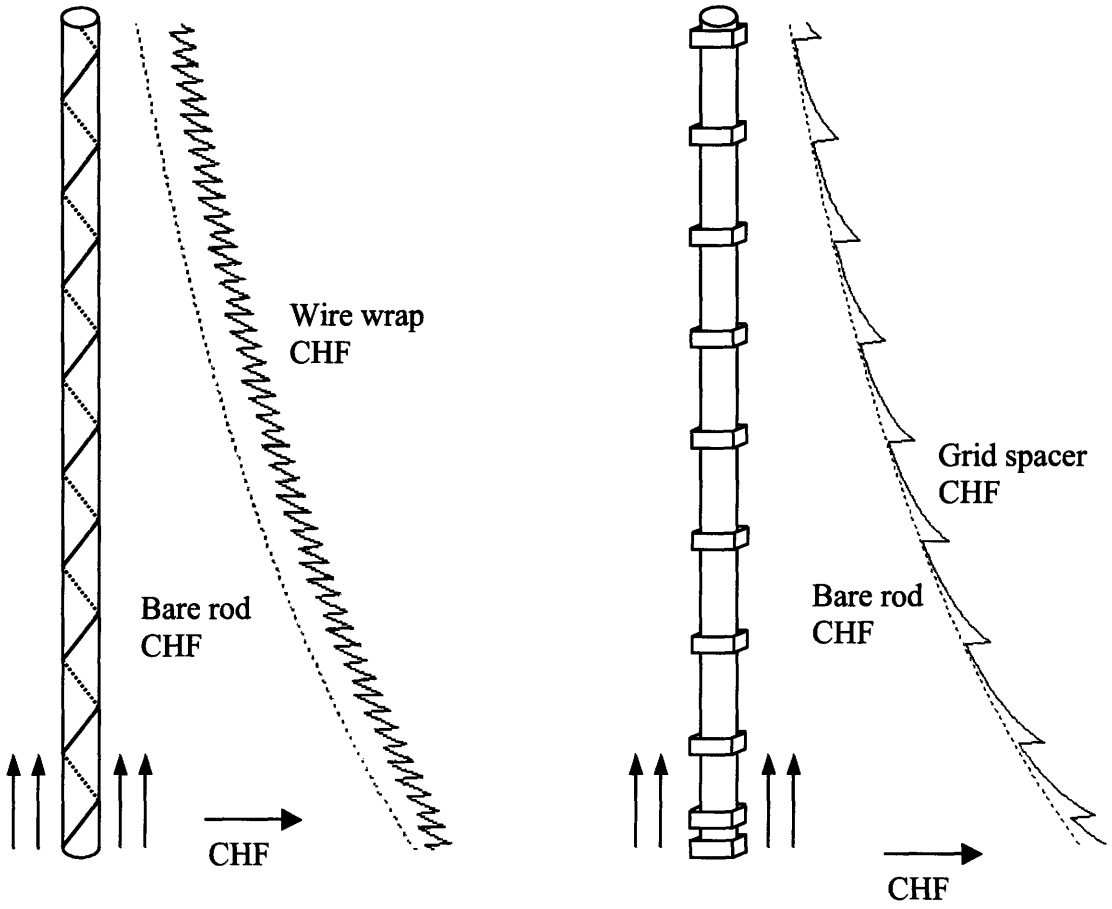

Figure 6.2 - Spacer Effect on Local CHF

6.3 - Experimental Database for Wire Wraps

The importance of CHF to nuclear reactors has led to extensive experimentation and investigation worldwide over the last several decades. This has led to a huge database and many correlations predicting the CHF given the flow conditions and geometry. However, the exact mechanisms of CHF are still unknown, due to the extremely complicated and variable nature of two-phase flow heat transfer.

Even correlating CHF from a purely empirical point of view is difficult, partly due to the huge number of variables (approximately 10 independent parameters for operating conditions and geometries). A correlation is developed using a limited database of experience, and extending the correlation outside of the tested range of parameters is highly speculative.

However, the experimental database for wire wraps is extremely limited. Fast Breeder Reactors (FBR's), the only type of reactor to actually implement wire wraps, used liquid sodium as the coolant. CHF is not a problem with the sodium coolant, so CHF was not tested for wire wraps in the FBR's. The only CHF experiments performed for wire wraps were those performed during research for high-conversion LWR's. These designs generally had tight geometries, to improve the conversion ratio. Table 6.1 summarizes the different wire wrap CHF experiments that are covered in this chapter.

Experiment	D (mm)	P/D	H/D	Comment
Cheng	9.5	1.147	20	Small P/D, H/D
Tong	10.72	1.412	35.5	Wire wrap not on all rods
Selivanov	9.1	1.110	9.9	Qualities tested outside of PWR range
Columbia	11.18	1.051	13.64	Small P/D, H/D

Table 6.1 - Wire Wrap CHF Experiments Reviewed in this Work

The lack of experimental data for the CHF of wire wraps is similar to the lack of experimental data for FIV of wire wraps: there has been little need for it in the past. Since all designs for high-conversion LWR's had tight geometries, the CHF experiments had correspondingly tight geometries. While it is speculative to predict the wire wrap CHF values outside of this narrow range of experimental CHF data, it is possible to qualitatively assess the geometries and use models to predict the CHF with some degree of accuracy.

6.3.1 - Cheng et al.: Direct CHF Comparison of Wire Wraps and Grid Spacers

Fortunately, there is some experimental data that compares the CHF of grid spacers and wires wraps. Cheng et al. **[17]** have performed CHF experiments on identical bundles of wire wraps and grid spacers. The geometry of the bundles are shown in Table 6.2.

Wire wrap and grid spacers		
Number of pins	N	7
Rod diameter	D	9.5 *mm*
Wire diameter	d_w	1.40 *mm*
Pitch	P	10.90 *mm*
Pitch to diameter ratio	P/D	1.147
Axial pitch	H	190 *mm*
Axial pitch to diameter ratio	H/D	20
Wire wrap hydraulic diameter	D_h	4.29 *mm*
Wire Wrap flow area	A_{flow}	16.01 mm^2

Table 6.2 - Cheng CHF Test Geometry

Figure 6.3 shows the Cheng's CHF results for wire wraps and grid spacers, and Figure 6.4 compares the two on separate graphs. The working fluid for this experiment was Freon-12, so the pressures and mass fluxes need to be scaled to be applicable to LWR's. Note that as it appears in Cheng's paper, Figure 6.4 (a) is for grid spacers and Figure 6.4 (b) is for wire wraps. However, this was inconsistent with Cheng's other results and conclusions, and Cheng confirmed **[18]** that the figure here is correct.

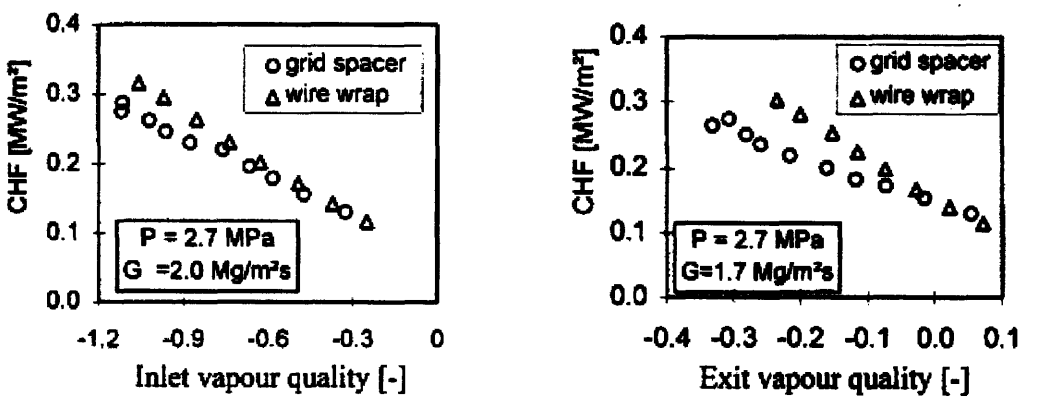

Figure 6.3 - Cheng's CHF Comparison of Grid Spacers and Wire Wraps Plotted Against Inlet and Outlet Conditions

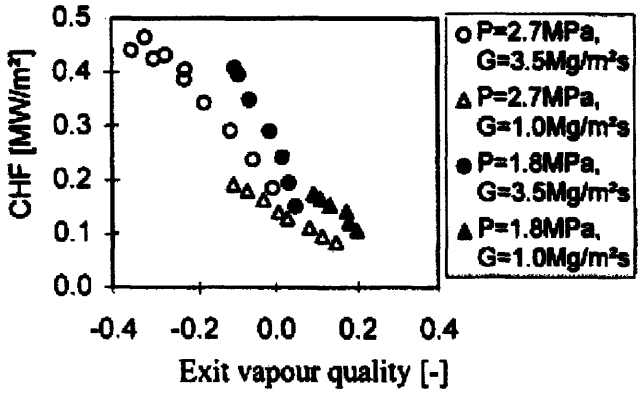

(a) 7-rod bundle with wire wraps

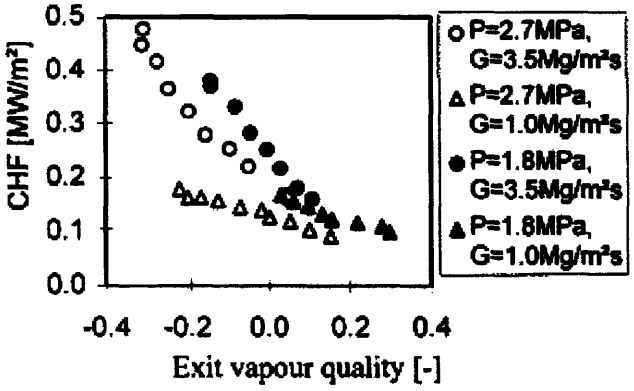

(b) 7-rod bundle with grid spacers

Figure 6.4 - Cheng's CHF Results for Wire Wraps and Grid Spacers in Freon-12

For the exit vapor quality of interest, the wire wrap CHF is approximately 20% higher than the grid spacers. Generally, for lower exit qualities, as is found in PWR's, wire wraps are substantially superior to grid spacers. While this result is for a single geometry, all experimental data points to a higher wire wrap CHF, regardless of the geometry.

The qualitatively and conceptually higher CHF for wire wraps is the basis of the Achievable Case MDNBR limit. The W-3L correlation will be applied to the wire wrap geometry, giving the same CHF prediction as for grid spacers. This will be conservative, as the CHF of wire wraps is proven to be superior to that of grid spacers. But grid spacer CHF is certainly achievable with wire wraps.

6.3.2 - Tong et al.: CHF Comparison of Partial Wire-Wrapped Assemblies to Grid Spacer Assemblies

In 1967, Tong **[19]** performed a DNB experiment that was intended to compare the CHF performance of wire wraps and grid spacers. Identical 19-rod assemblies with grid spacers and wire wraps were used, with the same axial pitch (the axial pitch for grid spacers is simply the distance between the grids). The geometries of the assemblies are in Table 6.3.

Wire wrap and grid spacers		
Number of pins	N	19
Rod diameter	D	10.72 *mm*
Wire diameter	d_w	4.42 *mm*
Pitch	P	15.14 *mm*
Pitch to diameter ratio	P/D	1.412
Axial pitch	H	381 *mm*
Axial pitch to diameter ratio	H/D	35.5
Wire wrap equivalent diameter	D_e	9.80 *mm*
Wire wrap flow area	A_{flow}	100.1 mm^2

Table 6.3 - Tong CHF Test Geometry

Figure 6.5 shows the CHF results as compared to the CHF predictions by the W-3 correlation. Tong concluded that as the mass flux increased (which in this experiment generally corresponds to higher $q"_{DNB,predicted}$ in Figure 6.5), the grid spacers' CHF performance improved faster than the wire wraps'. However, for every single test point, wire wraps performed equal or better than the prediction according to the W-3 correlation. In addition, the wire wrap CHF was greater than the grid spacer CHF by an average of 8% at every point with the same operating parameters. Thus, using the W-3 correlation for wire wraps will give a conservative answer. Note that the W-3 correlation is different than the W-3L correlation used in this study (see Appendix **B.9**). The "L" represents a grid spacer factor which accounts for the increased mixing due to L-type mixing vane grid spacers. For reasons discussed later, the wire wrap construction used by Tong will have lower values of CHF than the design considered here, making the W-3 correlation overly conservative. As a result, the W-3L correlation will be used in this

study, with the anticipation that the wire wrap CHF will be larger than the mixing vane grid spacer CHF for the operating parameters of the PWR.

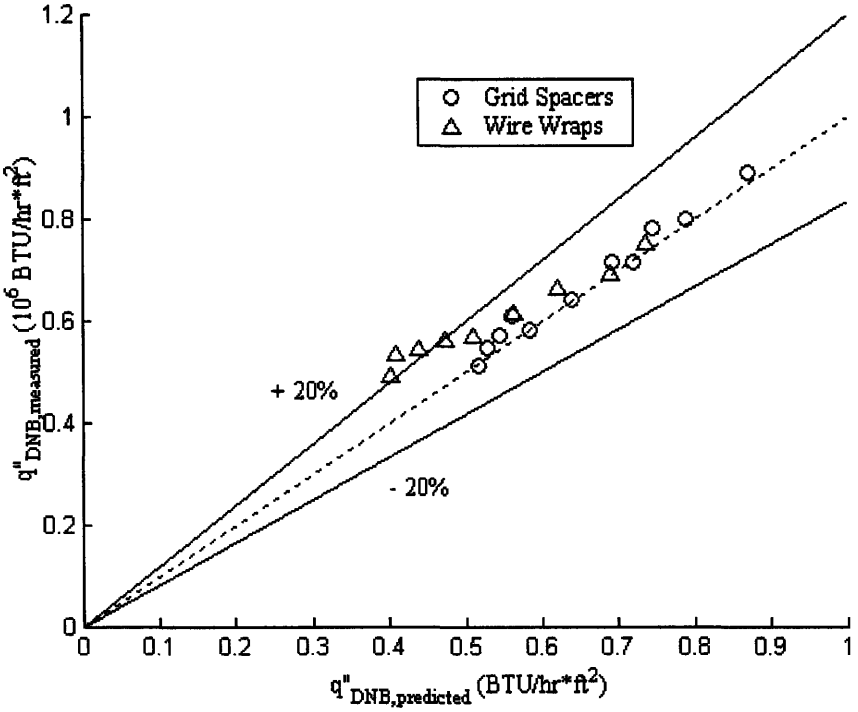

Figure 6.5 - Tong's CHF Comparison of Wire Wraps and Grid Spacers

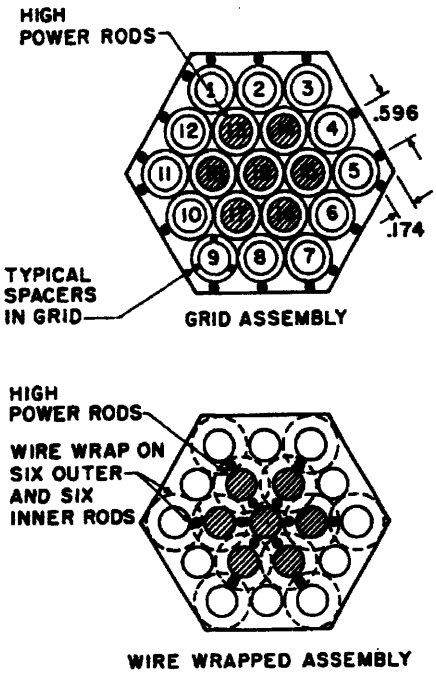

Figure 6.6 - Tong's Test Geometry

Tong's wire wrap and grid spacer assemblies are shown in Figure 6.6. There are substantial differences between Tong's wire wrap assembly and the wire wrap assemblies considered in this study. Tong only put wire wraps on the rods that needed it for support. Since the wires of adjacent rods provide support for a given rod, any individual rod does not need its own wire for its support. Taking advantage of this, Tong chose not to wrap wire on the center rod. The lack of wire on the center rod is detrimental to the CHF, as the mixing in the adjacent channels is decreased. In addition, the wire wrap location around the periphery of the rods is not uniform. As Figure 6.6 shows, all of the wires contact the center rod at the same axial location. The result is that the mixing of the center subchannels occurs only once per axial pitch, instead of 6 times per axial pitch for the design considered. The wire wrap mixing benefit shown in Figure 6.2 is negated, and the overall CHF is decreased. Thus, Tong's CHF results for wire wraps should be taken as conservative.

The grid spacer geometry is also different than the grid spacer configuration considered in this study. Grid spacers currently used in PWR's exclusively have mixing vanes and springs to support the rods. The grids that Tong used were short hollow cylinders which encircled the individual heater rods. The rods were centered by three longitudinal warts inside each of the cylinders. However, since the CHF results using these grid spacers were consistent with the W-3 correlation, the difference is not considered to be crucial.

6.3.3 - Selivanov et al., Russian Work on CHF

SSC RF IPPE (Obninsk, Russia) **[20]** performed CHF experiments on wire wraps. The resultant correlation is a critical quality correlation, Equations 6.1 and 6.2.

$$x_{crit} = 1 - 0.86\exp\left(-19/\omega\right) \qquad \textbf{[6.1]}$$

$$\omega = \rho G\sqrt{\frac{D_e}{\sigma\rho}} \qquad \textbf{[6.2]}$$

where _ is the coolant density, _ is the surface tension, and x_{crit} is the critical quality. The referenced paper **[20]** refers to a wire wrap CHF experiment. The title indicates that the experiment was performed for a PWR. Unfortunately, the Russian notation "PWR" refers

to their "vapor-liquid reactor" **[21]**, i.e. BWR. Consequently, these experiments were exclusively performed over high outlet quality ranges ($-0.03 < x_{in} < 0.3$, $0.15 < x_{out} < 0.45$). For the hot channel in this study, $x_{in} = -0.34$ and $x_{out} = 0.03$. As a result, the experimental data created by Selivanov is not applicable to the PWR situation considered in this study. In addition, the range of the critical quality correlation is 0.14 _ 1. Since the qualities considered in this study are always less than 0.14, Equation 6.1 will never predict a boiling crisis, regardless of the imposed heat flux. Thus, the critical quality and experimental data are both inapplicable to this study.

6.4 - Dalle Donna et al.: CHF Correlation for Wire Wraps

In 1979, Bowring **[22]** published the WSC-2 correlation, a CHF correlation specifically designed to cover the operating range of BWR's. The WSC-2 correlation appears in Appendix **B.9** in its entirety. This correlation has a spacer coefficient, V, that is intended to take the mixing vanes on grid spacers into account. Bowring intended for this term to be a constant, depending only on the geometry of the mixing vanes of the grid spacers. However, this correlation was not created using wire wrap data. Bowring's WSC-2 correlation is

$$\varphi_{CHF} = \frac{A + B \cdot \Delta H_i}{C + ZY} \qquad \textbf{[6.3]}$$

$$C = C'V\left[1 + \frac{Y - 1}{G + 1}\right] \qquad \textbf{[6.4]}$$

where φ_{CHF} is the CHF of the subchannel, and terms other than C do not involve the spacer coefficient, V.

In 1984, Dalle Donne et al. **[4]** expanded on Bowring's WSC-2 correlation, changing constants based on additional grid spacer data. Previously, the spacer coefficient was constant, with a recommended value of 0.7 for grid spacers with mixing vanes. Dalle Donne also found a dependence of the spacer coefficient on mass flux, G, and introduced a correlation for the grid spacer coefficient, Equation 6.5.

$$V = 0.252 - 2.789\,exp(-3.874G) + 1.915\,exp(-0.234G) \qquad \textbf{[6.5]}$$

where G is the mass flux, in Mlb/hr*ft^2. In addition, Dalle Donne analyzed wire wrap CHF data from Columbia, and modified the spacer coefficient to take the wire wrap effect into account. An analogous effect of mass flux on the wire wrap spacer coefficient was found, and the corresponding correlation is Equation 6.6.

$$V = 1 - [0.336 + 0.09G - 0.697\,exp(-2.68G)] \qquad \textbf{[6.6]}$$

However, this correlation for the wire wrap spacer coefficient is only proper for the single geometry tested in the Columbia paper. The geometry is detailed in Table 6.4.

Wire Wrap Geometry		
Number of pins	N	12
Rod diameter	D	11.18 *mm*
Wire diameter	d_w	0.56 *mm*
Pitch	P	11.74 *mm*
Pitch to diameter ratio	P/D	1.051
Axial pitch	H	152.4 *mm*
Axial pitch to diameter ratio	H/D	13.64
Center subchannel hydraulic diameter	D_h	2.29 *mm*
Center subchannel flow area	A_{flow}	21.13 mm^2

Table 6.4 - Columbia Experimental Wire Wrap CHF Geometry

Dalle Donne created a model for the CHF of wire-wrapped bundles with different geometries, based on the hypothesis that the effect of the wire wraps on V is proportional to the increase in the friction factor of the cluster caused by the wire wraps. This assumption results in the following correction to the wire wrap spacer coefficient equation.

$$V = 1 - \frac{f - f_{bare}}{f_{ref} - f_{bare}}\left[0.336 + 0.09G - 0.697\,exp(-2.68G)\right] \qquad \textbf{[6.7]}$$

f = friction factor of the considered bundle with wire wraps

f_{bare} = friction factor of the considered bundle with no spacers

f_{ref} = friction factor of the Columbia geometry (Table 6.4)

Dalle Donne used Rehme's correlation **[23]** for the friction factor of wire-wrapped bundles. The resulting equation for the wire wrap spacer coefficient is

$$V = 1 - 2.6695\left(F^{0.915} - 1\right)\left[0.336 + 0.09G - 0.697\,exp(-2.68G)\right] \qquad \textbf{[6.8]}$$

where F is a geometry factor developed by Rehme that is proportional to f. As Rehme wrote F,

$$F = \left(P/D\right)^{0.5} + \left[7.6\frac{d_m}{H}\left(P/D\right)^3\right]^{2.16} \qquad \textbf{[6.9]}$$

where
$$d_m = P \qquad \textbf{[6.10]}$$

The $\frac{d_m}{H}$ term, and subsequently F, can be written in terms of H/D and P/D, as was done by Dalle Donne.

$$\frac{d_m}{H} = \frac{P}{H} = \frac{D\left(P/D\right)}{H} = \frac{\left(P/D\right)}{\left(H/D\right)} \qquad \textbf{[6.11]}$$

$$F = \left(P/D\right)^{0.5} + \left[7.6\frac{\left(P/D\right)}{\left(H/D\right)}\left(P/D\right)^3\right]^{2.16} = \left(P/D\right)^{0.5} + \left[7.6\frac{\left(P/D\right)^3}{\left(H/D\right)}\right]^{2.16} \qquad \textbf{[6.12]}$$

6.4.1 - Effect of V on CHF

From Equation 6.3,

$$\varphi_{CHF} = \frac{A + B \cdot \Delta H_i}{C + ZYY'} \propto \frac{1}{C + ZYY'} \qquad [6.13]$$

Recalling that C is proportional to the spacer coefficient, V,

$$C = C'V\left[1 + \frac{Y - 1}{G + 1}\right] \qquad [6.4]$$

Only considering the effect of V on CHF, the ZY term can be viewed as a constant. Physically, this analysis is equivalent to investigating the effect of the spacer on CHF without changing anything else about the subchannel, including operating conditions and geometry. The definition of MDNBR is

$$MDNBR = \frac{\varphi_{CHF}}{\varphi_{actual}} \qquad [6.14]$$

In this analysis, the actual heat flux (φ_{actual}) is unchanging, so the change to the CHF (φ_{CHF}) is reflected by changes in MDNBR, a parameter much easier to calculate using VIPRE. The MDNBR was calculated for the reference geometry at reference power by VIPRE, and V was varied between 0 and 1.

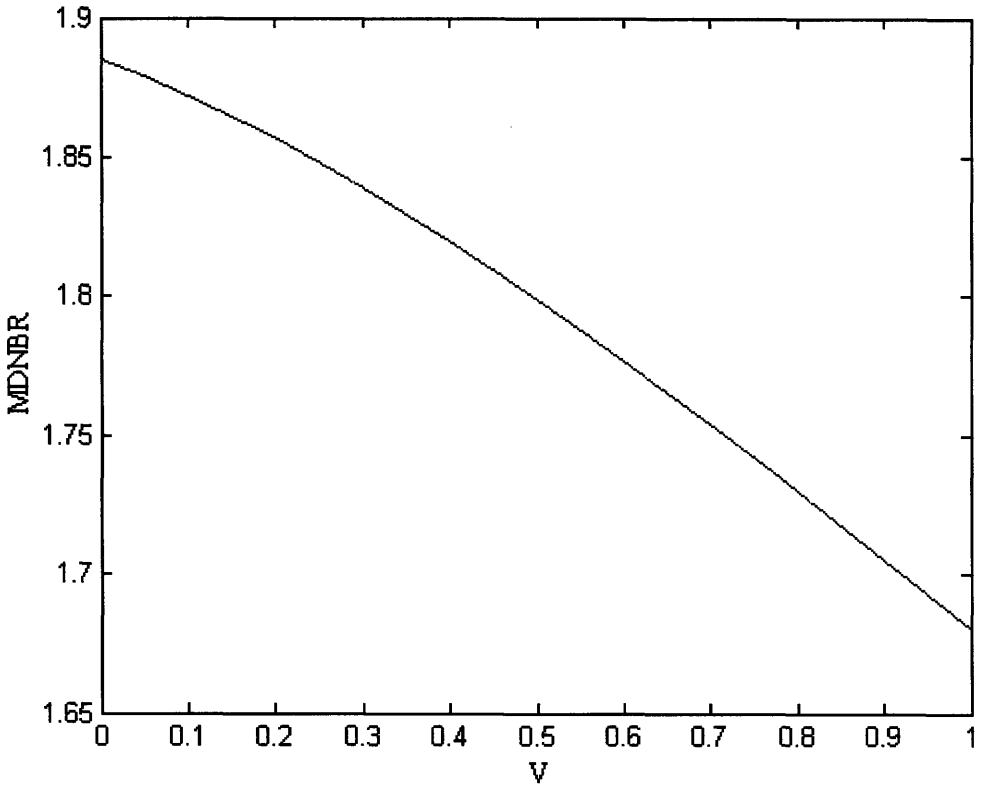

Figure 6.7 - Effect of Spacer Coefficient (V) on MDNBR for Reference Geometry at Reference Power

From Equation 6.4, as V goes to zero, C goes to zero. As this happens, the ZY term in Equation 6.13 becomes dominant, and the effect of changing V on the CHF becomes less. This trend is apparent in Figure 6.7, since as V goes to zero, its slope becomes flatter. V clearly has a large effect on the MDNBR though. For $V = 0$, MDNBR = 1.885, and for $V = 1$, MDNBR = 1.68, a 12.2% decrease. The effect of the spacer on the CHF can clearly be substantial.

6.4.2 - Effect of Axial Position on CHF

The CHF depends strongly on the local subcooling of the fluid: the more subcooled the fluid is, the higher the CHF value, since the bubble layer will be less developed. Since the local subcooling decreases along the length of the bundle, the CHF is a decreasing function of the axial position. In addition, the actual heat flux is not constant along the length of the bundle. It is generally approximated by a cosine shaped power curve. Figure 6.8 plots the actual heat flux and the CHF, as well an inset of the DNB, of the

core-wide average rod power and enthalpy gain for the reference core with grid spacers, as calculated by Bowring's WSC-2 correlation.

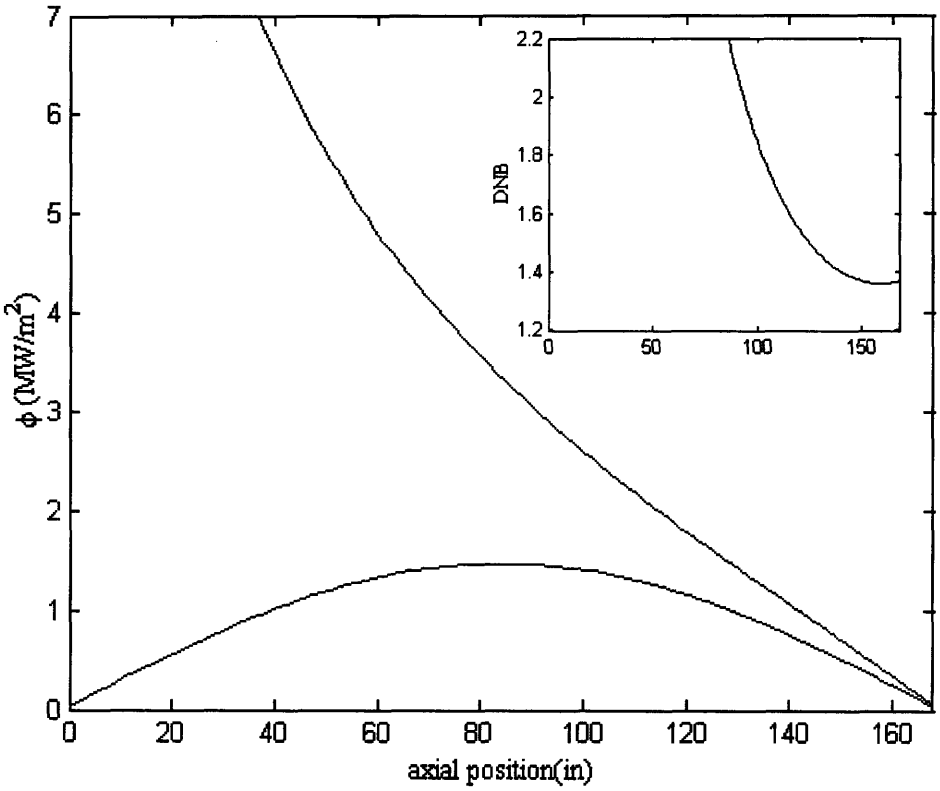

Figure 6.8 - φ_{CHF} and φ_{actual} for the Reference Geometry at Reference Power

From the inset DNB, it is clear that the MDNBR of the subchannel does not occur at the exit, so it is necessary to evaluate the DNBR of the entire channel to find the minimum. Due to the relatively small heat flux at the exit, the DNB generally occurs farther up the channel, so the CHF must be calculated along the entire channel.

6.4.3 - Negative V values

Bowring originally optimized the WSC-2 correlation using experimental data from clusters with relatively non-obstructive grid spacers with $V = 1$. Thus, having $V > 1$ is not physically achievable and therefore meaningless. Better mixing results in a smaller V value, so $V < 1$ is achievable. So Bowring constructed the correlation with $V = 1$ as an upper limit, but did not create a lower limit for the correlation. If the mixing if

substantial enough, V will become negative. A negative V does not have a different physical meaning than a positive V, it is simply a result of the construction of the WSC-2 correlation.

This is generally not a problem for grid spacers, but as discussed before, wire wrap mixing is substantially better than grid spacers, and negative V values can occur with wire wraps. However, negative V values create a computational problem for the WSC-2 correlation. Rewriting Equation 6.13 again,

$$\varphi_{CHF} = \frac{A + B \cdot \Delta H_i}{C + ZYY'} \propto \frac{1}{C + ZYY'} \qquad \textbf{[6.13]}$$

Z is the axial position, and as such the ZY term goes from zero at the entrance of the channel to being an order of magnitude greater than C at the exit. C, on the other hand, is relatively constant for most of the length of the channel.

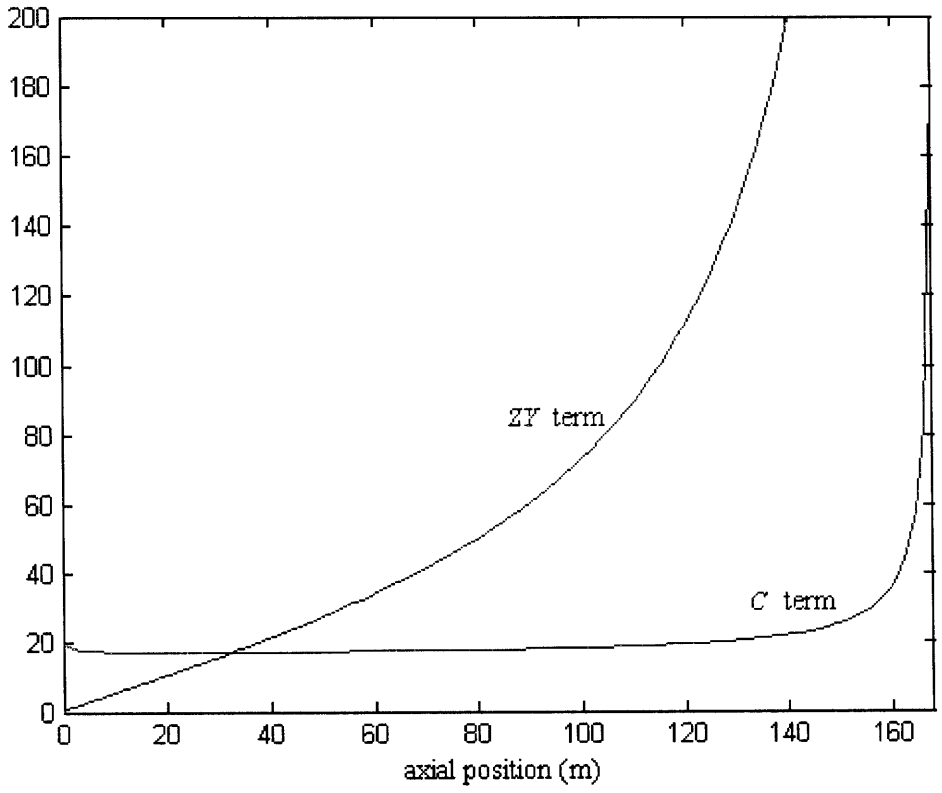

Figure 6.9 - Relative Magnitude of ZY and C Terms for the Reference Geometry at Reference Power Over the Length of the Bundle

The trends in this graph are valid regardless of the operating conditions and geometry. The *ZY* term starts at zero then becomes larger than the *C* term.

Recalling the definition of *C*,

$$C = C'V\left[1 + \frac{Y-1}{G+1}\right] \qquad \textbf{[6.4]}$$

When *V* becomes negative, *C* becomes negative. Since the *ZY* term is negligible near the entrance of the channel, the CHF is negative. This creates problems computationally, because some of the DNBR values are negative, making the MDNBR negative. In addition, when the *ZY* term is equal in magnitude to *C*, the denominator of the CHF becomes zero, and a discontinuity occurs.

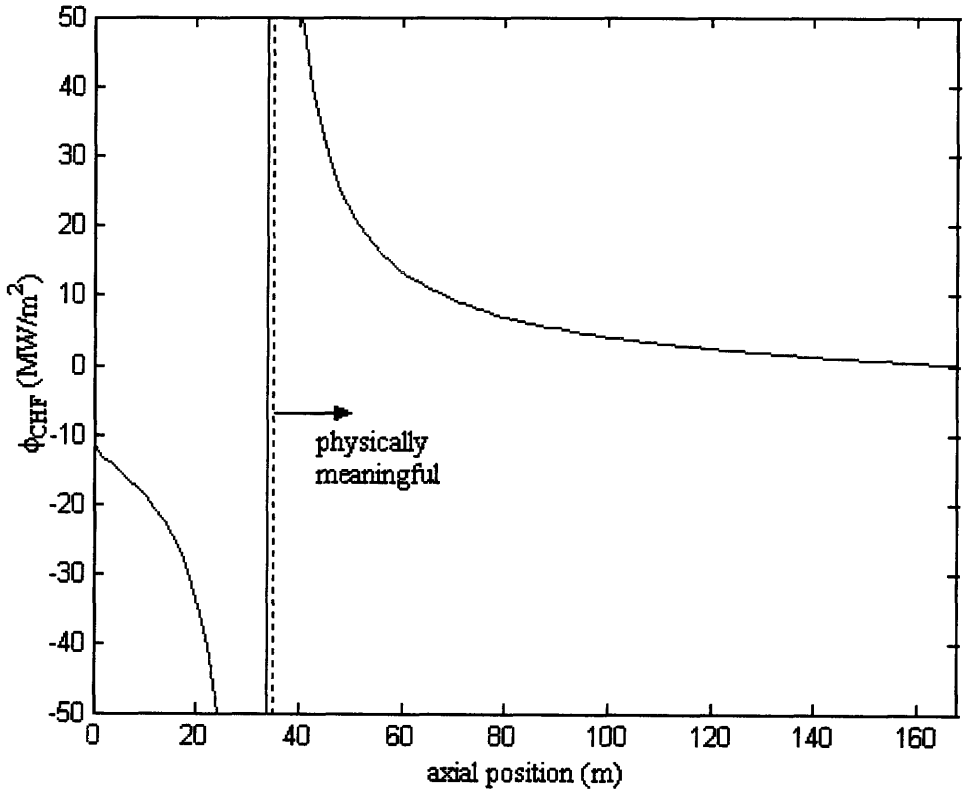

Figure 6.10 - φ_{CHF} with $V = -1$ for the Reference Geometry at Reference Power

Thus, when a negative V value occurs, Bowring's correlation cannot predict the CHF over the entire length of the bundle, and the resulting CHF distribution looks physically meaningless. But after the discontinuity, the CHF is physically meaningful, and also captures the additional benefit of the spacers. While the MDNBR will not occur at the exit, it will occur close to the exit, while the discontinuity will occur close to the entrance of the bundle. As a result, if the CHF prediction before the discontinuity is simply ignored, a valid MDNBR can be calculated for a negative V value, which will be greater than the MDNBR of a non-negative V value.

So negative V values are acceptable and even beneficial, but VIPRE is not programmed to handle this particular situation. Instead, if a negative V value is inputted, VIPRE simply resets the value to zero. This negates the benefit of negative V values, but the result will be conservative.

6.5 - CHF Correlations' Validity Ranges

Due to the inherent limitations of empirical correlations that are necessary to accurately predict CHF, all CHF correlations are valid strictly for the ranges covered by the experimental data which composes them. The two correlations considered by this work, the W-3L and WSC-2, have the following ranges of validity. Due to the large range of geometries and operating conditions considered here, the parameters do not always stay inside of the correlations' prescribed ranges.

While the exact numbers that result from calculations outside of the range of validity are incorrect, the trends are still captured. Indeed, for a lot of the parameter ranges considered, there is no experimental data, so these correlations are as good as any method to approximate the performance of the designs considered here. This is particularly true of the mass flux, since large mass fluxes are required to accommodate power uprates while holding the enthalpy rise constant. An exact number is not necessary, since the goal of this work is to show promising new parameter ranges for experimentation.

6.5.1 - W-3L Correlation

The W-3L correlation ranges, as reported by the VIPRE manual are given in Table 6.5. The equivalent heated diameter is based on the heated perimeter, and is defined as

$$D_h = \frac{4 \cdot A_{flow}}{P_h} \qquad [6.15]$$

where P_h is the heated perimeter of the channel, and A_{flow} is the flow area. Similarly,

$$D_e = \frac{4 \cdot A_{flow}}{P_w} \qquad [6.16]$$

where P_w is the wetted perimeter of the channel, which includes the wires.

D_e	hydraulic diameter	mm	5.08 to 17.78
G	mass flux	Mlb/ft^{2}hr	1.0 to 5.0
L	heated length	in	10 to 144
p	pressure	psia	1000 to 2300
x	steam quality at exit	-	-0.15 to 0.15
H_i	inlet enthalpy	kJ/kg	> 930
P_h/P_w	heated to wetted perimeter ratio	-	0.88-1.00

Table 6.5 - W-3L Ranges of Validity

Most of these parameters are straightforward, but the hydraulic diameter changes over the power map. This restricts the geometries that are considered valid. The correlation will still be evaluated for these geometries outside of the correlation's range, but the validity must be accounted for when interpreting the results. Figure 6.11 shows the areas of the power map that are not inside of the range of validity for the W-3L correlation. However, as there is no CHF correlation that is valid for geometries that have small equivalent diameters, the W-3L correlation will be used for the entire power map. Since

the geometries not covered by the W-3L correlation are not limited by CHF, the use of the W-3L correlation outside of its range will not affect the results.

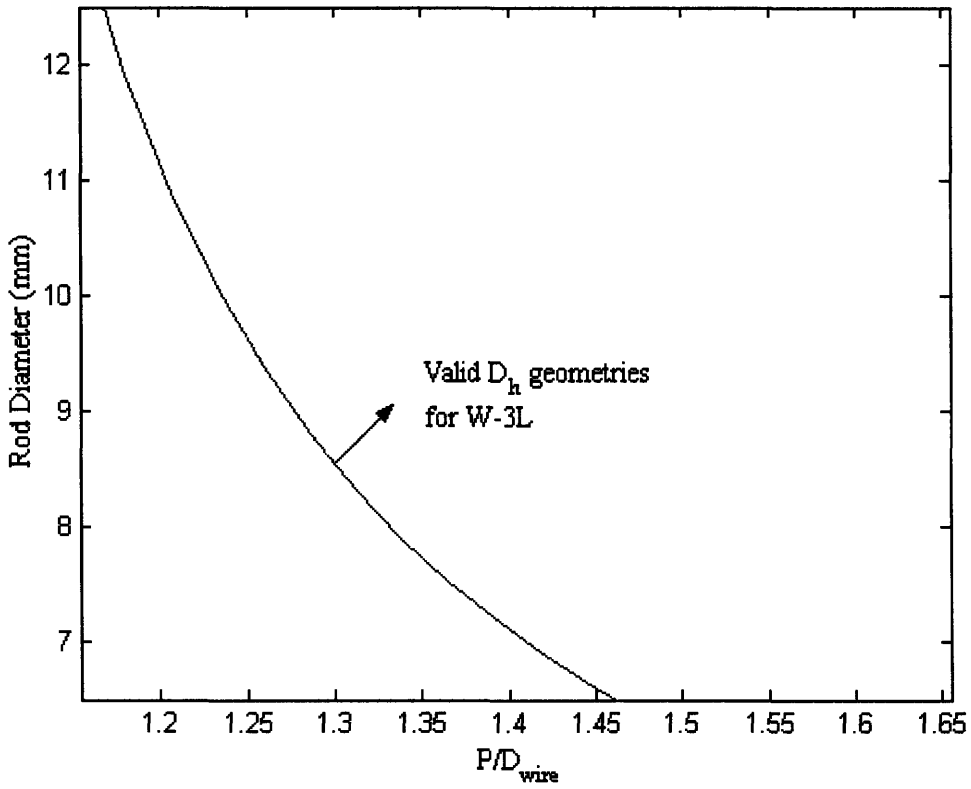

Figure 6.11 - W-3L Valid Geometries for P/D_{wire}

6.5.2 - Bowring's WSC-2 Correlation

Bowring customized his correlation to three specific channel geometries: hexagonal, square and outer. Outer subchannels are those that are adjacent to the edge of the bundle. In this work, only the hexagonal subchannels were considered, as the wire wrap geometry is hexagonal. For each of these he used different data, so they have different applicability ranges. The VIPRE manual simply chooses the widest range of applicability for all of the channel geometries. The complete table of applicability is shown in Table 6.6.

Subchannel Parameter		Range		
		Hexagonal	Square	Outer
D rod diameter	mm	12.7 to 20.3	10.1 to 20.3	10.1 to 17.8
D_h equivalent heated diameter	mm	5.1 to 30.5	7.6 to 28.0	5.1 to 25.4
D_w equivalent wetted diameter	mm	5.1 to 30.5	7.6 to 28.0	2.5 to 0.4
G mass flux	Mlb/ft^2hr	0.2 to 3.0	0.4 to 3.7	0.2 to 2.9
_H_i inlet subcooling	kJ/kg	12 to 756	12 to 1000	23 to 570
L heated length	in	18 to 180	48 to 180	30 to 180
p pressure	psia	435 to 1270	440 to 2400	480 to 2400
x steam quality	-	0.06 to 0.86	-0.20 to 0.86	7 to 86
Y' imbalance factor	-	0.4 to 1.0	0.6 to 1.1	0.3 to 1.2
c rod gap	mm	.76 to 7.6	0.76 to 7.6	1.5 to 5.1
$_p$ heat flux	MW/m^2	0.32 to 3.2	0.32 to 4.42	0.32 to 3.5
$_z$ axial peaking factor	-	1.0 to 1.7	1.0 to 1.7	1.0 to 1.7
F_p radial peaking factor	-	1.0 to 1.7	1.0 to 1.4	1.0

Table 6.6 - WSC-2 Ranges of Validity

Note that the diameter and equivalent diameters are rather large. However, Dalle Donne's extended database, including wire wraps, covered diameters as low as 6.35 mm, and equivalent wetted diameters (the more constraining of the two) as low as 5.0 mm. Using these two as the lower limits of validity of the geometry gives the range of geometries over which the Bowring correlation is valid, as shown in Figure 6.12.

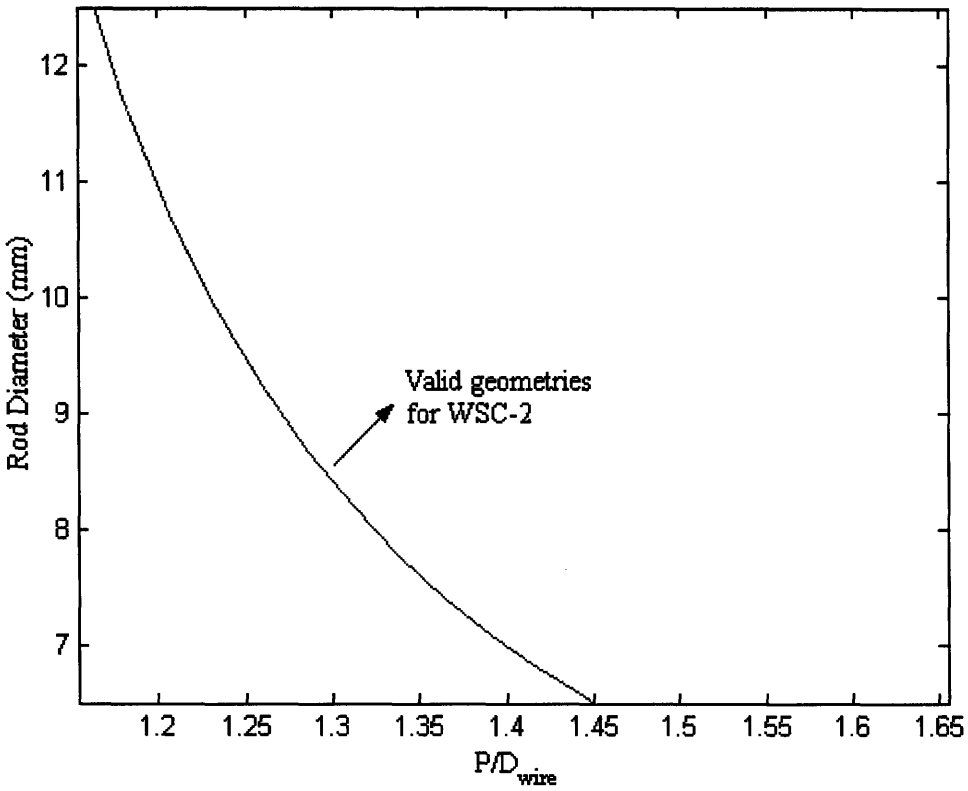

Figure 6.12 - WSC-2 Valid Geometries for P/D_{wire}

6.6 - MDNBR Approach for Achievable and Stretch Cases

6.6.1 - Achievable Case

For the achievable case, the W-3L correlation is used to calculate the MDNBR. Tong's experiments **[19]** show that using the W-3 correlation gives conservative CHF results. The "L" in the W-3L correlation represents a mixing vane factor, and is not exactly the W-3 correlation used by Tong, which was determined to give overly conservative results. The W-3L correlation is expected to give results that are more representative of the wire wrap CHF.

6.6.2 - Stretch Case

The stretch case takes the wire wrap effect on CHF into account by using an MDNBR limit equivalent to that used for the Achievable Case with the W-3L correlation, and accounting for the wire wrap using Dalle Donne's spacer coefficient. It is preferable to use the Bowring CHF correlation with a Dalle Donne spacer coefficient, as the Dalle Donne correlation was created for (see Section 6.4). However, Bowring's correlation and

the W-3L correlation behave differently over the power map. In particular, the effect of hydraulic diameter on the CHF is calculated differently, resulting in two inherently different power maps for the W-3L and Bowring correlations. These inherently different power maps make it impossible to directly evaluate the effect of wire wraps (as calculated by Dalle Donne) to the effect of the grid spacers (as calculated by W-3L). Since a major goal of this study is to make the comparison of wire wraps to grid spacers, a new method of calculating the MDNBR with wire wraps is used, which uses both the W-3L and Dalle Donne correlation.

For the achievable case, a constant MDNBR limit of 2.17 was used. This is the MDNBR as calculated by VIPRE using the W-3L correlation for the reference core at reference power. Thus, using the W-3L correlation with a limit of 2.17 constrains the reference geometry to reference power. Analogously, Bowring's MDNBR at the reference geometry and reference power can be calculated (with V = 0.7), resulting in a value of 1.716. These two constraints on the MDNBR (W-3L of 2.17 and Bowring of 1.716) can be considered to be equivalent for the reference core, as they result in the same maximum power (reference power).

For each geometry, the achievable case MDNBR is constrained to be less than 2.17, as calculated by the W-3L correlation. To eliminate the different effects of geometry with Bowring's correlation, a Bowring MDNBR limit equivalent to a W-3L limit of 2.17 was calculated for each geometry. This is the same concept as the equivalent MDNBR's of 2.17 with W-3L and 1.716 with Bowring for the reference geometry; the Bowring limit that gives the same maximum power as the W-3L limit is calculated for each geometry.

To do this, a special run was performed, where the power was only constrained by the MDNBR. For each geometry, the power was increased until the W-3L MDNBR was 2.17. The Bowring MDNBR at that power was calculated, and set as the limit. In this way, the maximum power using the W-3L MDNBR limit of 2.17 and the equivalent Bowring MDNBR limit would give the same maximum power for that geometry. Thus, while the constant W-3L limit of 2.17 was used for the Achievable Case, the Stretch Case uses different MDNBR limits for each geometry, as shown in Figure 6.13.

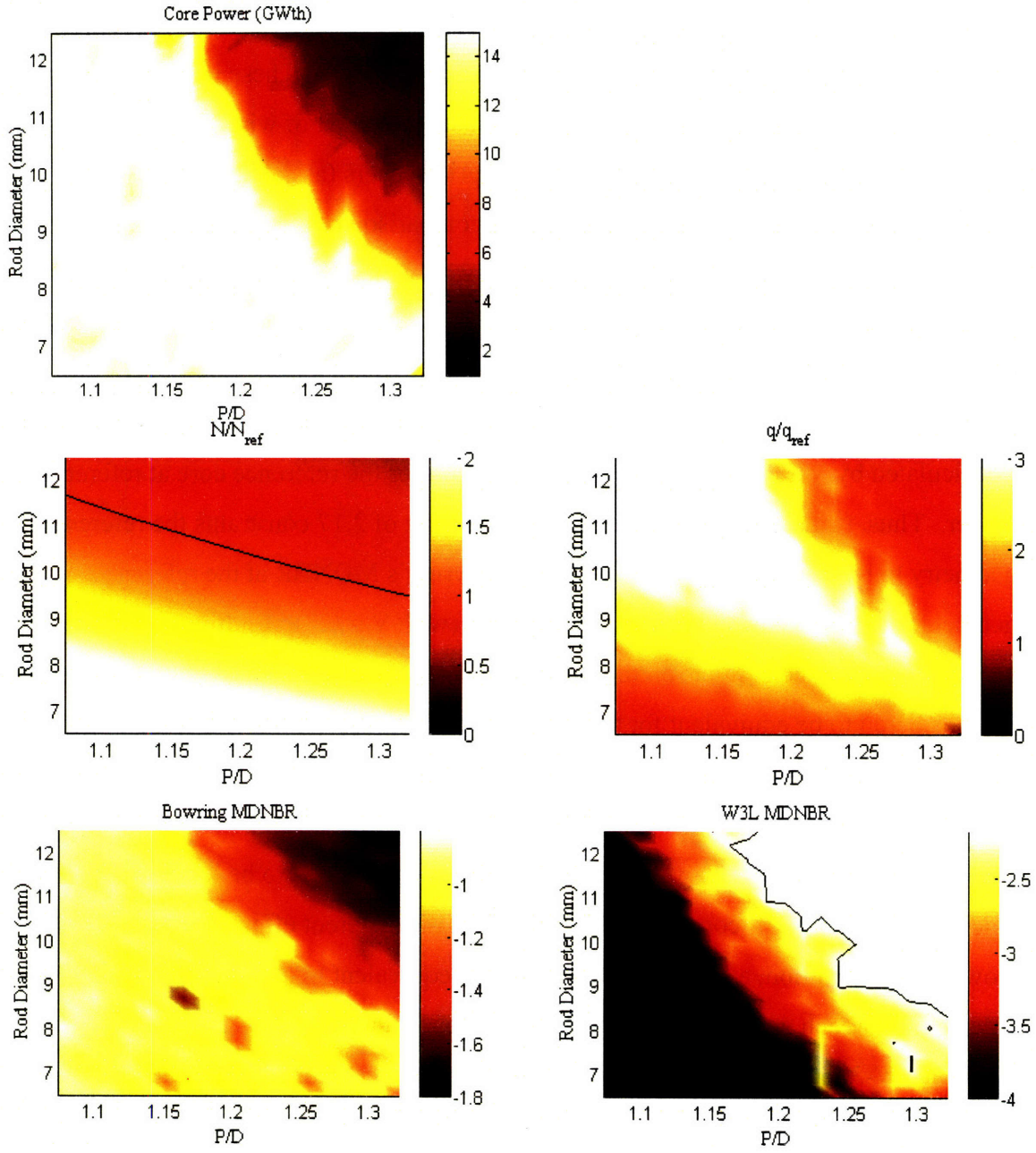

Figure 6.13 - Equivalent Bowring and W-3L MDNBR Run

Note that the W-3L MDNBR is not 2.17 for the entire power map, as is preferable. The core power required to achieve a W-3L MDNBR value of 2.17 is phenomenal for some geometries. VIPRE was not able to converge on a solution for these very high powers, so a power limit of 15 GWth was imposed. If the W-3L MDNBR was not less than 2.17 at 15 GWth, the MDNBR values were simply recorded. For these geometries, using the

W-3L MDNBR values at 15 GWth as the limits will allow a core power of 15 GWth before the MDNBR is constraining. Since the Bowring MDNBR limit for these geometries is equivalent to a W-3L MDNBR greater than 2.17, so using these Bowring MDNBR values as limits will ensure that the equivalent W-3L MDNBR will be greater than 2.17, satisfying the MDNBR constraint. Powers in the range of 15 GWth are never achieved in the final steady-state results, so using Figure 6.13 as equivalent MDNBR values is valid.

It should be noted that in no way does Figure 6.13 represent the achievable power of a real reactor, as only the W-3L MDNBR is constraining. Very high powers are experienced at tight geometries (small equivalent diameter), for several reasons, all of which serve to increase the CHF, listed as follows.

1. The W-3L correlation is very sensitive to equivalent diameter, which is smaller with wire wrap in general, and especially small with the small equivalent diameters of tight geometries with wire wrap.
2. Tighter geometries allow more rods to be placed inside the core, decreasing the linear power required to achieve the same core power, as shown in Figure 6.13.
3. Tighter geometries have less flow area. Instead of allowing the enthalpy rise to increase, this study increases the mass flux to achieve the same power. While allowing the enthalpy to rise would be very detrimental to the CHF, increasing the mass flux actually improves the CHF.

These effects combine to allow very high powers for tight geometries while staying within the MDNBR constraint. Unfortunately, all of these effects are detrimental to other constraining parameters, specifically flow-induced vibration and pressure drop. These parameters will counter the MDNBR preference for tight geometries, and an intermediate geometry with a power much lower than 15 GWth will be found to be the maximum power that satisfies all parameters.

Chapter 7: Wire Wrap Equivalence

Jon Malen and Stu Blair recently developed a series of MATLAB programs that allow the maximum power to be determined over a range of geometries. One of the programs creates an input deck for VIPRE, which includes optimizing the bundle size to fit the maximum number of rods in the core, as well as placing control rods regularly. However, these programs create square arrays. Instead of creating a new set of programs to create hexagonal arrays, Carter Shuffler proved that hexagonal arrays with grid spacers have the same thermal hydraulic performance as square arrays if the pin diameter and water-to-fuel volume ratio are identical. This chapter will develop an analogous equivalence between square arrays with grid spacers and hexagonal arrays with wire wraps, allowing for the use of the square array construction programs when calculating the thermal-hydraulic performance of hexagonal arrays with wire wraps.

Subchannels that are equivalent have the same neutronic and thermal-hydraulic performance. If two subchannels have the same Hydrogen to Heavy Metal ratio (H/HM), their neutronic performance will be the same. In PWR's, the working fluid is highly turbulent water. Water has a relatively high Pr, meaning that the exact geometry of the channel does not make a substantial difference to its thermal-hydraulic performance. Thus, subchannels with the same flow area, heated and wetted perimeter will have equivalent thermal-hydraulic performance in a PWR. If two subchannels have equal neutronic and thermal-hydraulic performance, they perform identically.

7.1 - Hexagonal Equivalence

The H/HM ratio for hydride fuel is developed as follows. Hydride fuels have hydrogen, heavy metal, and zirconium in the matrix, although zirconium has no effect on the equivalence and is not considered here. While this analysis is specific to hydride fuel, the same methodology will produce an identical equivalence for oxide fuel, and the equivalence is applied equally to oxide fuel in this study. The parameters used in the analysis are described in Table 7.1. The number of hydrogen atoms can be written according to Equation 7.1.

$$H_{H_2O} = 2\frac{N_A \rho_{H_2O} V_{H_2O}}{M_{H_2O}} \qquad H_{fuel} = X\frac{N_A \rho_{fuel} V_{fuel}(1-w)}{M_{fuel}} \qquad H = H_{H_2O} + H_{fuel} \qquad [7.1]$$

$$V_{H_2O} = A_{flow} L \qquad V_{fuel} = A_{rod} L \qquad [7.2]$$

where V is volume, M is molecular weight, N_A is Avagadro's number, X is the number of hydrogen atoms per atom of the hydride matrix element, and w is the weight percent heavy metal of the fuel. The number of HM atoms can be written as

$$HM = Y\frac{N_A \rho_{fuel} w V_{fuel}}{M_{HM}} \qquad [7.3]$$

where Y is the number of heavy metal atoms per unit of heavy metal; its value is usually 1.

$$\frac{H}{HM} = \left(\frac{2}{Y}\right)\cdot\left(\frac{1}{w}\right)\cdot\left(\frac{M_{HM}}{M_{H_2O}}\right)\cdot\left(\frac{\rho_{H_2O}}{\rho_{fuel}}\right)\cdot\left(\frac{V_{H_2O}}{V_{fuel}}\right)\cdot\left(\frac{X}{Y}\right)\cdot\left(\frac{M_{HM}}{M_{fuel}}\right)\cdot\left(\frac{1-w}{w}\right) \qquad [7.3]$$

7.1.1 - Square Array with Grid Spacers

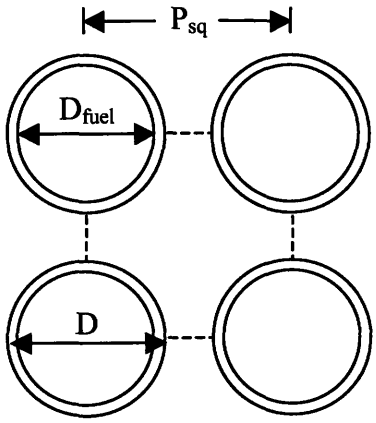

Figure 7.1 - Geometry of Square Array

Solving for the H/HM ratio for the square array of Figure 7.1,

$$\frac{H}{HM}=\left(\frac{2}{Y}\right)\cdot\left(\frac{1}{w}\right)\cdot\left(\frac{M_{HM}}{M_{H_2O}}\right)\cdot\left(\frac{\rho_{H_2O}}{\rho_{fuel}}\right)\cdot\left(\frac{P_{sq}^2-\frac{\pi}{4}D_{rod}^2}{D_{pellet}^2}\right)\cdot\left(\frac{X}{Y}\right)\cdot\left(\frac{M_{HM}}{M_{fuel}}\right)\cdot\left(\frac{1-w}{w}\right) \qquad \textbf{[7.4]}$$

setting: gap and cladding combined thickness as 8.3% of the pellet diameter

then: $D_{rod}=2D_{pellet}(0.083)+D_{pellet}=1.166\cdot D_{pellet}$

substituting this into **[7.4]** and solving for P/D,

$$\left(P/D\right)_{sq}=\sqrt{\left[\frac{Y\cdot w}{2}\cdot\left(\frac{H}{HM}-\left(\frac{X}{Y}\right)\cdot\left(\frac{M_{HM}}{M_{fuel}}\right)\cdot\left(\frac{1-w}{w}\right)\cdot\left(\frac{M_{H_2O}}{M_{HM}}\right)\cdot\left(\frac{\rho_{fuel}}{\rho_{H_2O}}\right)\right)+(1.166)^2\right]\cdot\frac{\pi}{4\cdot(1.166)^2}} \qquad \textbf{[7.5]}$$

7.1.2 - Hexagonal Array with Grid Spacers

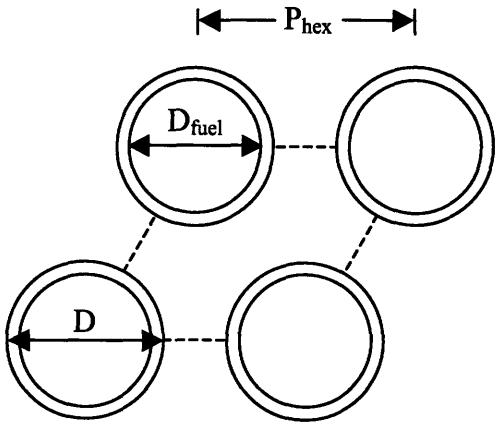

Figure 7.2 - Geometry of Hexagonal Array

Solving similarly for the H/HM of the hexagonal array shown in Figure 7.2,

$$\frac{H}{HM} = \left(\frac{2}{Y}\right)\cdot\left(\frac{1}{w}\right)\cdot\left(\frac{M_{HM}}{M_{H_2O}}\right)\cdot\left(\frac{\rho_{H_2O}}{\rho_{fuel}}\right)\cdot\left(\frac{\frac{\sqrt{3}}{2}P_{sq}^2 - \frac{\pi}{4}D_{rod}^2}{D_{pellet}^2}\right)\cdot\left(\frac{X}{Y}\right)\cdot\left(\frac{M_{HM}}{M_{fuel}}\right)\cdot\left(\frac{1-w}{w}\right) \qquad \textbf{[7.8]}$$

$$\left(P/D\right)_{hex} = \sqrt{\left[\frac{Y\cdot w}{2}\cdot\left(\frac{H}{HM} - \left(\frac{X}{Y}\right)\cdot\left(\frac{M_{HM}}{M_{fuel}}\right)\cdot\left(\frac{1-w}{w}\right)\cdot\left(\frac{M_{H_2O}}{M_{HM}}\right)\cdot\left(\frac{\rho_{fuel}}{\rho_{H_2O}}\right)\right) + (1.166)^2\right]\cdot\frac{\pi}{2\sqrt{3}\cdot(1.166)^2}} \qquad \textbf{[7.9]}$$

7.1.2 - Hexagonal Equivalence

H/HM in Equation 7.9 can be set equal to H/HM in Equation 7.5. The subchannels will now be neutronically equivalent, and it is possible to solve for the relationship of P/D_{sq} to P/D_{hex} by dividing Equation 7.9 by Equation 7.5. The resulting relationship is:

$$\left(P/D\right)_{hex} = \sqrt{\frac{2}{\sqrt{3}}}\left(P/D\right)_{sq} = 1.0746\cdot\left(P/D\right)_{sq} \qquad \textbf{[7.10]}$$

As demonstrated next, this result can be arrived at by a much simpler method. The H/HM ratio will be the same for the square and hexagonal subchannels if the following conditions are met.

Conditions for Neutronic Equivalence

- Same flow area
- Identical rods

Setting the flow areas equal to each other will ensure that there is the same amount of hydrogen in the coolant, and making the fuel rods identical ensures that there is the same

amount of hydrogen and heavy metal in the rods. By construction, the H/HM ratio is the same. Making the fuel rods identical leads to the following constraint:

$$D_{hex} = D_{sq} = D \qquad \textbf{[7.11]}$$

Setting the flow areas equal to each other leads to the other constraint, Equation 7.14

$$A_{flow,sq} = P_{sq}^2 - \frac{\pi}{4}D^2 \qquad A_{flow,hex} = \frac{\sqrt{3}}{2}P_{hex}^2 - \frac{\pi}{4}D^2 \qquad \textbf{[7.12]}$$

$$P_{sq}^2 = \frac{\sqrt{3}}{2}P_{hex}^2 \qquad \textbf{[7.13]}$$

$$\left(P/D\right)_{hex} = \sqrt{\frac{2}{\sqrt{3}}}\left(P/D\right)_{sq} = 1.0746 \cdot \left(P/D\right)_{sq} \qquad \textbf{[7.14]}$$

Note that this is identical to the result of the H/HM analysis. This will be referred as a hexagonal analysis, and is only valid for bare rod or grid spacer assemblies.

7.1.3 - Thermal-Hydraulic Hexagonal Equivalence

Now the question becomes whether these neutronically equivalent subchannels also have the same thermal-hydraulics. Again, the requirements for thermal-hydraulic equivalence are:

Parameters that must be the same for thermal-hydraulic equivalence

- Flow area
- Heated perimeter
- Wetted perimeter

The flow area and rods were already set equal, according to Equations 7.11 and 7.12. Comparing the heated and wetted perimeter,

$$P_{h,hex} = P_{w,hex} = \pi D \qquad P_{h,sq} = P_{w,sq} = \pi D \qquad [7.15]$$

$$P_{h,sq} = P_{h,hex} \qquad P_{w,sq} = P_{w,hex} \qquad [7.16]$$

Thus, these subchannels are fully equivalent. This was borne out in a full hexagonal core VIPRE calculation performed by Carter Shuffler, which confirmed practically identical thermal-hydraulic performance of the equivalent hexagonal geometries.

7.2 - Wire Wrap Equivalence

As mentioned before, the hexagonal equivalence is only valid for grid spacers. Wires substantially complicate matters, as they obstruct flow area and add wetted perimeter without adding heated perimeter. However, it is extremely convenient and rather illustrative to create a wire wrap hexagonal and square subchannel equivalence (see Figure 7.3). Equivalent square channels will be used when performing steady-state analyses for wire-wrapped bundle.

The equivalence between square subchannels and hexagonal wire-wrapped subchannels will be referred to as the wire wrap equivalence. The only difference between this equivalence and the hexagonal equivalence is the presence of wires.

7.2.1 - Neutronic Equivalence

The presence of wires make it difficult to perform a full H/HM analysis for wire wraps as was done before for grids. There is an extra pitch term that complicates solving for P/D, and the derivation would be obtuse. Instead, the simpler approach of equating flow area and diameter will be used.

The idea of the neutronic equivalence is to find a square geometry that has the same neutronic performance as the wire-wrapped hexagonal geometry. To this end, the flow area and rods of the square subchannel will be set to the flow area and rods of the wire wrap subchannel. This will result in an identical number of hydrogen and heavy metal atoms, and therefore an identical neutronic performance.

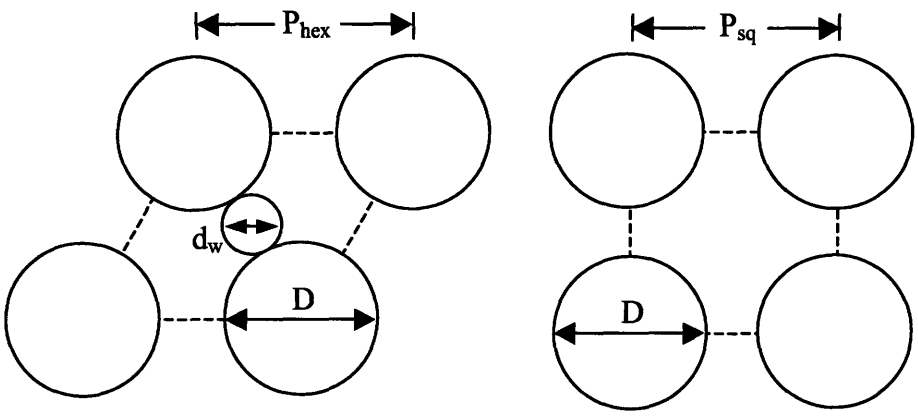

Figure 7.3 - Wire wrap and equivalent square subchannels

where d_w is the wire diameter, $d_w = P_{wire} - D$

As before, the square fuel rod can be set equal to the wire fuel rod, resulting in equal diameters. The flow area of the square channel remains the same

$$A_{sq} = P_{sq}^2 - \pi/4 D^2 \qquad [7.17]$$

For the wire wrap subchannel, each rod has one wire associated with it, but the wire affecting the flow area will move around the rod helically. However, since at any axial location, for N rods, there are N wires, the average flow area of the wire wrap subchannel is given by Equation 7.18

$$A_{wire} = \frac{\sqrt{3}}{2} P_{wire}^2 - \frac{\pi}{4} D^2 - \frac{\pi}{4} (P_{wire} - D)^2 \qquad [7.18]$$

Setting $A_{sq} = A_{wire}$ and solving for P/D_{sq},

$$P/D_{sq} = \sqrt{\frac{\sqrt{3}}{2} (P/D)_{wire} - \frac{\pi}{4} ((P/D)_{wire} - 1)} \qquad [7.19]$$

Notice that the relationship is no longer linear, as it is for P/D_{hex}. It is also useful to express P/D_{wire} in terms of P/D_{sq}.

$$\left(P/D_{wire}\right) = \frac{-\pi/2 + \sqrt{\sqrt{3}\pi/2 + \left(2\sqrt{3} - \pi\right)\left(P/D_{sq}\right)^2}}{\sqrt{3} - \pi/2} \qquad [7.20]$$

Figure 7.4 shows the shape of the dependence of the equivalent wire geometry on P/D_{sq}. In Figure 7.4, "With Wire" refers to the wire wrap equivalence, "Without Wire" refers to the hexagonal equivalence. As P/D_{sq} increases, the discrepancy between the two becomes larger. This is because the wire becomes a larger obstruction with larger P/D_{wire}, so the pitch has to be even larger to offset the increased obstruction of the wire.

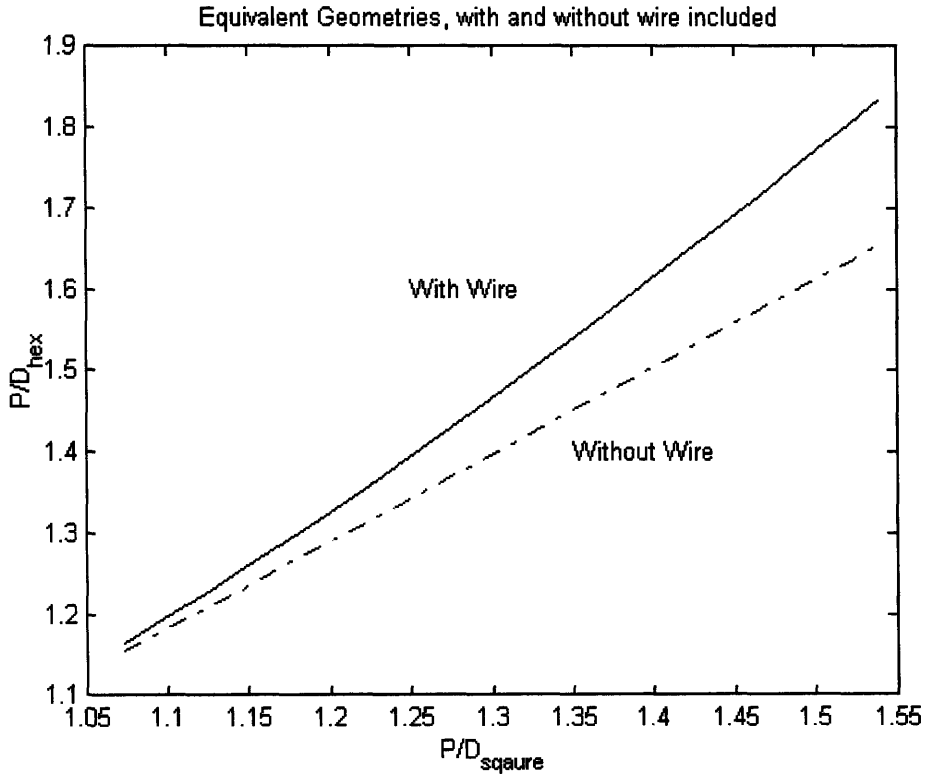

Figure 7.4 - Plot of Wire Wrap Neutronic Equivalent Geometries

The neutronic equivalence developed here needs to be qualified. One assumption in its development is that the amount of structural material (cladding, grid spacers and wire-wrapped spacers) present in the core is assumed to have no effect on the neutronics. The Zircaloy which composes the structural materials is designed to have minimal impact on the neutronics, making its impact much smaller than that of the H/HM ratio. However, there is still an impact of the structural material on the neutronics, and this effect is not

taken into account in this analysis. The amount of structural material will change when considering different geometries with grid spacers, and additionally with the change from grid spacers to wire-wrapped spacers. While it is beyond the scope of this work to take into account the effect of the change in structural material on the neutronics analysis, the amount of Zircaloy required for a given geometry can be compared to the amount of Zircaloy in the reference core. The required volume of Zircaloy in the grid spacer assemblies was composed of the grid spacers and the fuel rod cladding. The required volume of Zircaloy in the wire wrapped assemblies was composed of the wire wraps, fuel rod cladding, and bundle walls. The bundle wall volume was calculated assuming 11-ring, 331 rod assemblies with 1 mm wall thickness. The ratio of the required volume of Zircaloy for a given geometry to the reference required volume is shown in Figure 7.5 for grid spacers and wire wraps. Wire wrapped assemblies generally require more Zircaloy than grid spacers, and the ratio for the Achievable Case maximum power geometry (D = 8.39 mm, P/D = 1.321) is 1.52 (52% more Zircaloy than the reference case). It is currently not clear what effect this change in the Zircaloy volume will have on the neutronics.

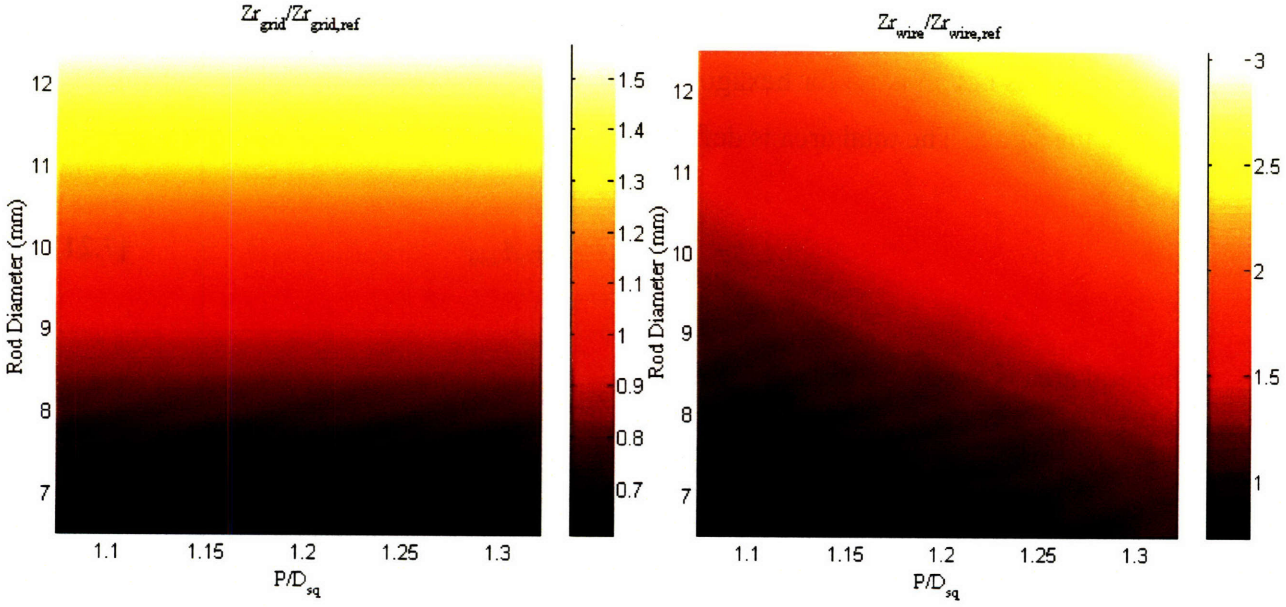

Figure 7.5 - Ratio of Zircaloy Volume with Wire Wraps and Grid Spacers over Reference Core

7.2.2 - Thermal-Hydraulic Equivalence

The thermal-hydraulic wire wrap equivalence is different from the neutronic wire wrap equivalence, due to the requirements for thermal-hydraulic equivalence. It is acceptable for the thermal-hydraulic equivalence to be different from the neutronic equivalence, since the two analyses will be done separately. For any given wire wrap geometry, the thermal-hydraulic analysis will be done with the thermal-hydraulic equivalence, and the neutronic analysis will be done with the neutronic equivalence.

Carter Shuffler analyzed the thermal-hydraulic hexagonal equivalence, and proved its validity in VIPRE. In Shuffler's work, the listed criteria for equivalence was that the following be the same for the two types of channels:

1. Wetted perimeter
2. Heated perimeter
3. Flow area

Indeed, two subchannels that meet these criteria will have equivalent thermal-hydraulic performance. However, one important criterion for thermal-hydraulic equivalence is implicit, as it is not an issue for hexagonal equivalence: the total area of the subchannels must be the same. The total area is defined as:

$$A_{tot} = A_{rods} + A_{flow} + A_{wire} \qquad [7.21]$$

The total area is the dotted area in Figure 7.6.

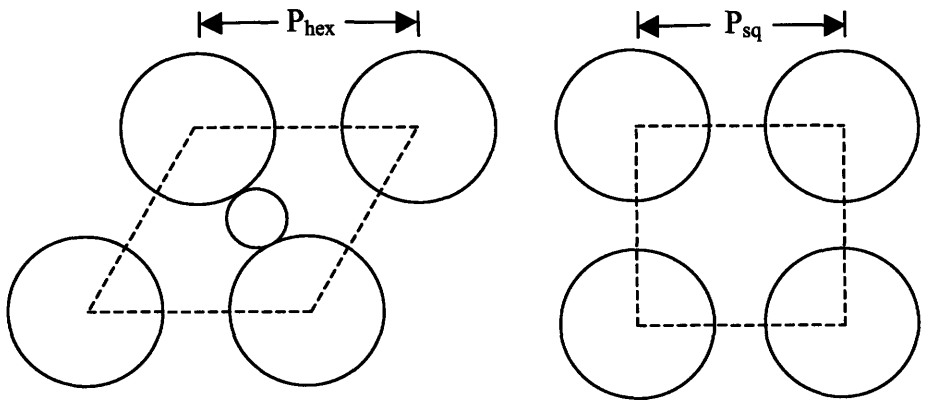

Figure 7.6 - Total Area of Subchannels

The total cross-sectional area of the core is the sum of these areas:

$$A_{core} = A_{tot} N_{rods} \qquad [7.21]$$

If the total area is different for the square and hexagonal subchannels, the number of rods that fit in the core is different, and the two cases will not give the same power on a core-wide basis, even though the power of the individual rods would be the same.

$$\dot{Q} = N_{rods} \cdot q' \cdot L \qquad [7.22]$$

Note that the total areas do not have to be the same for neutronic equivalence. This is because the neutronic analysis is based entirely on individual subchannel analysis, and does not depend on how many rods can fit in the core.

The complete list of criteria for equivalence is that the following have to be the same for the different subchannels:

1. Wetted perimeter
2. Heated perimeter
3. Flow area
4. Total area

Setting the square heated perimeter equal to the wire heated perimeter gives

$$D_{wire} = D_{sq} = D \qquad [7.23]$$

The total area for the two channels is calculated as:

$$A_{tot,sq} = P_{sq}^{\ 2} = \left(\left(P/D \right)_{sq} \right)^2 D^2 \qquad [7.24]$$

$$A_{tot,wire} = P_{wire} \cdot \left(P_{wire} \cos 30°\right) = 0.866 P_{wire}^{\ 2} = 0.866 \left(\left(P/D\right)_{wire}\right) D^2 \qquad [7.25]$$

Setting the two total areas equal to each other gives

$$\left(P/D\right)_{wire} = 1.0746 \cdot \left(P/D\right)_{sq} \;\; ; \;\; \left(P/D\right)_{wire} = \left(P/D\right)_{hex} \qquad [7.26]$$

Since for the thermal-hydraulic equivalence, $P/D_{wire} = P/D_{hex}$, the two will be used interchangeably. The relationship between P/D_{sq} and P/D_{hex} is the same as the P/D relationship that Shuffler derived. But neither the wetted perimeter nor flow area is the same for the two subchannels, due to the presence of the wire. This means that both of these have to be modified in the MATLAB core construction code to account for the presence of wires. The wetted perimeter relationship is derived as follows:

$$P_{w,sq} = \pi D \qquad [7.27]$$

$$P_{w,wire} = \pi D + \pi\left(P_{wire} - D\right) = \pi P_{wire} = \pi D \left(P/D\right)_{wire} \qquad [7.28]$$

$$P_{w,wire} = P_{w,sq} \frac{P_{w,wire}}{P_{w,sq}} = P_{w,sq} \left(P/D\right)_{wire} \qquad [7.29]$$

This is a useful form for MATLAB, as it calculates the wetted perimeter for square subchannels, which can be simply multiplied by the wire P/D to obtain the correct wire wrap wetted perimeter.

Similarly, the flow area ratio must be calculated.

$$A_{flow,sq} = P_{sq}^{\ 2} - \frac{\pi}{4} D^2 \qquad [7.30]$$

$$A_{flow,wire} = P_{wire} \cdot \left(P_{wire} \cos 30^\circ\right) - \frac{\pi}{4} D^2 - \frac{\pi}{4}\left(P_{wire} - D\right)^2 \qquad [7.31]$$

Taking the ratio of the flow areas, and dividing D^2 out gives

$$\frac{A_{flow,wire}}{A_{flow,sq}} = \frac{\left(\frac{\left(P/D\right)_{wire}}{1.0746}\right)^2 - \frac{\pi}{4} - \frac{\pi}{4}\left(\left(P/D\right)_{wire} - 1\right)}{\left(\left(P/D\right)_{sq}\right)^2 - \frac{\pi}{4}} \qquad [7.32]$$

Substituting $(P/D)_{sq}$ for the $(P/D)_{wire}$ terms in the numerator gives the final result.

$$A_{flow,wire} = A_{flow,sq}\left(1 - \frac{\frac{\pi}{4}\left(1.0746 \cdot \left(P/D\right)_{sq} - 1\right)^2}{\left(\left(P/D\right)_{sq}\right)^2 - \frac{\pi}{4}}\right) \qquad [7.33]$$

Again, this is a useful form for MATLAB, since it is possible to multiply the square flow area (which MATLAB automatically calculates) by a factor which is in terms of the square P/D.

7.3 - Creating an Equivalent Input Deck

While the channels have equivalent geometries, this does not mean that the input deck for a purely square geometry will yield the same results as that for a wire-wrapped hexagonal geometry. To create a square input deck that yields the same results as a wire-wrapped hexagonal geometry, the input deck has to be changed somewhat. The changes are listed in the following sections. To prove that a square input deck with these changes gives equivalent results to a true wire wrap input deck, a true wire wrap input deck was constructed for a single geometry. The results of this true wire wrap input deck and the square core equivalent input deck are compared to confirm their equivalence.

7.3.1 - Square Equivalent Geometry

The necessary changes to the geometry of the square subchannels, as developed in Section 7.2.2 are summarized in Equations 7.26, 7.29, and 7.33. For example, it is necessary to multiply the wetted perimeter as calculated for the square core by 1.0746. The resultant wetted perimeter is now equivalent to a wire wrap wetted perimeter.

$$\left(P/D\right)_{wire} = 1.0746 \cdot \left(P/D\right)_{sq} \quad [7.26]$$

$$P_{w,wire} = P_{w,sq}\left(P/D\right)_{wire} \quad [7.29]$$

$$A_{flow,wire} = A_{flow,sq}\left(1 - \frac{\frac{\pi}{4}\left(1.0746 \cdot \left(P/D\right)_{sq} - 1\right)^2}{\left(\left(P/D\right)_{sq}\right)^2 - \frac{\pi}{4}}\right) \quad [7.33]$$

7.3.2 - Square Equivalent Pressure Drop

The pressure drop can be calculated using Equation 7.34.

$$\Delta P = f\frac{L}{D_h}\frac{G^2}{2\rho} \quad [7.34]$$

For square and hexagonal equivalence, the pressure drop of the square subchannel has to be set to equal that of the hex subchannel. G, L and _ are the same by construction. D_h is given as:

$$D_h = \frac{4A_{wire}}{D} = \frac{4A_{sq}}{D} \quad [7.35]$$

So setting the square friction factor equal to the hex friction factor will give the same pressure drop for both.

$$f_{wire} = \frac{C_{fT,wire}}{Re^{0.18}} \qquad [7.36]$$

Since Re is the same for hex and square geometries,

$$C_{fT,sq} = C_{fT,wire} \qquad [7.37]$$

will give the same friction factor. So it suffices to use the hex P/D to calculate C_{fT}, and the pressure drops will be the same.

7.3.3 - Square Equivalent Mixing Coefficient

This is not as clear, since the gap size changes between square and hexagonal geometries. However, as before, we want to set the square geometry so that we have the same mass flow through the gap as for a hex subchannel. The mass interchange per unit length for the hex geometry can be given as:

$$W'^{T}_{wire} = \beta_{wire}\rho V_1 (P - D)_{wirex} = \beta_{wire}\rho V_1 \left(\left(P/D\right)_{wire} - 1\right)D \qquad [7.38]$$

where $\_hex$ is the mixing coefficient, calculated as a function of the geometry of the hex channel. So for the square mass interchange to be equal to the hex one,

$$\beta_{sq} = \beta_{wire} \quad \text{and} \quad \left(P/D\right)_{sq} = \left(P/D\right)_{wire} \qquad [7.40a \text{ and } 7.40b]$$

The input of the mixing coefficient _ is specified for each channel, but VIPRE performs the calculation with the P/D_{sq}. Thus, it is not possible to get the same mixing coefficients as the hex with the square equivalent, and it is not immediately clear whether using $\_sq$ or $\_wire$ will give closer results. However, using $\_wire$ with changing _ has little effect on the results, so the difference between $\_sq$ and $\_wire$ is irrelevant. See Chapter 5 for more information on the effect of _.

7.4 - MATLAB Changes

This section contains an list of the changes made in the MATLAB code to achieve wire wrap equivalence. The control rod diameter is changed to account for the wire. Previously, the control rod diameter was a function of the pitch, and generally larger than the fuel rods. However, due to the nature of wire-wrapped assemblies, the control rod diameter must be the same as the fuel rod diameter. This will not significantly impact the control rods' neutronic performance.

1. The control rod diameter is set to the fuel rod diameter
2. The wetted perimeter is multiplied by $(P/D)_{wire}$
3. The subchannel flow area is multiplied by $A_{flow,wire}/A_{flow,sq}$, as in Equation 7.33
4. The friction coefficient C_{fT} is calculated using Equation 4.17
5. The mixing coefficient _ is calculated using Equation 5.3
6. Removed the grid spacer effect

7.5 - Proof of Equivalence

To prove that the equivalence proposed here is valid, a full core hexagonal input deck was created. The results of the VIPRE analysis are compared to the full core square equivalent input deck, and the agreement between these results proves equivalence. For the hexagonal input deck, Shuffler's hexagonal input deck was modified to take the wires into account. The following changes were made:

1. Modified subchannel area and wetted perimeter to account for wires
2. Removed the grid spacer effect
3. Modified the fuel rod to control rod ratio to match that of the square input deck
4. Changed the mixing parameters to take into account the wire wraps' effect on mixing

7.5.1 - Equivalence Test Results

Since the desired result of the equivalence is to have the same achievable power, iteration was performed until the achievable power was found for both the square and hexagonal array. If the arrays are equivalent, the achievable powers should be identical.

	Square Array	Wire Array
D	6.5 mm	6.5 mm
P/D	1.29	1.387
Heated Rods	111,760	108,433
q'	2.89 kW/ft/rod	2.87 kW/ft/rod
Q_{th}	4569 MWth	4394 MWth
Limiting Constraint	Velocity	Velocity

Table 7.1 - Geometries and Results of Equivalence Proof

In this case, velocity was the limiting constraint while for Shuffler's pressure drop was limiting. This makes sense because velocity is more constraining for wire wrap. The difference in the overall power Q_{th} is approximately 3.8%. As before, much of this has to do with the difference in the number of rods in the core. Due to the extremely large size of the reactor, the actual number of rods that can fit in the core will approximately be the same for hexagonal and square assemblies. So it is better to look at the difference in the linear heat rates q', which is about 0.9%.

However, this result shows little about the difference in behavior of the other constraints, since velocity was the only constraint that actually limited power. The errors for each of the constraints shows how close they were to limiting the maximum power. For example, the velocity error is defined as:

$$Error_{velocity} = (Max.\ Observed\ Velocity - Velocity\ Limit) / Velocity\ Limit$$

There are four different errors, and for equivalence all four errors should be comparable between the two cases. The errors at maximum power are as follows

	MDNBR	***Fuel Temp.***	***Pressure Drop***	***Velocity***
Hexagonal Array	-0.5453	-0.3379	-0.1742	-0.0011
Square Array	-0.5522	-0.3378	-0.1650	-0.0074

Table 7.2 - Individual Errors in Equivalence Proof

Since all of the errors are comparable, equivalence between the cores is proven.

Chapter 8: Steady-State Results

8.1 - Details of Wire Wrap Core Construction

Jon Malen [1] developed the core construction programs used by this study, and should be referenced for more details of the core construction. The core construction programs have not been changed for this study except to change the wetted perimeter, flow area, and control rod diameter, as is shown in Section 7.4. This section details some of the specific methodology used by the core construction programs when constructing the VIRPE input deck.

8.1.1 - Bundle Size

There is substantial incentive to fit the most rods possible into the pressure vessel, as this increases the achievable power without changing the linear power of the rods. Since rod assemblies are placed in integral bundles, there will always be some space between the periphery of the core and the circular pressure vessel. Choosing the appropriate bundle size can have a substantial effect on the achievable power of a given geometry. Malen developed a method for optimizing the bundle size so as to optimize the rod packing, that is maximize the number of rods in the core. However, Malen's optimization is not applicable to wire wraps, since these bundles are hexagonal instead of square. As a result, the number of rods used for wire wraps is calculated assuming that partial assemblies are feasible. The final calculated power is normalized, assuming that the rod packing is as good as the reference assembly. That is, the same cross-sectional area occupied by the reference core bundles is available to all values of P/D and D. The resulting number of rods in the core can be calculated according to Equation 8.1.

$$N_{norm} = \frac{N_{ref} \cdot A_{tot,ref}}{A_{tot}} = \frac{N_{ref} \cdot P_{sq,ref}^2}{P_{sq}^2} \qquad [8.1]$$

where A_{tot} is the total subchannel area, as defined in Equation 7.21. While the assumption of partial assemblies is not valid, power maps generated with this assumption are much clearer, as the rod packing does not limit certain geometries more than others. In Section 8.7, a preliminary analysis is performed to determine the optimal hexagonal

bundle size for the maximum power geometry of the Achievable Case. Section 8.7 will also address other aspects of bundle size design, but since the exact bundle size of the large bundles that will be considered has little effect on any of the constraints, the constraints will not be modified based on the bundle size. Generally, since hexagonal bundles are closer to circles than square bundles, more hexagonal bundles should be able to fit around the periphery of the core, and thus achieve better rod packing than square bundles.

8.1.2 - Control Rods

Since all wires have to be the same size to provide consistent supports, one consequence of using wire-wrapped rods is that all rods, including the control rod thimbles, have to be the same size. However, the exact size of the control rods does not strongly affect their absorption properties. For this design, the control rod thimble diameter will be set equal to the rod diameter, with the control rods sized as necessary to fit inside of the thimble. The exact design of the control rods within the thimble is not addressed, as it does not affect the thermal-hydraulic performance of the core.

Within a bundle, control rods are placed in a square array, such that there are 2 fuel rods between each of them. The centermost assembly is shown in Figure 8.1.

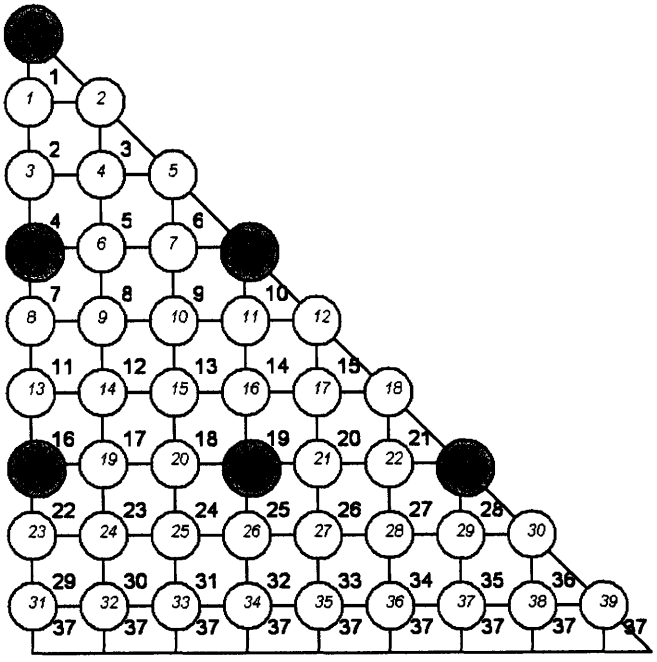

Figure 8.1 - Centermost bundle (control rods are gray)

This square array is used for both the Achievable Case and the Stretch Case. However, the wire wrap hexagonal values for the flow area, heated and wetted perimeter are used in the core construction, and the control rod diameter is set to the fuel rod diameter. The equivalence proof in Chapter 7 confirms that this approach is valid.

8.1.3 - 1/8th Core Methodology

Due to symmetry, an 1/8th section slice of a square assembly core (analogous to the 1/8th section of a square bundle, as shown in Figure 8.1) is sufficient for the thermal-hydraulic analysis performed by VIPRE. The resultant power is multiplied by a factor of 8 to attain the full core power. Because of the differences in geometry, a hexagonal core cannot be represented by an 1/8th core, but is instead represented by a 1/6th core. The resultant power for hexagonal cores is multiplied by 6 to attain the full core power, which should be the same as the equivalent square core full power. The full core power equivalence is proved in Chapter 7, where the square array was an 1/8th core, and the hexagonal array was a 1/6th core, and the full core powers were equivalent.

8.1.4 - Channel Lumping

For the geometries considered in this study, the number of rods can easily approach 100,000. Modeling each of the associated subchannels would be computationally impractical. The behavior of individual channels is only of interest when finding the maximum axial velocity and fuel temperature, and MDNBR of the core. Fortunately, all of these values are found in the hot assembly, as this is where the highest power occurs. This is no coincidence, since the hot assembly is generally the assembly of most interest, as it is usually the location of a reactor where the limits are most closely approached.

Since the peripheral channels are not of individual interest, as the hot assembly channels are, they are lumped by MATLAB. The only thermal hydraulic difference between individual channels and lumped channels is that the lumped channels average the characteristics of the individual channels. For n individual channels that are lumped,

$$\dot{m}_x = \sum_{i=1}^{n} \dot{m}_i \qquad A_f = \sum_{i=1}^{n} A_{f,i} \qquad P_w = \sum_{i=1}^{n} P_{w,i} \qquad P_h = \sum_{i=1}^{n} P_{h,i} \qquad D_e = \frac{4 \cdot A_f}{P_w} \qquad \textbf{[8.2]}$$

8.1.5 - Clad and Gap Thickness

The correlations for the clad and gap thickness are shown below, where D is in mm.

$$t_{clad} = max(0.508, (0.508 + (D - 7.747) \cdot 0.0362)) \quad \textbf{[8.3]}$$

$$t_{gap} = max(0.0635, (0.0635 + (D - 7.747) \cdot 0.0108)) \quad \textbf{[8.4]}$$

8.1.6 - Gap Conductivity

For both hydride and oxide fuels, the gap is assumed to be filled with liquid metal. The thermal conductivity of the gap is assumed to be 35 W/m-K.

8.2 - Constraint Behavior with Maximum Power Iterations

The total core power can be expressed using the following thermodynamic relationship.

$$Q = \dot{m}_{tot} \Delta h \quad \textbf{[8.5]}$$

where $\dot{m}_{tot}$ is the total mass flow rate, and $\_h$ is the core-wide average enthalpy rise. The inlet temperature (and associated enthalpy) is constrained to be at least the saturation temperature of the secondary side. The fuel temperature and CHF would rapidly degrade if the outlet enthalpy were allowed to rise. For these reasons, in this study both the inlet and outlet temperatures, and thus the enthalpy rise, have been fixed at the reference core values. As a result, from Equation 8.5, the only way to change the power is to change the mass flow rate. Conversely, changing the mass flow rate requires a change in power to maintain the enthalpy rise.

Consequently, when the power is iterated by VIPRE, the mass flux varies with it. This is the reason that the pressure drop increases substantially with increased power, as $\Delta P \propto \dot{m}^2$. Since the flow area is fixed, the axial velocity also increases with the increased mass flow rate associated with increased power, according to Equation 8.6.

$$V = \frac{\dot{m}}{\rho \cdot A_f} \quad \textbf{[8.6]}$$

The centerline fuel temperature is approximated as

$$T_{CL} = T_b + \frac{q'}{k_{eff}} \qquad \textbf{[8.7]}$$

where T_b is the bulk fluid temperature, q' is the linear heat generation rate, and k_{eff} is the effective conductivity of the fuel, cladding and fluid as calculated by VIPRE. When the mass flux is increased with increasing power, k_{eff} increases slightly due to the decreased thermal flow resistance with improved turbulence. However, by far the main effect of the power change is the change caused to the linear heat generation rate, which follows Equation 8.8.

$$Q = N \cdot q' \cdot L \qquad \textbf{[8.8]}$$

Consequently, an increase in power will result in an increase in the centerline fuel temperature. A similar analysis can be performed to show that the average fuel temperature is similarly affected by changes in power. In addition, increased mass flow rate has a substantial positive effect on the CHF, due to the improved mixing provided by the increased turbulence. Recall that the definition of MDNBR is

$$MDNBR = \frac{\phi_{CHF}}{\phi_{actual}} \qquad \textbf{[2.1]}$$

While an increased power leads to an increased mass flow rate and CHF, the actual heat flux also increases. The actual heat flux increase dominates over the CHF increase, with the net result of decreased MDNBR with an increase in power. However, this MDNBR decrease is mitigated by CHF increases. Thus, an increase in power brings each of the constraints (pressure drop, axial velocity, fuel temperature, and MDNBR) closer to their limit. This is consistent with the maximum power methodology, that the power can be constrained by any of the constraints.

8.3 - Behavior of Constraints in Constant Power Case

8.3.1 - Constant Power Case Methodology

This section presents the results of the Constant Power Case, which shares the Achievable Case soft limits, but instead of presenting the results for the maximum power, the results are for the constant reference power. However, instead of iterating to find the maximum power that does not exceed any of the constraint limits, the values of the constraints are simply recorded. The result is that for some geometries, the constraint limits are exceeded, while for other geometries the power could be increased before any constraint is exceeded. The difference in methodology is detailed below:

Achievable Case Methodology

1. MATLAB constructs input deck
2. VIPRE is run for reference power
3. MATLAB iterates power until maximum power is found.
4. Constraints and power are recorded

Constant Power Case Methodology

1. MATLAB constructs input deck
2. VIPRE is run for reference power
3. Constraints and power are recorded

The Constant Power Case is extremely useful for showing the behavior of the different constraints for varying geometries, thereby helping to gain an understanding of the maximum power results presented later. The soft limits still apply, and are detailed in Table 8.1. The power map in Figure 8.2 is for the Constant Power Case with hydride.

Soft Constraint	*Limit*
Pressure Drop	60 psia
Axial Pitch	H_{grid}
H/D	H/D < 50
Diameter	D > 6.5 mm
P/D	P/D < 1.42

Table 8.1 Soft limits used for Constant Power Case

For computational reasons, the power used varied slightly for the Constant Power case varied slightly with different geometries, resulting in slight discrepancies in the behavior of q/q_{ref} and $Power/Power_{ref}$.

Figure 8.2 - Constant Power Case, Hydride Fuel

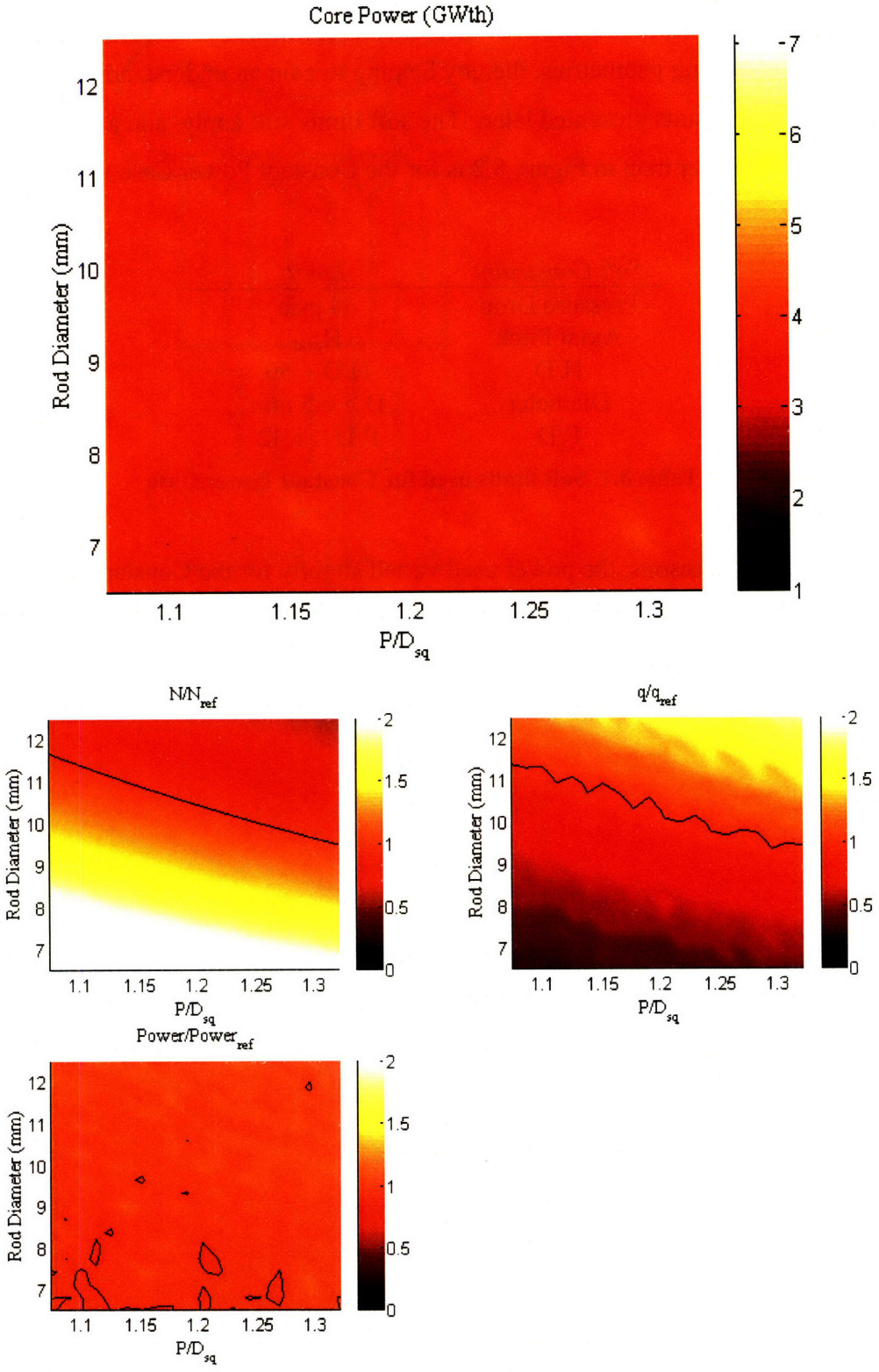

Figure 8.3 - Constant Power Case constraints (black lines are constraint limits)

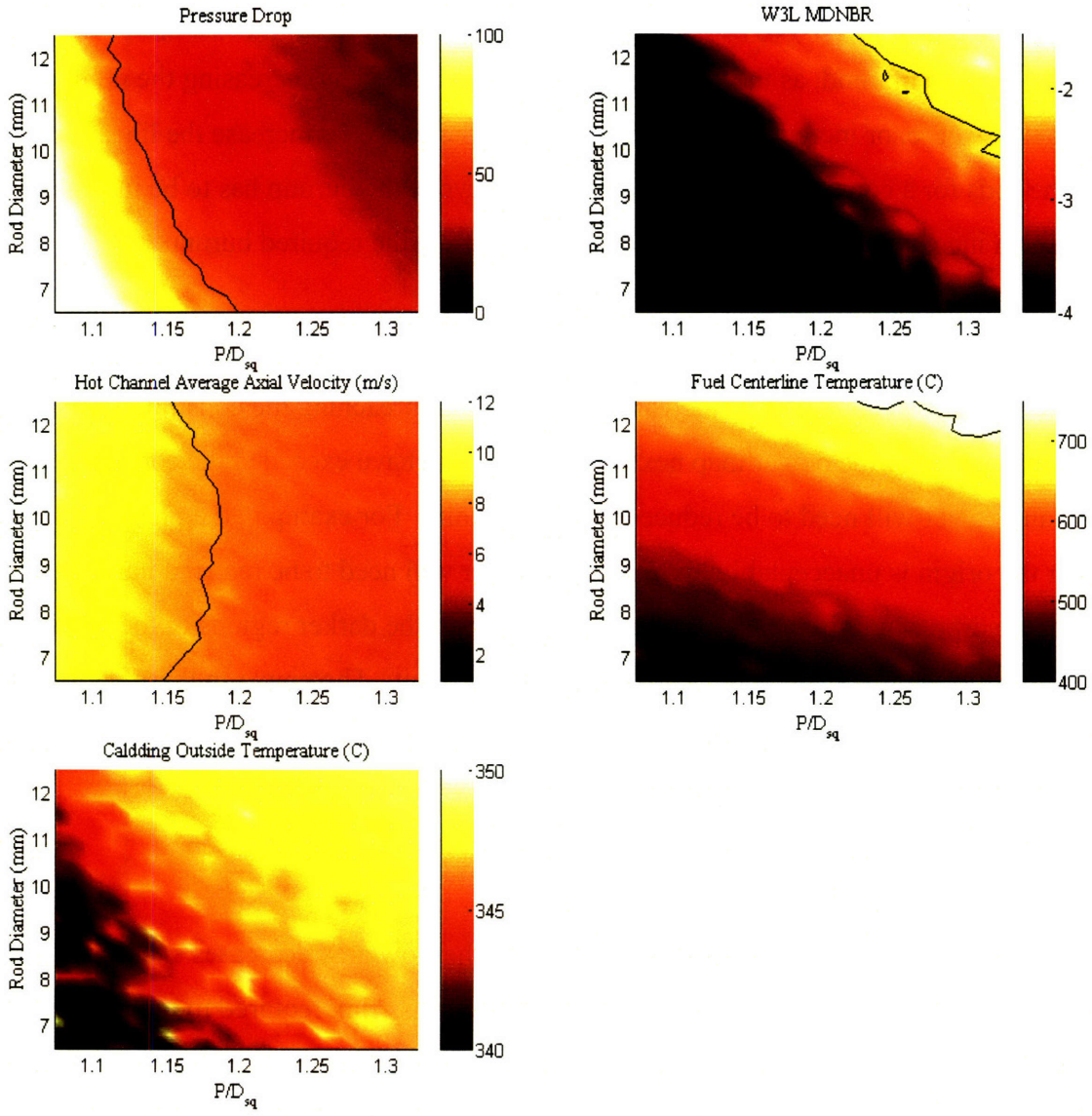

In Figure 8.2, N, q' and Power (or Q) are the number of rods in the core, linear heat rate and core power respectively, which can be related by Equation 8.2. These parameters are useful to keep in mind, as the power can either be increased by increasing the number of rods in the core, or increasing the linear power of the rods. To increase the linear power of the rods for a constant HM inventory and core cycle, the burnup has to be increased, while an increase to the number of rods does not affect the required burnup.

The black lines in Figure 8.3 represent constraint limits, indicating that the power for those geometries could not be increased more without breaching the constraint. The lighter regions of the power map next to the black line have exceeded the constraint limit, and the power will need to be reduced to within limits. For example, the pressure drop near the origin is unacceptably high, and the power will need to be reduced until the pressure drop is within the 60 psia limit. By contrast, the darker regions of the power map next to the black line have values less than the limit. The power in these regions can be increased in these regions only if none of the other constraints have exceeded their respective limits.

8.3.2 - Pressure Drop

The pressure drop is sensitive to P/D changes, as the flow area decreases substantially with decreasing P/D (see figure 4.2), increasing the mass flux required to maintain the mass flow rate, according to Equation 8.9.

$$\Delta P_{fric} = f \frac{L}{D_e} \frac{\left(\dot{m}/A_f\right)^2}{2\rho} \qquad [8.9]$$

where A_f is the flow area and D_e is the equivalent diameter. The equivalent diameter decreases with a decrease in D, leading to an increased pressure drop. Both of these trends are present in Figure 8.3 (increased pressure drop with decreased D and P/D).

8.3.3 - MDNBR

The MDNBR behavior is more difficult than the pressure drop to understand. The W-3 correlation is shown in Equation 8.10.

$$q''_{CHF} = 10^6 \left[\left(b_1 - b_2 p \right) + \left(b_3 - b_4 p \right) e^{\left(\left(b_5 - b_6 p \right) x \right)} \right] \left[\left(b_7 - b_8 x + b_9 x |x| \right) G / 10^6 + b_{10} \right] \left[\left(b_{13} + b_{14} e^{\left(-b_{15} D_e \right)} \right) \left(b_{16} + b_{17} \left(h_f - h_{in} \right) \right) \right] \quad \textbf{[8.10]}$$

where b_x are constants, p is the pressure, G is the mass flux, and D_e is the equivalent diameter. The CHF, and thus the MDNBR, increases with increased mass flux and decreased equivalent diameter. The increased mass flux improves the subchannel mixing, which helps to transport bubbles from the fuel rod surface which otherwise might cause a boiling crisis. A decrease in equivalent diameter effectively makes the channel smaller, limiting the difference between the bulk temperature and fuel rod surface temperature that leads to subcooled boiling. The result is that subcooled boiling occurs farther along the channel and is less extreme, making a boiling crisis less likely.

The effect of the mass flux on the MDNBR is relatively weak compared to the effect of equivalent diameter. As a result, the MDNBR closely follows the equivalent diameter. Lines of constant equivalent diameter are shown in Figure 8.4. The lines of constant MDNBR clearly follow the lines of equivalent diameter closely, and the MDNBR increases for decreasing equivalent diameter.

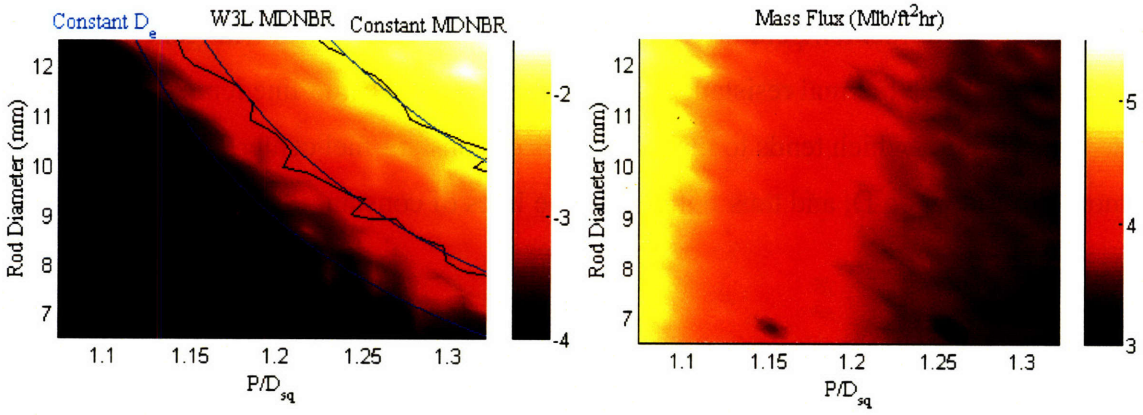

Figure 8.4 - Lines of Constant Diameter (in blue) Superimposed on MDNBR Plot

8.3.4 - Axial Velocity

The axial velocity is largely determined by the average core velocity, which is purely dependent on the water volume fraction. The smaller the water volume fraction, the faster the water has to move through the core to keep the enthalpy rise constant, since less water is still required to absorb the same amount of heat. If the velocity is not increased, the water will remain in the core too long and the exit enthalpy will be higher than allowed. The water volume fraction, and associated required average core velocity, is independent of D.

$$WVF = \frac{A_f}{A_{tot}} = \frac{0.866 \cdot P_{hex}^2 - \frac{\pi}{4} D^2 - \frac{\pi}{4}(P_{hex} - D)^2}{0.866 \cdot P_{hex}^2} = 1 - 0.907 \cdot \left[\frac{1}{\left(P/D\right)_{hex}} + \left(1 - \frac{1}{\left(P/D\right)_{hex}} \right)^2 \right] \quad \textbf{[8.11]}$$

where *WVF* is the water volume fraction, dependent only on P/D. This independence of the axial velocity on D is shown in Figure 8.3. Since the *WVF* decreases with decreasing P/D, the axial velocity must increase for the Constant Power Case. The shape of the constraint limit for the axial velocity is consistent with the shape shown in Figure 3.6.

8.3.5 - Fuel Centerline Temperature

While the total core power is constant, the linear heat generation rate changes for different geometries, as the number of rods changes. From Equation 8.7, the fuel centerline temperature varies linearly with the linear heat generation rate, resulting in lines of constant fuel temperature following lines of constant linear heat generation. Since most of the thermal resistance is in the fuel, the fuel centerline temperature is also dependent on D, which tends to make the lines of constant fuel centerline temperature more dependent on D, and thus flatter than the lines of constant linear heat generation.

8.4 - Achievable Case Steady-State Results

The Achievable Case is a wire wrap power map which shows the power increases when making conservative assumptions throughout.

8.4.1 - Oxide and Hydride Differences

The only difference between the oxide and hydride runs for both the Achievable and Stretch Cases were the fuel properties and temperature limits imposed. For hydride, the maximum centerline temperature is 750°C, and 2800°C for oxide. The centerline temperature limit was never active for oxide fuels, but an additional oxide average fuel temperature limit of 1400°C was active. The differences between the hydride and oxide temperature limits are shown in Table 8.2.

Temp. Limit	*Hydride Fuel*	*Oxide Fuel*
Average Fuel Temp.	--	1400°C
Centerline Fuel Temp.	750°C	2800°C

Table 8.2 - Temperature Limits for Hydride and Oxide Fuels

Even though the temperature limits of oxide fuels are much higher than the hydride, the lower thermal conductivity of oxide fuels leads to higher temperatures than hydride fuels at the same power. The average oxide fuel temperature limit is more constraining than the centerline oxide fuel temperature limit. As a result, the centerline oxide fuel temperature is never active, and consequently is not shown.

8.4.2 - Hydride Fuel

This section details the results of the Achievable Case using hydride fuel. From Chapter 2, the constraint limits for the Achievable Case with hydride fuel are:

Hard Constraint	*Acceptable Values*	*Calculated using*
CHF	MDNBR>$MDNBR_{ref}$	W-3L correlation
Axial Velocity	$V < V_{ref}$	Connors analysis
Fuel Temp.	$T_{CL} < 750$ °C	VIPRE
Clad Temp.	$T_{Clad} < 400$ °C	VIPRE

Table 2.2 - Hard Constraints for Achievable Case

Soft Constraint	*Acceptable Values*
Pressure Drop	< 60 psia
Axial Pitch	H_{grid}
H/D	H/D < 50
Diameter	D > 6.5 mm
P/D	$P/D_{wire} < 1.42$

Table 2.3 - Soft Constraints for Achievable Case

Applying these constraints using the methodology outlined in Chapter 2 gives the Achievable Case power map shown in Figures 8.5 and 8.6. The maximum power reported for the Achievable Case compares very favorably to both the reference core and the maximum power computed for grid spacers over a larger power map, as shown in Table 8.3.

	Achievable Case Maximum Power	*Reference Core*	*Grid Max. Power (Shuffler, 2004)*
Maximum Power	6251 MWth	3800 MWth	5489 MWth
D	8.39 mm	9.5 mm	6.82 mm
P/D_{sq}	1.321	1.326	1.4173
Pressure Drop	57.34 psia	29.0 psia	45.34 psia
Axial Velocity	10.83 m/s	5.75 m/s	7.2 m/s
H	420 mm	522 mm	522 mm

Table 8.3 - Maximum power of Achievable Case compared to other cases

While the geometry of the wire wrap maximum power is comparable to the reference core in both D and P/D, the grid maximum power occurs at a geometry with less fuel volume ratio, and at a very small diameter, which might not be manufacturable. So not only is the maximum power higher with wire wraps, the maximum power geometry is much more desirable.

The constraints are shown in Figure 8.6. All graphs are for the hydride power map except for the fuel average temperature for oxide. The lines and indicated areas show geometries where the constraint is actively constraining the power. The maximum power occurs at a triple intersection of CHF, pressure drop, and axial velocity constraints, so all three of these are close to being constraining, implying that the correct value of axial pitch (H) was chosen. This is because increasing H would make axial velocity and CHF more constraining, decreasing the achievable power. Decreasing H would make the pressure drop more constraining, with the same effect of decreased achievable power.

8.4.3 - Oxide Fuel

For the Achievable Case, the oxide and hydride temperature limits behaved very similarly and were not constraining for the maximum power. As a result, the power maps are very similar, as shown in Figure 8.5. The maximum powers are different by less than 1%, but since the temperature is not constraining for the region of maximum power (see Figure 8.6) in practice the maximum powers will be identical. Since the power maps are almost identical, the entire oxide results are not shown. The difference in the maximum power geometry for hydride and oxide fuel is also coincidental, and has no physical meaning or impact.

Figure 8.5 - Achievable Case, Hydride and Oxide Fuel

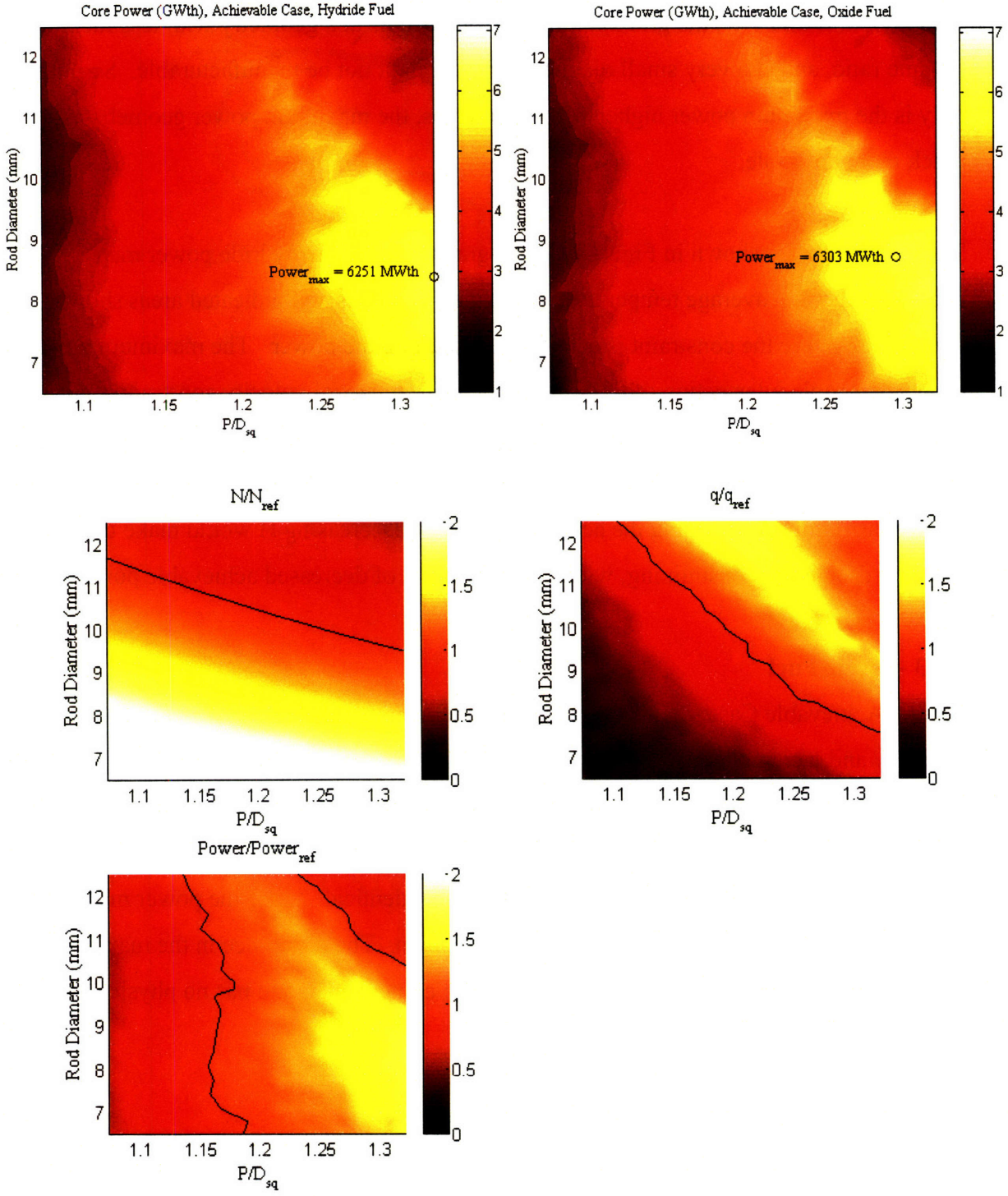

Figure 8.6 - Achievable Case Constraints

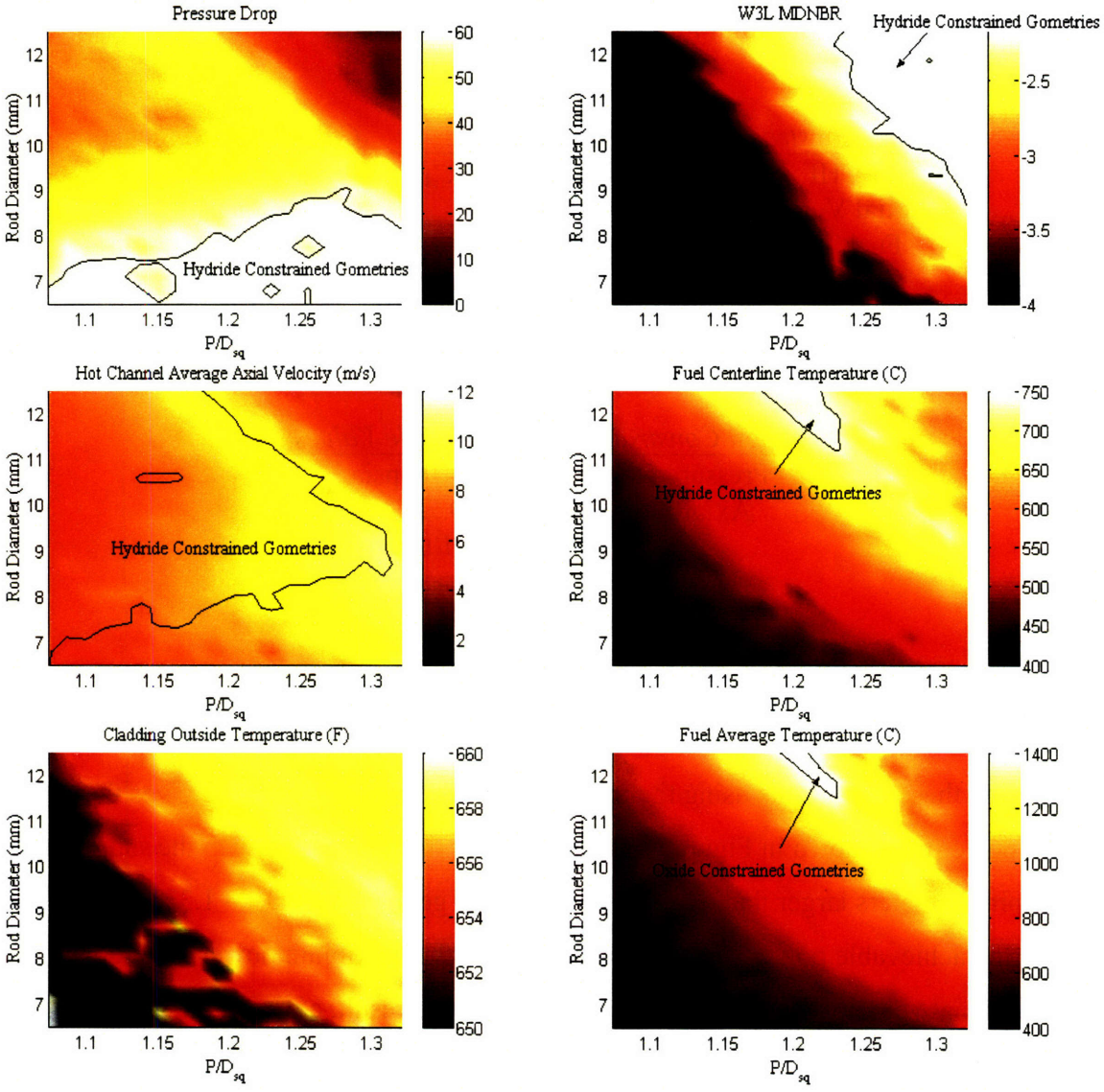

8.5 - Stretch Case Steady-State Results

From Chapter 2, the constraint limits for the Stretch Case are:

Hard Constraint	*Acceptable Values*	*Calculated using*
CHF	MDNBR>$MDNBR_{ref}$	Dalle Donne
Axial Velocity	$V < V_{ref}$	Connors analysis
Fuel Temp.	$T_{CL} < 750$ °C	VIPRE
Clad Temp.	$T_{Clad} < 400$ °C	VIPRE

Table 2.4 - Hard Constraints for Stretch Case

Soft Constraint	*Acceptable Values*
Pressure Drop	< 90 psia
Axial Pitch	$0.75 \cdot H_{grid}$
H/D	H/D < 50
Diameter	D > 6.5 mm
P/D	P/D < 1.42

Table 2.5 - Soft Constraints for Stretch Case

Applying these constraints using the methodology outlined in Chapter 2 gives the Stretch Case power map shown in Figures 8.6 and 8.7. For the geometries with the same P/D but with pin diameters larger than the maximum power geometry ($P/D_{sq} = 1.3214$, D = 7.13 mm), the achievable power was almost identical to the maximum power, due to very similar axial velocity limits for these geometries. As a result, a preferable geometry ($P/D_{sq} = 1.3214$, D = 8.71 mm) has been identified. The achievable power of the preferable geometry is only 0.5% less than the maximum power, and the diameter is much larger, very desirable for the manufacturability of the design. As a result, the preferable geometry will be taken as the ideal geometry, and the maximum power geometry will be ignored.

The preferable geometry power reported for the Achievable Case compares very favorably to both the reference core and the maximum power computed for grid spacers over a larger power map, as shown in Table 8.4.

	Stretch Case Pref. Geom. Power	*Reference Core*	*Grid Max. Power (Shuffler, 2004)*
Maximum Power	7156 MWth	3800 MWth	5489 MWth
D	8.71 mm	9.5 mm	6.82 mm
P/D_{sq}	1.321	1.326	1.4173
Pressure Drop	76.52 psia	29.0 psia	45.34 psia
Axial Velocity	12.67 m/s	5.75 m/s	7.2 m/s
H	391.5 mm	522 mm	522 mm

Table 8.4 - Preferable geometry power of Stretch Case compared to other cases

The geometry of maximum power for the Stretch Case turns out to be close to equivalent to the reference core, and is certainly a reasonable geometry. As with the Achievable Case, the maximum power using grid spacers is lower, and the associated geometry is not nearly as reasonable. Note that both the pressure drop and the axial velocity are substantially higher than the reference geometry. The wire wrap axial velocity is higher because Connors' analysis predicts a higher maximum axial velocity for wire wraps, and the pressure drop is higher because it is a soft constraint, not important enough to require a reduction in power.

The maximum power for hydride fuels is shown in Figure 8.7. The maps in Figure 8.7 look extremely similar due to the similar behavior of the temperature limits of hydride and oxide fuels. Generally, the oxide temperature limit gives slightly higher powers than the hydride. While the transient performance of hydride and oxide fuels is essentially identical, hydride fuel is predicted to be able to achieve much higher burnups than oxide, improving its economic performance. As discussed later, however, the burnup maps used for hydride fuel do not take into account the effect of burnable poisons.

The constraints are shown in Figure 8.8. As for the Achievable Case, since the steady-state results for the oxide and hydride runs are so similar, the only oxide constraint shown is the oxide fuel average temperature. Pressure drop is not constraining at all, because for each geometry another constraint limited the power before the pressure drop. This is a desired result, since pressure drop is a soft constraint and should not be very limiting to

the power. Note that the MDNBR constrained geometries do not have a constant MDNBR value. This is because the limiting value of MDNBR varies with geometry, as developed in Section 6.6.2.

Figure 8.7 - Stretch Case, Hydride and Oxide Fuel

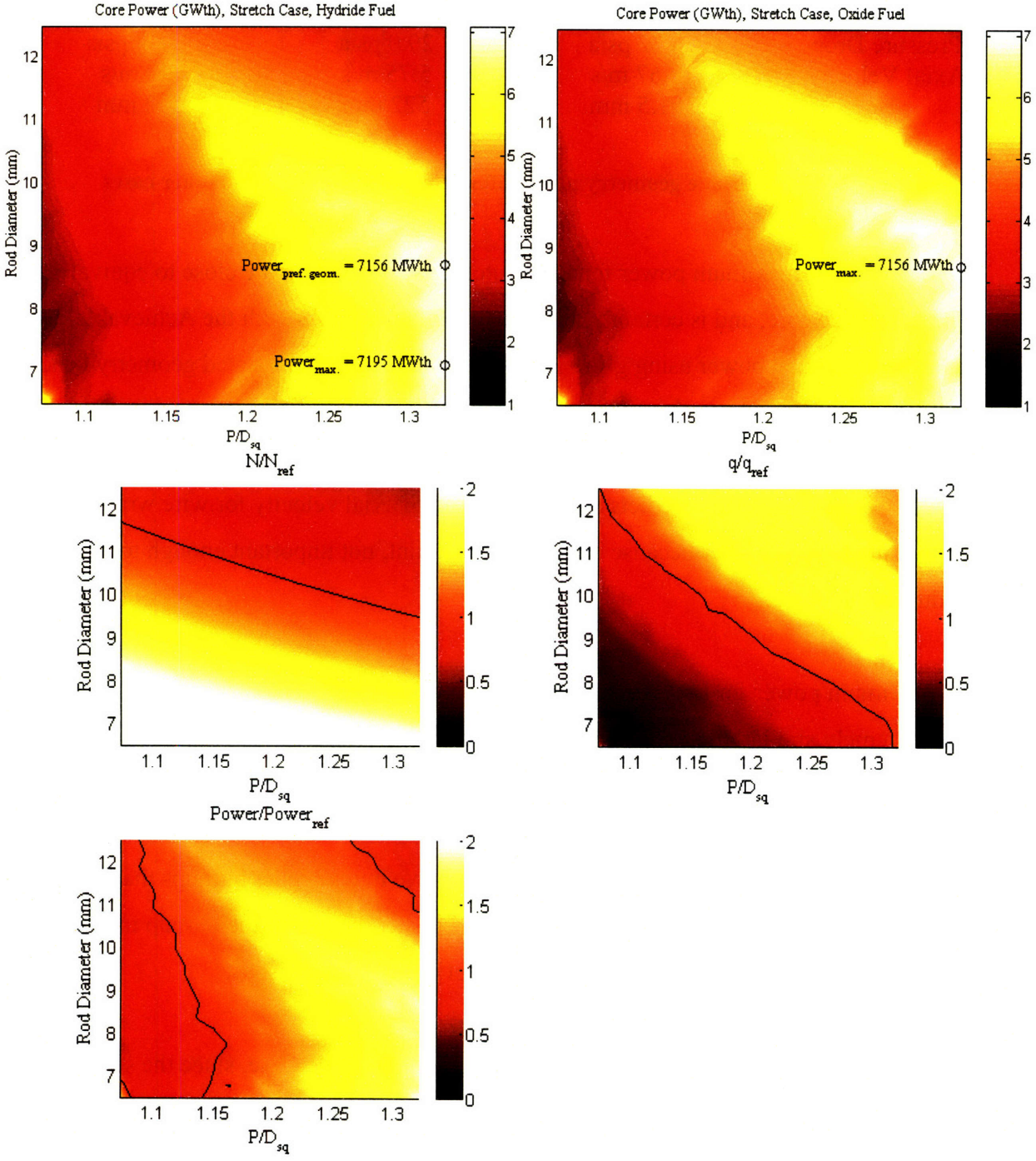

Figure 8.8 - Stretch Case Constraints

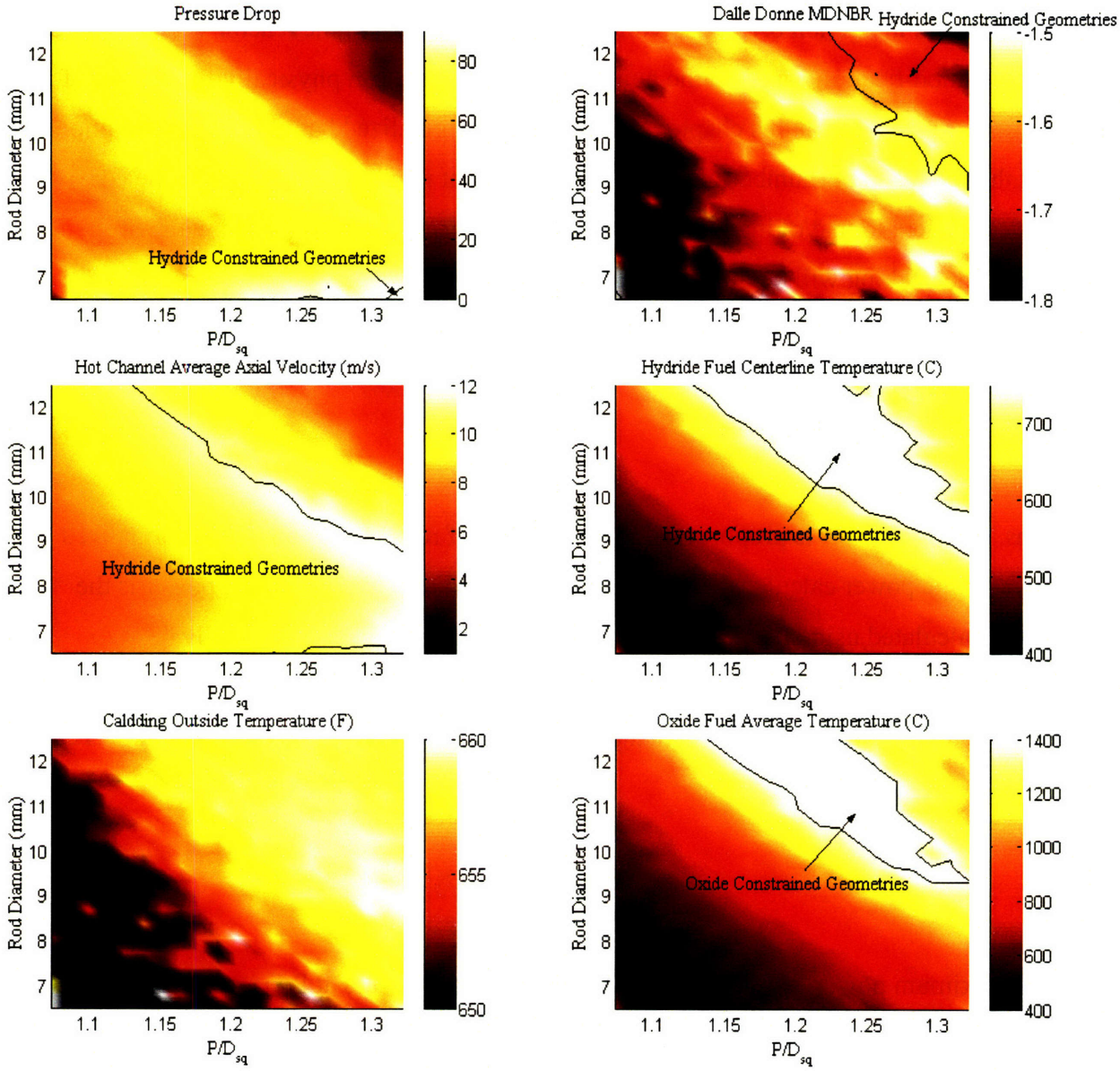

8.6 - Rod Packing for Achievable Case Maximum Power Geometry

As discussed in Section 8.1.1, the reality of integral bundles in the reactor vessel requires a power modification based on the number of bundles that can physically fit. For all of the results presented in this chapter, the power was normalized based on the assumption that the rod packing (number of bundles, and resultant number of fuel rods in the core) was equivalent to that of the reference core. However, in the final design with wire wraps, the packing will be different, due to the difference in bundle geometry. The number of rods affects the core power according to Equation 8.8, repeated here.

$$Q = N \cdot q' \cdot L \qquad \textbf{[8.8]}$$

Thus, the core power is proportional to the number of rods in the core. The normalized power is the power calculated assuming reference rod packing, the actual power is the power calculated using the number of hexagonal bundles that would actually be implemented. The linear power and bundle length are essentially unaffected by rod packing, so the normalized and actual power can be related according to Equation 8.12.

$$\frac{Q_{act}}{Q_{norm}} = \frac{N_{act}}{N_{norm}} \qquad \textbf{[8.12]}$$

The maximum power geometry of the Achievable Case occurs at $P/D_{sq} = 1.32$ and D = 8.39 mm, giving $P_{sq} = 11.1$ mm. N_{norm} is calculated according to Equation 8.13, using N_{ref} and P_{ref} from Table 1.1.

$$N_{norm} = \frac{N_{ref} \cdot P_{sq,ref}^2}{P_{sq}^2} = \frac{50956 \cdot 12.6^2}{11.1^2} = 65811 \qquad \textbf{[8.13]}$$

The actual bundle size is computed using a program that evaluates the number of hexagonal assemblies that fit within the core for different bundle sizes. The calculation of the size of an assembly takes into account the porosity and the wall thickness. The calculation for the flat-to-flat distance of an assembly is given by Equation 8.14.

$$\text{Flat-to-flat} = \sqrt{3} \cdot P \cdot (R-1) + 2 \cdot P - D + 2 \cdot P_o \qquad \textbf{[8.14]}$$

where P is the pitch, D is the rod diameter, R is the number of rings, including the center ring, and P_o is the sum of the porosity and wall thickness, assumed to be 2 mm.

However, there are a couple of other constraints that are in play when considering the optimal bundle. If the bundle is too small, then there will be a very large number of assemblies in the core, increasing the refueling time substantially. If the bundle is too large, the heavy metal loading will cause the bundle weight to exceed the crane's specifications. The reference core bundle size is 17x17, or 289 rods. The optimal hexagonal bundle size computed for the Achievable Case maximum power geometry was an 11-ring (including the center rod) bundle. This bundle has 331 rods in it, and the core has 63799 rods. The Achievable Case maximum power geometry and reference core geometry are compared in Table 8.5.

	Reference	Achievable Case Maximum Power
P/D_{sq}	1.326	1.32
D	9.5 mm	8.39 mm
Bundle size	17x17, 289 rods	11-ring, 331 rods
Number of Assemblies	193	211
N	50952	63799

Table 8.5 - Reference and Achievable Case Maximum Power Geometries

The smaller rod diameter of the Achievable Case maximum power geometry mitigates the larger number of rods, and the resultant assembly weight turns out to be slightly less than the reference assembly. This is taken to be a reasonable bundle size.

Due to symmetry, a hexagonal core can be represented by a $1/12^{th}$ slice, which is used in rod number calculations. A $1/12^{th}$ slice of the chosen bundle size for the Achievable Case maximum power geometry is shown in Figure 8.9.

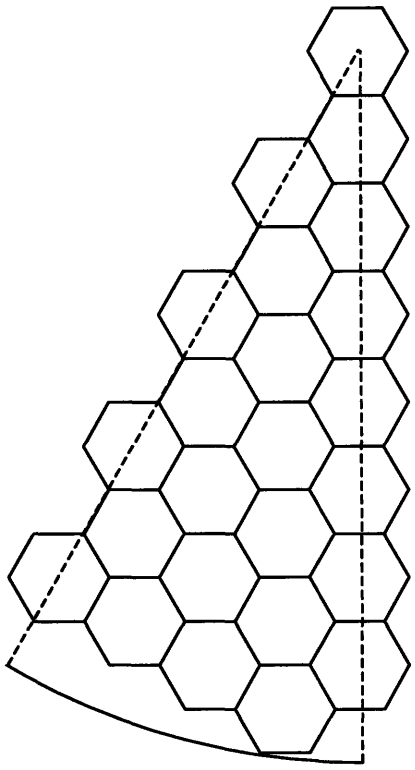

Figure 8.9 - 1/12th Section of Hexagonal Core

The actual maximum power for the Achievable Case is calculated using Equation 8.12, with the normalized power and the number of rods given in Table 8.4 and Equation 8.13. The resultant actual maximum power is given by Equation 8.14.

$$Q_{act} = Q_{norm} \cdot \frac{N_{act}}{N_{norm}} = 6251 MWth \cdot \frac{63799}{65811} = 6060 MWth \qquad \textbf{[8.14]}$$

The actual power is 3% less than the normalized power. In general there will be a small modification in the achievable power required due to the rod packing. If the rod packing of hexagonal bundles is better than the reference core rod packing for a given geometry, the modification will be a power increase over the results presented previously in this section, but the power modification for rod packing should be minor regardless.

Chapter 9 : Transient Analysis

The transient analysis performed here for wire wraps is modeled on the analysis performed by Jarrod Trant **[2]** for grid spacers. Trant's analysis covered 3 power-limiting transients: the loss of coolant accident (LOCA), overpower analysis, and loss of flow accident (LOFA). The overpower and LOFA analysis are modeled after Trant's analysis, while the LOCA analysis uses RELAP with a new input deck developed by a research group at MIT **[24]**. The transient analysis will be combined with the steady-state analysis to produce a final power map that satisfies both. However, since the transient analysis performed here is preliminary, the economics results for the final power map and the steady-state power map will be presented separately.

9.1 - Overpower Transient

As outlined in the South Texas Project Electric Generating Station (STPEGS) Final Safety Analysis Report (FSAR) **[25]**, there are two types of ANS Condition II overpower transients considered: a main steam line break at power and a rod bank withdrawal at power. Both of these transients result in a linear heat rate limit. The rod bank withdrawal, with the more limiting heat rate limit, will be considered here. The main steam line break at power will also be satisfied by this approach.

9.1.1 - Methodology

According to South Texas, the overpower value of the reference oxide core at the limiting MDNBR is 17.267%. That is, the MDNBR is below a critical value for an overpower greater than 17.267%. The exact value of this limiting MDNBR is propriety, but as calculated by the W-3L correlation in VIPRE, is 1.578. The premise of this analysis is that the MDNBR of a given geometry at 17.267% overpower must be greater than the reference core MDNBR value of 1.578. This overpower MDNBR limit of 1.578 replaces the steady-state MDNBR limit of 2.173.

A modified form of the steady-state VIPRE analysis will be used to analyze the overpower transients (see Chapter 8). The following changes are necessary for the Achievable and Stretch Cases, and for both hydride and oxide fuels.

1. The MDNBR limit is the W-3L value of 1.578. As for the steady-state case, an equivalent Bowring MDNBR limit will be calculated for each geometry, and the Dalle Donne spacer coefficient correlation will be used for the Stretch Case to account for the MDNBR effect of wire wraps (see Section 6.6).
2. The linear heat rate is increased by 17.267%. The overpower transient has the same pumping power available to it as the steady-state power. There will be a lower average mixture density in the core due to the higher quality associated with overpower, causing increased natural convection and a slightly higher flow rate. However, this effect is ignored, and the flow rate is assumed to be the same as that for the steady-state analysis.

These are the only differences between the steady-state and overpower analysis, and are summarized in Table 9.1. In general, the overpower analysis guarantees that with 17.267% overpower, a given geometry will perform at least as well as the reference core with 17.267% overpower.

	Power	MDNBR Limit	Flow Rate	Inlet Temp.	Enthalpy Rise
Steady-State	Q	2.173	$Q/\dot{m}\cdot\Delta h$	T_{in}	$\_h$
Overpower	$1.17267\cdot Q$	1.578	$Q/\dot{m}\cdot\Delta h$	T_{in}	$1.17267\cdot\Delta h$

Table 9.1 - Steady-State and Overpower Differences

9.1.2 - Results

The overpower transient was run for the Achievable and Stretch cases with both oxide and hydride fuels. As with the steady-state results, the oxide and hydride power maps and constraint behavior of pressure drop, axial velocity and CHF for the overpower transient are so similar that the entire oxide result will not be shown. Instead of presenting the standard power map for the overpower case, the power is divided by the steady-state power to show the power reduction required to comply with the overpower constraint. The overpower results for the Achievable Case are shown in Figures 9.1 and

9.2. The marked geometries display power reductions required for the maximum power geometries for the steady-state Achievable Case results.

Figure 9.1 - Overpower for Achievable Case, Hydride and Oxide Fuel

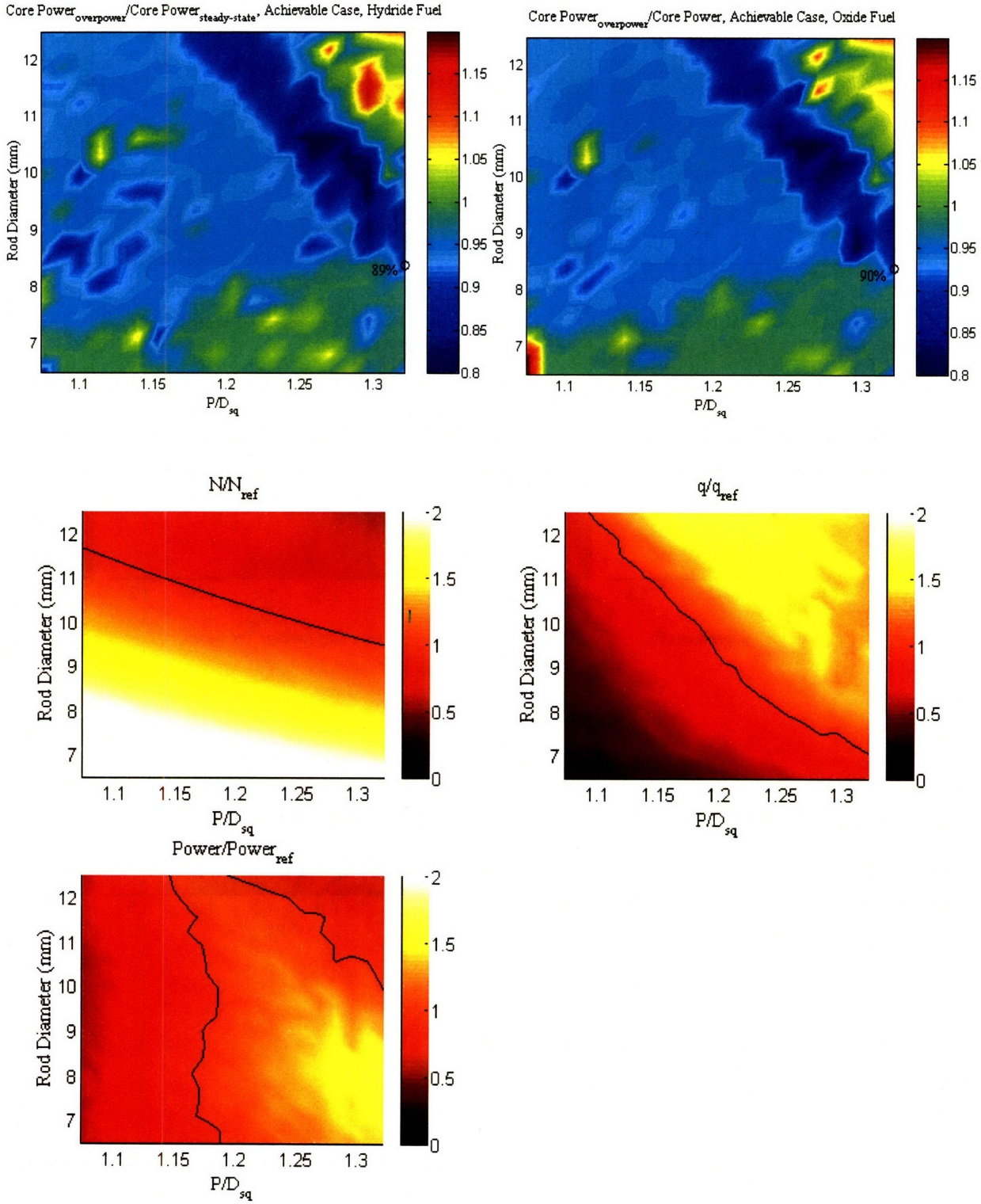

Figure 9.2 - Achievable Case Constraints with Overpower

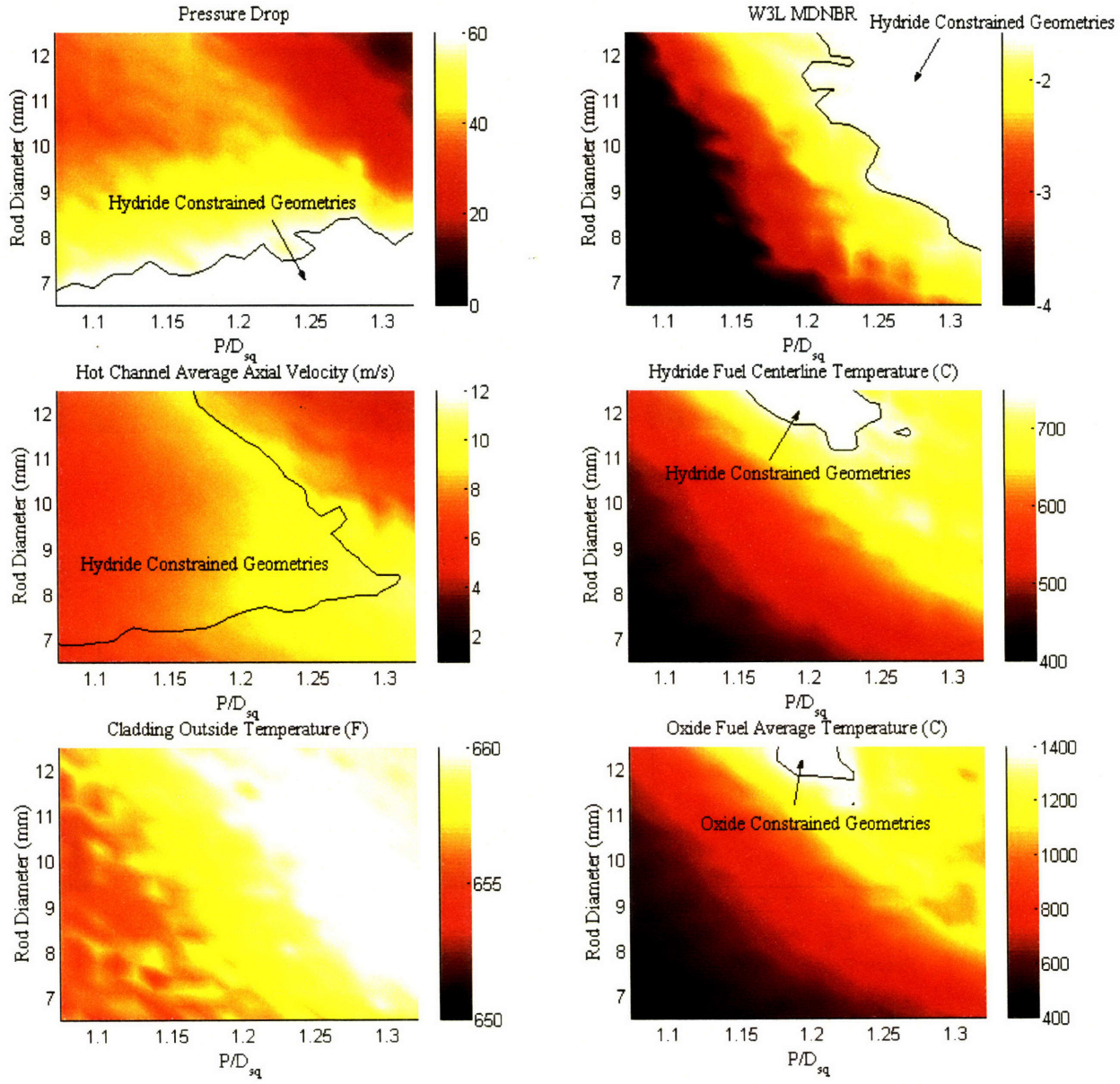

Achievable Case

As it turns out, the MDNBR limit for the overpower transient is slightly more constraining than the steady-state MDNBR limit. A maximum power comparison of the overpower and steady-state Achievable Case results is shown in Table 9.2. The maximum power is 3.6% less with the overpower transient than the steady-state, and at a slightly smaller diameter, which is less constrained by the MDNBR.

	Steady-State Maximum Power	*Overpower Maximum Power*
Maximum Power	6251 MWth	6025 MWth
D	8.39 mm	8.09 mm
P/D_{sq}	1.321	1.321
Pressure Drop	57.34 psia	59.5 psia
Axial Velocity	10.83 m/s	10.90 m/s
H	420 mm	420 mm

Table 9.2 - Achievable Case Hydride Maximum Power of Steady-State and Overpower

Over the power map in Figure 9.1, almost all of the geometries have a lower achievable power under the overpower transient (these are the blue regions), implying that the overpower transient is more constraining than the steady-state limits. The difference between the achievable powers of steady-state and overpower will be qualitatively considered here. There are two distinct regions, where the overpower transient limits the power in different ways. The first is the MDNBR-limited region, as defined by the line in the MDNBR plot of Figure 9.2. Rather than attempt a detailed explanation as to the causes of the behavior of the power map in this region, suffice it to say that the MDNBR limits and values are different, affecting the achievable power for MDNBR-limited regions. For geometries of interest (small D, large P/D), the effect of the MDNBR is a substantial penalty to steady-state power in MDNBR-limited regions, requiring a power reduction of up to 20% of the steady-state power to satisfy the overpower transient.

The other region is the velocity-limited region. The reason for the power difference between steady-state and overpower in this region is more subtle, as the flow rate does not change. The underlying cause of the power difference is the subchannel mixing due to diversion cross flow (see Section 5.1.1), as well as density changes associated with increased quality. Both of these

effects should serve to increase the hot channel axial velocity in the overpower transient, which in turn requires a power reduction in velocity-limited regions to bring the axial velocity within its constraint. This is generally true, and the average power reduction for the overpower transient is about 5% for velocity-limited regions. However, for reasons that are not entirely clear, some geometries with small D actually experience a power increase with the overpower transient.

Stretch Case

A maximum power comparison of the overpower and steady-state Stretch Case results is shown in Table 9.3.

	Stretch Case Pref. Geom. Power	*Overpower Maximum Power*
Maximum Power	7156 MWth	6808 MWth
D	8.71 mm	7.13 mm
P/D_{sq}	1.321	1.321
Pressure Drop	76.52 psia	76.62 psia
Axial Velocity	12.67 m/s	11.96 m/s
H	391.5 mm	391.5 mm

Table 9.3 - Stretch Case Hydride Maximum Power of Steady-State and Overpower

The maximum power for the overpower transient is 5% lower than for the steady-state results. In addition, the diameter is much smaller for the overpower, and is therefore less feasible. For the Stretch Case preferable geometry (8.71 mm), the overpower transient requires a power reduction of 12%.

The results for the Stretch Case are shown in Figures 9.3 and 9.4. The MDNBR and velocity-limited regions behave as for the Achievable Case, but now the fuel temperature-limited region is also substantial, and limiting to geometries of interest. The maximum fuel and cladding temperatures occur in the upper half of the bundle, as the coolant temperature is highest there. With overpower, the coolant temperature in the upper half of the bundle is higher, and the associated fuel temperature is higher, making the fuel temperature limit more constraining. This has an effect on the Stretch Case maximum power, as the fuel temperature constrains the

maximum power. The power reduction required for the overpower transient in the temperature-limited regions is practically constant at 5%, as the outlet temperature, while higher, is still fixed.

Figure 9.3 - Overpower for Stretch Case, Hydride and Oxide Fuel

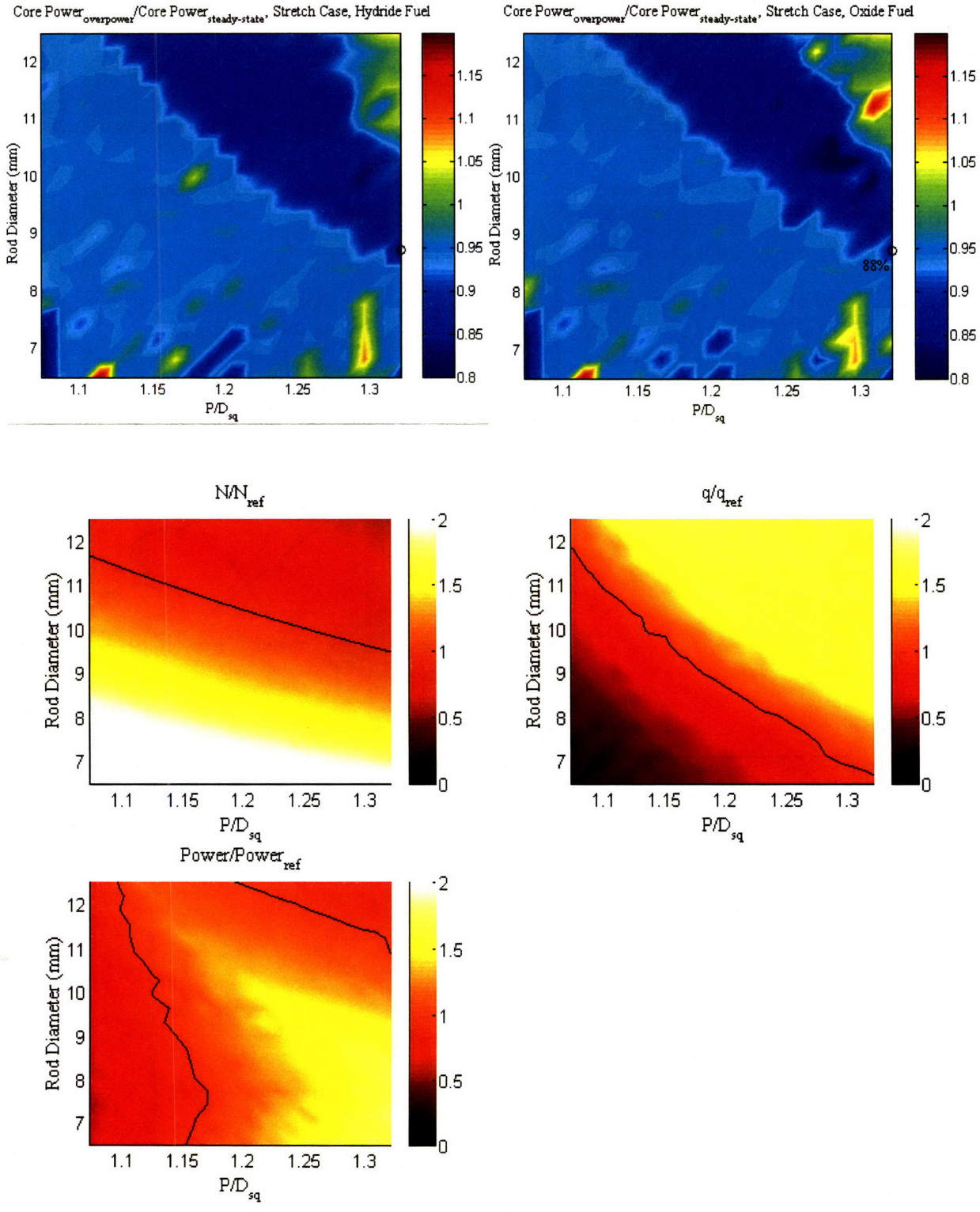

Figure 9.4 - Stretch Case Constraints with Overpower

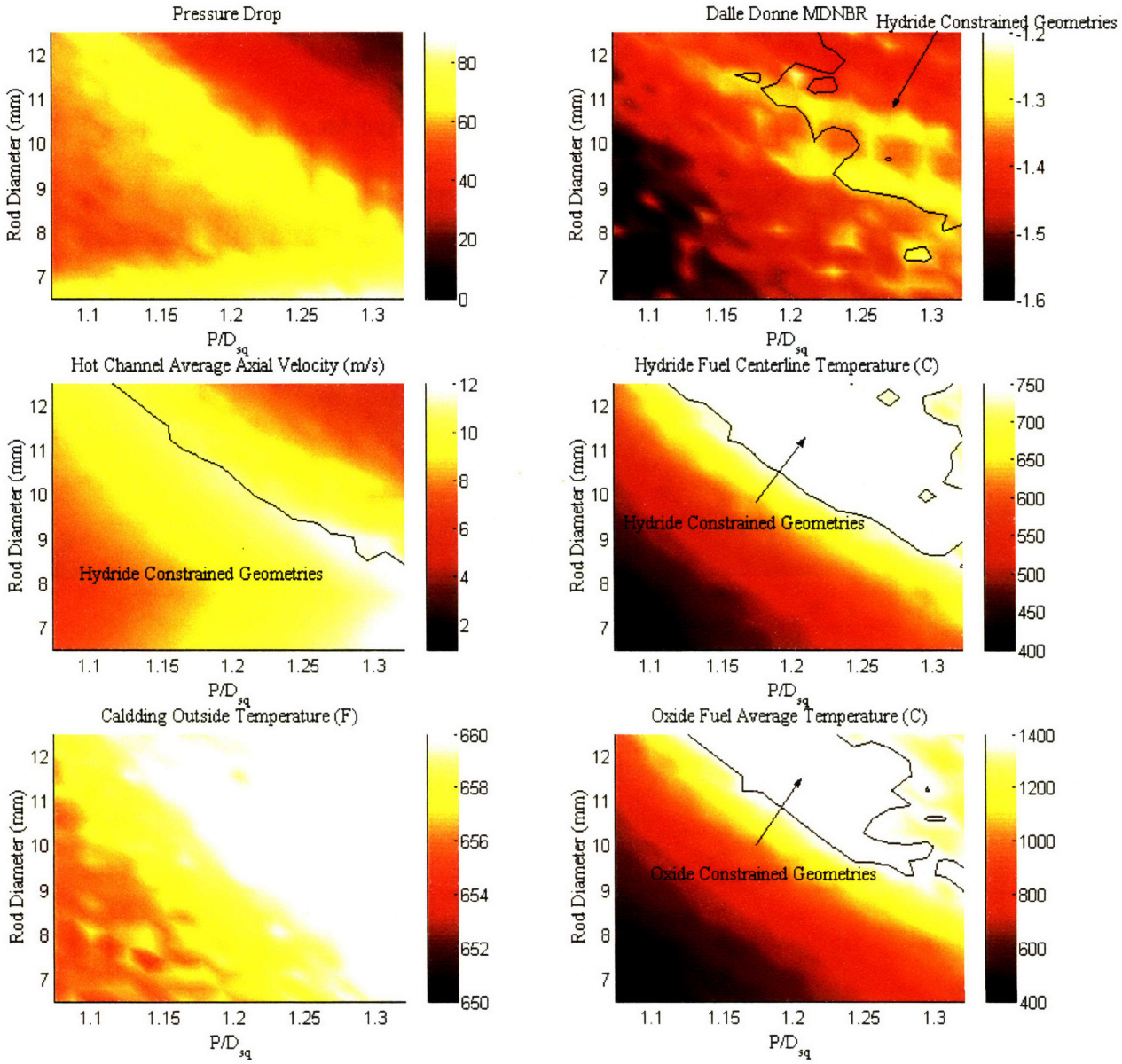

9.1.3 - Overpower Conclusions

The overpower transient analysis is extremely similar to the steady-state analysis. Due to the effects of the increased power on the axial velocity, fuel and cladding temperature, and MDNBR, the achievable powers under the overpower transient are generally lower than the steady-state achievable powers. A power reduction of up to about 10% might be necessary to accommodate for the overpower transient.

9.2 - Loss of Coolant Accident (LOCA)

9.2.1 - LOCA Constraints

Federal Regulations as described in 10CFR50.46 **[26]** outline two types of LOCA events: the large break LOCA (LBLOCA) and the small break LOCA (SMLOCA). The LBLOCA, being more constraining, will be considered here. The limiting conditions in a LBLOCA as detailed in 10CFR50.46 are as follows:

1. The calculated peak fuel element clad temperature is below the requirement of 2,200 °F.
2. The amount of fuel element cladding that reacts chemically with water or steam does not exceed 1 percent of the total amount of Zircaloy in the reactor.
3. The clad temperature transient is terminated at a time when the core geometry is still amenable to cooling. The localized cladding oxidation limits of 17 percent are not exceeded during or after quenching.
4. The core remains amenable to cooling during and after the break.
5. The core temperature is reduced and decay heat is removed for an extended period of time, as required by the long-lived radioactivity remaining in the core.

Due to the complexity of determining 2. and 3., these constraints are not addressed in this analysis, and only the temperature limit is considered. There is an additional temperature requirement for hydride fuels. For thermal temperature ranges, the crystalline structure of $UZrH_{1.6}$ (the hydride fuel considered by this project) is _-phase (face centered cubic) **[3]**, **[27]**. However, at temperatures above 1050°C, the hydride matrix converts partially to a _ phase (body centered cubic). This causes the structure to become much more

brittle, and is considered unacceptable. Thus, the maximum allowable hydride fuel temperature is 1050°C.

The constraints on the LOCA performance considered in this study for hydride and oxide fuels are shown in Table 9.4 in Kelvin, the unit used by RELAP. The oxide temperature limit is the melting temperature of UO_2.

	Hydride Fuel ($UZrH_{1.6}$)	*Oxide Fuel (UO_2)*
Fuel Temp.	1323 K	3073 K
Cladding Temp.	1478 K	1478 K

Table 9.4 - Active LOCA constraints

9.2.2 - Approach to LOCA analysis

RELAP was used to calculate the LOCA performance of a given geometry at a given power. The input deck is a modified Westinghouse 4-loop PWR. Figure 9.5 shows the result for the Westinghouse reference geometry at reference power with hydride and oxide fuel. The only functional difference between this core and the reference core considered in this study is the rod length and core power. The Westinghouse rod length is 12' compared to this study's rod length of 14'. This extra length is accounted for in the form loss. The Westinghouse power is 3479 MWth, while this study's reference power is 3800 MWth. For this LOCA analysis, the desired power was normalized by the Westinghouse power of 3479 MWth to find the uprating that will result in the desired power.

The temperature results for different axial locations are provided, but only the location with the highest Peak Cladding Temperature (PCT) is shown, as this is the most constraining axial location. For the entire transient, the fuel temperature is higher than the cladding temperature. A contrary result would be nonsensical, implying that heat would be moving from the coolant to the fuel rod. Since the hydride fuel temperature limit is lower than the cladding temperature limit, the fuel temperature limit will always be breached first. Consequently, the cladding temperature limit is considered inactive for

the hydride analysis, and will be implicitly satisfied when the fuel temperature limit is satisfied. However, due to the low heat flux, the cladding and fuel temperature difference is always small for a LOCA (31 K PCT difference for the reference case, see Figure 9.5). As a result, the oxide cladding temperature constraint will always be constraining before the fuel temperature constraint, and the fuel temperature constraint is considered to be inactive.

Figure 9.5 - LOCA for Reference Geometry, 3479 MWth

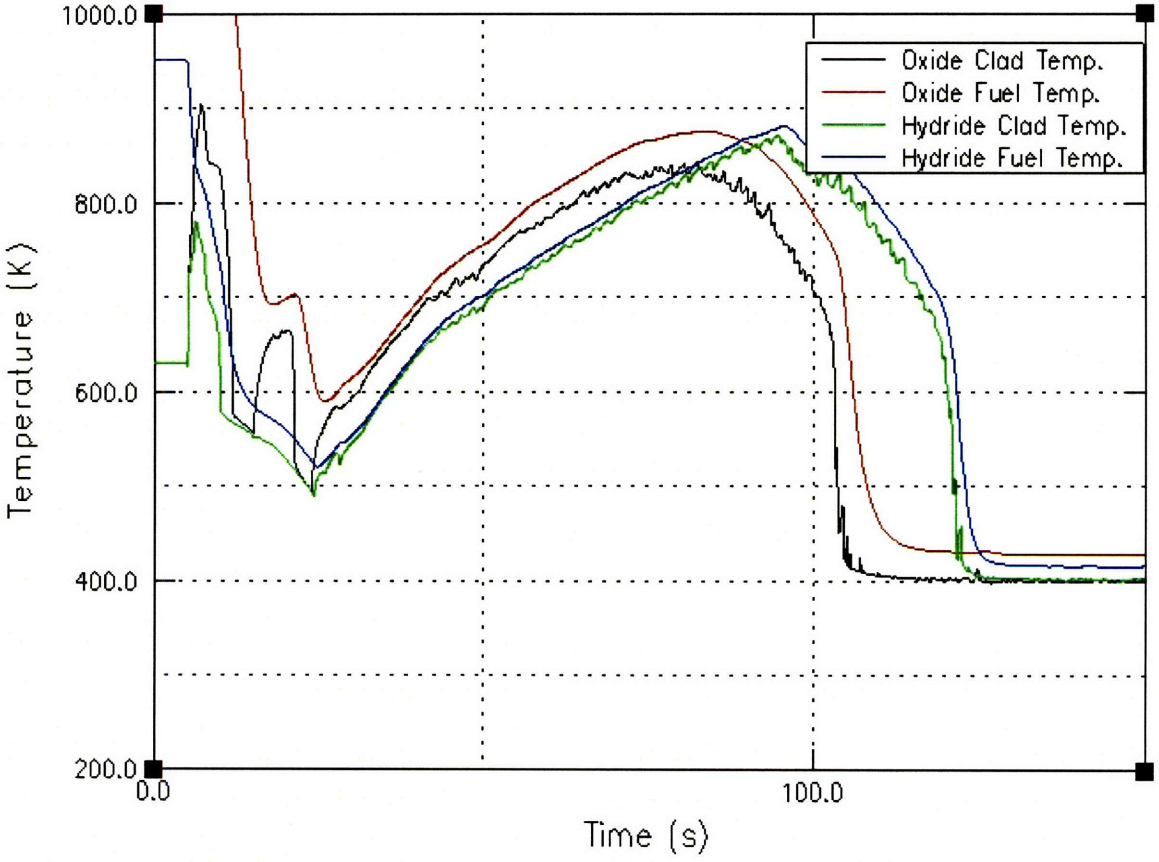

The following changes are made when performing a LOCA analysis at different geometries and different powers.

1. Flow resistance - increased flow resistance (in the form of decreased equivalent diameter or increased form loss) can make it harder for generated steam to escape the core, thus slowing the quenching process and increasing PCT.
2. Linear heat rate - the decay heat rate is proportional to the linear heat rate. Increasing the decay heat rate makes the unquenched rods heat up faster,

increasing PCT directly, and also slowing the quenching process, indirectly increasing PCT further.

3. Rod diameter - the net effect of rod diameter is not immediately clear, as a smaller rod diameter lessens the stored heat in the rod but also increases the flow resistance with a smaller equivalent diameter.
4. Fuel thermal conductivity - Oxide fuel has a much lower thermal conductivity, making it harder to remove the heat from the rod and quench.

It was found that changing the flow resistance had no net effect on PCT. However, there was a substantial stochastic effect on PCT with even small changes in flow resistance. The reason for the stochastic effect is not clear, but it is either a programming error in RELAP, computational limitation, or a reflection of the true stochastic nature of the LOCA. Regardless, this creates an uncertainty in the final PCT results, which should be considered to be preliminary. The trends (in particular the PCT trend with power) are still valid, and very illustrative of the potential power reduction required to comply with the LOCA restrictions.

It is not possible to interface RELAP with MATLAB, as it is with VIPRE, making it impractical to consider the LOCA behavior of the entire power map. In addition, the stochastic nature of the RELAP results render it impossible to try to converge on a maximum power that does not exceed the LOCA temperature constraints, as was done with VIPRE. As a result, only the RELAP results for the Achievable and Stretch Cases at the Achievable Case maximum power geometry will be presented here. However, this will allow preliminary conclusions to be drawn.

9.2.3 - LOCA Analysis for Achievable Case Maximum Power Geometry

Figure 9.6 shows the LOCA for the Achievable Case maximum power geometry, at the Westinghouse reference power. The number of assemblies and assembly configuration for this geometry is the same as was developed in Section 8.7. Table 8.5 is shown here again to show the difference in the geometries.

Table 8.5 - Reference and Achievable Case Maximum Power Geometries

	Reference	*Achievable Geometry*
P/D_{sq}	1.326	1.32
D	9.5 mm	8.39 mm
Bundle size	17x17, 289 rods	11-ring, 331 rods
Number of Assemblies	193	211
N	50952	63799

Figure 9.6 - LOCA for Hydride Fuel, Reference Geometry and Achievable Geometry, 3479 MWth

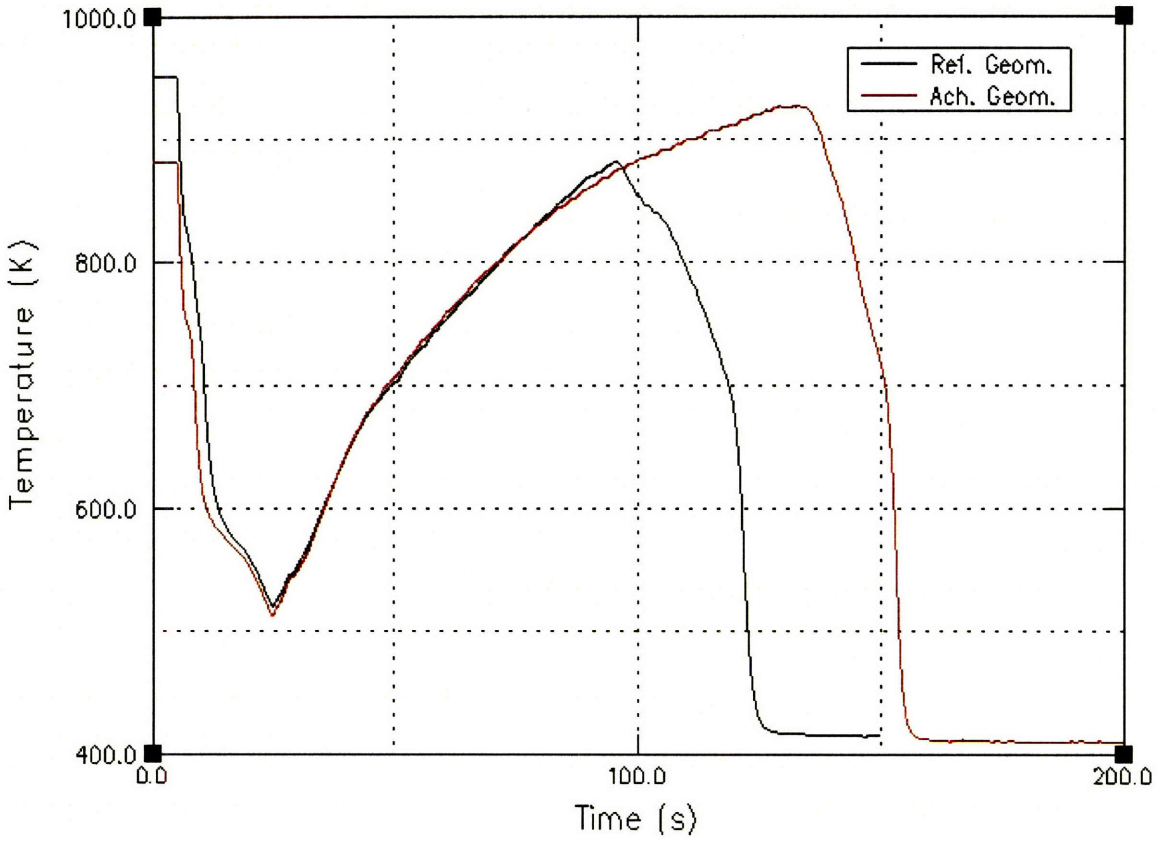

As Figure 9.6 shows, the LOCA performance for the different geometries is relatively similar, with slightly different quenching times. The PCT for hydride fuel at the Achievable Case geometry (927 K) is 55 K higher than for the reference geometry as shown in Figure 9.5 (872 K). Both of these curves are still well within the PCT limit.

While changes in geometry, fuel type, and flow resistance result in changes in LOCA performance that are generally minor, changing the power results in a dramatic change in LOCA performance. Figure 9.7 shows the effect of increasing the power on LOCA performance on hydride fuels at the Achievable geometry. 180% power corresponds to the Achievable Case maximum power (6251 MWth), and 206% power corresponds to the Stretch Case maximum power (7156 MWth). Both power increases result in a breach of the temperature limit. In addition, neither of the high power cores quenches at the end of the time considered, and it is possible that they will never quench.

Figure 9.7 - LOCA for Hydride Fuel, Achievable Case Geometry, Varying Power

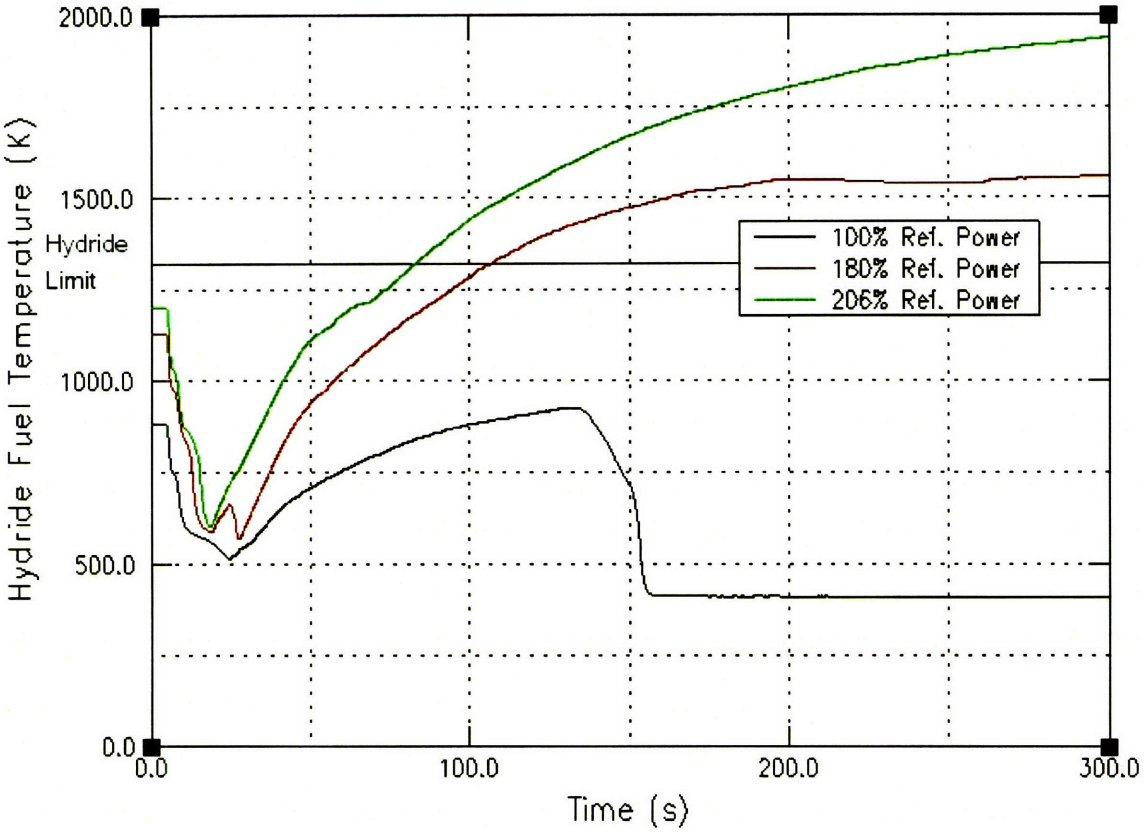

9.2.4 - LOCA Performance Improvements through Safety System Increases

Fortunately, there are other ways to improve the LOCA performance. In particular, the size and capacity of two safety systems, the safety injection (SI) system and accumulator. However, it should be noted that increasing the size of the accumulator requires a substantial amount of space, which is at a premium inside of the containment. As a result, increases to the SI are preferable to increases in the accumulator.

The capacity additions considered by this study to both of these safety systems are proportional to the power increase. The results of upgrades to the safety systems are shown in Figure 9.8 for 180% (corresponding to the Achievable Case maximum power) with the Achievable Case geometry.

Figure 9.8 - LOCA for Hydride Fuel, Achievable Geometry, Achievable Power, with Safety System Upgrades

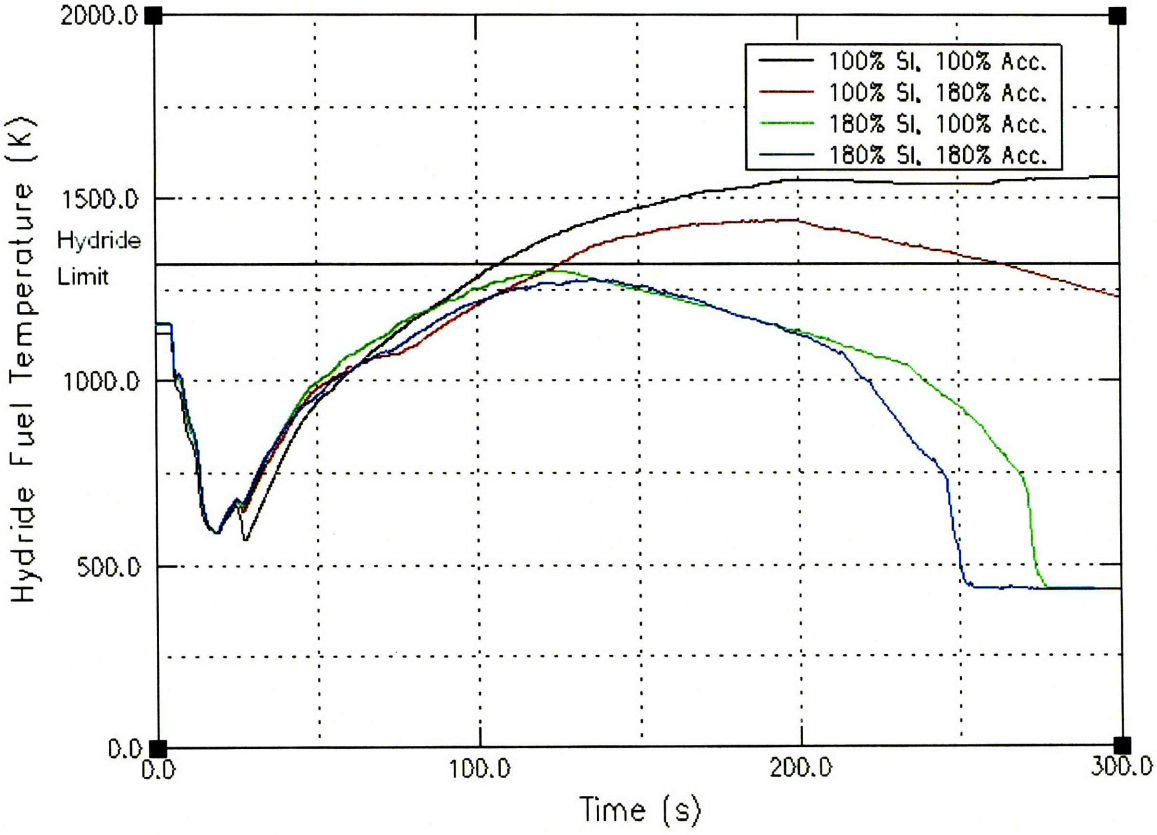

While the PCT of the additional accumulator capacity (in red) still breaches the temperature limit, the PCT begins to decrease. The real benefit to LOCA performance comes with increased SI capacity (in green). Simply increasing the SI capacity keeps the PCT under the limit, and allows the core to completely quench by 300 sec. Additionally increasing the accumulator (in blue) reduces the PCT by 25 K. However, due to the high cost and impracticality of increasing the accumulator size, combined with its marginal effect on the PCT, the final design considered by this analysis will increase the SI capacity with power, but leave the accumulator size unchanged.

The natural question that arises is by what means the safety systems are able to dramatically lower the PCT. To put more insight into this, Figure 9.9 was generated,

which shows the collapsed water levels for the downcomer and hot channel. The collapsed water level represents what the water level would be if the liquid and vapor phases were separated, and is useful for determining the gravity pressure drop driving

Figure 9.9 - Collapsed Water Levels for Hydride Fuel, Achievable Geometry

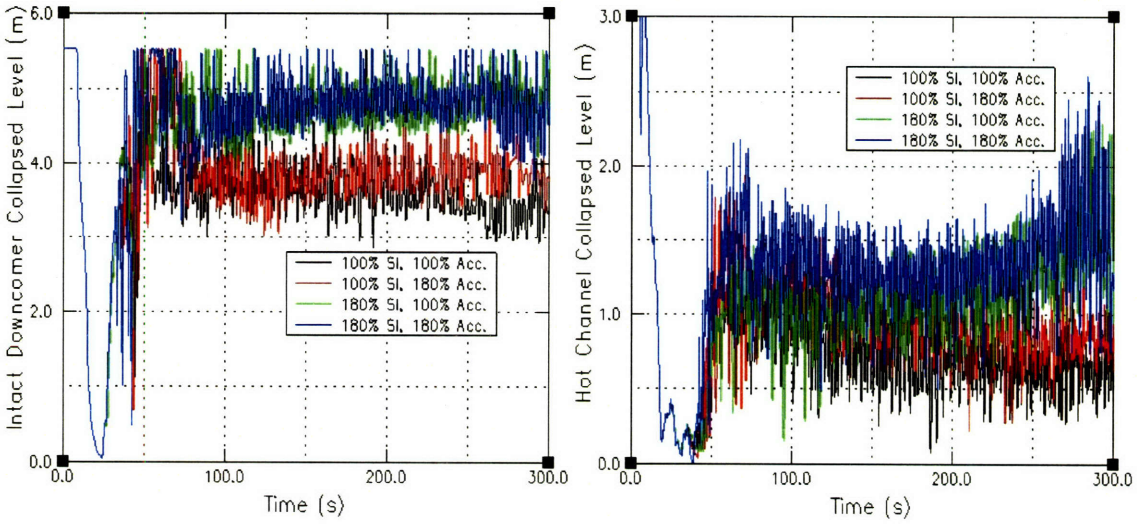

flow through the core. Since the downcomer collapsed water level (on the left of Figure 9.9) is much higher when the SI is increased (blue and green), there is a larger force driving flow through the core, causing it to quench faster. The quenching can be seen as increased collapsed water level in the hot channel for the cases where SI is increased (on the right of Figure 9.9). Notice that the accumulator size has little effect on the downcomer water level. This is the reason that the accumulator size has little effect on the PCT.

Figure 9.10 shows the final results for the LOCA analysis. The SI is increased proportional to the power for the Achievable Case and Stretch Case powers at the Achievable geometry. The Stretch Case analysis was performed at the Achievable Case geometry for convenience. From Section 8.5, the Stretch Case power for the Achievable geometry is in practice the same as the maximum power for the stretch case. However, RELAP encountered a processing error when attempting to run oxide fuel at 206%. As a result, the power was reduced to 200%, which RELAP was able to successfully complete.

Figure 9.10 - Hydride and Oxide, Achievable Geometry, Powers of Interest, SI ~ Power

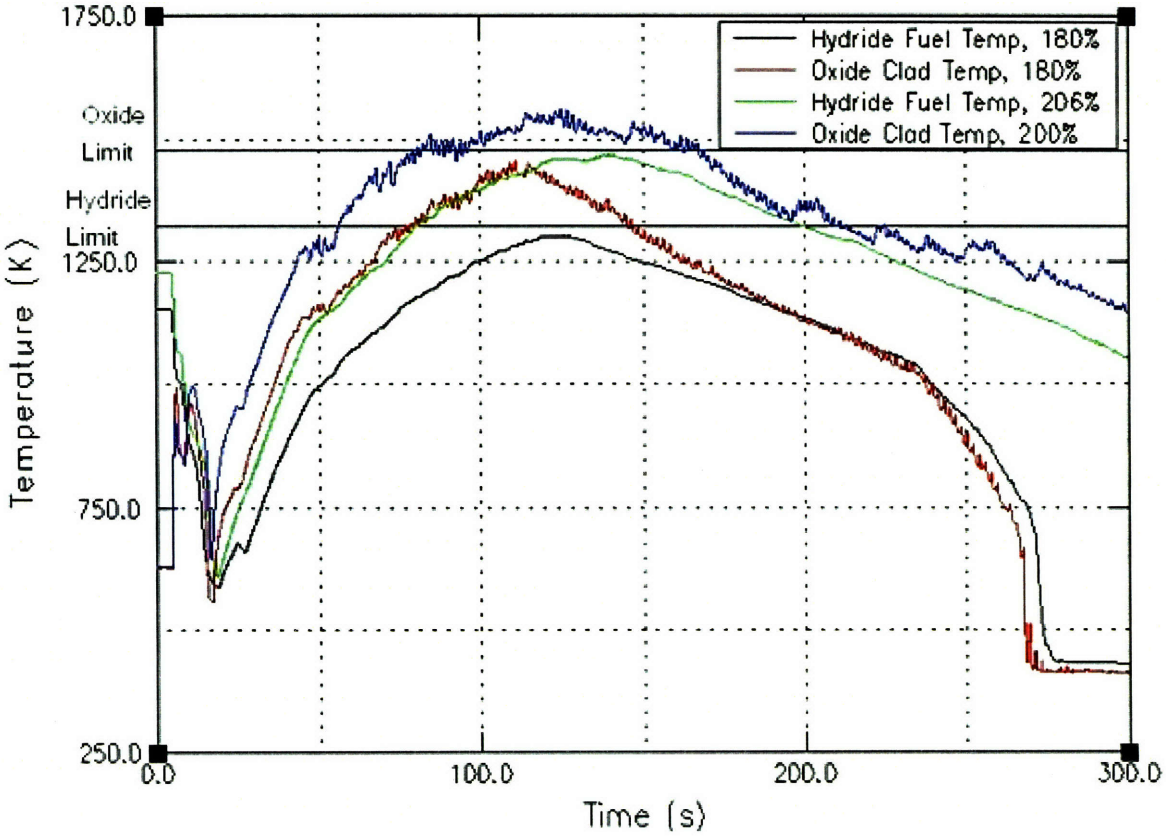

9.2.5 - Conclusions

The performance of the two fuels against their respective temperature limits is coincidentally (and surprisingly) similar. While the PCT's for both fuels come close to their temperature limits for 180%, neither exceed it. Thus, the LOCA is not considered to be constraining to the maximum power for the Achievable Case, provided that the SI is increased.

This is not true for either fuel for the Stretch Case power. While the oxide case is not even at full Stretch Case power, its PCT still exceeds the temperature limit. Linearly extrapolating the PCT from the 180% and 200% cases, the PCT of the oxide is expected to exceed its limit by 118 K at 206%. The hydride performance is even worse, as the PCT exceeds the temperature limit by 146 Kat 206%. Recalling that the preferred Stretch Case geometry had a slightly larger diameter than the Achievable geometry (8.71 mm vs. 8.39 mm), it would be possible to get a slightly lower PCT by analyzing the Stretch Case

at the preferred Stretch Case geometry. In addition, it might be possible to get a lower PCT by further increasing the SI capacity past proportionality (e.g. 300% SI for 206% power).

It is particularly surprising that even with hydride's lower temperature constraint, its LOCA performance did not surpass that of oxide, given hydride fuel's superior fuel conductivity. Both the oxide and hydride fuels at the Achievable Case maximum power came close to breaching the temperature limits without breaching them. Since power is the variable that has the strongest effect on the LOCA performance, the Achievable Case maximum power (6251 MWth) is assumed by this study to be a universal LOCA constraint, and will be applied to all geometries for the Achievable and Stretch Cases.

9.3 - Loss of Flow Accident (LOFA)

The complete loss of flow accident (LOFA) is considered an ANS condition III incident (infrequent accident). However, the South Texas Project Electric Generating Station (STPEGS) Final Safety Analysis Report (FSAR) analyzed this event to ANS condition II criteria as part of the non-emergency AC event power event **[25]**. ANS condition II incidents are defined as faults of moderate frequency. Condition II faults are those that cause the reactor to trip, at worst, with the plant remaining capable of returning to operation. In addition these faults do not propagate to cause more serious faults. The primary concern during a LOFA is the rise in coolant temperature leading to a departure from nucleate boiling. As such, the MDNBR will be the limiting factor during this transient.

Trant **[2]** analyzed the LOFA for several specific cores at specific powers, as it was computationally impractical to analyze the entire power map. RELAP was used to calculate the flow coastdown and linear heat rate as a function of time during the LOFA. These values were input into VIPRE for each time step, and the MDNBR was calculated. The minimum MDNBR over the LOFA was found and compared to the reference core minimum MDNBR. As is typical for this project, the design was considered to be acceptable if the minimum MDNBR was less than the minimum MDNBR of the reference core. Unlike VIPRE, the RELAP code does not currently have the capability to

be used in conjunction with MATLAB to efficiently cover the entire range of geometries. As such, the LOFA was not applied to the entire range of geometries. Instead it was applied only to the high power cores and most economic core, as determined by Shuffler **[2]**, in order to determine if they are limited by the LOFA.

Due to time limitations, it was not possible to perform a LOFA analysis for wire wraps. However, conclusions can be drawn from a simplified qualitative approach. Assuming constant density, Bernoulli's equation can be simplified **[2]** for the primary flow loop to Equation 9.1.

$$\left(\frac{1}{A}\right)_T \frac{d\dot{m}}{dt} = -\dot{m}^2 \left[\sum_i \left(f \frac{L_i}{D_{e,i} \cdot A_i^2} + \frac{k_i}{A_i^2} \right)\right] \qquad \textbf{[9.1]}$$

where $\frac{d\dot{m}}{dt}$ is the flow coastdown rate,. $\left(\frac{1}{A}\right)_T$ is effectively a constant, and the bracketed term represents what will be termed the flow resistance. Under steady-state operating conditions, the flow coastdown rate is zero, and the flow resistance is compensated by the primary pumps. When these pumps stop (the definition of the LOFA), the mass flow rate starts to coast down under the uncompensated frictional and form losses around the primary loop. The rate of coastdown depends on the steady-state mass flow rate and the flow resistance, as shown in Equation 9.1. The control rods are inserted partway through the transient, reducing the power.

For the reference core, the normalized reactor power and mass flow rate are shown in Figure 9.11. Figure 9.12 shows the corresponding MDNBR, as calculated by VIPRE. The MDNBR occurs at 2.5 seconds into the transient, 0.5 seconds after the rods begin to be inserted. The reduction in flow rate causes the enthalpy rise across the core to rise, increasing the outlet temperature and decreasing the MDNBR. The insertion of the control rods decreases the power and mitigates the continuing rise in enthalpy due to the decreasing mass flow rate. But more importantly, the heat flux decreases, proportionally increasing the MDNBR.

Figure 9.11 - LOFA Reactor Power and Flow for Reference Core

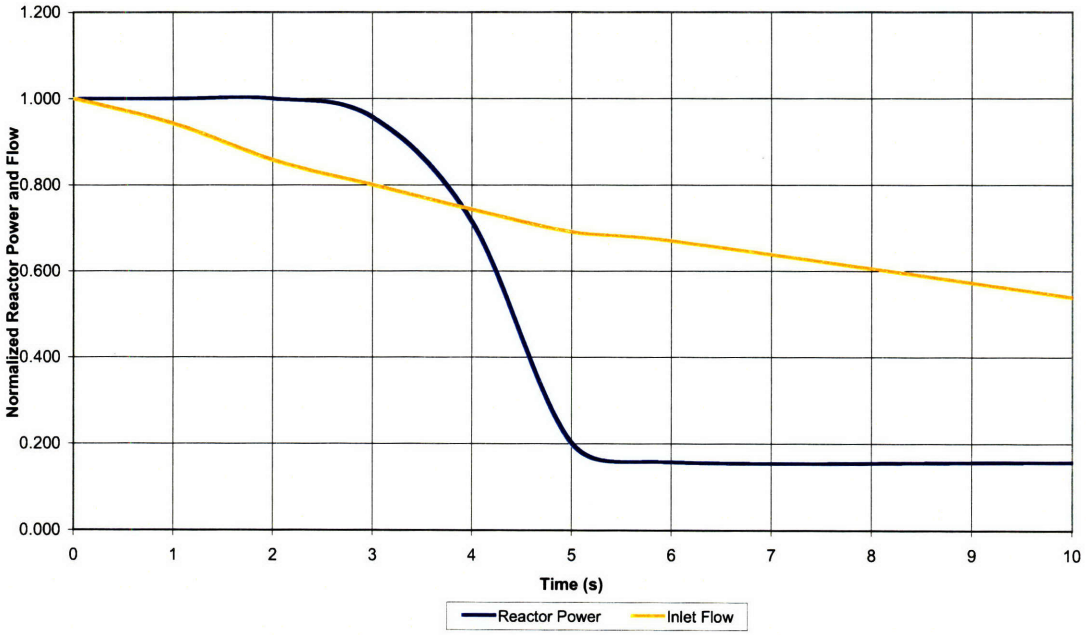

Figure 9.12 - LOFA MDNBR for Reference Core

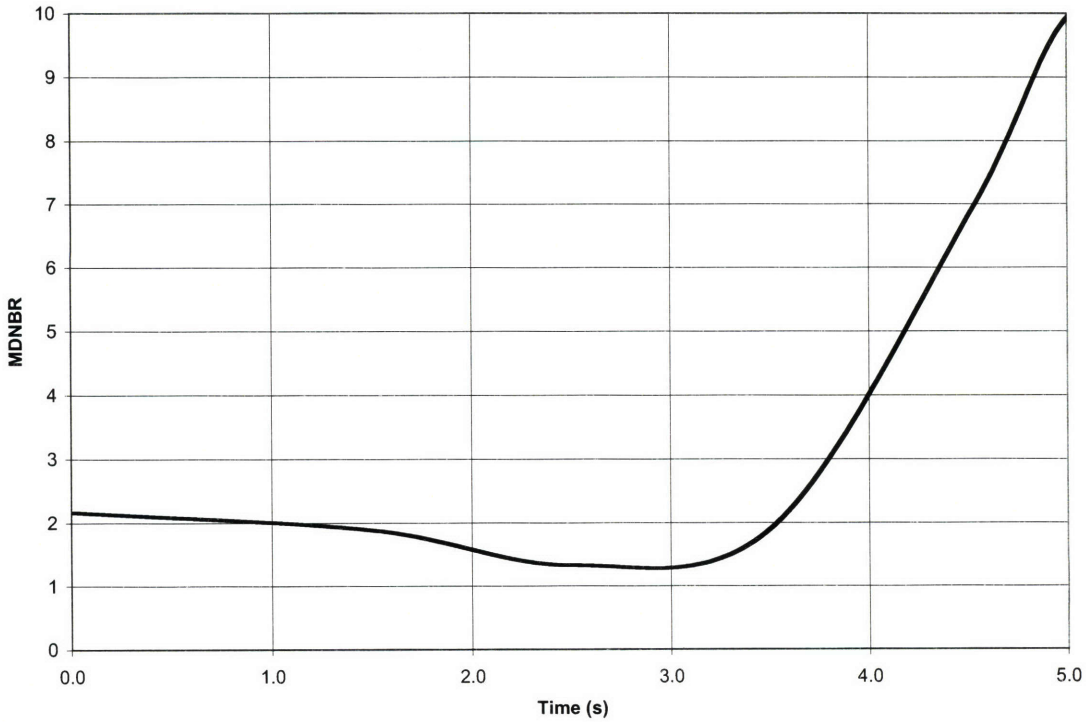
MDNBR
10
9
8
7
6
5
4
3
2
1
0
0.0
1.0
2.0
3.0
4.0
5.0
Time (s)

These two effects of power reduction on MDNBR, combined with the fast rate of power reduction when the rods are inserted, cause the power reduction to have a larger effect on the MDNBR than the flow coastdown, and the minimum MDNBR occurs very close to the beginning of rod insertion. Thus, the question becomes what the flow coastdown value is at the beginning of rod insertion. Since for this study, the steady-state mass flow rate is proportional to the power, increasing the power will cause an increase in steady-state $\dot{m}$ (an initial condition for Equation 9.1), increasing the flow coastdown rate and degrading the LOFA performance. All of the powers of interest in this study (the maximum powers of the Achievable and Stretch Cases) are higher than the reference power, so this effect will be detrimental to the maximum power LOFA performance.

However, the wire wrap cores also have a lower flow resistance than the reference core. For the same mass flow rate, lower flow resistances will result in lower pressure drops. A lower flow resistance will have a lower pressure drop for the same mass flow rate, as was the case with the Constant Case. Figure 9.13 shows the pressure drop of the Constant Case. The geometries with a lower pressure drop than the reference core have a smaller flow resistance than the reference geometry. The pressure drop of the Achievable Case maximum power geometry (D = 8.39 mm, P/D_{sq} = 1.321) is 8.6% lower than the reference core pressure drop. The other geometries of interest will generally have smaller flow resistances than the reference core.

Figure 9.13 - Core Pressure Drop of Constant Case for Flow Resistance Comparison

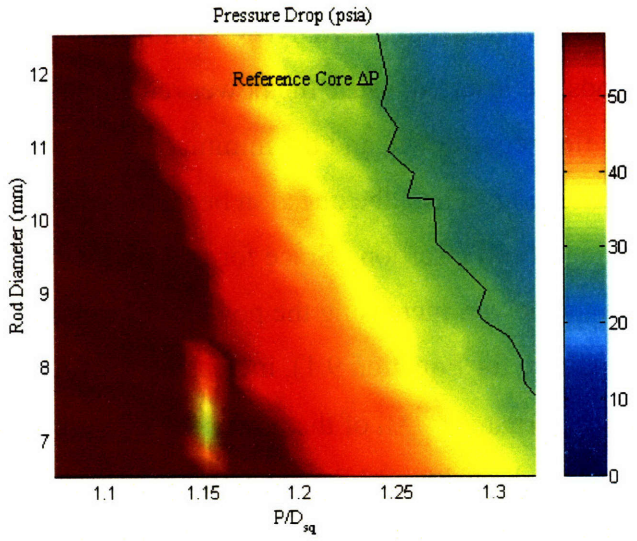
Pressure Drop (psia)
Reference Core ΔP
Rod Diameter (mm)
12
11
10
9
8
7
1.1
1.15
1.2
1.25
1.3
P/D_sq
50
40
30
20
10
0

The wire wrap maximum powers considered by this study have not been explicitly analyzed for their LOFA performance. These have higher powers (and associated mass flow rates) but lower flow resistances than the reference core. Since these changes will have conflicting effects, it is not immediately clear if the wire wrap maximum powers will have better LOFA performance than the reference core. Trant found that increasing the power but decreasing the flow resistance resulted in inferior LOFA performance compared to the reference case, requiring a power reduction of 6% from the overpower results for the maximum power geometry. However, the power uprates considered by Trant were modest compared to the power uprates possible with wire wraps (29%-37% with grid spacers vs. 65%-88% with wire wraps with overpower results). While in Trant's case the flow resistance was reduced by increased subchannel area, and with wire wraps the flow resistance is reduced by elimination of grid spacer form losses, the net effect of a decrease in the flow resistance is the same, through Equation 9.1. Thus, it is inconclusive whether a power reduction due to LOFA will be necessary with wire wraps. However, it is also possible to improve the LOFA performance by increasing the size of the pump flywheel, which could possibly improve LOFA performance to the point where power reductions for LOFA constraints are not necessary. In this study, it will be assumed that the LOFA is not limiting, but this assumption needs to be tested through RELAP and VIPRE work.

9.4 - Final Power Maps

The final power maps satisfy both the steady-state and transient constraints, and are constructed by using the minimum power of the steady-state, LOCA, and overpower constraints. The LOFA is assumed to never limit the power. To review, the derivation of these constraints is as follows.

1. The steady-state power map is constructed by finding the maximum power for each geometry subject to pressure drop, MDNBR, fuel temperature, and axial velocity constraints.
2. The overpower map is constructed identically to the steady-state power map, but with increased linear heat rates.

3. The LOCA is assumed to be independent of geometry, and only a function of the core power. The maximum core power subject to the LOCA constraint is the Achievable Case maximum power, 6251 MWth.

Figure 9.14 shows the progression of maximum power when the steady-state maximum powers are reduced to satisfy transient constraints for the Achievable and Stretch Case. For all of the constraints (steady-state and transient), hydride and oxide fuels have the same performance, and the only differences come about in the economic analysis.

Figure 9.14 - Maximum Power with Steady-State and Transient Constraints

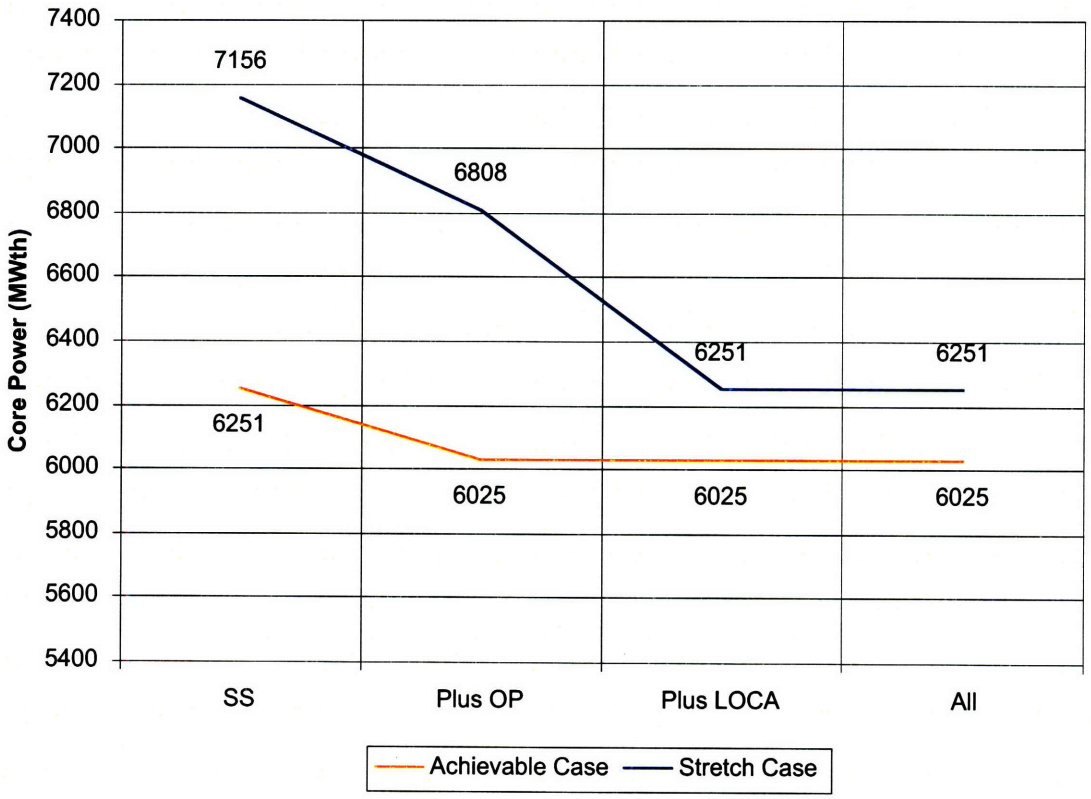

Figures 9.15 and 9.16 show the final power maps, and compare them to the steady-state power maps for the Achievable and Stretch Cases. The maximum power geometry changes slightly for the Achievable Case due to the change in the MDNBR constraint for the overpower transient from P/D = 1.321, D = 8.39 mm to P/D = 1.321, D = 8.08 mm. Due to the constant power LOCA constraint, the maximum power for the Stretch Case

occurs over a range of geometries with slightly smaller diameters, and thus are less desirable than the steady-state preferred geometry (8.39 mm vs. 8.71 mm).

Figure 9.15 - Achievable Case Hydride Power Maps

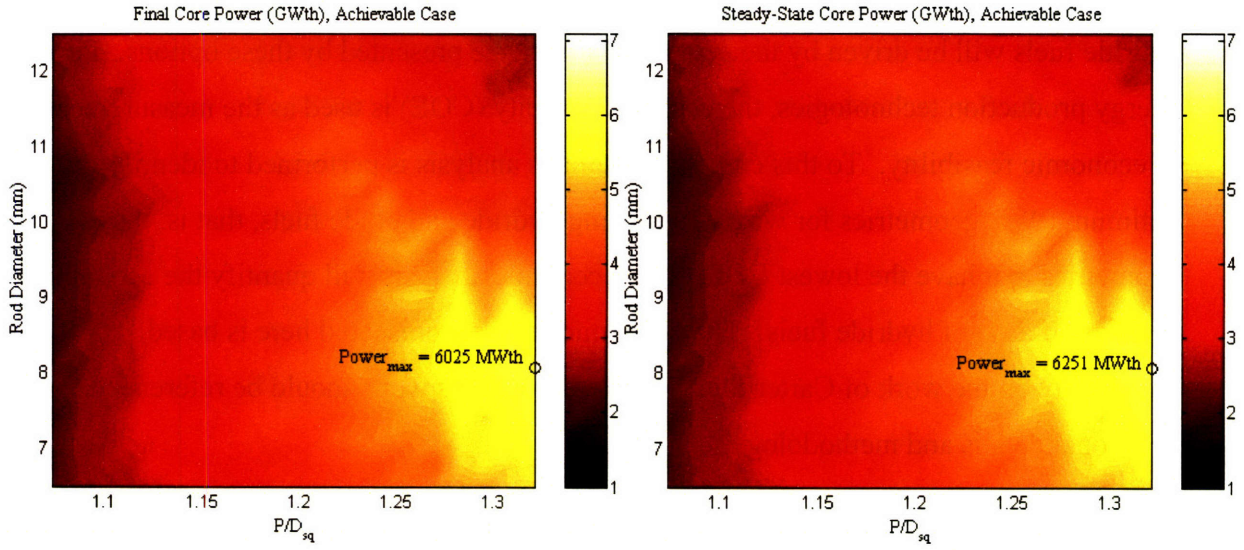

Figure 9.16 - Stretch Case Hydride Power Maps

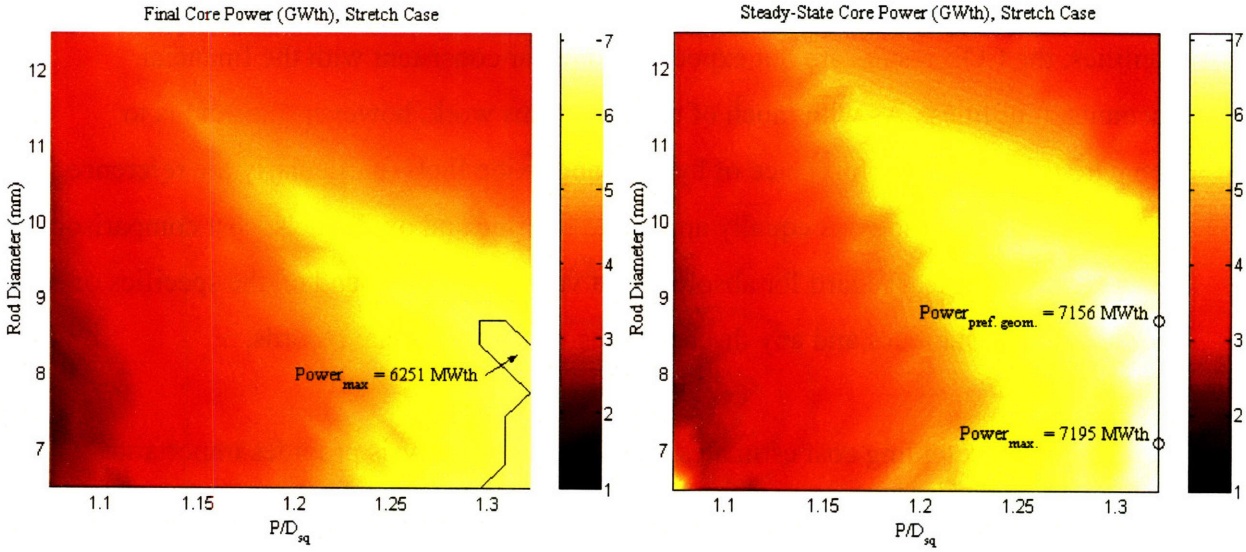

Chapter 10: Economics

10.1 - Introduction

The previous chapters have only made power comparisons between hydride ($UZrH_{1.6}$) and oxide (UO_2) fueled cores. However, the actual implementation of wire wraps and/or hydride fuels will be driven by the economic advantage presented by these options. For energy production technologies, the cost of electricity (COE) is used as the measurement of economic feasibility. To this end, an economics analysis is performed to identify the optimum PWR geometries for wire wraps using hydride and oxide fuels, that is, those geometries that have the lowest COE. This economic analysis will quantify the economic benefits (if any) of hydride fuels. The economic analysis presented here is based completely on the work of Carter Shuffler **[2] [28]** and his work should be referenced for additional details and methodology.

Specific assumptions are made regarding plant and fuel costs and the economic parameters that influence them over time. Due to these assumptions and the numerous models available for both collecting and interpreting economic information for nuclear facilities, the COE results are not expected to appear consistent with the financial accounts of utilities. As with much of the rest of this work, however, the goal is to compare the relative performance of hydride and oxide fuels (particularly the reference core). Because the model is equally applied to hydride and oxide fuels, cost comparisons can be made with less regard for absolute cost values which depend on the specifics of the modeling techniques and any discrepancies with commercial records.

In addition to presenting cost estimates, the economics analysis provides important information for utilities considering the fuel switch from oxide to hydride. For example, the operating cycle length, plant capacity factor, annual energy production and outage length are all byproducts of core power and burnup results which are inputs to the COE calculations.

10.1.1 - Analysis Approach

The COE is composed of three cost components: fuel cycle, operation and maintenance (O&M), and capital costs. The economics analysis seeks the COE using these components for the Achievable Case, the Stretch Case, and C. Shuffler's grid spacer case, using both hydride and oxide fuels. Results are presented for both fuels at enrichments of 5%, 7.5%, and 10%. Results are also presented for 12.5% enriched hydride.

From Section 1.3.1, two types of backfits are possible for reactors in general: the major and minor backfit. Due to the inherent shift in geometry from square to hexagonal channels that is required for the implementation of wire wraps, as presented here, minor backfits are not possible for wire wraps, and will not be considered here. For the major backfit, the vessel head and core internals must be replaced, as well as upgrades of the steam generators and high pressure turbine.

10.2 - Methodology

The structure for the economics analysis was originally laid out by Jacopo Saccheri **[29]**, and further developed and applied to hydride fuels by C. Shuffler. This approach is consistent with OECD/NEA reports on the economic evaluation of nuclear fuel cycles **[30]**. The primary inputs include the maximum power from the steady-state and transient thermal-hydraulic analyses, and the maximum burnup from neutronics and fuel performance studies. The fuel cycle, O&M, and capital costs are then determined for each geometry and fuel type.

The economic analysis ties together all of the work on hydride fuels. The entire procedure, from start to finish, can be summarized as follows.

1. Steady-state power maps are created using VIPRE subject to steady-state constraints.
2. The steady-state power maps are further limited by transient constraints, resulting in final power maps.
3. Burnup maps limited by fuel performance are created using FRAPCON.

4. Burnup maps limited by neutronics are created by the collaborators in this study at UC Berkeley [31].
5. For each geometry, the minimum of the neutronics and fuel performance limited burnups is taken to be the achievable burnup.
6. This final power map (incorporating steady-state and transient constraints) and the final burnup map (incorporating fuel performance and neutronics) are fed into the economics programs. These programs calculate the fuel cycle, O&M, and capital COE's for the power and burnup, as a final method of comparison.

10.2.1 - Reference Core Economic Evaluation

The COE can be effectively compared for different potential major backfits (different geometries, hydride or oxide fuels, grid spacers or wire wraps) using the methodology presented above. However, the economic justification still needs to be established for the utilities to perform a backfit as opposed to purchasing a new reactor or leaving the reference core as is. Calculating the COE for the reference core (in a manner that is consistent with this analysis, so as to facilitate comparison) involves only fuel cycle and O&M costs, as there is no capital expenditure required.

A fair basis of comparison for the competing options of a backfit and new reactor is the cost associated with achieving the same power for both. The result is the following methodology for determining the COE of a new reactor that gives the same additional power as a backfit. The new reactor, in conjunction with the reference core, compose a system and provide the same overall power as the backfit. The capital cost for the newly constructed PWR is assumed to be 1800 $/kWe.

1. The backfit optimal power (the power with the lowest COE) is calculated based on the methodology of Section 10.2.
2. A new reactor is required to compensate for the additional power provided by the competing backfit alternative. That is, the power of the new reactor is:

$$Q_{new} = Q_{backfit} - Q_{ref} = Q_{backfit} - 3800 MWth \qquad \textbf{[10.1]}$$

where $Q_{backfit}$ is the backfit optimal power, which should correspond closely to the maximum power.

3. This required additional power Q_{new} is assumed to be a portion of a new reactor. Thus, the capital COE for Q_{new} is simply the capital COE of a new reactor.
4. The total COE of Q_{new} is factored into the COE calculation for the reference core, resulting in a COE for the system of the reference core and new reactor. This can be compared to the COE of the major backfit.

10.2.2 - Lifetime Levelized Cost Method

To measure the value of costs that occur at different times, the lifetime levelized cost method is employed. This method determines the levelized cost of electricity per unit of energy produced over the plant's lifetime. It is also called the levelized busbar unit cost of electricity, to reflect that all expenses up to the plant/transmission line interface are included. The term "levelized" means that discrete costs are equated to one continuous stream of expenses over the plant life. This is a convenient form for application to power plants, as the revenue stream can also be viewed to be continuous. The lifetime levelized cost method facilitates simple economic comparisons of cash flows that look vastly different. The basic equations relating discrete cash flows and levelized costs are presented here.

To start any investment analysis, a desired rate of return, r, has to be identified. This rate of return is also commonly called the discount rate, or nominal interest rate. Discrete expenditures for fuel cycle, O&M, and capital costs are incurred at different times during the plant's life. To get the levelized cost, these expenditures are discounted back to a reference date, at which $t = 0$. In this case, the reference date is chosen to be the start of irradiation for the first fuel cycle. Discounting all expenditures to this date with continuous compounding of interest yields the present value of all costs, PV_{costs}, another viable form of comparing the economics of different reactors. Equation 10.1 shows PV_{costs} of N expenditures.

$$PV_{costs} = \sum_{N} C_N \cdot e^{-rt_N} \qquad \textbf{[10.1]}$$

where C_N and t_N are the value and time of the N^{th} expenditure. PV_{costs} can be related to the lifetime levelized cost ($\overline{C}_{lev}$) according to Equation 10.2, where T_{plant} is the plant lifetime.

$$PV_{costs} = \int_0^{T_{plant}} \overline{C}_{lev} \cdot e^{-rt}\, dt \qquad \textbf{[10.2]}$$

Integrating Equation 10.2 with respect to time and solving for the lifetime levelized costs,

$$\overline{C}_{lev} = PV_{costs} \cdot \left[\frac{r}{1 - e^{-rT_{plant}}}\right] \qquad \textbf{[10.3]}$$

where: $capital\ recovery\ factor = \left[\frac{r}{1 - e^{-rT_{plant}}}\right]$

The capital recovery factor is one way of expressing the time value of money. The lifetime levelized cost of electricity, $\overline{c}_{lev}$ ($/kW-hr), is obtained by normalizing $\overline{C}_{lev}$ ($/yr) by the energy production of the plant (kW-hr/yr). The annual energy production, E_{annual}, from the plant is given by Equation 10.4.

$$E_{annual} = Q_{th} \cdot \eta \cdot L \cdot 8766 \qquad \textbf{[10.4]}$$

where Q_{th} is the core thermal power, _ is the thermal efficiency, and L is the plant capacity factor. The final relationship for the lifetime levelized unit cost of electricity is given by the definition of $\overline{c}_{lev}$ in Equation 10.5.

$$\overline{c}_{lev} = \frac{\overline{C}_{lev}}{E_{annual}} = \frac{PV_{costs}}{Q_{th} \cdot \eta \cdot L \cdot 8766}\left[\frac{r}{1 - e^{-rT_{plant}}}\right] \qquad \textbf{[10.5]}$$

If costs and core thermal power are recorded in \$ and kW_{th} respectively, and interest rates are annualized (yr^{-1}), the Equation 10.5 reports $\bar{c}_{lev}$ in mills/kW-hr, where 1 mil = \$0.001. To get the individual levelized unit costs for the fuel cycle, O&M, and capital components, Equation 10.5 is applied with the relevant cash flow histories incorporated into the PV_{costs} term. The levelized unit COE is simply the sum of the cost contributions from these individual components, as expressed in Equation 10.6.

$$\bar{c}_{lev} = \bar{c}_{lev-fcc} + \bar{c}_{lev-O\&M} + \bar{c}_{lev-cap} \qquad \textbf{[10.6]}$$

10.2.3 - Assumptions

The lifetime levelized cost method requires predictions for all costs and the rate of return. This is particularly difficult for the application of this method to a nuclear power plant, as the time frame considered is 20 years. Since everything concerning nuclear power is subject to change over the next 20 years, any cost estimates will be inherently speculative. Because of the uncertainty and the speculative nature of most long term cost projections for nuclear power, several assumptions are necessary to keep this analysis simple and ultimately focused on the comparison of hydride and oxide fuels, and wire wraps and grid spacers in PWR's.

- *Only direct costs associated with the fuel cycle, O&M, and capital are considered.* This assumption does not account for the first of a kind costs that accompany the development and certification of introducing hydride fuels into the marketplace.

- *Discount rates are constant over the plant's life.* This assumption is a very standard one in financial analyses, as a variable discount rate would require accurate prediction of future economic situations and risk.

- *The unit cost information available for commercial PWR's is cautiously extended to new hydride and oxide fueled designs.* The unit costs for the fuel cycle, O&M, and capital portions of the COE analysis are widely available for existing PWR's

using oxide fuel. However, no economic data is currently available for hydride unit costs, or the oxide unit costs over the large range of geometries considered in this study that deviate significantly from standard PWR designs.

10.2.4 - Analysis Details

This section lists some of the specific details about the analysis performed. For more information, see C. Shuffler's work on the subject **[2] [28]**.

- *Fuel Cycle Unit Costs*. The nuclear fuel cycle has costs associated with procurement and fabrication of fuel assemblies, as well as storage and disposal of spent fuel. Fuel cycle unit costs are derived from two sources: the June, 2004 US spot market for uranium services, and OECD/NEA recommendations **[30]**. The cost of burnable poisons that may be necessary for hydride fuel are not taken into account.

- *Cost of Assembling Fuel into Fuel Bundles*. 50% of the total fuel assembly fabrication cost is assumed to be dependent to the number of fuel rods in the core; the other 50% is due to the heavy metal (HM) loading. The fabrication costs for hydride and oxide are assumed to be identical for equivalent volumes of fuel. Note that this cost is only in assembling the bundles; enrichment, conversion, and ore/mining costs are accounted for separately in the fuel cycle cost calculation.

- *Operations and Maintenance Unit Costs*. O&M includes all costs associated with energy production that are not directly related to the fuel cycle. The O&M unit costs are derived from expert recommendations acquired by J. Saccheri **[29]**.

- *Capital Costs*. Capital costs include the cost of replacing the steam generators, vessel head, core internals, and upgrading the turbine generator. In addition, the cost of the existing unburned fuel in the reactor is taken into account. The turbine costs are taken from DOE's "Nuclear Energy Cost Database", while the cost estimates for the steam generators, vessel head, and core internals are obtained

from R. Ballinger of MIT, an observer familiar with industry cost experience. Upgrades to the pumping systems, such as the main feedwater pump and safety injection system, as well as additional holddowns will be required, but these costs are relatively minor and are not considered in this analysis.

- *Plant Operating Parameters.* The refueling outage length is taken to be 20 days/cycle, based on the most efficient units operating commercially today.

- *Plant Life.* Based on current NRC license extensions for existing LWR's, 20 years of additional plant life is assumed.

This approach, while acceptable for modest power uprates in the 0-15% range consistent with the current PWR experience, may not be fully adequate for larger uprates in the extended 15-80% range, which this work indicates is technically feasible. Extra costs not accounted for in this latter case, such as those involving required modifications to additional systems and charges for replacement power during the extended outage may also be incurred in the actual execution of such large uprate projects. In addition, this work provides for the uprates of certain components (such as the turbine) when they might need to be duplicated outright for large power uprates.

10.3 - Burnups

10.3.1 - Equivalence

Both types of burnup map (fuel performance limited and neutronics limited) have been created for square arrays with grid spacers. To facilitate the comparison of wire wraps and grid spacers, previously in this work the results for wire-wrapped hexagonal arrays have been plotted using the square core equivalent pitch to diameter ratio (P/D_{sq}). However, as the economic comparison allows direct comparison of the performance of different geometries at different powers, all wire wrap results will now be plotted using P/D_{wire}, using the relationships developed in Section 7.2. Note that the geometry ranges covered by this analysis are the same as used in the steady-state power analysis. The following P/D_{wire} range was used consistently throughout this entire work:

$$1.15 \le \left(P/D\right)_{wire} \le 1.42 \qquad \textbf{[10.7]}$$

This P/D_{wire} range is equivalent to two different P/D_{sq} ranges, depending on whether the desired equivalence is thermal-hydraulic or neutronic.

- *Thermal-Hydraulic Equivalence.* This equivalence is used for equating thermal-hydraulic performance, and was based on achieving the same subchannel total area while holding D constant. This results in the following relationship:

$$\left(P/D\right)_{wire} = 1.0746 \cdot \left(P/D\right)_{sq} \qquad \textbf{[7.26]}$$

The resultant thermal-hydraulic equivalent square P/D range is given in Equation 10.8. This is the P/D_{sq} range presented for the steady-state results.

Thermal-Hydraulic Equivalent P/D Ranges $1.15 \le \left(P/D\right)_{wire} \le 1.42 \Leftrightarrow 1.07 \le \left(P/D\right)_{sq} \le$

- *Neutronic Equivalence.* This equivalence is used for equating neutronic performance, and is based on the assumption that subchannels with the same rod diameter and H/HM ratio are neutronically equivalent, resulting in the following relationship:

$$\left(P/D_{wire}\right) = \frac{-\pi/2 + \sqrt{\sqrt{3}\pi/2 + \left(2\sqrt{3} - \pi\right)\left(P/D_{sq}\right)^2}}{\sqrt{3} - \pi/2} \qquad \textbf{[7.20]}$$

The resultant neutronic equivalent square P/D range is given in Equation 10.9. This is the P/D_{sq} range used for the neutronics limited burnup maps.

Neutronic Equivalent P/D Ranges

$$1.15 \le \left(P/D\right)_{wire} \le 1.42 \Leftrightarrow 1.07 \le \left(P/D\right)_{sq} \le 1.27 \qquad \textbf{[10.9]}$$

10.3.2 - Neutronics Limited Burnup

The neutronics analysis serves two roles. First, it provides the reactivity-limited burnups for hydride and oxide fuels that can maintain the critical nuclear reaction in the core. Second, it provides the range of geometries with acceptable (negative) fuel and moderator temperature coefficients. For these burnup maps, UC Berkeley employed SAS2H, which is part of the SCALE module, to determine the unit cell 3-batch burnup for hydride and oxide fuels as a function of pin geometry and fuel enrichment. The maximum burnup is reached when the core average K_∞ drops below 1.05. As expected, higher burnups are obtained for higher enrichment fuels. The addition of hydrogen to the fuel matrix shifts the optimum geometries for neutronics to tighter configurations, because less coolant is needed for neutron moderation. Figures 10.1 and 10.2 show the neutronics limited burnups for the enrichments considered over the range of geometries considered in this study. For each geometry, the neutronics limited burnup is used if it is more restrictive than the fuel performance limited burnup.

Figure 10.1 - $UZrH_{1.6}$ Neutronically Achievable Burnup for Wire Wrap Arrays [31]

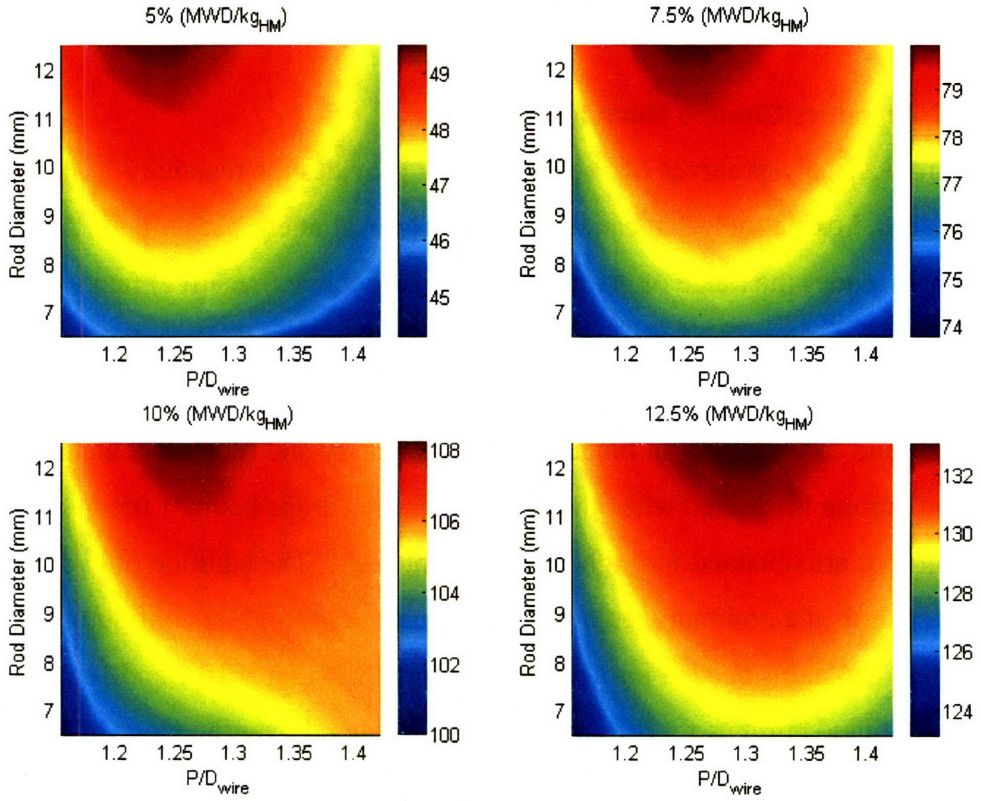

Figure 10.2 - UO_2 Neutronically Achievable Burnup for Wire Wrap Arrays [31]

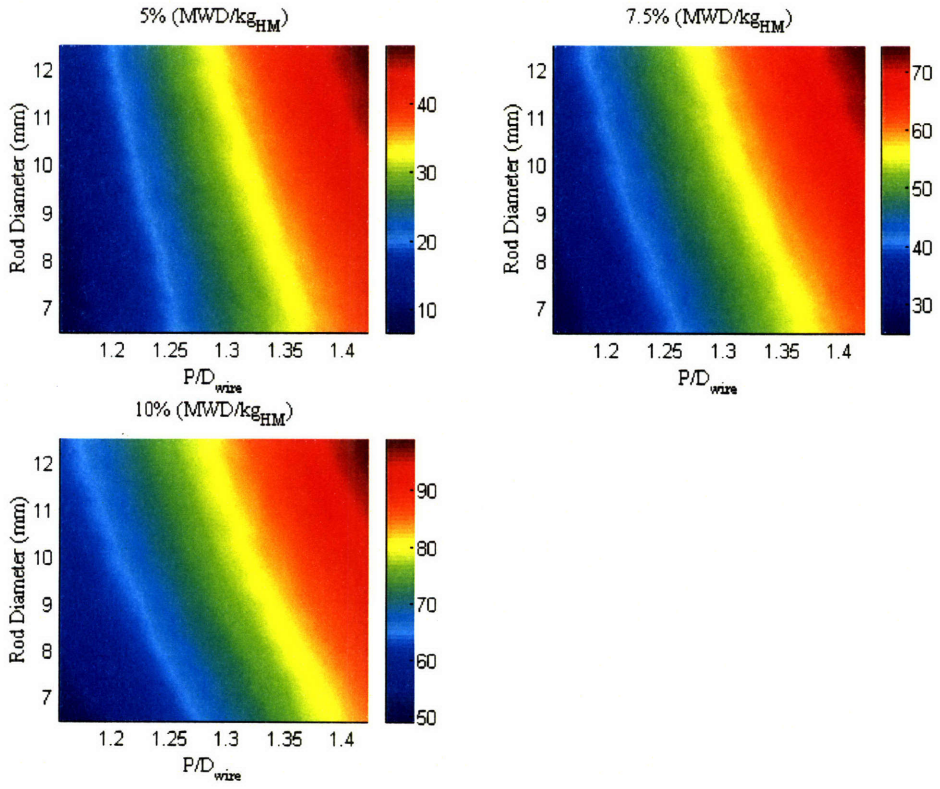

10.3.3 - Neutronics Limited Geometries

UC Berkeley found that the entire range of geometries considered in this study was feasible with 7.5% enriched UO_2. The range of geometries with acceptable temperature coefficients for 5% enriched UO_2 is (note that P/D_{wire} is derived using neutronic equivalences):

$$\left(P/D\right)_{sq} \leq 1.4 \qquad 6.5mm \leq D_{rod} \leq 8.5mm \qquad \textbf{[7.21]}$$

$$\left(P/D\right)_{sq} \leq 1.3 \qquad 8.5mm \leq D_{rod} \qquad \textbf{[7.22]}$$

Since this encompasses the entire range of geometries considered in this study (the maximum P/D considered in this study is 1.27), it is justifiable to consider 5% enriched UO_2 to be universally acceptable neutronically.

With the use of only the soluble boron required to compensate for the excess reactivity at BOL for $UZrH_{1.6}$, the moderator temperature coefficients (MTC) for all geometries were positive. UC Berkeley has investigated ways around this problem, most notably the use of burnable poisons, or the introduction of thorium into the fuel matrix. Both of these solutions decrease the amount of soluble boron required at BOL. For $UThH_2ZrH_{1.6}$ with 55% ThH_2 and 12.5% enriched U, the range of acceptable geometries is comparable to that of 5% enriched UO_2, although the burnups are different than those of $UZrH_{1.6}$ (see Section 10.4.2 for more details on $UThH_2ZrH_{1.6}$).

It was also found that the use of Erbium as a burnable poison results in negative reactivity coefficients for the life of the fuel **[34]**. However, there is still a penalty to the neutronics limited burnup associated with the use of Erbium. As this penalty increases with increased Erbium loading, it is desirable to use the minimum amount of Erbium that will still keep the reactivity coefficients negative.

Hydride fuel with either Erbium or thorium is acceptable for the entire geometry range. In addition, since the most economic enrichment of oxide fuel is 5%, for which the entire

geometry range is neutronically acceptable, neutronics geometry limits are not directly applied to the following economic analysis.

10.3.4 - Fuel Performance Limited Burnup

In addition to reactivity considerations, the discharge burnup is also limited to protect the integrity of the fuel pin during irradiation. In the fuel performance analysis, design constraints are placed on internal fuel pin pressure and fission gas release, clad strain and clad oxidation. The fuel performance analysis was performed with the FRAPCON code **[2]** and considered three fuel integrity impairing mechanisms:

(a) Clad corrosion on the water side - the maximum tolerable oxidation thickness is assumed to be 0.1 mm, independent of the fuel rod diameter.

(b) Clad Strain - the limit is assumed to be 1%, in tension; it includes both elastic and plastic contributions and is due to the external coolant pressure, differential thermal expansion between the fuel and the cladding, fuel swelling due to irradiation and buildup of fission gases.

(c) Clad Internal Pressure - the maximum acceptable internal gas pressure is assumed 2500 psia. Contributions to the gas pressure buildup accounted for are release of volatile fission products and helium produced by neutron absorption in ^{10}B of the IFBA.

Because FRAPCON can only be used to simulate burnup in UO_2 fuel, additional assumptions were required to extend its use to $UZrH_{1.6}$.

- The internal pressure constraint was neglected due to the low fission gas release of $UZrH_{1.6}$.
- The thermal expansion properties of the fuels, which affect clad deformation and the limit on clad strain, were assumed to be identical.
- The fuel performance limit that dominates over most of the design range is clad corrosion, which depends on the amount of time the fuel remains in the core. Because the heavy metal loading in UO_2 is 2.5 times greater than $UZrH_{1.6}$ at the same geometry, the residence time for $UZrH_{1.6}$ will be 40% of the residence time for UO_2 if the same burnup limit is applied. It is therefore assumed that an

equivalent FRAPCON burnup for $UZrH_{1.6}$ can be obtained by multiplying the output from the code without the internal pressure constraint by 2.5. This ensures that the residence time for both fuels in the core at discharge will be the same. Of the three, the second assumption is the most difficult to justify, but its impact is minimized because clad corrosion limits most geometries.

This analysis requires a power map as an input. Due to time constraints it was not possible to perform this analysis for any of the final (fully-constrained) wire wrap power maps. However, the fuel performance limited burnup is generally less constraining than the neutronics limited burnup, and as a result is not crucial. The burnup maps created using the 60 psia grid spacer power map is assumed to be valid for wire wrap power maps, as the wire wrap powers are closest to this power map. The burnup maps for hydride and oxide are presented in Figure 10.3, where P/D_{wire} is the thermal-hydraulic equivalent of P/D_{sq}.

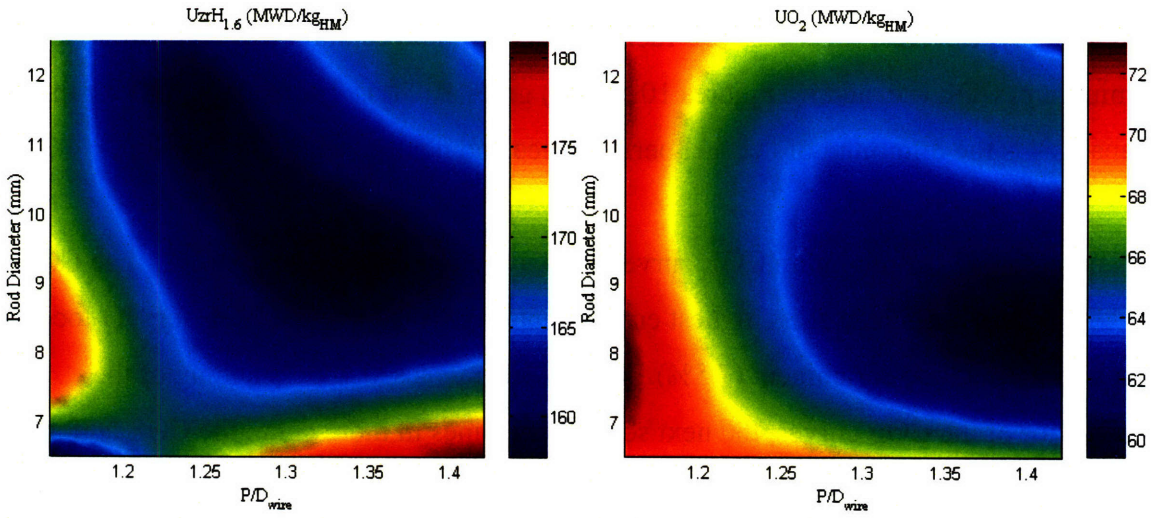

Figure 10.3 - Fuel Performance Limited Burnup for Hydride and Oxide

10.3.5 - Power Map Input

The power maps inputted into the economic analysis are the steady-state power maps for the Achievable and Stretch Cases. Transient performance is approximated by power limits due to the overpower and LOCA transients, as developed in Chapter 9. LOFA is assumed to not limit the power. Furthermore, the power limitations would apply almost

equally to hydride and oxide fuels, and thus would not have any effect on the comparison of the two, which is the main reason for the economic analysis.

10.4 Lifetime Levelized Unit COE

Due to the sheer number of cases considered, the full results from the economics analysis are presented in this section for the hydride and oxide fuels only for the steady-state Achievable Case. The most economic geometries are presented for the Stretch Case, as well as for grid spacers, for hydride and oxide, using both the final power maps and the steady-state power maps. The wire wrap COE for all cases is presented as a function of P/D and enrichment. The results are presented in P/D_{wire}, with a range equivalent to that of P/D_{sq} considered earlier in this work. The lifetime levelized unit cost of electricity for the steady-state Achievable Case is shown in Figures 10.4 and 10.6 for different enrichments of $UZrH_{1.6}$ and UO_2. The black lines show the diameters of minimum COE for each P/D_{wire}. These lines are re-plotted in Figures 10.5A and 10.7A independent of rod diameter to provide a clearer comparison of the COE among different enrichments and fuel types. Also shown are the fuel cycle, O&M, and capital costs that comprise the minimum COE (i.e. adding Figures 10.5(B-D) gives 10.5A). The burnup used for this analysis is the minimum of the fuel performance and neutronics limited burnup.

Next compare the minimum COE curves shown in Figures10.5A and 10.7A. The COE is $UZrH_{1.6}$ are minimized at its highest enrichment (12.5%), while the COE for UO_2 occurs at its intermediate enrichment (7.5%). To provide increased understanding of the behavior of the COE curves, the next section examines in more detail the COE and its individual components for 12.5% $UZrH_{1.6}$, and 7.5% UO_2. These enrichments are chosen because they provide the lowest overall COE. The fuel cycle cost is lower for some higher enrichments because the increased burnup of higher enrichments mitigates, or even dominates, their increased front-end production costs. For both $UZrH_{1.6}$ and UO_2, the capital costs jump at P/D = 1.15 because the power becomes greater than the reference power, necessitating the replacement of the steam generators and upgrades to the turbine. Following this examination is a full comparison of the minimum COE for grid spacers, and the Achievable and Stretch Cases for wire wraps, for both $UZrH_{1.6}$ and

UO_2, with specific attention given to geometries where cost savings can be realized for hydride fuel.

Figure 10.4 - Lifetime Levelized Unit COE for Steady-State Achievable Case with $UZrH_{1.6}$

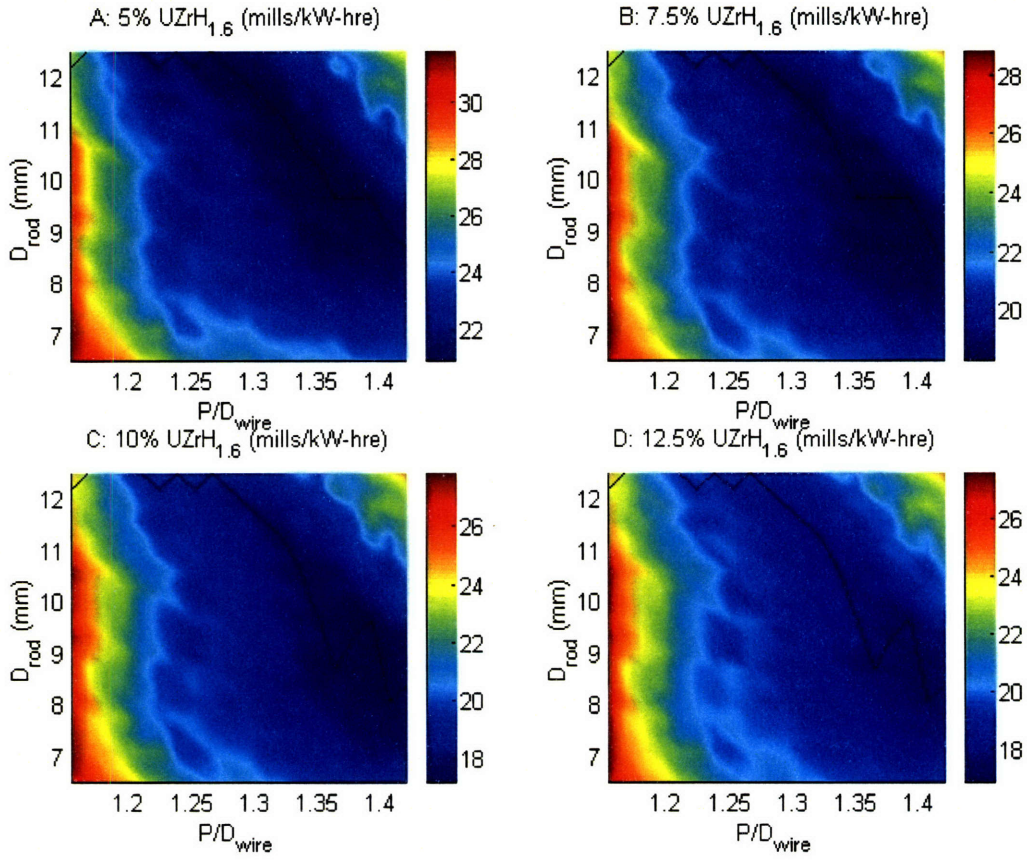

Figure 10.5 - Minimum COE and its Components vs. P/D for Steady-State Achievable Case with $UZrH_{1.6}$

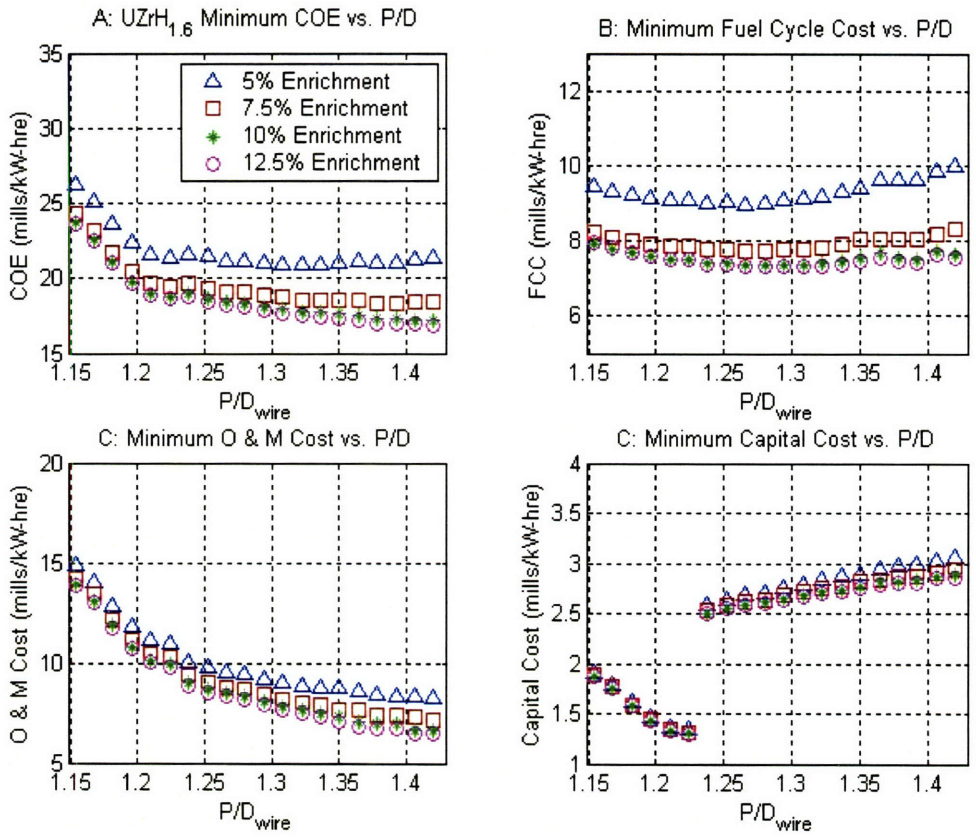

Figure 10.6 - Lifetime Levelized Unit COE for Steady-State Achievable Case with UO_2

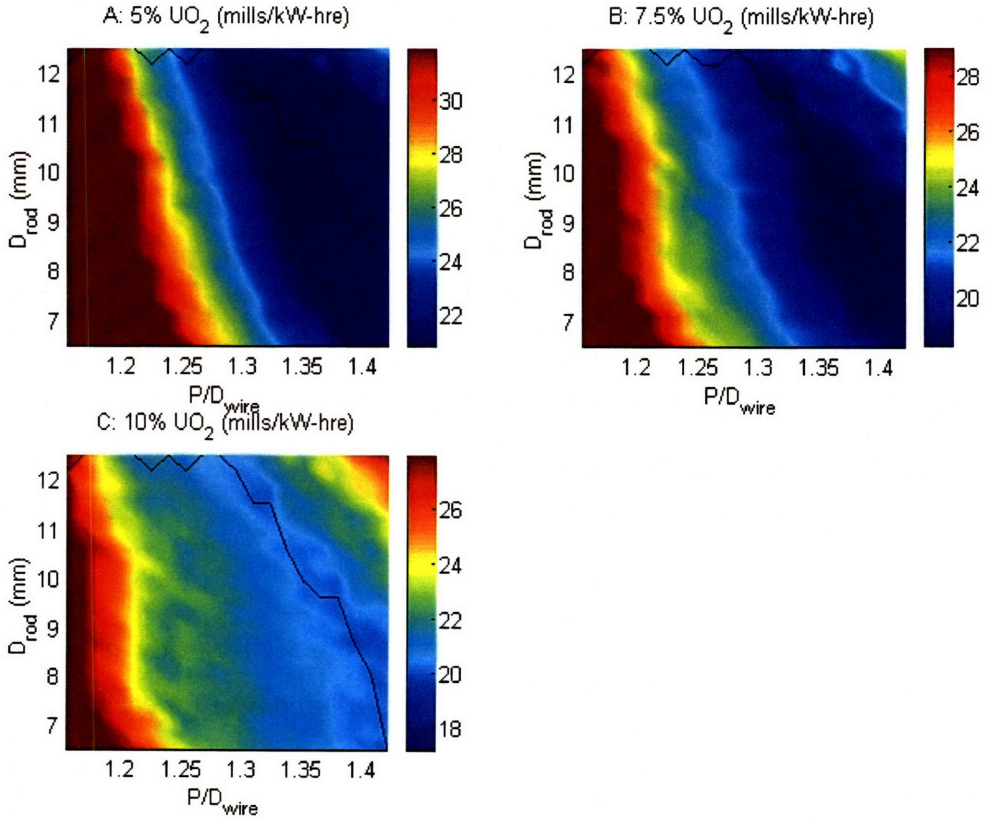

Figure 10.7 - Minimum COE and its Components vs. P/D_{wire} for Steady-State Achievable Case with UO_2

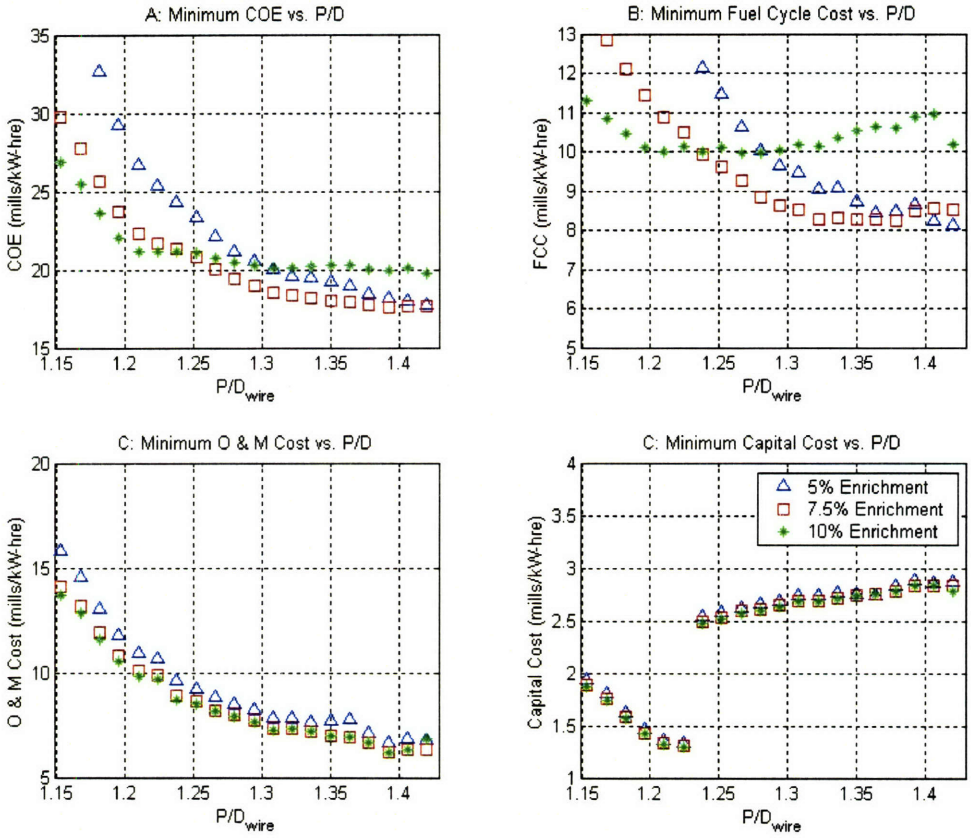

Figure 10.8 - Steady-State Achievable Case, Hydride and Oxide Fuels

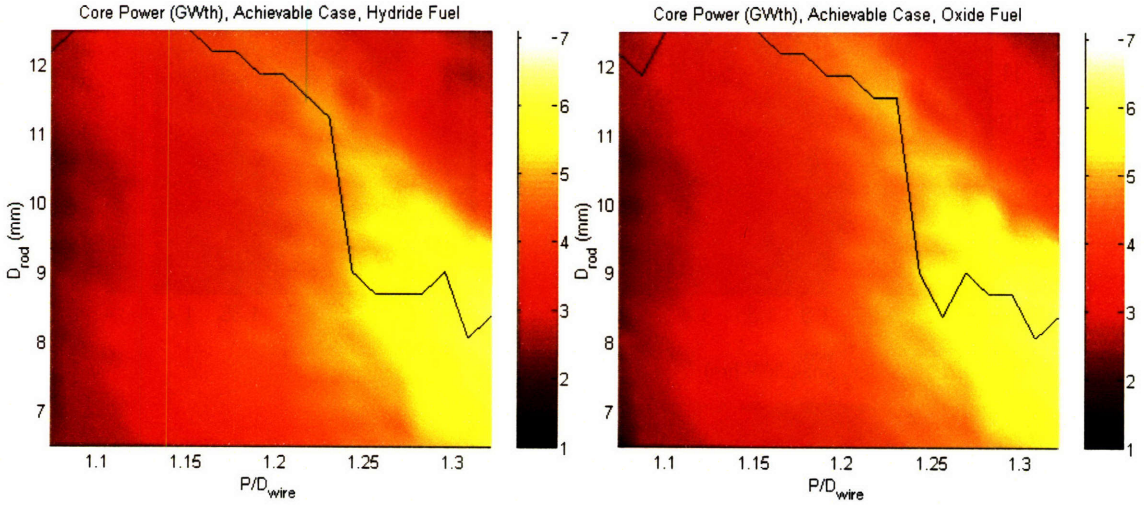

Figure 10.8 shows the power maps for the Achievable Case with steady-state limits imposed. The black lines show the diameters of maximum power for each P/D_{wire}. These lines are extremely similar to the lines shown in Figures 10.4 and 10.6, illustrating the large effect that the power has on the COE.

10.4.1 - COE Breakdown for Steady-State Achievable Case with 7.5% UO_2 and 12.5% $UZrH_{1.6}$

Figures 10.9-10.14 show the various operating parameters for the steady-state Achievable Case with $UZrH_{1.6}$ and UO_2. Included are the various levelized costs (Figures 10.9 and 10.12) and operating conditions (Figures 10.10, 10.11, 10.13 and 10.14), including core power, burnup, capacity factor, and cycle length.

Effect of Operating Cycle Length on COE Components

One of the effects of increased power on the COE is an effect on the cycle length, illustrated in Figures 10.11B and 10.14B. For a fixed burnup, increasing the power reduces the cycle length, making refueling outages more frequent. This decreases the capacity factor, reducing the annual energy production. Since the COE is comprised of costs that are relatively independent of power divided by the annual energy production, a decrease in capacity factor associated with an increase in power directly affects COE. However, this indirect effect of capacity factor changes on COE components is overshadowed by the direct effect of core power on COE components.

Figure 10.9 - COE Breakdown for Steady-State Achievable Case with 12.5% $UZrH_{1.6}$

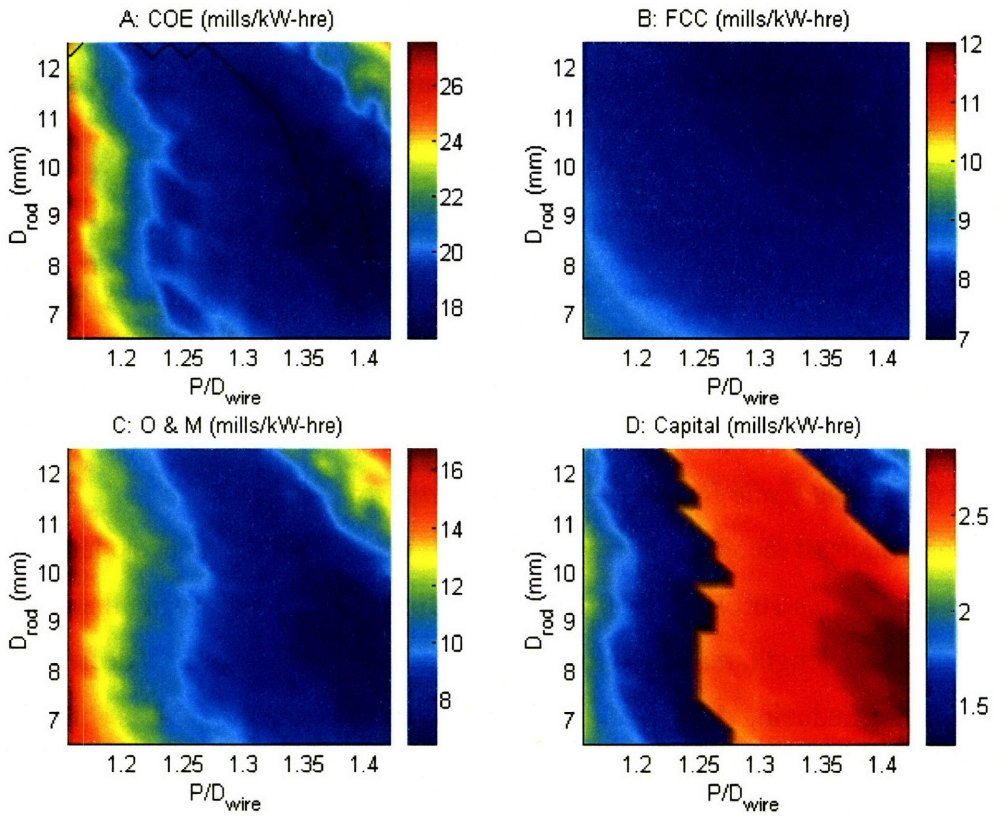

Figure 10.10 - Plant Operating Conditions for Steady-State Achievable Case with 12.5% UZrH1.6

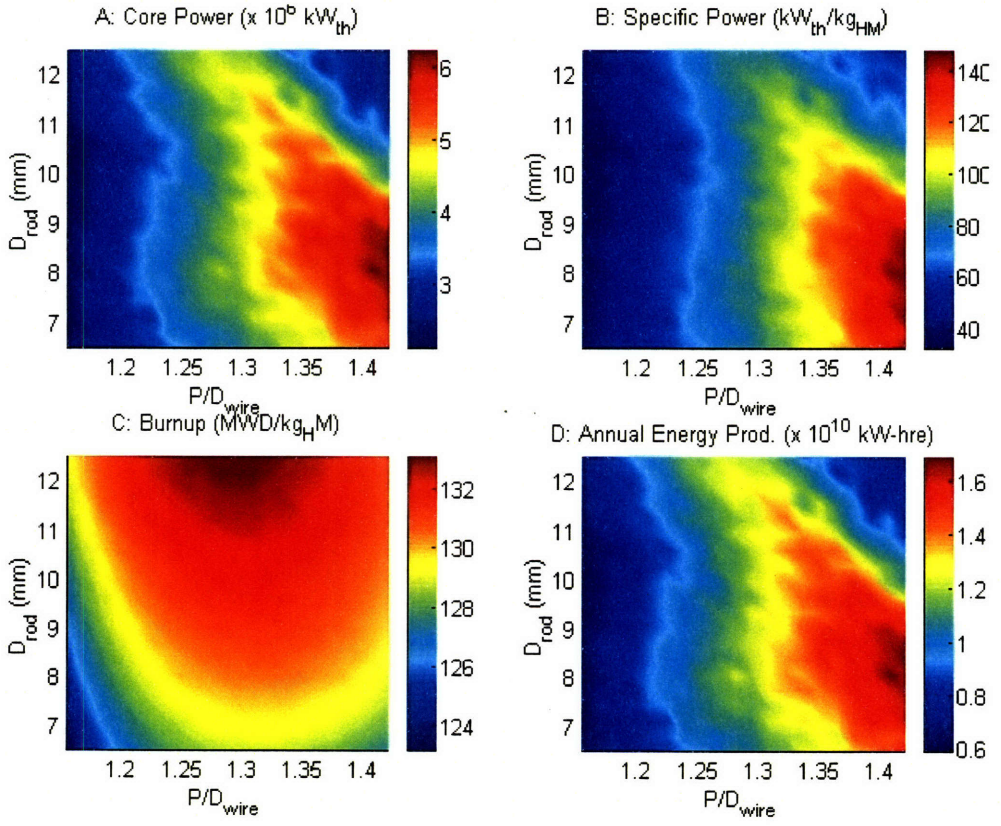

Figure 10.11 - Plant Operating Conditions for Steady-State Achievable Case with 12.5% UZrH1.6

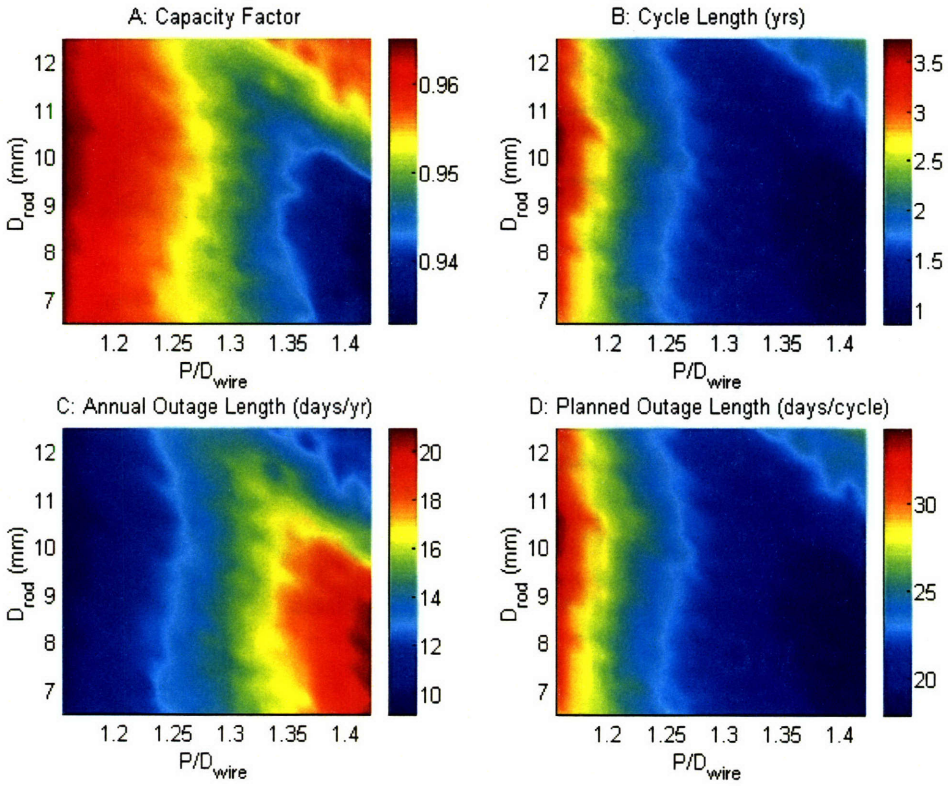

Figure 10.12 - COE Breakdown for Steady-State Achievable Case with 7.5% UO_2

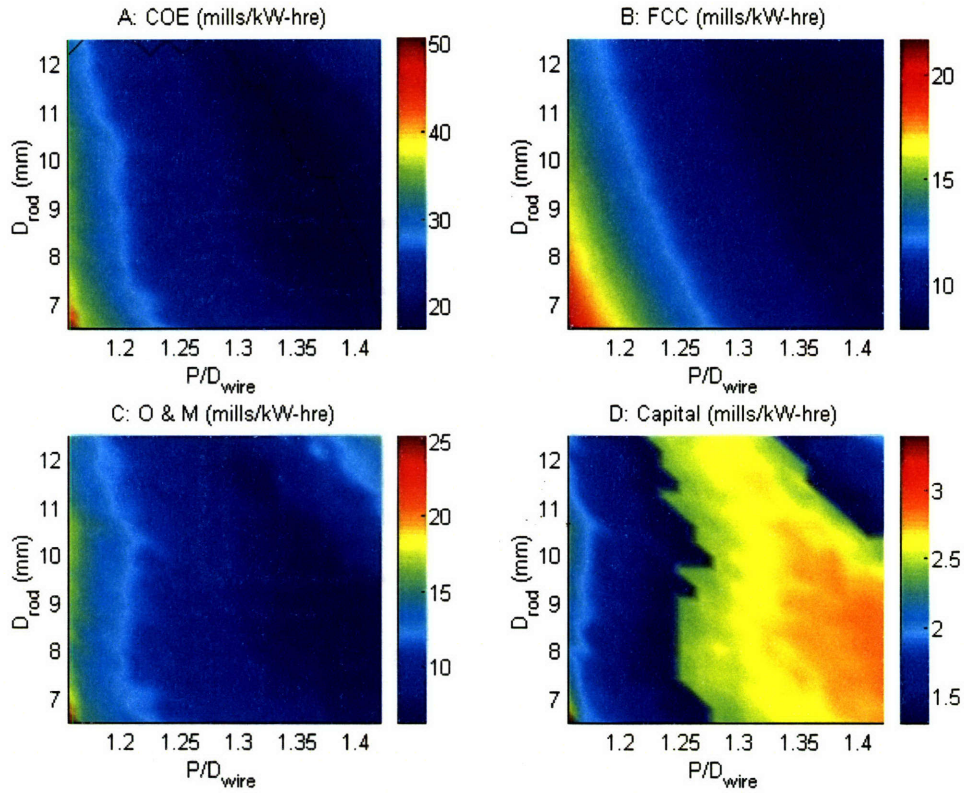

Figure 10.13 - Plant Operating Conditions for Steady-State Achievable Case with 7.5% UO_2

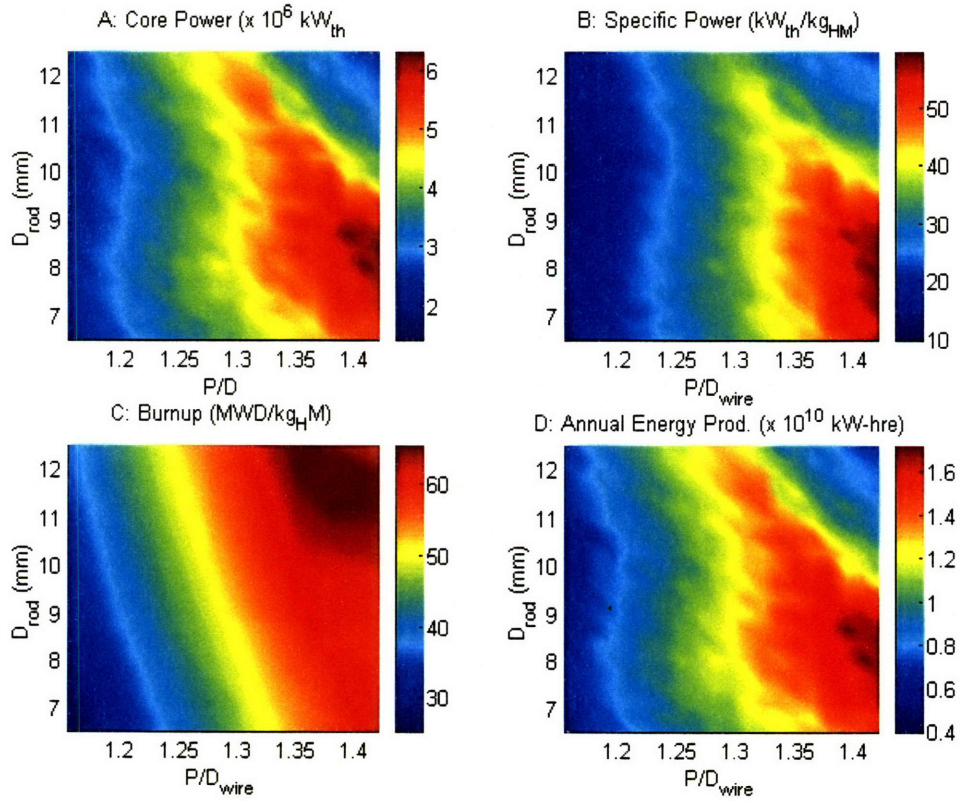

Figure 10.14 - Plant Operating Conditions for Achievable Case with 7.5% UO_2

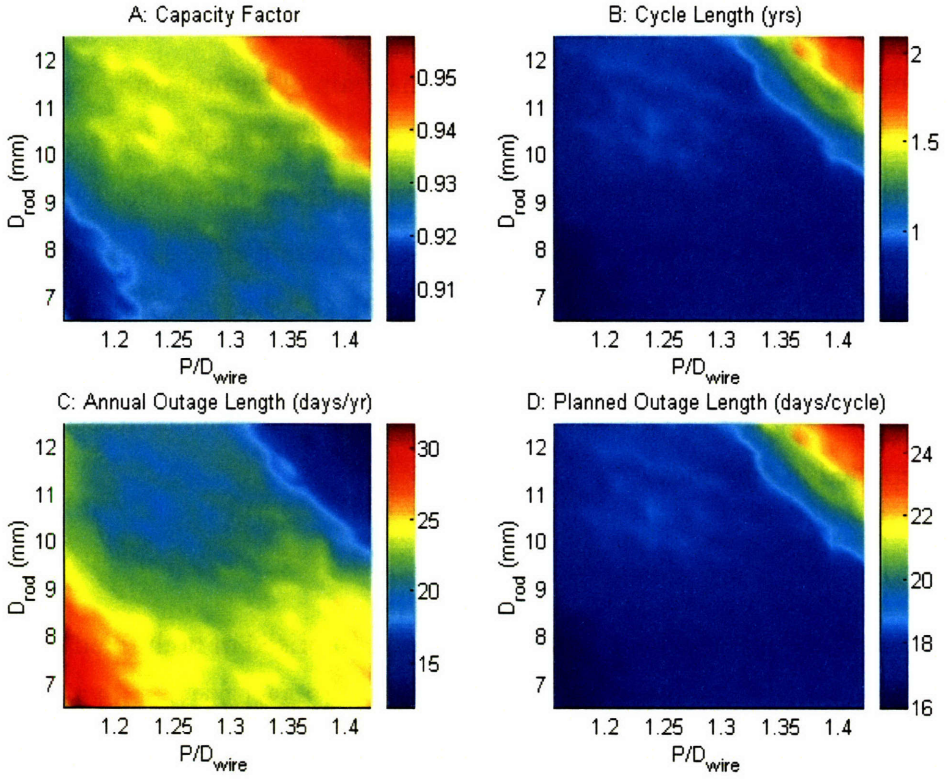

Fuel Cycle Costs (FCC)

The fuel cycle cost is a significant contributor to the COE. The total fuel cycle cost for a single operating cycle depends on the mass of heavy metal in the core. The lifetime levelized unit fuel cycle cost, $\overline{c}_{lev-fcc}$, is equal to the refueling cost divided by the energy produced during the operating cycle. The energy production is the product of the fuel burnup and the mass of heavy metal in the core. Thus for a fixed geometry, $\overline{c}_{lev-fcc}$ can be increased or decreased by varying the burnup in the fuel. It is therefore not a surprise that the plots of $\overline{c}_{lev-fcc}$ for 12.5% $UZrH_{1.6}$ and 7.5% UO_2 in Figures 10.9B and 10.12B show a striking resemblance to the fuel burnups in Figures 10.10C and 10.13C. The figures are practically inverted, with the minimum fuel cycle costs corresponding to regions of maximum burnup. Since increased burnup substantially decreases fuel cycle costs, which are a significant component of COE, the burnup is a very important factor when considering the economics of a design.

One of the most important factors in the burnup is the enrichment. While increased enrichment allows for higher burnups, which substantially affect COE, highly enriched fuel has larger front end enrichment costs. These two competing effects determine the optimal enrichment for a given fuel. The marginal gain of burnup with increased enrichment outpaces the marginal cost of increased enrichment for $UZrH_{1.6}$ (Figure 10.5B), while the relationship between enrichment costs and burnup for UO_2 (Figure 10.7B) is not as clear-cut. The net result of these competing effects drives hydride to higher enrichments than oxide for the minimum COE (12.5% vs. 7.5%). However, the hydride burnups reported here do not account for burnable poisons or thorium that would be necessary for the BOL. This will reduce the burnup gains with increased enrichment that are reported in this study.

O&M Costs

The operations and management (O&M) costs are comprised of both fixed and variable costs and is reported in Figures 10.9C and 10.12C for 12.5%$UZrH_{1.6}$ and 7.5%UO_2 respectively. Fixed costs are associated with plant personnel and variable costs are associated with outages, whether forced or refueling outages. The fixed O&M costs are independent of power, so the fixed cost contribution to the levelized O&M costs, $\bar{c}_{lev-O\&M}$, is inversely proportional to the power. The variable O&M costs depend on the annual outage length, but for reasonable cycle lengths (i.e. greater than six months), the fixed component comprises the majority of the annual O&M cost. For the large power uprates considered in this study, additional fixed O&M costs associated with larger capacity (i.e. if another turbine hall was required) are not considered here.

Capital Costs

The capital costs are unique among the COE components because they occur only once, at the time of expenditure. For the major backfit scenario, which is required for conversion to a wire wrap geometry, the capital costs depend on two conditions:

- whether a geometry offers increased power relative to the reference core.
- if an increase is reported, its magnitude.

$\bar{c}_{lev-cap}$ is plotted in Figures 10.9D and 10.12D. Each cost figure is clearly divided into two sections per the conditions described above. In the regions where the power is below the reference core power, the capital expenditure is fixed (replacement of core internals, vessel head, remaining value of lost fuel), and so $\bar{c}_{lev-cap}$ depends solely on the power/energy production from the plant. For regions where the maximum power is greater than the reference core power, additional costs are incurred for replacement of the steam generators and upgrades to the turbine. $\bar{c}_{lev-cap}$ therefore jumps in this region where power increases are reported, but is mitigated due to the increases in the power production. However, when these capital costs are levelized, they turn out to be much smaller than the O&M and fuel costs over most of the power map, and thus are not considered to be a driving force in the optimal geometry and power.

Figure 10.15 - COE Difference and Fuel Enrichment for Steady-State Achievable Case with $UZrH_{1.6}$ and UO_2

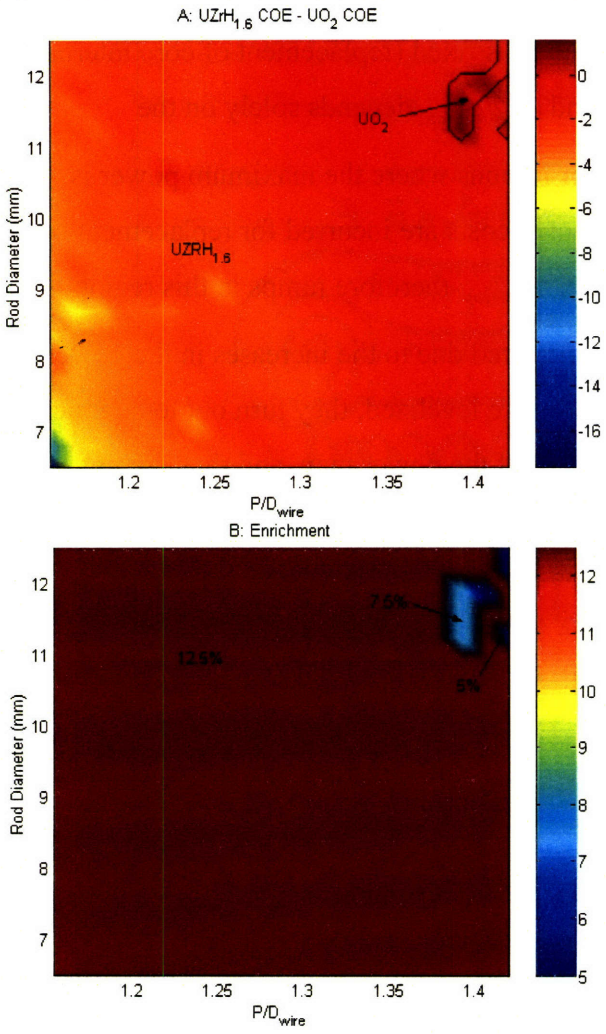

Overall Cost of Electricity

Figure 10.15 is a direct comparison of $UZrH_{1.6}$ and UO_2 fuel. Figure 10.15A shows the difference between the minimum COE at a given geometry. The areas marked $UZrH_{1.6}$ have a lower COE with $UZrH_{1.6}$, and the areas marked UO_2 have a lower COE with UO_2. The optimal enrichments are shown in Figure 10.15B. For almost the entire power map, 12.5% $UZrH_{1.6}$ fuel is gives the lowest COE of all geometries and enrichments considered. The COE of $UZrH_{1.6}$ is 0.8 mils/kW-hre less than UO_2 for the geometry of maximum power (D = 8.39 mm, P/D_{wire} = 1.42). This difference is largely due to the systematic difference in fuel costs, as shown in Figure 10.5B and 10.7B.

Figures 10.16-10.19 show the minimum COE as a function of P/D for the steady-state and final power (steady-state and transient constrained) for the Achievable and Stretch Cases with $UZrH_{1.6}$ and UO_2. For the same fuel type, the curves have the same shape, and the values do not change much between the cases. The steady-state Stretch Case (Figure 10.16) and the final power Achievable Case (Figure 10.19) have the highest and lowest powers, respectively, and can be considered to be bounding cases of the actual wire wrap performance.

Figure 10.16 - Stretch Case, Steady-State

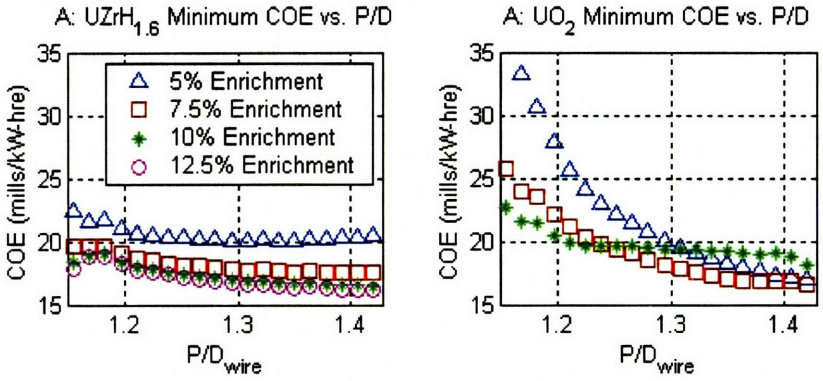

Figure 10.17 - Stretch Case, Final Power (with Transients)

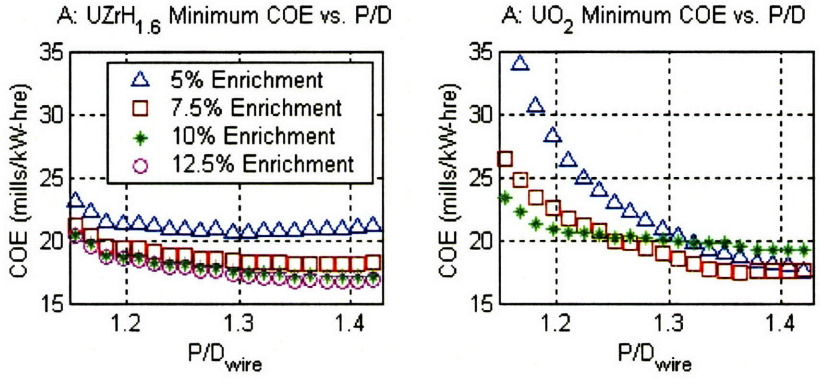

Figure 10.18 - Achievable Case, Steady-State

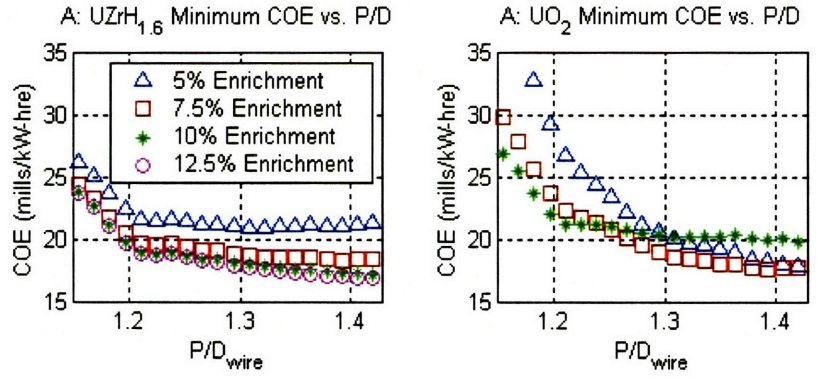

Figure 10.19 - Achievable Case, Final Power (with Transients)

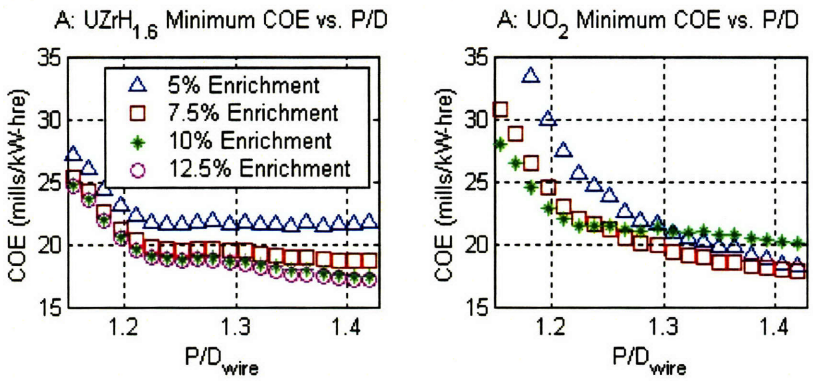

Table 10.1 shows the minimum COE geometries for the following cases (recall that the final power Achievable Case and the steady-state Stretch case bound the wire wrap results):

- Final Power Achievable Case (with transients and steady-state)
- Steady-State Stretch Case
- 60 psia grid spacer (the grid spacer core with constraints equivalent to the wire wrap Achievable Case **[2]**, chosen as a comparison to the Final Power Achievable Case)
- Reference Core
- New Core (3800 MWth from existing core and 2211 MWth from newly constructed core of reference design to achieve the maximum power for Final Power Achievable Case, see Section 10.2.1)

For all of these cases, the minimum COE is the minimum of all enrichments and all fuel types, which are also displayed in Table 10.1. 12.5% enriched $UzrH_{1.6}$ is the highest enrichment considered in this study, but it is likely that a lower COE could be obtained by moving to higher enrichments.

Characteristic	*Major Backfit*			*No Backfit*	
	Wire Wraps		*Grid Spacers*		
	Achievable Case	*Stretch Case*	*Grid Spacer Uprate* **[2]**	*New Core*	*Reference Core*
Fuel Type	$UZrH_{1.6}$	$UZrH_{1.6}$	UO_2	UO_2	UO_2
Enrichment	12.5%	12.5%	5%	5%	5%
Power (MWth)	6011	7156	4929	6011	3800
D (mm)	8.08	8.71	6.5	9.5	9.5

P/D_{actual}	1.41	1.42	1.39	1.326	1.326
Linear Heat Rate (kW/ft)	6.05	8.23	3.56	5.30	5.30
Capacity Factor	0.94	0.93	0.94	0.95	0.95
Cycle Length (yrs)	0.90	0.76	0.9	1.22	1.22
COE (mils/kWe-hr)	**17.11**	**16.11**	**17.9**	**26.98**	**17.75**
Fuel Cycle Cost	7.63	7.45	7.13	7.65	7.65
O&M Cost	6.65	5.74	8.1	10.1	10.1
Capital Cost	2.83	2.92	2.7	9.23	0

Table 10.1 - COE Comparison of Grid Spacers and Wire Wraps

P/D_{actual} is the actual P/D of the assembly, regardless of the geometry; this is P/D_{sq} for reference and grid spacer geometries, and P/D_{wire} for the Achievable and Stretch Cases. There is a clear advantage to moving to wire-wrapped hydride assemblies, as the cost savings could be as much as 1.64 mils/kWe-hr, or 9% as compared with the oxide reference core, and 10.87 mils/kWe-hr, or 40% when compared to the oxide "new core". Tables 10.2 and 10.3 compare wire-wrapped assemblies with oxide and hydride fuels. With $UZrH_{1.6}$, the most conservative COE estimate still provides a .64 (4%) mils/kWe-hr savings with wire wraps over the reference core. With UO_2, the most conservative COE estimate is slightly more than the reference core, but still 33% less than a new core.

Characteristic	*Achievable Case*	*Stretch Case*	*Achievable Case*	*Stretch Case*
Fuel Type	UO_2	UO_2	$UZrH_{1.6}$	$UZrH_{1.6}$
Enrichment	7.5%	7.5%	12.5%	12.5%
Power (MWth)	6303	6830	6251	7156
D (mm)	8.71	9.66	8.39	8.71
P/D_{actual}	1.39	1.36	1.42	1.42
Linear Heat Rate (kW/ft)	6.98	8.92	6.79	8.23
Capacity Factor	0.94	0.94	0.93	0.93
Cycle Length (yrs)	1.01	1.00	0.86	0.76
COE (mils/kWe-hr)	**17.56**	**16.84**	**16.87**	**16.11**
Fuel Cycle Cost	8.48	8.21	7.57	7.45
O&M Cost	6.24	5.76	6.44	5.74
Capital Cost	2.84	2.87	2.86	2.92

Table 10.2 - COE Comparison of Oxide and Hydride for Steady-State Wire Wraps

Characteristic	*Achievable Case*	*Stretch Case*	*Achievable Case*	*Stretch Case*
Fuel Type	UO_2	UO_2	$UZrH_{1.6}$	$UZrH_{1.6}$

Enrichment	7.5%	7.5%	12.5%	12.5%
Power (MWth)	5878	6121	6011	6251
D (mm)	7.13	9.34	8.08	8.71
P/D_{actual}	1.42	1.27	1.41	1.39
Linear Heat Rate (kW/ft)	4.55	7.49	6.05	7.80
Capacity Factor	0.94	0.94	0.94	0.94
Cycle Length (yrs)	1.03	1.10	0.90	0.90
COE (mils/kWe-hr)	**17.84**	**17.50**	**17.11**	**16.73**
Fuel Cycle Cost	8.37	8.33	7.63	7.49
O&M Cost	6.67	6.35	6.65	6.39
Capital Cost	2.80	2.82	2.83	2.85

Table 10.3 - COE Comparison of Oxide and Hydride for Final Power Wire Wraps (Transient and Steady-State Constraints)

10.4.2 - Notes on Hydride Fuel COE

It turns out that the hydride-fueled cores considered above have positive moderator temperature coefficient of reactivity due, primarily, to the relatively large amount of soluble boron they have to use. A couple of approaches were investigated at UC Berkeley to alleviate this problem – use of Erbium as burnable poison, and the use of ThH2 as a partial replacement for ZrH1.6.

Erbium

The use of erbium was found to penalize the attainable burnup and adds to the fuel cost. Using enriched erbium lowers the burnup penalty but increases the fuel cost. Figures 10.20 and 10.21 **[34]** show the burnup penalty for specific geometries associated with the attainment of a negative coolant temperature coefficient of reactivity when using natural erbium or enriched erbium, respectively,. The coolant temperature coefficient limits the attainable burnup more than the other reactivity coefficients.

Figure 10.20 - Achievable Burnup with Natural Erbium

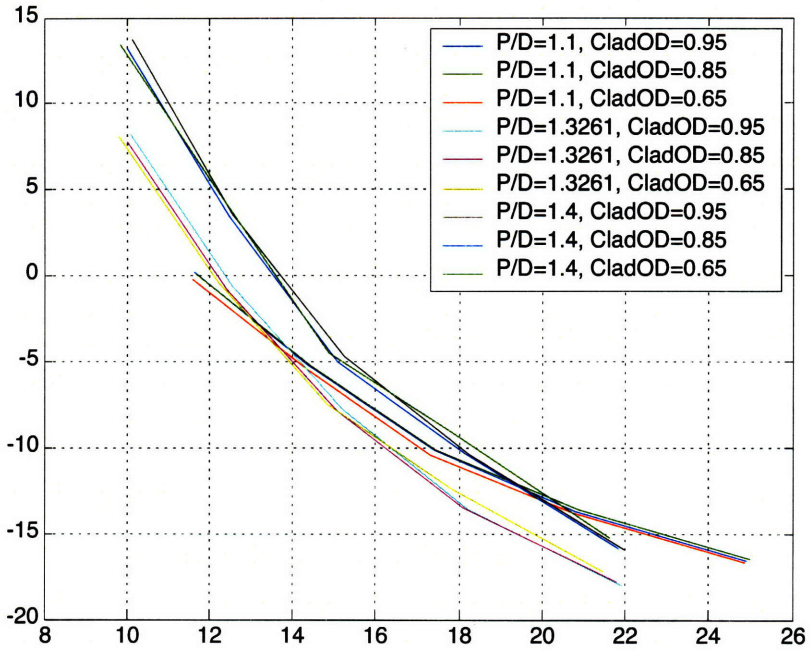

Figure 10.21 - Achievable Burnup with Enriched Erbium

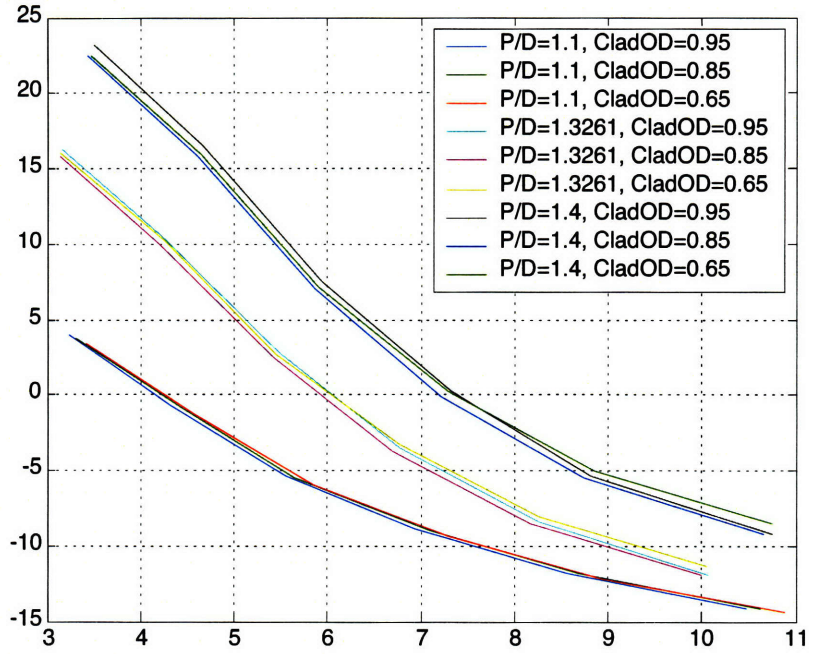

For the Achievable Case maximum power geometry (D = 8.39 mm, P/D_{wire} = 1.42), the attainment of –5 pcm/K coolant temperature reactivity coefficient corresponds to a burnup penalty of ~14% with natural erbium and ~6.6% with enriched erbium. These burnup penalties, as well as expected increases in the FCC associated with the purchase of erbium, were used to calculate the COE of hydride fuel with erbium with natural and enriched erbium. The results are shown for wire wraps using the final power maps in Table 10.4 (analogous to Table 10.3). Note that the cost of natural erbium is assumed to be negligible. The cost of enriched erbium is assumed to be $5,500/kg, and it is also assumed that 2.1% of the weight of the uranium is required. Assuming that uranium costs $4000/kg, the addition of erbium would increase the FCC by 2.5%.

Table 10.4 - COE of Hydride Fuel with Erbium at Final Power

Characteristic	*Achievable Case, w/out Erbium*	*Achievable Case, enriched Erbium*	*Achievable Case, natural Erbium*
Fuel Type	$UZrH_{1.6}$	$UZrH_{1.6}$	$UZrH_{1.6}$
Enrichment	12.5%	12.5%	12.5%
Power (MWth)	6011	6011	6011
D (mm)	8.08	8.08	8.08
P/D_{actual}	1.41	1.41	1.41
Linear Heat Rate (kW/ft)	6.05	6.05	6.05
Capacity Factor	0.94	0.93	0.93
Cycle Length (yrs)	0.90	0.85	0.73
COE (mils/kWe-hr)	**17.11**	**17.79**	**18.93**
Fuel Cycle Cost	7.63	8.04	9.19
O&M Cost	6.65	6.71	6.88
Capital Cost	2.83	2.84	2.86
Burnup penalty	N/A	6.6%	14%
Additional FCC of Erbium	N/A	2.5%	0%

By using uranium enriched to more than 12.5%, it may be possible to increase the attainable burnup and lower the COE. Additional optimization is required to find the optimal uranium enrichment when using Erbuim burnable absorber.

Thorium Fuel

Thorium fuel has been investigated as another means of addressing the over-moderation of hydride fuels for the geometries of interest **[31]**. Burnup studies were completed of ThH_2 plus IFBA compensate for the positive reactivity coefficient of $U\text{-}ZrH_{1.6}$ with soluble boron in the moderator. These were done for a single geometry of interest, D = 8.5 mm, $P/D_{wire} = 1.42$, with uranium enrichments of 12.5% and 20%. The thorium concentration was optimized to maximize the burnup between values of 5.50% and 27.50%. The burnup values were normalized to the corresponding uranium HM loading, and the results are shown in Table 10.5.

Table 10.5 - Uranium-Normalized Burnup and Optimal Thorium Concentration

Uranium Enrichment	*12.5%*	*20%*
Thorium Concentration	11.0%	22.0%
Normalized Burnup (MWD/kg-HM)	130.22	206.31

An economic analysis was performed for these cases (12.5% and 20% enriched uranium). In addition, the burnup values for 15% and 17.5% were linearly interpolated from the burnup values in Table 10.5, and an economic analysis using the Achievable Case at Final Power was performed for each of these cases. The results for all thorium cases are shown in Table 10.6, as well as the results for $UZrH_{1.6}$ with enriched Erbium for comparison. For this analysis, the cost of thorium was assumed to be equal to the cost of the zirconium it replaces The burnup values for thorium at 17.5% and 20% are limited by fuel performance, not neutronics. As a result, increasing the enrichment from 17.5% to 20% has no effect on the burnup, but the increased enrichment still adds to the COE, resulting in a 5% COE increase for the 20% enrichment.

Table 10.6 - COE of Hydride Fuel with Thorium

Characteristic	*Enriched Erbium*	*Thorium (ThH_2) with IFBA*			
Enrichment	12.5%	12.5%	15%	17.5%	20%
D (mm)	8.5	8.5	8.5	8.5	8.5
P/D_{actual}	1.42	1.42	1.42	1.42	1.42
Burnup (MWD/kg_{HM})	121.91	130.22	155.58	162.04	162.04
COE (mils/kWe-hr)	**18.23**	**17.52**	**17.25**	**17.88**	**18.79**

At 12.5% enrichment, the COE of thorium is only 2.4% greater than that of the Achievable Case without erbium or thorium. Thus, the addition of thorium shows promise in providing negative temperature coefficients, and also demonstrates that the solution to the over-moderation problem may involve practically no COE increase.

Chapter 11: Conclusions

The primary goal of this study was to determine the economic feasibility/advantage of backfitting existing PWR's by replacing grid spacer assemblies with wire-wrapped assemblies. Due to the availability of data, all of the designs analyzed here are single start hexagonal wire-wrapped assemblies. This design can be accomplished in conjunction with the replacement of oxide (UO_2) fuel with hydride ($UZrH_{1.6}$). All of the analyses presented here were performed for hydride and oxide fuel, and for an Achievable Case (guaranteed performance) and a Stretch Case (best estimate performance). The economic analysis was completed by first performing a steady-state analysis of the achievable power, which follows Malen's **[1]** analysis. This was facilitated by a thermal-hydraulic and neutronic equivalence between hexagonal wire-wrapped assemblies, and square grid spacer assemblies. The steady-state analysis resulted in a power map of achievable powers for different geometries (D and P/D). A transient analysis was performed, which follows Trant's **[2]** analysis. An overpower transient was imposed, and a preliminary LOCA constraint was applied. Finally, an economic analysis was performed, which follows Shuffler's **[2]** analysis, and the cost of electricity (COE) for wire wraps and grid spacers was calculated, using both oxide and hydride fuels.

11.1 Steady-State

Malen established a methodology for determining the maximum power that does not exceed steady-state performance constraints. Constraints were placed on the MDNBR, core average pressure drop, axial flow velocity, and fuel temperature. The power is increased by increasing the mass flow rate; the average enthalpy rise is fixed. This analysis was modified to accommodate wire wraps, and the resultant steady-state power maps are shown in Figure 11.1, for the Achievable and Stretch Case. Fuel temperature is the only limit that depends on fuel type. The fuel temperature limits result in very similar power maps, and are never constraining for regions of maximum power. Consequently, the steady-state achievable power for hydride and oxide is almost identical, and in practice is identical for the regions of maximum power.

Figure 11.1 - Steady-State Maximum Achievable Power for Wire Wraps

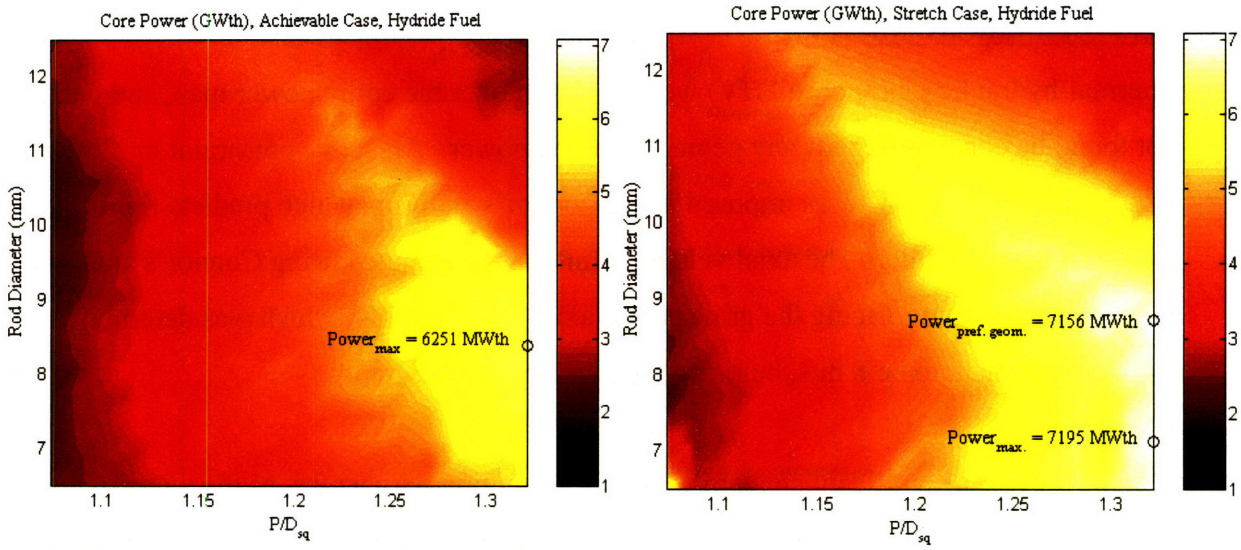

A 64.5% power increase is obtained for the Achievable Case, and 88.3% for the Stretch Case. The Achievable Case maximum power geometry is D = 8.39 mm, P/D_{wire} = 1.42, equivalent to P/D_{sq} = 1.321. The Stretch Case maximum power geometry is D = 8.71 mm, $P.D_{wire}$ = 1.42.

The equivalence between hexagonal wire-wrapped assemblies and square grid spacer assemblies was developed analytically, under the assumption that two channels with the same rod diameter, flow area, and heated and wetted perimeter will have identical thermal-hydraulic performance. This was proved using a full-core hexagonal wire wrap model, and comparing the results to the equivalent full-core square model. The achievable linear heat rates for these two cores were different by less than 1%.

The achievable powers for wire wraps are generally much higher than for grid spacers at the same geometry. This is due to wire-wrapped assemblies' improved CHF, pressure drop, and vibrations performance. As predicted by this analysis, every aspect of the wire-wrapped assemblies' performance is superior to grid spacer assemblies. It is likely that the achievable power will need to be reduced in light of fretting wear constraints. This is

not due to inferior fretting wear of wire wraps (the fretting wear rate of wire wraps is actually anticipated to be less than that of grid spacers), but due to the increased power, which is associated with higher fretting wear rates.

11.2 - Vibrations Analysis

Thermal-hydraulic vibrations (THV) were analyzed over the entire power map, and were not found be constraining for any geometry at any power. An active constraint on flow-induced vibrations (FIV) was imposed using Connor's analysis, which predicts fluid-elastic instability limits. The axial velocity limit was determined using Connor's analysis for each geometry, replacing the grid spacers axial velocity limit, which was determined by team judgment to be 8 m/s, but is not applicable to wire wraps.

Fretting wear is a significant concern when implementing wire wraps, as the wires of one rod directly contact the adjacent rod. Shuffler previously calculated the total fretting wear over the fuel cycle, and constrained this to be less than the reference core total fretting wear. Due to time constraints, in this study, the fretting wear rate was calculated for only the reference geometry at the reference power. This was done using grid spacers and wire wraps, and the wire wrap fretting wear rate was found to be 10.4% lower than the grid spacer fretting wear rate. This is promising, but fretting wear experiments are needed perhaps more than any other type of experiment to verify wire wrap performance.

11.3 - Transient Performance

The transient performance of wire wraps was analyzed for the overpower transient and the loss of coolant accident (LOCA). The overpower transient was evaluated using the MATLAB/VIPRE interface, analogous to the steady-state analysis. The only difference is that the average linear heat rate of the core is increased by 17.267%, the stated overpower value of the reference core. The MDNBR of the reference core is recalculated with the new linear heat rate, and is taken as the new MDNBR limit for the overpower transient. This new MDNBR limit is more constraining than the steady-state MDNBR limit and the axial velocity is generally higher as well. As a result, the achievable powers of the overpower transient are lower than the steady-state. Figure 11.2 shows the predicted power reduction to comply with the overpower transient. As for the steady-

state analysis, the hydride and oxide power maps are essentially identical. The results of this study predict a 5% reduction in maximum power necessary to comply with the overpower transient. The results from the overpower and LOCA analyses were incorporated into the final power maps.

Figure 11.2 - Power Reduction Required for Overpower Transient

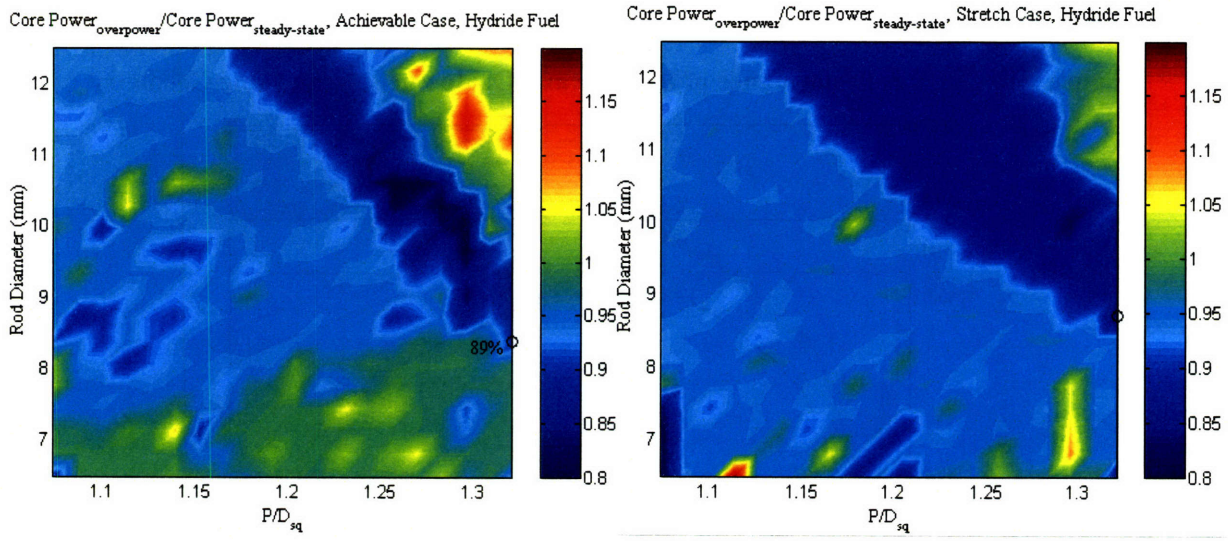

The LOCA performance of wire wraps was calculated using RELAP for both hydride and oxide fuels. The safety injection (SI) system was assumed to scale with the power, allowing the core to eventually cool, even for power uprates on the order of 100%. The cladding temperature limits oxide fuel, while the fuel temperature limits hydride fuel. Coincidentally, the two fuels again performed very similarly against their respective limits. The Achievable Case power is within the limits for both of the fuels, while both of the fuels exceed their limits for the Stretch Case. While RELAP captures well the behavior of the LOCA with increased power, substantial stochastic effects were observed with changes to other operating parameters. No power reduction was applied as the stochastic behavior of RELAP makes it impossible to converge on a maximum power. The LOCA results for the Achievable Case (180%) and Stretch Case (206%) using both hydride and oxide fuels are shown in Figure 9.10. Since the power was determined to be the variable that affected LOCA performance the most, the maximum power for the

Achievable Case (6251 MWth), which was close to breaching its temperature limit, was taken to be the maximum allowable power for the entire power map.

Due to time constraints, it was not possible to perform a full LOFA analysis for wire wraps, as Trant **[2]** did for grid spacers. A qualitative assessment of the wire wrap LOFA performance was inconclusive in determining whether a power reduction is necessary.

Figure 9.10 - LOCA Performance of Hydride and Oxide Fuels, Achievable Geometry

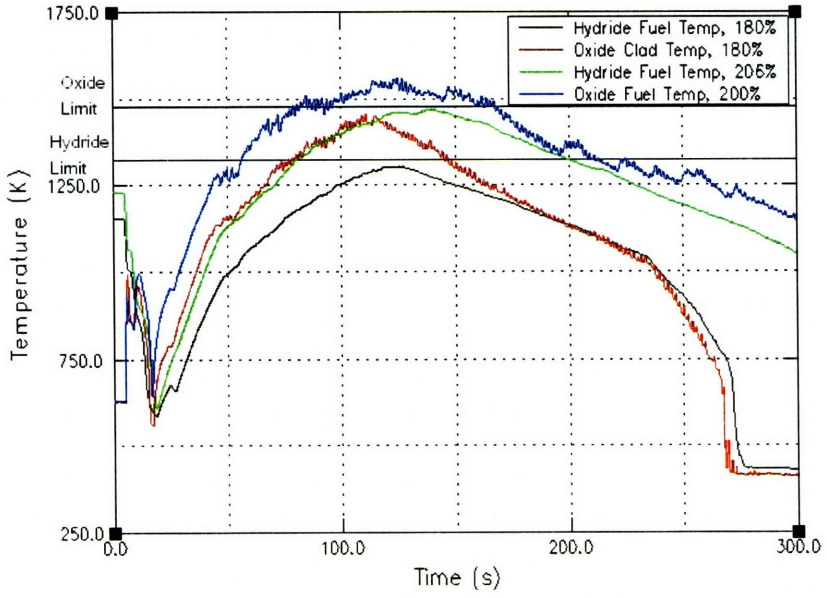

11.4 - Maximum Powers Attainable

The transient-constrained power was combined with the steady-state power maps, to create final power maps for the Achievable and Stretch Cases, which satisfy both the transient and steady-state constraints. This necessarily involves reductions in the maximum power, which can be tracked with the additional transient constraints that are applied, as shown in Figure 9.14.

Figure 9.14 - Maximum Power with Steady-State and Transient Constraints

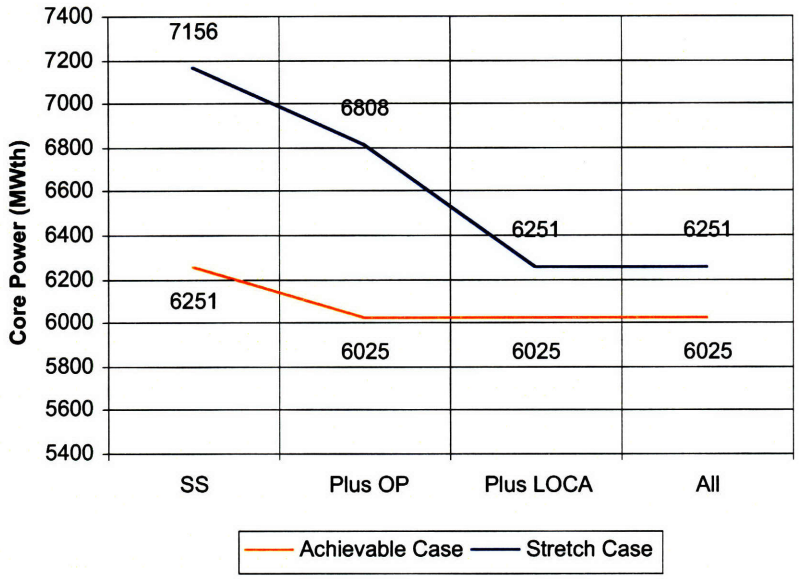

Note that the maximum final power of the Stretch Case is 6251 MWth, 4% higher than the maximum final power of the Achievable Case, 6025 MWth. Considering the liberal assumptions applied to the Stretch Case, this marginal increase in power undermines the case for further consideration of the Stretch Case. Even with the most conservative assumptions in this study (Achievable Case with steady-state and transient limits applied), the maximum power is 6025 MWth, a 59% power increase over the reference core.

Due to the VIPRE modeling approach, for this analysis it was not possible to take into account the effect of the canned bundles necessary for wire-wrapped assemblies. This will have an effect on the core-wide enthalpy distribution, and orificing may be necessary. The bundle cans can be perforated and thus provide for certain amount of cross flow between bundles.

It should also be noted that for both oxide and hydride analyses, the gap between the fuel and the clad was assumed to be filled with liquid metal with a conductivity of 35W/m-K.

11.5 - Economic Analysis

Shuffler **[2]** performed an economics analysis to determine the cost of backfitting reactors with grid spacer assemblies. This analysis was repeated to determine the wire wrap cost of electricity (COE) for both hydride and oxide fuels for the Achievable Case. Fuel cycle, operations and maintenance, and capital costs were considered. The inputs to the economics model included the maximum power from the steady-state analysis, and the burnup from the neutronics and fuel performance studies. For wire wraps, the optimal (lowest COE) enrichment was 7.5% for oxide and 12.5% for hydride. Table 11.1 compares the COE performance of wire wraps and grid spacers. The Achievable Case shown was created with the final power map (with steady-state and transient constraints), while the Stretch Case shown was created only using the steady-state constraints. These act as bounding cases for the economic performance of wire wraps. The hydride cases shown in Table 11.1 assume that enriched Erbium is used to ensure that the temperature coefficients are negative, and carries a burnup penalty of 6.6% and its cost increases the FCC by 2.5%. An economic analysis of Thorium ($UThH_2ZrH_{1.6}$) revealed that the hydride problem with over-moderation can be solved with as little as a 2.4% COE increase. Note that even the Final Power Achievable Case with Erbium (the most conservative wire wrap analysis) has a lower COE than all grid spacer alternatives.

However, even comparing the COE of these alternatives gives an incomplete picture. Ultimately utilities are not interested in minimizing COE, but maximizing profits. The lower COE of the proposed uprates would make the power more profitable, in $/kWe. Additionally, the increase in power increases profits, something not captured by the COE, and consequently a direct comparison of the COE of the uprates and reference core is unfair, since the powers are not the same. However, a COE comparison at the same power is fair, for example that between the "new core" and uprates. This comparison should be viewed as a fair evaluation of the wire wrap $UZrH_{1.6}$ uprates, and shows up to a 40% lower COE for the uprates.

Table 11.1 - COE Comparison of Grid Spacers and Wire Wraps

Characteristic	*Major Backfit*	*No Backfit*

	Wire Wraps		*Grid Spacers*		
	Achievable Case	*Stretch Case*	*Grid Spacer Uprate* **[2]**	*New Core*	*Reference Core*
Fuel Type	$UZrH_{1.6}$	$UZrH_{1.6}$	UO_2	UO_2	UO_2
Enrichment	12.5%	12.5%	5%	5%	5%
Power (MWth)	6011	7156	4929	6011	3800
D (mm)	8.08	8.71	6.5	9.5	9.5
P/D_{actual}	1.41	1.42	1.39	1.326	1.326
Linear Heat Rate (kW/ft)	6.05	8.23	3.56	5.30	5.30
Capacity Factor	0.94	0.93	0.94	0.95	0.95
Cycle Length (yrs)	0.90	0.76	0.9	1.22	1.22
COE (mils/kWe-hr)	**17.11**	**16.11**	**17.9**	**26.98**	**17.75**
Fuel Cycle Cost	7.63	7.45	7.13	7.65	7.65
O&M Cost	6.65	5.74	8.1	10.1	10.1
Capital Cost	2.83	2.92	2.7	9.23	0

Chapter 12: Future Work

The future work is divided into three sections: analysis approach, design possibilities, and wire wrap implementation. The analysis approach deals with needed refinements to the analysis presented in this work. Design possibilities are possible changes to the design presented here: UO_2 and $UZrH_{1.6}$ fuel with hexagonal single-lead wire wraps. Wire wrap implementation outlines the process needed for a full implementation of wire wraps, and includes experimentation and preliminary implementation.

12.1 - Analysis Approach

12.1.1 - Pressure Drop

The pressure drop limit derivation was based on the achievable pressure drop across the core with the expected future capacity of primary system pumps. However, this is a conservative approach. Since the pump compensates for the entire primary system, increasing the pressure drop capability two to four-fold over the reference pump would allow more than a two to four-fold increase in the core pressure drop, assuming that the pressure drop of the rest of the system remained constant. But accounting for this effect is still simplistic, as not only the pressure drop, but also the flow rate, needs to be changed. The flow rate would need to be increased by up to 88% to accommodate the higher powers of an uprate. Designing for the increased flow rate would require knowledge of the whole future achievable pump curve, not just at a single flow rate. RELAP (or a model) will need to be used to approximate the entire primary system pressure drop, and the pressure drop limit will need to be the future achievable pump curve, not just a single pressure drop.

12.1.2 - Fretting Wear Limit

The fretting wear analysis in this study was preliminary, and only focused on one geometry for the comparison of grid spacer and wire wrap performance. The fretting wear is a time-dependent phenomenon, however, and depends on the burnup. Shuffler incorporated a more sophisticated fretting wear limit, based on ensuring that the fretting wear is not constraining at the end of life, and reducing the power as necessary. Since a reduction of power due to fretting wear constraints affects both the fretting wear, and the

fuel performance limited burnup (which can determine the fretting wear at the end of life), this is an iterative process. These iterations will need to be performed for wire wraps, to determine the achievable power and burnup with fretting wear constraints. Sliding wear and vortex-shedding lock-in constraints should also be added, but these are much less constraining than the other vibrations limits and are not anticipated to affect the final results.

12.1.3 - Critical Heat Flux

The CHF correlation used as a base for the wire wrap CHF was the W-3L correlation, which assumes "L"-type mixing vanes. However, the justification for this approach, which was based on experiments comparing the CHF performance of wire wraps to grid spacers, came under question at the end of this study. In particular, most of the grid spacer CHF experiments performed do not give details about the specific type of grid spacer used, so there is no conclusive evidence that wire wrap CHF is larger than mixing vane CHF. Since there is conclusive evidence that wire wrap CHF outperforms the W-3 correlation, which assumes standard grid spacers (see Tong **[19]**), the W-3 correlation would be a more conservative approach and therefore should be assessed. At this point, there is no experimental evidence that wire wraps will outperform the W-3L correlation, and as such, the W-3 correlation is preferable. From preliminary results, it is expected that using the W-3 instead of the W-3L correlation will result in a power reduction of 5-10%.

12.1.4 - Transient Analysis

The LOFA needs to be analyzed further. A full RELAP LOFA model needs to be created and run for the wire wrap geometry of interest, and any power reductions need to be made to remain within the limit.

12.1.5 - Fuel Performance Analysis

The fuel performance limited burnup used for this study was actually created using FRAPCON with the power map for grid spacers. A fuel performance analysis needs to be performed for wire wraps, as part of the iterative process involving fretting wear.

12.1.6 - Neutronics

The neutronics should continue to be refined, and new burnup maps should be created with the use of Erbium. U-PuH2-$ZrH_{1.6}$ is also a promising version of hydride fuel which promises to have superior performance to MOX fuels **[35]**.

12.2 - Design Possibilities

There are many variances of wire wraps from the wire wrap design presented in this study, which could further improve the wire wrap design, ease of implementation and range of impact. The design considered here is single-lead, hexagonal lattice wire wraps in PWR's. Many of these design possibilities are introduced as a means of decreasing the risk and investment required for the potential conversion to wire wrap arrays.

12.2.1 - Square Arrays of Wire Wraps

Since wire wraps have largely been considered for tight-lattice assemblies (which are generally hexagonal arrays), square arrays of wire wraps have hardly been considered. One notable exception is Tong **[19]**, who performed wire wrap CHF experiments with both square and hexagonal lattices. It was noted in Section 6.3.2 that Tong's construction of wire wraps was detrimental to their CHF performance, as the center rod of the 7-rod assembly was not wrapped. Unfortunately, in the construction of his square wire wrap array, only half of the rods were wrapped, which is even more detrimental to the CHF. From his results, it appears that wire wrap square arrays have poor CHF performance, but it is possible that if every rod was wrapped with wire, the CHF would outperform the grid spacer CHF.

Square arrays hold a huge advantage in their implementation: they allow for minor backfits. The economic evaluation of backfits, as performed by Shuffler, do not take into account a key factor in the nuclear industry today: risk. With such huge amounts of investment (time and capital) involved, utilities are very sensitive to the risk of new designs. A minor backfit involves substantially less investment than major backfits, so a square array minor backfit holds a huge advantage over the required major backfit with hexagonal arrays, at least in the initial implementation. In addition, it is highly desirable

to implement a single bundle in an existing fuel cycle to evaluate the performance of wire wraps before any backfit is performed. This requires a square array.

12.2.2 - Multiple-Lead Wire Wraps

Multiple-lead wire wraps have several wires (leads) on the rod, instead of one. In hexagonal lattices, there can be either 1, 2, 3, or 6 leads. Square lattices can either have 1, 2, or 4 leads. See Figure 12.1 for an illustration of the fuel rod cross-section with single and double leads. For the same number of contact points, the wire wrap angle will be less with more leads, improving the pressure drop performance. An interesting effect also occurs with an even number of leads. The wires would appear to clash with each other, making it necessary to wrap the rods with wire that is half the diameter of the gap. At junction points, these wires cross each other, and *never contact adjacent rods*. This is a huge potential advantage of wire wraps, as there is now no contact between adjacent wires and the fuel rod. The crossed wires rub against each other, and no fretting wear is experienced on the fuel rod. This is a claim that even grid spacers cannot make, as fuel rods are allowed to rub on the grids. Provided that the crossed wires do not excessively fret (a real possibility, as there is little material in the wire) or become misaligned and contact the adjacent rods or allow adjacent rods to contact each other (a problem that could only occur with very small axial pitch), fretting wear

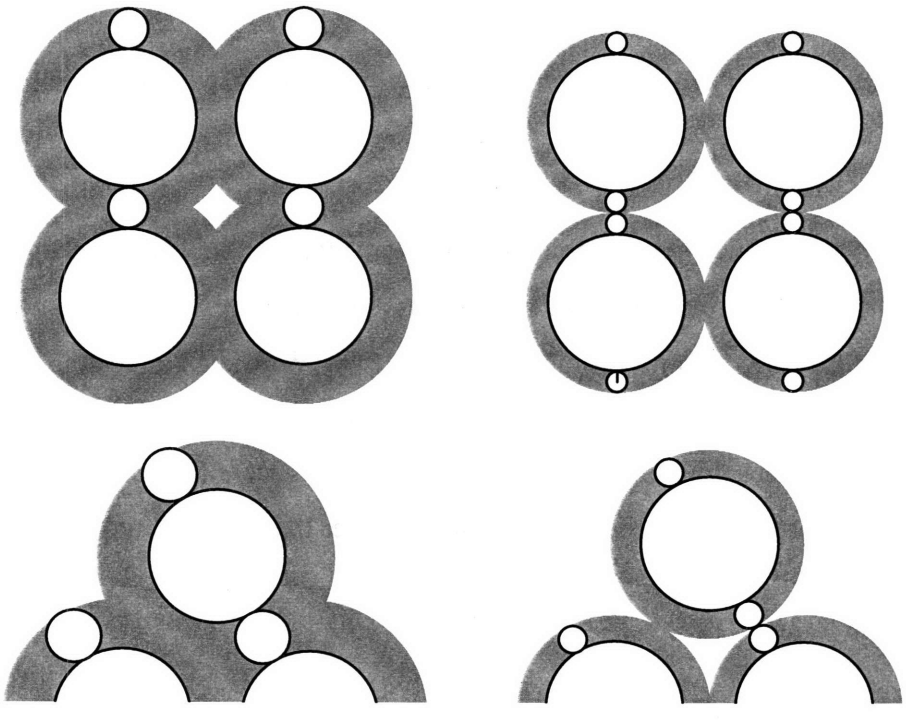

Figure 12.1 - Equivalent Square and Hexagonal Wire Wrap Geometries with Single and Double Leads, and Wire Sweep Areas Illustrated

will not be a problem for designs with crossed wires. Additional possible changes to the wire-wrap method are available through non-uniform wrapping (wrapping only some rods, wrapping the wires in opposite directions, or starting the wires in different locations around the rod perimeter, as Tong did), but these design changes are expected to sacrifice more than they gain.

12.2.3 - Axial Pitch

The axial pitch of the wire wrap was assumed to be close to that of the grid spacers. However, there is no reason that this has to be true. Dalle Donne (see Section 6.4) predicts that smaller axial pitches yield better CHF, and smaller axial pitches yield higher axial velocity limits (see Section 3.2.4). While decreased axial pitch has a detrimental effect on the pressure drop (see Section 4.4.1), the pressure drop is a soft limit and probably could be sacrificed to a greater extent than expressed here. Wire wraps are advantageous for small axial pitches, since the pressure drop penalty with a smaller axial pitch is less severe with wire wraps than with grid spacers. Square arrays of wire wraps will have a larger equivalent diameter, and thus lower pressure drop, than the equivalent hexagonal wire wrap arrays. Additionally using crossed wires decreases the wire wrap projected area over the channel, essentially leaving the center of the channel unobstructed by support of any kind. Figure 12.1 shows the difference in wire wrap projected area with crossed wires for the reference geometry and equivalent hexagonal geometry. The mixing provided by the wires would still benefit the CHF performance of such an array, but the pressure drop would be improved due to the lack of obstructions at the center of

the channel. In such an array, the axial pitch could be reduced dramatically to improve the vibrations and CHF, without a prohibitive penalty to pressure drop. However, a lower limit on axial pitch exists for crossed wires, as the tighter the wire is wrapped, the easier it is for the wires to become misaligned and contact adjacent rods.

12.2.4 - Hybrid Assemblies

Concern exists with the potential freedom of movement that wire wraps have within an assembly, due largely to the porosity on the outside of the bundle. One possibility for mitigating the effect of the porosity on the rod vibrations would be to use a hybrid wire wrap/grid spacer assembly. This assembly would be identical to a standard wire wrap assembly (with either single wires or crossed wires) except that the hybrid assembly would have grid spacers around its edges (dubbed here as edge spacers) on the assembly wall to help eliminate the effect of the porosity. The edge spacers are expected to have little effect on the thermal-hydraulic performance of the bundle, as the hot channels are generally center subchannels. As such, it is expected to be feasible to add edge spacers at every contact point with the wall ($1/6^{th}$ axial pitch for hexagonal arrays, $1/4^{th}$ axial pitch for square arrays), adding substantial support to the assembly. These edge spacers could be designed so that the assembly is easy to construct, as the edge spacers would help guide the rods into the assembly. Due to the nature of wire contact with the assembly walls, the edge spacers would only encompass the entire assembly periphery with crossed wires. See Figure 12.2 for an illustration of the location of the edge spacers around the assembly for single lead wires. These edge spacers would transform the three-

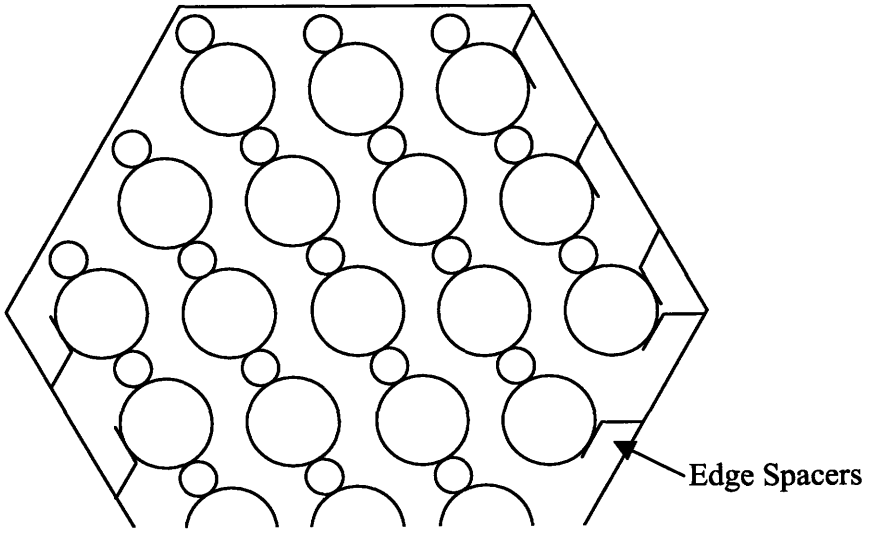

Figure 12.2 - Edge Spacers

dimensional support provided by traditional wire-wrap assemblies to two-dimensional support that behaves more like grid spacers. With wire wraps the support occurs six times over an axial pitch (four times for square arrays), which is already likely to be smaller than the grid spacer axial pitch. The resultant natural frequency will be much higher than the natural frequency with grid spacers, improving the vibrations performance (both fretting wear and FIV) dramatically.

12.2.5 - Applicability to BWR's

This study has focused exclusively on using wire wraps in PWR's, but they could be applied equally to BWR's. While the design issues are somewhat different with BWR's than PWR's, many of the advantages of wire wraps would translate to BWR's. The mixing with wire wraps could improve the MCPR performance of BWR's, but according to Cheng **[17]**, wire wraps are detrimental to the CHF for the exit quality range of BWR's. More importantly for BWR's, and in particular natural circulation BWR's, wire wraps provide improved pressure drop performance. This would increase the safety and viability of a natural circulation BWR under transients.

12.3 - Wire Wrap Implementation

This section outlines the anticipated progression of the implementation of wire-wrapped assemblies, including the expected experimentation that will be necessary to prove wire wrap performance. The implementation is designed to expose utilities to the smallest risk possible, as the wire wraps will be implemented in stages, starting with a small investment and risk and moving to larger investments while keeping the risk small, as the wire wrap performance will be gradually proved.

12.3.1 - Initial Testing

The first step is to choose a preliminary design. This design will have the same geometry as the reference core as is necessary for the in-core testing, so for western-designed PWR's the design will be a square array, but the axial pitch and the number of leads will need to be determined through testing. The required tests to prove the potential of wire wraps are:

1. Flow-Induced Vibration - FIV tests are less expensive than CHF tests, and a good starting point. These tests will hopefully be performed with various axial pitches and with all combinations of multiple start leads to get an idea of the effect that the various parameters have. V. Fedotovskii et al. **[33]** report critical axial velocities of up to 11.9 m/s for crossed wire wrap assemblies. The porosity for these tests should be as small as is feasible for the final design. If FIV proves to be a problem, edge spacers should be implemented.
2. Critical Heat Flux - CHF tests will need to be performed to confirm the improved CHF performance of wire wraps. This will be a big selling point for PWR designers, and should be performed for tight axial pitches as well. If possible, these tests should have data applicable for BWR's as well.

12.3.3 - In-Core Testing

After a preliminary design is selected based on the FIV and CHF experiments, a single assembly should be implemented in a fuel cycle, reducing the risk to the utility. However, to do this, the design's pressure drop characteristics will need to be determined. Unlike PWR grid spacer assemblies, wire wrap assemblies are canned (similarly to BWR assemblies), and there is no mass exchange between assemblies. If the flow resistance of the test assembly is too low, the mass flow rate through the assembly would be higher than desired. This would improve the CHF performance of the assembly, as the exit enthalpy will be less, but the FIV performance will be degraded, as the flow velocity would be higher. If the flow resistance is found to be too low, orificing will need to be introduced to achieve the desired flow rate. If the flow resistance is found to be too high, the design would need to be modified to decrease the flow resistance. Design changes

that could accomplish this are increasing the axial pitch, changing the number of wire leads, and removing edge spacers, if they are implemented. The in-core tests should provide the initial performance evaluation of wire wraps, and in particular the fretting wear performance will be telling.

12.3.4 - Reference Geometry Implementation

If the in-core tests prove promising, the next step is to implement a batch of the design. Not only will wire wraps require no change to the core internals or vessel head, since the design will be the same as the reference geometry, the utilities will be able to incorporate the wire wraps into an existing batch cycle without discarding any grid spacer batches. The incremental risk with this is minimal, and at this point the utilities can start uprating the plant.

12.3.5 - Major Backfits, New Design

If the reference geometry implementation is successful and allows for a large power uprate, the nuclear engineering community will start to realize the potential of wire wraps. This study provides a guide for the evaluation of an optimal design. At this point, the power uprates of over 50% can be achieved. Wire wraps could also be chosen for the construction of new plants, which could either produce more power, or design for substantially smaller pressure vessels, allowed by the higher volumetric power density of wire wraps.

References

[1] J.A. Malen, N Todreas, A. Romano, "Thermal Hydraulic Design of Hydride Fueled PWR Cores", MIT-NFC-TR-062, MIT, Department of Nuclear Engineering, (March 2004).

[2] C.A. Shuffler, A. Romano, N.E. Todreas, and J.M. Trant, "Application of Hydride Fuels to Enhance Pressurized Water Reactor Performance", MIT-NFC-TR-072, MIT, Department of Nuclear Engineering, (August 2005).

[3] H. Garkisch, B. Petrovic, "Reference Data and Constraints for Uranium-Zirconium-Hydride and Uranium-Thorium Hydride Fuels for Light Water Reactors", Rev. 6, p. 14, 23, Westinghouse Electric Company.

[4] M. Dalle Donne, W. Hame, "Critical Heat Flux Correlation for Triangular Arrays of Rod Bundles with Tight Lattices, Including the Spiral Spacer Effect", Nuclear Technology, Vol. 71, (Oct. 1985), p. 111-124.

[5] T. Shulz (Westinghouse), personal communication with N.E. Todreas, July 18, 2005.

[6] A. Otsubo, T. Okada, N. Takahashi, K. Sato, N. Hattori, "The Occurrence of Wear Marks on Fast Reactor Fuel Pin Cladding", Journal of Nuclear Science and Technology, Vol. 36, No. 6 (June 1999), p. 522-534.

[7] A.P. Sorokin, personal communication with N.E. Todreas, November 15, 2004.

[8] H.J. Connors, "Fluid-elastic Vibration of Tube Arrays Excited by Cross-flow, Flow-Induced Vibrations of Heat Exchangers", ASME Special Publication edited by D.D. Reiff, (1970), p. 42-56.

[9] A.W. Graves, I. Catton, "A Numerical Model of Heat transfer in Rod Bundle with Helical Wire-wrap Spacers", ASME Paper No. 72-HT-55 (August 1972).

[10] R.E. Collingham, W.L. Thorne, J.D.McCormack, "Coolant Mixing in a Fuel Pin Utilizing Helical Wire Wrap Spacers", Nuclear Engineering and Design 24 (1973), p. 393-409.

[11] H. Garkisch, personal communication with author, April 28, 2005.

[12] M. Carelli, personal communication with author, May 26, 2005.

[13] M.K. Au-Yang, "Flow-Induced Vibration of Power and Process Plant Components", p. 62, 259, 265-267, 308, ASME Press, New York, 2001.

[14] S.K. Cheng, N.E. Todreas, "Hydrodynamic Models and Correlations for Bare and Wire-wrapped Hexagonal Rod Bundles - Bundle Friction Factors, Subchannel Friction Factors and Mixing Parameters", Nuclear Engineering and Design, Vol. 92, No. 2 (1986), p. 227-51.

[15] W.K. In, D.K. Oh, T.H. Chun, "Empirical and Computational Pressure Drop Correlations for Pressurized Water Reactor Fuel Spacer Grids", Nuclear Technology, Vol. 139, No. 1 (July 2002), p. 72-79.

[16] M.-H. Chun, K.-W. Seo, "An Experimental Study and Assessment of Existing Friction Factor Correlations for Wire-wrapped Fuel Assemblies", Annals of Nuclear Energy, Vol. 28, No. 17, (November 2001), p 1683-1695.

[17] X. Cheng, U. Müller, "Critical Heat Flux and Turbulent Mixing in Hexagonal Tight Rod Bundles", International Journal of Multiphase Flow, Vol. 24 (1998), p. 1245-1263.

[18] X. Cheng, personal communication with author, April 21, 2005.

[19] L.S. Tong, H. Chelemer, "Critical Heat Flux (DNB) in Square and Triangular Array Rod Bundles", JSME 1967 Semi-International Symposium, 4^{th}-8^{th} September, p. 25-34.

[20] V.M.Selivanov, V.A.Vorobiev, "Processing and Analysis of Experimental Data on Temperature Behavior of PWR Core Performed in the 7-tube Model", Report on R&D work N°7763, IPPE, Obninsk, 1990.

[21] G. Bogoslovskaia, personal communication with author, August 4, 2005.

[22] R. W. Bowring, "WSC-2: A Subchannel Dryout Correlation for Water-Cooled Clusters over the Pressure Range 3.4-15.9 MPa", Winfrith: Atomic Energy Establishment (1979), AEEW-R-983.

[23] K. Rehme, "Pressure Drop Correlations for Fuel Element Spacers", Nuclear Technology, Vol. 17, p. 15-23.

[24] D. Feng et al., "Safety Analysis of High Power Density Annular PWR Fuel", Proceedings of ICAPP '05, 15^{th} –19 May, Paper 5481.

[25] South Texas Project Electric Generating Station Final Safety Analysis Report, Revision 12.

[26] Acceptance Criteria for Emergency Core Cooling Systems for Light Water Cooled Nuclear Power Reactors, 10CFR50.46 Appendix K of 10CFR50.

[27] P. MacDonald et al., "Feasibility Study of Supercritical Light Water Cooled Fast Reactors for Actinide Burning and Electric Power Production", 3^{rd} Quarterly Report, NERI Project 2001-001, INEEL/EXT -02-00925.

[28] E. Greenspan et al., "Optimization of UO_2 Fueled PWR Core Design", Proceedings of ICAPP '05, 15^{th} –19 May, Paper 5569.

[29] J.G.B. Saccheri, "A Tight Lattice, Epithermal Core Design for the Integral PWR", Ch. 4, PhD Dissertation, MIT, Department of Nuclear Engineering, August 2003.

[30] NEA/OECD, *The Economics of the Nuclear Fuel Cycle*, OECD Publications, Paris, 1994.

[31] F. Ganda, E. Greenspan, "Neutronic Analysis of Hydride Fuels for PWR: Summary of Work Done During the Second Project Year", NERI-02-180-UCB-6 (November, 2004).

[32] F. Ganda, "Use of Erbium to extend the feasibility of U $ZrH_{1.6}$ to large P/D", internal publication, University of California, Berkeley (June 1, 2005).

[33] V. S. Fedotovskii et al., "Oscillations of an Artificially Roughened Rod in a Lengthwise Flow of Liquid", Soviet Atomic Energy (English translation of Atomnaya Energiya), Vol. 63, No. 1, (Jul. 1987), p. 499-501.

[34] F. Ganda, personal communication with author, October 20, 2005.

[35] F. Ganda and E. Greenspan, "Incineration of Plutonium in PWR Using Hydride Fuel," Proc. 2005 International Conference on Advances in Nuclear Power Plants; ICAPP–2005, Seoul, Korea, May 15-19, 2005.

Appendices Table of Contents

Nomenclature

A.1 - GENERAL NOTATION

A: Cross-sectional Area
C: Monetary Cost
C_d: grid spacer form loss
C_{fbT}: Wire Wrap Friction Factor Constant for Turbulent Flow
C_{fT}: Bare Rod Friction Factor Constant for Turbulent Flow
$\overline{C}_{lev}$: Lifetime Levelized Cost
$\overline{c}_{lev}$: Lifetime Levelized Cost of Electricity
C_M: Added Mass Coefficient
C_{mT}: Turbulent Mixing Parameter
D: Fuel Rod Diameter
D_h,D_e: Hydraulic Diameter
d_w: Wire Diameter
D_*: Non-Dimensional Diameter
E: Young's Modulus of Elasticity
E: Energy
f: Natural Frequency
Friction Factor
F_p: Radial Peaking Factor
G: mass flux
G_F: Random Force Power Spectral Density
G_p: Pressure Power Spectral Density
_h: Core Enthalpy Rise
_H_i: Inlet Enthalpy Subcooling
H/HM: Hydrogen to Heavy Metal Ratio
H: Axial Pitch, # of Hydrogen Atoms
H_i: Inlet Enthalpy
HM: # of Heavy Metal Atoms
I: Moment of Inertia
k: Thermal Conductivity
L: Active Fuel Length
Plant Capacity Factor
L_s: Span Length, equal to axial pitch
m: Linear Mass
$\dot{m}$: Mass Flux
M: Molecular Weight
N: Number of Heated Rods
n: Vibration Mode #
N_A: Avagadro's Number
n_s: Number of Spans
_P: Core Pressure Drop
P/D: Pitch to Diameter Ratio

P: Lattice Pitch (hexagonal or square)
p: System Pressure
P_o: Porosity
P_w: Wetter Perimeter
Q, $\dot{Q}$,Q_{th}: Thermal Power
q': Linear Heat Rate
R: Core Radius
r: Distance from Core Center
Rate of Return
R: Number of Rings in a Hexagonal Assembly, Including the Center Pin
Re,Re_v: Reynolds Number (based on A_{cross})
Re_L: Reynolds Number (based on grid spacer strap length)
S,c: Gap Width between Fuel Rods
_T: Core Temperature Rise
T: Temperature
t: Thickness
V,V_2: Axial Velocity
V: Bowring's Spacer Coefficient
V_c: Critical Cross-flow Velocity
V_T,V_{cross}: Cross-flow Velocity
w: Weight Percent Heavy Metal of the Fuel
w', W'^T: Turbulent Interchange
x: Equilibrium Quality
X: Number of Hydrogen Atoms per Unit Fuel Matrix
Y: Number of Heavy Metal Atoms per Unit Heavy Metal
Bowring Heat Flux Coefficient
y_{max}: Maximum Rod Response
y_{rms}: RMS rod response
_: Connors' Constant
Mixing Coefficient
_: Damping Ratio
_: Thermal Efficiency
μ: Viscosity
ρ: Density
_: Surface Tension
_: Heat Flux

A.2 - SUBSCRIPTS

act: actual
ave: core average
b: fluid bulk
cap: capital
CHF: critical heat flux
CL: cladding
const: constant
core: core-wide

crit:	critical
eff:	effective
fcc:	fuel cycle costs
FL:	fluid
gap:	fuel gap
hex:	hexagonal array
hot:	hot channel
in:	inlet
lev:	levelized
mv:	mixing vane
norm:	normalized
O&M:	operation and maintenance
pellet:	fuel pellet
ref:	reference core
rod:	fuel rod
sq:	square array with grid spacers
T,t:	total
	grid spacer strap
tot:	total
v:	bare rod
wire:	wire wraps

Listed Assumptions of VIPRE Thermal Hydraulic Analysis

The thermal hydraulic assumptions are taken from **[1]**, and modified to be applicable for wire wraps. Assumptions for grid spacers are also included.

B.1 - Channel Geometry

1. Core Height: 4.59m (181.1")
2. Active Fuel Length: 4.267m (168")
3. Axial Nodes: 100

B.3 - Fuel Rod Geometry

1. Clad thickness (as in Section 8.1.5)

$$t_{clad} = max(0.508, (0.508 + (D - 7.747)\cdot 0.0362)) \quad \textbf{[B.1]}$$

2. Gap thickness (as in Section 8.1.5)

$$t_{gap} = max(0.0635, (0.0635 + (D - 7.747)\cdot 0.0108)) \quad \textbf{[B.2]}$$

3. Radial nodes: 6
4. Gap heat transfer coefficient (LM only): $h_g = k_g/R_{fo}\ln(R_{ci}\ln(R_{ci}/R_{fo}))$

B.4 - Operating Conditions

1. Axial power profile: chopped cosine curve, peak-to-average = 1.55
2. Radial power profile peaking factor: peak-to-average = 1.65
3. Inlet temperature: 294 °C
4. Operating pressure: 15.516 MPa (2250 psia)
5. Heat generated directly in the coolant scaled as $H_C/(H_C+H_F)$, where HC is the amount of H in the coolant and H_F is the amount of H in the hydride fuel. The reference case is 2.6% direct deposition

B.5 - Grid Spacers

1. Square: 10 grids spaced axially at the following positions in m, subscript corresponds to loss coefficients used: 0.00_1, 0.148_2, 0.529_2, 1.051_2, 1.573_2, 2.356_2, 2.878_2, 3.139_2, 3.661_2, 4.183_2
2. From Section 4.3, $C_{b,1}$ for non-mixing vane grids, where $_1$ corresponds to the nomenclature above.

$$C_{b,1} = \left[C_{d,form}\frac{\varepsilon}{(1-\varepsilon)^2}\right]_A + \left[C_{fric,grid}\frac{A_{grid}}{A_v}\frac{1}{(1-\varepsilon)^2}\right]_B + \left[C_{fric,rod}\frac{A_{grid}}{A_v}\frac{1}{(1-\varepsilon)^2}\right]_C \quad \textbf{[B.3]}$$

$$\varepsilon = \frac{A_s}{A_v} \qquad A_s = H\cdot P_{w,grid,axial} \qquad A_v = H\cdot P_{w,rod,cross} \quad \textbf{[B.4]}$$

$$t_{spacer} = 0.5mm \qquad H = 38mm \quad \textbf{[B.5]}$$

$$C_{d,form} = 2.75 - 0.27\log_{10}(Re_v) \qquad Re_v = \frac{GD_e}{\mu} \qquad D_e = \frac{4A_v}{\pi D} \qquad \textbf{[B.6]}$$

$$C_{fric,grid} = C_{fric,lam}\frac{L_t}{H} + C_{fric,turb}\frac{H - L_t}{H} \qquad L_t = \frac{30{,}000 \cdot \mu}{G} \qquad \textbf{[B.7]}$$

$$C_{fric,lam} = 1.327 \cdot Re_L^{-0.5} \qquad C_{fric,turb} = \frac{0.523}{ln^2(0.06 \cdot Re_L)} \qquad Re_L = \frac{G(H - L_T)}{\mu} \qquad \textbf{[B.8]}$$

$$C_{fric,rod} = f\frac{H}{D_e} \qquad f = \frac{0.184}{Re_v^{0.2}} \qquad \textbf{[B.9]}$$

3. From Section 4.3, $C_{b,2}$ for mixing vanes grids includes an additional term due to the addition flow constriction of mixing vanes.

$$C_{b,2} = C_{b,1} + \left[C_{d,mv}\frac{\varepsilon_{mv}}{(1-\varepsilon_{mv})^2}\right]_D \qquad \textbf{[B.10]}$$

$$\varepsilon_{mv} = \frac{A_{mv}}{A_v} \qquad C_{d,mv} = 0.72 \qquad \textbf{[B.11]}$$

B.6 - Bare Rod Pressure Loss Correlations

The Cheng/Todreas bare rod correlation is used when calculating the grid spacer pressure drop, assuming that all channels are interior. For laminar and turbulent flow, the friction factor for bare rods in a square array is calculated as:

$$f_L = \frac{C_{fL}}{Re} \qquad C_{fL} = a + b_1\left[\left(P/D\right) - 1\right] + b_2\left[\left(P/D\right) - 1\right]^2 \qquad \textbf{[B.12]}$$

$$f_L = \frac{C_{fT}}{Re^{0.18}} \qquad C_{fT} = a + b_1\left[\left(P/D\right) - 1\right] + b_2\left[\left(P/D\right) - 1\right]^2 \qquad \textbf{[B.13]}$$

where the constants in the correlation are taken from Table B.1

	$1.0 \le P/D \le 1.1$			$1.1 \le P/D \le 1.5$		
	a	b_1	b_2	a	b_1	b_2
Laminar	26.37	374.2	-493.9	35.55	263.7	-190.2
Turbulent	0.09423	0.5806	-1.239	0.1339	0.09059	-0.09926

B.7 - Wire Wrap Pressure Loss Correlations

Instead of the bare rod friction factor correlation, the simplified Cheng\Todreas wire wrap friction factor correlation is used for wire wraps.

$$f = \frac{C_{fbT}}{Re^{0.18}} \qquad \textbf{[B.14]}$$

$$C_{fbT} = \left(0.8063 - 0.9022\left(\log\left(H/D\right)\right) + 0.3526\left(\log\left(H/D\right)\right)^2\right) \cdot \left(P/D\right)_{hex}^{3.7} \cdot \left(H/D\right)^{7.8-2.0\left(P/D\right)_{hex}} \quad \textbf{[B.15]}$$

$$1.025 \le \left(P/D\right)_{hex} \le 1.42 \qquad 8.0 \le \left(H/D\right) \le 50.0 \quad \textbf{[B.16]}$$

B.8 - Heat Transfer Correlations (see [1] for more details)

1. Flow correlations
   a. Subcooled void: Levy
   b. Bulk void/quality: homogeneous
   c. Two phase friction multiplier: homogeneous
2. Heat Transfer Correlations
   a. Single phase forced convection: Dittus-Boelter for turbulent flow
   b. Subcooled nucleate boiling: Thom w/ Dittus-Boelter for single phase
   c. Saturated nucleate boiling: Thom w/ Dittus-Boelter for single phase
   d. Transition boiling: Condie-Bengston
   e. Film boiling: Groeneveld 5.7

B.9 - CHF Correlations

1. W-3 Correlation (10^6 Btu/hr-ft^2), where h_f is the saturated liquid enthalpy at p, with p in psia, G in 10^6 lb/hr-ft^2, enthalpies are in (Btu/lbm) and D_e in ft

$$\varphi_{CHF} = \left[\left(b_1 - b_1 p\right) + \left(b_3 - b_4 p\right) e^{\left(b_5 - b_6 p\right)x}\right]\left[\left(b_7 - b_8 x + b_9 x|x|\right)G + b_{10}\right]\left(b_{11} - b_{12} x\right) \left[\left(b_{13} + b_{14} e^{-b_{15} D_e}\right)\left(b_{16} + b_{17}\left(h_f - h_{inlet}\right)\right)\right] \quad \textbf{[B.17]}$$

$$\begin{array}{llll} b_1 = 2.022 & b_6 = 0.004129 & b_{11} = 1.157 & b_{16} = 0.8258 \\ b_2 = 0.0004302 & b_7 = 0.1484 & b_{12} = 0.869 & b_{17} = 0.000794 \\ b_3 = 0.1722 & b_8 = 1.596 & b_{13} = 0.2664 & \\ b_4 = 0.0000984 & b_9 = 0.1729 & b_{14} = 0.8357 & \\ b_5 = 18.177 & b_{10} = 1.037 & b_{15} = 3.151 & \end{array} \quad \textbf{[B.18]}$$

2. W-3L Correlation, where L_H is heated length in ft

$$\varphi_{CHF,W-3L} = F_{grid(RL)} \cdot \varphi_{CHF,W-3} \quad \textbf{[B.19]}$$

$$F_{grid(RL)} = F_g\left[\left(1.445 - 0.0371 \cdot L_H\right)\left(P/225.896\right)^{0.5}\left[e^{(x+0.2)^2} - 0.73\right] + K_s G\left(TDC/0.019\right)^{1.35}\right] \quad \textbf{[B.20]}$$

$$TDC = 0.042 \qquad K_s = 0.066 \qquad F_g = 1$$

3. Bowring's WSC-2 correlation for vaned spacers, where F_p is the local subchannel peaking factor, p is in kpsia, D_h is in inches, _ is the latent heat of evaporation in Btu/lb, G is in 10^6 lb/hr-ft^2, $\_H_i$ is the inlet subcooling in Btu/lb, and Z is distance from channel inlet in inches

$$\varphi_{CHF} = \frac{A + B \cdot \Delta H_i}{C + ZYY'} \quad \textbf{[B.21]}$$

$$A = \frac{0.25GD\lambda F_1 Q_1}{1 + Q_2 F_2 GD} \qquad B = 0.25GD \qquad C = C'V\left[1 + \frac{Y-1}{G+1}\right] \qquad D = F_p D_h \quad \textbf{[B.22]}$$

$$C' = \frac{Q_4 F_3 \sqrt{GDY'}}{D_h} \qquad Y = \frac{\frac{1}{Z}\int_0^Z \varphi \cdot dz}{\varphi} \qquad Y' = \frac{0.25GD_h(H - H_i)}{\int_0^Z \varphi \cdot dz} \quad \textbf{[B.23]}$$

$$F_1 = p^{0.982} e^{[1.17(1-p)]} \qquad F_2 = p^{0.841} e^{[1.424(1-p)]} \qquad F_3 = p^{1.851} e^{[1.241(1-p)]} \quad \textbf{[B.24]}$$

$$Q_1 = 1.329 \quad Q_2 = 2.372 \quad Q_3 = -1.0$$
$$Q_4 = 12.26 \quad V = 0.7$$

4. Dalle Donne's correlation for V for wire wraps

$$V = 1 - 2.6695\left(F^{0.915} - 1\right)\left[0.336 + 0.09G - 0.697e^{-2.68G}\right] \quad \textbf{[B.25]}$$

$$F = \left(P/D\right)_{hex}^{0.5} + \left[7.6\frac{\left(P/D\right)_{hex}}{\left(H/D\right)}\right]^{2.16} \quad \textbf{[B.26]}$$

B.10 - Mixing Coefficient for Internal Channel

1. Rogers-Tahir for grid spacers

$$\beta = \beta_{bare} + \beta_{grid} \qquad \beta_{rods} = \frac{w_{ij}}{G \cdot s} \qquad s = P - D \quad \textbf{[B.27]}$$

$$\text{square arrays:} \quad w_{ij} = 0.005\mu Re^{0.9}\left(\frac{s}{D}\right)^{0.106} \quad \textbf{[B.28]}$$

$$\text{hex. arrays:} \quad w_{ij} = 0.0018\mu Re^{0.9}\left(\frac{s}{D}\right)^{-0.4} \quad \textbf{[B.29]}$$

a conservative estimate for the total mixing coefficient for the reference core is 0.038, and the grid component is found using Equation B.28

$$\beta_{grid} = 0.038 - \beta_{rods,ref} = 0.0335 \quad \textbf{[B.30]}$$

the mixing coefficient between lumped channels equals the mixing coefficient between individual subchannels divided by the centroid to centroid distance of the lumped channels

$$\beta_{lumped} = \frac{\beta}{L_{ij,lumped}} \quad \textbf{[B.31]}$$

2. Cheng/Todreas for wire wraps, with lumped channel mixing coefficients calculated according to Equation B.31

$$\beta = C_{mT}\sqrt{\frac{A_{r1}}{A_1'}}\left(\frac{\pi}{H/D}\right) \qquad \textbf{[B.32]}$$

$$A_{r1} = \pi(D + d_w)d_w/6 = \frac{\pi D^2}{6}(P/D)_{wire}\left((P/D)_{wire} - 1\right) \qquad \textbf{[B.33]}$$

$$A_1' = D^2\left[\frac{\sqrt{3}}{4}(P/D)_{wire} - \frac{\pi}{8}\right] \qquad C_{mT} = 0.14\cdot\left((P/D)_{wire} - 1\right)^{0.5} \qquad \textbf{[B.34]}$$

B.10 - Lateral Drag

VIPRE default of uniform lateral resistance factor multiplied by centroid to centroid distance divided by the pitch

$$C_{D,lateral} = 0.5\frac{L_{ij}}{P} \qquad \textbf{[B.35]}$$

C. VIPRE Input Deck for Proof of Equivalence

```
* Input for Hydride Core with Wire-Wrapped, Hexagonal Arrays
* D_rod = 6.5 mm, P/D = 1.3866
*
1,0,0
Hydride Core Square Subchannel
*
*================
*CHANNEL GEOMETRY
*================
*
* GEOM.1
geom,?* INFLAG
91,?* NCHANL, # of channels
0,?* NCARD, compressed geometry
100,?* NDX, number of axial nodes
0,?* NAZONE, uniform axial node length
12,?* NCTYP, # of channel types
0*  MBWR, for non-BWR's
*
*
* GEOM.2
181.10,?* ZZ, rod length
0.0,?* THETA, bundle orientation
0.00*  SL, gap parameter, inputted in GEOM4
*
*
* GEOM.5 (description of channel type 1)
57,?* MCHN, # of channels of this type
0.02496,?* CAREA, channel flow area (in^2)
0.557379,?* CPW, channel wetted perimeter (in)
0.401975,*  CPH, channel heated perimeter (in)
* GEOM.6 (channels of type 1)
1,2,3,4,5,6,10,11,12,16,20,21,22,23,24,25
26,30,31,32,33,34,35,36,37,38,39,40,41,42,43,44
48,49,50,51,55,56,57,58,62,63,64,65,66,67,71,72
73,74,75,76,77,78,79,80,81
*
*
* GEOM.5 (description of channel type 2)
24,0.02496,0.557379,0.267984
* GEOM.6 (channels of type 2)
7,8,9,13,14,15,17,18,19,27,28,29,45,46,47,52
53,54,59,60,61,68,69,70
*
1,0.229,5.2022,3.751771*1st lumped subchannel, outer edge of 1/6th
82
*
1,7.167,160.2,99.29*1/2 of assembly
83
*
1,28.67,640.6,397.15*2 assemblies
84
*
1,47.78,1067.7,661.92*3.33 assemblies
85
*
1,66.89,1494.83,926.7*4.67 assemblies
86
*
1,86.007,1922,1191.5*6 assemblies
87
```

```
*
1,105.1,2349,1456.2*7.33 assemblies
88
*
1,124.23,2776.1,1721*8.67 assemblies
89
*
1,143.34,3203.2,1985.8*10 assemblies
90
*
1,437.19,9769.7,6056.6*30.5 assemblies
91
*
*
*GEOM.7
126,?* NK, number of gaps
0,?* NGTYP, not used
1,?* NGAP, gaps are input individually
0,?* NROW, not used
0,?* ISYM, not used
0 *  NSROW, not used
*
*GEOM.11
1,?* K, gap identification number
1,?* I, lower channel connected
3,?* J, upper channel connected
0.09894,?* WIDTH, width of gap
0.20487*  CENT, centroid distance of gap
*
2,2,3, 0.09894,0.20487
3,2,6, 0.09894,0.20487
4,3,4, 0.09894,0.20487
5,4,8, 0.09894,0.20487
6,5,6, 0.09894,0.20487
7,5,11, 0.09894,0.20487
8,6,7, 0.09894,0.20487
9,7,8, 0.09894,0.20487
10,7,13, 0.09894,0.20487
11,8,9, 0.09894,0.20487
12,9,15, 0.09894,0.20487
13,10,11, 0.09894,0.20487
14,10,18, 0.09894,0.20487
15,11,12, 0.09894,0.20487
16,12,13, 0.09894,0.20487
17,12,20, 0.09894,0.20487
18,13,14, 0.09894,0.20487
19,14,15, 0.09894,0.20487
20,14,22, 0.09894,0.20487
21,15,16, 0.09894,0.20487
22,16,24, 0.09894,0.20487
23,17,18, 0.09894,0.20487
24,17,27, 0.09894,0.20487
25,18,19, 0.09894,0.20487
26,19,20, 0.09894,0.20487
27,19,29, 0.09894,0.20487
28,20,21, 0.09894,0.20487
29,21,22, 0.09894,0.20487
30,21,31, 0.09894,0.20487
31,22,23, 0.09894,0.20487
32,23,24, 0.09894,0.20487
33,23,33, 0.09894,0.20487
34,24,25, 0.09894,0.20487
35,25,35, 0.09894,0.20487
```

```
36,26,27, 0.09894,0.20487
37,26,38, 0.09894,0.20487
38,27,28, 0.09894,0.20487
39,28,29, 0.09894,0.20487
40,28,40, 0.09894,0.20487
41,29,30, 0.09894,0.20487
42,30,31, 0.09894,0.20487
43,30,42, 0.09894,0.20487
44,31,32, 0.09894,0.20487
45,32,33, 0.09894,0.20487
46,32,44, 0.09894,0.20487
47,33,34, 0.09894,0.20487
48,34,35, 0.09894,0.20487
49,34,46, 0.09894,0.20487
50,35,36, 0.09894,0.20487
51,36,48, 0.09894,0.20487
52,37,38, 0.09894,0.20487
53,37,51, 0.09894,0.20487
54,38,39, 0.09894,0.20487
55,39,40, 0.09894,0.20487
56,39,53, 0.09894,0.20487
57,40,41, 0.09894,0.20487
58,41,42, 0.09894,0.20487
59,41,55, 0.09894,0.20487
60,42,43, 0.09894,0.20487
61,43,44, 0.09894,0.20487
62,43,57, 0.09894,0.20487
63,44,45, 0.09894,0.20487
64,45,46, 0.09894,0.20487
65,45,59, 0.09894,0.20487
66,46,47, 0.09894,0.20487
67,47,48, 0.09894,0.20487
68,47,61, 0.09894,0.20487
69,48,49, 0.09894,0.20487
70,49,63, 0.09894,0.20487
71,50,51, 0.09894,0.20487
72,50,66, 0.09894,0.20487
73,51,52, 0.09894,0.20487
74,52,53, 0.09894,0.20487
75,52,68, 0.09894,0.20487
76,53,54, 0.09894,0.20487
77,54,55, 0.09894,0.20487
78,54,70, 0.09894,0.20487
79,55,56, 0.09894,0.20487
80,56,57, 0.09894,0.20487
81,56,72, 0.09894,0.20487
82,57,58, 0.09894,0.20487
83,58,59, 0.09894,0.20487
84,58,74, 0.09894,0.20487
85,59,60, 0.09894,0.20487
86,60,61, 0.09894,0.20487
87,60,76, 0.09894,0.20487
88,61,62, 0.09894,0.20487
89,62,63, 0.09894,0.20487
90,62,78, 0.09894,0.20487
91,63,64, 0.09894,0.20487
92,64,80, 0.09894,0.20487
93,65,66, 0.09894,0.20487
94,65,82, 0.09894,1.4307
95,66,67, 0.09894,0.20487
96,67,68, 0.09894,0.20487
97,67,82, 0.09894,1.0793
98,68,69, 0.09894,0.20487
```

```
 99,69,70, 0.09894,0.20487
 100,69,82,0.09894,0.73215
 101,70,71,0.09894,0.20487
 102,71,72,0.09894,0.20487
 103,71,82,0.09894,0.39786
 104,72,73,0.09894,0.20487
 105,73,74,0.09894,0.20487
 106,73,82,0.09894,0.17994
 107,74,75,0.09894,0.20487
 108,75,76,0.09894,0.20487
 109,75,82,0.09894,0.39786
 110,76,77,0.09894,0.20487
 111,77,78,0.09894,0.20487
 112,77,82,0.09894,0.73215
 113,78,79,0.09894,0.20487
 114,79,80,0.09894,0.20487
 115,79,82,0.09894,1.0793
 116,80,81,0.09894,0.20487
 117,81,82,0.09894,1.4307
 118,82,83,3.68,1.7076
 119,83,84,7.36,4.567
 120,84,85,14.8,5.743
 121,85,86,22.06,5.817
 122,86,87,29.41,5.842
 123,87,88,36.77,5.8535
 124,88,89,44.12,5.8593
 125,89,90,51.47,5.863
 126,90,91,58.83,9.74
*
*
*================
*FLUID PROPERTIES
*================
*
*PROP.1
prop,?* INFLAG
0,?* NPROP, # of entries in fluid preperty tables
0,?* ISTEAM, no superheated properties
2,?* NFPROP, 0 for EPRI properties
1* IPVAR, 1 for property evaluation at local pressure
*
*RODS.1
rods,?* INFLAG
1,?* NAXP, # of axial profiles
60,?* NROD, # of rods
1,?* NC, 1 for conduction model
2,?* NFUELT, # of rod geometry types
1,?* NMAT, # of sets of rod properties
0,?* IGPFF, no gap conduction forcing fcn.
0,?* NGPFF, no gap conduction forcing fcn.
0,?* NOPT, normal rod layout
0,?* IPOWV, constant axial profiles w/ time
0,?* ICPR, no CPR calculation
0* IRFF, constant radial power factors w/ time
*
*
*=========
*ROD INPUT
*=========
*
*RODS.2
168,?* ZZH, heated length
3.5,?* ZSTRT, beginning of heated profile
```

```
0,?* NODALS
0* NODALT
*
*RODS.3
-1* NAXN, chopped cosine power profile
*
*RODS.5
1.55* PSTAR, Peak/Average axial power
*
*RODS.9
1,?* I, rod ID
1,?* IDFUEL, rod geometry type
1.6402,?* RADIAL, rod radial power factor
1,?* IAXP, axial power profile table flag
1,?* LRDUM, channel # that recieves heat
0.1666,* PHIDUM, fraction of power going to channel #
* Repeat LRDUM and PHIDUM for all channels connected to rod
*
2,1,1.6421,1,1,0.1666,3,0.1666,2,0.1666
3,1,1.6421,1,1,0.1666,3,0.1666,4,0.1666
4,1,1.6438,1,2,0.1666,6,0.1666,5,0.1666
5,1,1.6434,1,2,0.1666,3,0.1666,4,0.1666,6,0.1666,7,0.1666,8,0.1666
6,1,1.6438,1,4,0.1666,8,0.1666,9,0.1666
7,1,1.6453,1,5,0.1666,11,0.1666,10,0.1666
8,1,1.6448,1,5,0.1666,6,0.1666,7,0.1666,11,0.1666,12,0.1666,13,0.1666
9,1,1.6453,1,9,0.1666,15,0.1666,16,0.1666
10,1,1.6466,1,10,0.1666,18,0.1666,17,0.1666
11,1,1.6461,1,10,0.1666,11,0.1666,12,0.1666,18,0.1666,19,0.1666,20,0.1666
12,1,1.6459,1,12,0.1666,13,0.1666,14,0.1666,20,0.1666,21,0.1666,22,0.1666
13,1,1.6461,1,14,0.1666,15,0.1666,16,0.1666,22,0.1666,23,0.1666,24,0.1666
14,1,1.6466,1,16,0.1666,24,0.1666,25,0.1666
15,1,1.6477,1,17,0.1666,27,0.1666,26,0.1666
16,1,1.647,1,19,0.1666,20,0.1666,21,0.1666,29,0.1666,30,0.1666,31,0.1666
17,1,1.647,1,21,0.1666,22,0.1666,23,0.1666,31,0.1666,32,0.1666,33,0.1666
18,1,1.6473,1,23,0.1666,24,0.1666,25,0.1666,33,0.1666,34,0.1666,35,0.1666
19,1,1.6477,1,25,0.1666,35,0.1666,36,0.1666
20,1,1.6485,1,26,0.1666,38,0.1666,37,0.1666
21,1,1.6482,1,26,0.1666,27,0.1666,28,0.1666,38,0.1666,39,0.1666,40,0.1666
22,1,1.6479,1,28,0.1666,29,0.1666,30,0.1666,40,0.1666,41,0.1666,42,0.1666
23,1,1.6479,1,30,0.1666,31,0.1666,32,0.1666,42,0.1666,43,0.1666,44,0.1666
24,1,1.6479,1,32,0.1666,33,0.1666,34,0.1666,44,0.1666,45,0.1666,46,0.1666
25,1,1.6482,1,34,0.1666,35,0.1666,36,0.1666,46,0.1666,47,0.1666,48,0.1666
26,1,1.6485,1,36,0.1666,48,0.1666,49,0.1666
27,1,1.6492,1,37,0.1666,51,0.1666,50,0.1666
28,1,1.6489,1,37,0.1666,38,0.1666,39,0.1666,51,0.1666,52,0.1666,53,0.1666
29,1,1.6487,1,39,0.1666,40,0.1666,41,0.1666,53,0.1666,54,0.1666,55,0.1666
30,1,1.6486,1,41,0.1666,42,0.1666,43,0.1666,55,0.1666,56,0.1666,57,0.1666
31,1,1.6486,1,43,0.1666,44,0.1666,45,0.1666,57,0.1666,58,0.1666,59,0.1666
32,1,1.6489,1,47,0.1666,48,0.1666,49,0.1666,61,0.1666,62,0.1666,63,0.1666
33,1,1.6492,1,49,0.1666,63,0.1666,64,0.1666
34,1,1.6497,1,50,0.1666,66,0.1666,65,0.1666
35,1,1.6495,1,50,0.1666,51,0.1666,52,0.1666,66,0.1666,67,0.1666,68,0.1666
36,1,1.6492,1,54,0.1666,55,0.1666,56,0.1666,70,0.1666,71,0.1666,72,0.1666
37,1,1.6492,1,56,0.1666,57,0.1666,58,0.1666,72,0.1666,73,0.1666,74,0.1666
38,1,1.6492,1,58,0.1666,59,0.1666,60,0.1666,74,0.1666,75,0.1666,76,0.1666
39,1,1.6493,1,60,0.1666,61,0.1666,62,0.1666,76,0.1666,77,0.1666,78,0.1666
40,1,1.6495,1,62,0.1666,63,0.1666,64,0.1666,78,0.1666,79,0.1666,80,0.1666
41,1,1.6497,1,64,0.1666,80,0.1666,81,0.1666
42,1,1.6499,1,65,0.1666,82,0.1666
43,1,1.6498,1,65,0.1666,66,0.1666,67,0.1666,82,0.5
44,1,1.6497,1,67,0.1666,68,0.1666,69,0.1666,82,0.5
45,1,1.6497,1,69,0.1666,70,0.1666,71,0.1666,82,0.5
46,1,1.6496,1,71,0.1666,72,0.1666,73,0.1666,82,0.5
```

```
47,1,1.6496,1,73,0.1666,74,0.1666,75,0.1666,82,0.5
48,1,1.6497,1,75,0.1666,76,0.1666,77,0.1666,82,0.5
49,1,1.6497,1,77,0.1666,78,0.1666,79,0.1666,82,0.5
50,1,1.6498,1,79,0.1666,80,0.1666,81,0.1666,82,0.5
51,1,1.6499,1,81,0.1666,82,0.5
52,2,1.6491,1,83,123.5
53,2,1.6271,1,84,494
54,2,1.5633,1,85,823.33
55,2,1.4674,1,86,1152.67
56,2,1.3495,1,87,1482
57,2,1.2208,1,88,1811
58,2,1.0917,1,89,2140.67
59,2,0.97321,1,90,2470
60,2,0.82846,1,91,7533.5*this centroid isn't certain
0*terminates rod layout input
*
* RODS.62
1,?* I, rod geoemtry type #
nucl,?* FTYPE, rod type
0.2559,?* DROD, rod outside diameter
0.2194,?* DFUEL, fuel pellet diameter
6,?* NFUEL, number of radial nodes in fuel pellet
0.0000,?* DCORE, cnetral void diameter
0.0200 * TCLAD, cladding thickness
*
* RODS.63
0,?* IRADP, 0 - uniform raidal power profile in pellet
1,?* IMATF, use fuel properties stored in table 1
0,?* IMATC, 0 - use VIPRE zircaloy tables for cladding
0,?* IGPC, 0 - uniform gap conductance
0,?* IGFORC, 0 - gap conductance is constant with time
98214.6267,?* HGAP, constant gap conductance
0.9550,?* FTDENS, fuel theoretical density
0.0000 * FCLAD, fraction of applied power generated in clad
*
* RODS.68
2, ?* I, rod geometry type #
dumy, ?* FTYPE, rod type
0.2559, ?* DROD, rod outside diameter
0.0000, ?* DFUEL, 0 - if FTYPE not a fuel
0 * NFUEL, 0 - if DUMY type rod
*
* RODS.70
1, ?* N, material type #
140, ?* NNTDP, number of entries in material properties table
515.4000 * RCOLD, cold state density of material (lb/ft^3)
   32.0,0.05985,10.16909,   77.0,0.06228,10.16909
  122.0,0.06468,10.16909,  167.0,0.06707,10.16909
  212.0,0.06943,10.16909,  257.0,0.07178,10.16909
  302.0,0.07411,10.16909,  347.0,0.07642,10.16909
  392.0,0.07872,10.16909,  437.0,0.08100,10.16909
  482.0,0.08326,10.16909,  527.0,0.08552,10.16909
  572.0,0.08776,10.16909,  617.0,0.09000,10.16909
  662.0,0.09222,10.16909,  707.0,0.09444,10.16909
  752.0,0.09665,10.16909,  797.0,0.09885,10.16909
  842.0,0.10105,10.16909,  887.0,0.10324,10.16909
  932.0,0.10543,10.16909,  977.0,0.10762,10.16909
 1022.0,0.10981,10.16909, 1067.0,0.11200,10.16909
 1112.0,0.11419,10.16909, 1157.0,0.11638,10.16909
 1202.0,0.11858,10.16909, 1247.0,0.12078,10.16909
 1292.0,0.12299,10.16909, 1337.0,0.12520,10.16909
 1382.0,0.12742,10.16909, 1427.0,0.12965,10.16909
 1472.0,0.13189,10.16909, 1517.0,0.13414,10.16909
```

```
1562.0,0.13641,10.16909, 1607.0,0.13868,10.16909
1652.0,0.14097,10.16909, 1697.0,0.14328,10.16909
1742.0,0.14560,10.16909, 1787.0,0.14794,10.16909
1832.0,0.15030,10.16909, 1877.0,0.15268,10.16909
1922.0,0.15508,10.16909, 1967.0,0.15750,10.16909
2012.0,0.15994,10.16909, 2057.0,0.16241,10.16909
2102.0,0.16490,10.16909, 2147.0,0.16742,10.16909
2192.0,0.16996,10.16909, 2237.0,0.17254,10.16909
2282.0,0.17514,10.16909, 2327.0,0.17777,10.16909
2372.0,0.18043,10.16909, 2417.0,0.18313,10.16909
2462.0,0.18586,10.16909, 2507.0,0.18863,10.16909
2552.0,0.19143,10.16909, 2597.0,0.19426,10.16909
2642.0,0.19714,10.16909, 2687.0,0.20005,10.16909
2732.0,0.20300,10.16909, 2777.0,0.20600,10.16909
2822.0,0.20903,10.16909, 2867.0,0.21211,10.16909
2912.0,0.21524,10.16909, 2957.0,0.21840,10.16909
3002.0,0.22162,10.16909, 3047.0,0.22488,10.16909
3092.0,0.22819,10.16909, 3137.0,0.23155,10.16909
3182.0,0.23496,10.16909, 3227.0,0.23842,10.16909
3272.0,0.24194,10.16909, 3317.0,0.24551,10.16909
3362.0,0.24913,10.16909, 3407.0,0.25281,10.16909
3452.0,0.25655,10.16909, 3497.0,0.26034,10.16909
3542.0,0.26420,10.16909, 3587.0,0.26811,10.16909
3632.0,0.27209,10.16909, 3677.0,0.27612,10.16909
3722.0,0.28022,10.16909, 3767.0,0.28439,10.16909
3812.0,0.28862,10.16909, 3857.0,0.29292,10.16909
3902.0,0.29728,10.16909, 3947.0,0.30172,10.16909
3992.0,0.30622,10.16909, 4037.0,0.31079,10.16909
4082.0,0.31544,10.16909, 4127.0,0.32016,10.16909
4172.0,0.32495,10.16909, 4217.0,0.32982,10.16909
4262.0,0.33477,10.16909, 4307.0,0.33979,10.16909
4352.0,0.34489,10.16909, 4397.0,0.35007,10.16909
4442.0,0.35533,10.16909, 4487.0,0.36067,10.16909
4532.0,0.36609,10.16909, 4577.0,0.37160,10.16909
4622.0,0.37719,10.16909, 4667.0,0.38287,10.16909
4712.0,0.38864,10.16909, 4757.0,0.39449,10.16909
4802.0,0.40043,10.16909, 4847.0,0.40647,10.16909
4892.0,0.41259,10.16909, 4937.0,0.41881,10.16909
4982.0,0.42512,10.16909, 5027.0,0.43152,10.16909
5072.0,0.43802,10.16909, 5117.0,0.44461,10.16909
5162.0,0.45131,10.16909, 5207.0,0.45810,10.16909
5252.0,0.46499,10.16909, 5297.0,0.47198,10.16909
5342.0,0.47908,10.16909, 5387.0,0.48627,10.16909
5432.0,0.49357,10.16909, 5477.0,0.50098,10.16909
5522.0,0.50849,10.16909, 5567.0,0.51611,10.16909
5612.0,0.52384,10.16909, 5657.0,0.53167,10.16909
5702.0,0.53962,10.16909, 5747.0,0.54768,10.16909
5792.0,0.55585,10.16909, 5837.0,0.56414,10.16909
5882.0,0.57254,10.16909, 5927.0,0.58105,10.16909
5972.0,0.58968,10.16909, 6017.0,0.59843,10.16909
6062.0,0.60730,10.16909, 6107.0,0.61629,10.16909
6152.0,0.62540,10.16909, 6197.0,0.63463,10.16909
6242.0,0.64399,10.16909, 6287.0,0.65347,10.16909
*
*
*===========
*OPER INPUT
*===========
*
*OPER.1
oper, ?* INFLAG
1, ?* IH, inlet condition specified as uniform inlet temp.
2, ?* IG, inlet flow condition specified by mass flux
```

```
0, ?* ISP, 0 - equal mass flux per channel at inlet
0, ?* NPOWR, 0 - power specified in units kW/ft
0, ?* NDNB, 0 - no MDNBR iteration
0, ?* IRUN, o - run only one case
0, ?* IFCVR, 0 - constant direct heat generation in coolant
0, ?* LUF, 0 - no forcing functions
0   * IHBAL, 0 - specify inlet enthalpy directly
*
*OPER.2
0.0000, ?* DPS, 0 - use inlet BC specified by IG and ISP
0.0000, ?* DNBRL, 0 - 0 if NDNB == 0
1.9597, ?* FCOOL, percent of heat generated in coolant
0.0010, ?* DNBRC, convergence factor for CHF iterations
0                                * IHROD - 0 if NDNB == 0
*
*OPER.5
2250.0000, ?* PREF, operating system pressure (psia)
561.2000, ?* HIN, enter average inlet temp.
3.911, ?* GIN, average inlet mass flux (Mlbm/hr-ft^2)
2.865, ?* PWRINP, core average power (kW/ft)
0 * HOUT, 0 - no exit flow reverse
*
*OPER.12
0,0,0,0,0,0 *no forcing functions used
*
*CORR.1
corr, ?* INFLAG
2, ?* NCOR, # of CHF correlations to use for DNBR calculations
1, ?* NHTC, use correlations for 1-phase conv. and NB only
0   * IXCHF, o if NHTC = 1
*
*CORR.2
levy, ?* NSCVD, subcooled void correlation
homo, ?* NBLVD, bulk/void quality correlation
homo, ?* NFRML, two-phase friction multiplier
none,  * NHTWL, no hot wall correction factor
*
*CORR.6
ditb, ?* NFCON, single-phase forced convection correlation
thsp, ?* NSUBC, subcooled nucleate boiling correlation
thsp, ?* NSATB, saturated nucleate boiling correlation
epri, ?* NCHFC, critical heat flux correlation
cond, ?* NTRNB, transition boiling correlation
g5.7   * NFLMB, film boiling correlation
*
*CORR.9
w-3l, ?* NCHF, DNB correlation
epri,  * NCHF, DNB correlation
*
*CORR.11
0.0420, ?* TDCL, L-grid mixing factor
0.0660, ?* SPK, grid spacing factor
1.0000   * FLGRID, L-grid factor converted to R-grid factor
*
*CORR.16
0, ?* KBWR, 0 - no cold wall correction factor
0, ?* NUC, 0 - no non-uniform axial flux correction factor
0.8500 *CGRID, grid loss coefficient for mixing grids
*
*
*==========
*MIXX INPUT
*==========
```

```
*
*
mixx, ?* NFLAG
0, ?* NSCBC
0, ?* NBBC, 0 - 2-phase mixing computed as for single phase
1   *  MIXK, 1 - a pair of coefficients is entered for each gap *MIXX.2 0.0000,
0.0000, 0.0000 *single coefficients not used
*
*MIXX.3
 0.12723, ?* ABETA(K), A coefficient of mixing correlation for gap K
0.0000, ?* BBETA(K), B coefficient of Reynold's number for gap K
0.12723, 0.0000,0.12723, 0.0000,0.12723, 0.0000
 0.12723, 0.0000,0.12723, 0.0000,0.12723, 0.0000,0.12723, 0.0000
 0.12723, 0.0000,0.12723, 0.0000,0.12723, 0.0000,0.12723, 0.0000
 0.12723, 0.0000,0.12723, 0.0000,0.12723, 0.0000,0.12723, 0.0000
 0.12723, 0.0000,0.12723, 0.0000,0.12723, 0.0000,0.12723, 0.0000
 0.12723, 0.0000,0.12723, 0.0000,0.12723, 0.0000,0.12723, 0.0000
 0.12723, 0.0000,0.12723, 0.0000,0.12723, 0.0000,0.12723, 0.0000
 0.12723, 0.0000,0.12723, 0.0000,0.12723, 0.0000,0.12723, 0.0000
 0.12723, 0.0000,0.12723, 0.0000,0.12723, 0.0000,0.12723, 0.0000
 0.12723, 0.0000,0.12723, 0.0000,0.12723, 0.0000,0.12723, 0.0000
 0.12723, 0.0000,0.12723, 0.0000,0.12723, 0.0000,0.12723, 0.0000
 0.12723, 0.0000,0.12723, 0.0000,0.12723, 0.0000,0.12723, 0.0000
 0.12723, 0.0000,0.12723, 0.0000,0.12723, 0.0000,0.12723, 0.0000
 0.12723, 0.0000,0.12723, 0.0000,0.12723, 0.0000,0.12723, 0.0000
 0.12723, 0.0000,0.12723, 0.0000,0.12723, 0.0000,0.12723, 0.0000
 0.12723, 0.0000,0.12723, 0.0000,0.12723, 0.0000,0.12723, 0.0000
 0.12723, 0.0000,0.12723, 0.0000,0.12723, 0.0000,0.12723, 0.0000
 0.12723, 0.0000,0.12723, 0.0000,0.12723, 0.0000,0.12723, 0.0000
 0.12723, 0.0000,0.12723, 0.0000,0.12723, 0.0000,0.12723, 0.0000
 0.12723, 0.0000,0.12723, 0.0000,0.12723, 0.0000,0.12723, 0.0000
 0.12723, 0.0000,0.12723, 0.0000,0.12723, 0.0000,0.12723, 0.0000
 0.12723, 0.0000,0.12723, 0.0000,0.12723, 0.0000,0.12723, 0.0000
 0.12723, 0.0000,0.12723, 0.0000,0.12723, 0.0000,0.12723, 0.0000
 0.12723, 0.0000,0.01822, 0.0000,0.12716, 0.0000,0.12716, 0.0000
 0.02415, 0.0000,0.12716, 0.0000,0.12716, 0.0000,0.03551, 0.0000
 0.12716, 0.0000,0.12716, 0.0000,0.06544, 0.0000,0.12716, 0.0000
 0.12716, 0.0000,0.14471, 0.0000,0.12716, 0.0000,0.12716, 0.0000
 0.06544, 0.0000,0.12716, 0.0000,0.12716, 0.0000,0.03551, 0.0000
 0.12716, 0.0000,0.12716, 0.0000,0.03509, 0.0000,0.12716, 0.0000
 0.18166, 0.0000,0.01528, 0.0000,0.00578, 0.0000,0.00454, 0.0000
 0.00454, 0.0000,0.00454, 0.0000,0.00454, 0.0000,0.00454, 0.0000
 0.00454, 0.0000,0.00268, 0.0000
*
*
*==========
*DRAG INPUT
*==========
*
*DRAG.1
drag, ?* INFLAG
1, ?* NCHTP, # of axial friction correlations to be specified
0, ?* NGPTP, 0 - apply constant loss coefficients to all gaps
1   * KIJOPT, lateral resistance option
*
*DRAG.2
0.1425,  ?* ATF, coefficient in turbulent rod friction factor correlation
-0.1800, ?* BTF, costant in turbulent rod friction factor correlation 0.0000,  ?* CTF,
costant in turbulent rod friction factor correlation 87.6256, ?* ALF, coefficient in
laminar rod friction factor correlation
-1.0000, ?* BLF, constant in laminar rod friction factor correlation
0.0000    * CLF, constant in laminar rod friction factor correlation
*
```

```
*DRAG.5
0.5000, ?* DUMKIJ, lateral resistance factor applied to all gaps
0.35484  * PPITCH, rod pitch
*
endd
0
```

D. MATLAB/VIPRE Interface, "sq_core_max_hydride", Modified for Wire Wraps

For an overpower analysis, change the linear heat rate and MDNBR limits at the OVERPOWER keywords

Steps for changing from wire wrap to grid spacers:

1. Grids - Comment Line 21, Un-Comment Line 22
2. Core Construction - Comment Lines 67 & 68, Un-Comment Lines 69 & 70
3. Friction Factor - Comment Line 74, Un-Comment Line 75
4. Velocity Limit - Comment Line 77
5. Mixing - Comment Line 114, Un-Comment Lines 112 & 113

```
1-  %THIS IS FOR THE ACHIEVABLE CASE WITH HYDRIDE FUEL, OXIDE DIFFERENCES ARE MINOR
2-  function sq_core_max_hydride;
3-  warning off;
4-  cd ..
5-  trans_folder=pwd;
6-  cd .\Assembly;
7-  %GIVE MATLAB ACCESS TO NECESSARY DIRECTORIES IN THE COMPUTER%
8-  addpath(trans_folder);
9-  addpath(strcat(trans_folder,'\steam_table_data'));
10- addpath(strcat(trans_folder,'\jacexample'));
11- %DEFINE THE EXCEL SPREADSHEET CONTAINING THE VIPRE INPUT%
12- vipre_spreadsheet = strcat(pwd,'\square_hydride_core.xls');
13- %GET HANDLE TO THE SPREADSHEET CONTAINING VIPRE INPUT%
14- [xl,xl_wb_specific] = get_spreadsheet(vipre_spreadsheet);
15- %NAME THE TEXT FILE THAT THE VIPRE INPUT DECK IS WRITTEN TO%
16- input_file_name = strcat('test_jac_input');
17- %NAME THE MATLAB FILE THAT HOLDS THE VIPRE INPUT VARIABLES IN MATLAB SPACE%
18- var_file_name = strcat('sq_core_test_var.mat');
19- %EXTRACT VIPRE INPUT DATA FROM EXCEL, AND SAVE TO SPECIFIED MATLAB FILE
    (var_file_name) USING S. BLAIR'S TOOLS%
20- %get_tri_excel_input DOES NOT CREATE A GRID CARD
21- get_tri_excel_input(xl_wb_specific,var_file_name);
22- %get_sq_excel_input(xl_wb_specific,var_file_name);
23- %SAVE AND CLOSE EXCEL SPREADSHEET%
24- invoke(xl_wb_specific,'Save');
25- invoke(xl_wb_specific,'Close');
26- %DELETE HANDLE TO EXCEL SPREADSHEET%
27- delete(xl);
28- load(var_file_name);
29- %LOAD FILE THAT CONTAINS VIPRE INPUT DATA- THIS INTRODUCES SEVERAL
30- %VARIABLE NAMES THAT HAVE NOT BEEN DEFINED WITHIN THIS PROGRAM%
31- loopindex = 0;%INITIALIZE LOOP INDEX
32- sq_or_tri = 1;%DEFINE THE SHAPE OF THE CHANNEL; THIS IS A MEANINGLESS DINOSAUR
33- core = 1;%DEFINE FULL CORE OR SINGLE CHANNEL ANALYSIS; FOR SINGLE CHANNEL CORE = 0,
    FOR FULL CORE CORE = 1
34- delta_p = 40;%INITIALIZE PRESSURE DROP VARIABLE; THIS IS NOT THE Delta_P LIMIT
35- min_diam = 6.5;%DEFINE LOWER BOUND OF ROD DIAMETER RANGE (mm)
36- max_diam = 12.5;%DEFINE UPPER BOUND OF ROD DIAMETER RANGE (mm)
37- diam_steps = 20;%DEFINE NUMBER OF STEPS IN DIAMETER RANGE
```

```
%DEFINE DIAMETER RANGE AS AN ARRAY OF diam_steps EQUALLY SPACED STEPS BETWEEN min_diam AND max_diam
diam_range = linspace(min_diam,max_diam,diam_steps);
enthalpy_rise = 204;%%DEFINE HOT CHANNEL ENTHALPY RISE (kj/kg)
%DEFINE CONSTRAINT LIMITS%
mdnbr_limit = 2.173;%MDNBR LIMIT
%mdnbr_limit = 1.578;%OVERPOWER MDNBR LIMIT
dp_limit = 60;%PRESSURE DROP LIMIT (psia)
temp_limit = 1382;%FUEL TEMPERATURE LIMIT (F)
velocity_limit = 8;%VELOCITY LIMIT (m/s)
%BEGIN A for LOOP THAT CYCLES BETWEEN THIS LINE, AND THE FINAL end STATEMENT diam_steps TIMES
%EACH TIME IT, CYCLES k INCREASES IN VALUE BY 1
for k = 1:diam_steps;
   min_pdratio = 1.0738;
   max_pdratio = 1.42/1.0746;
   pitch_steps = 20;%DEFINE THE NUMBER OF PITCHES TO BE EVALUATED FOR EACH ROD DIAMETER
   pdratio_range = linspace(min_pdratio, max_pdratio, pitch_steps);
   pitch_range = pdratio_range.*diam_range(k);
   hex_pdratio_range = pdratio_range*1.0746;
   hex_pitch_range = hex_pdratio_range.*diam_range(k);
   axial_pitch = min(522,50*diam_range(k));
   %BEGIN A for LOOP THAT  CYCLES BETWEEN THIS LINE AND THE SECOND TO LAST end STATEMENT pitch_steps TIMES
   %EACH TIME IT CYCLES, l INCREASES IN VALUE BY 1
   for l = 1:pitch_steps;
      %CREATE THE GEOMETRY AND ROD INPUT FOR THE SQUARE CORE- MOST VARIABLES ARE DESCRIBED IN THE VIPRE INPUT MANUAL
      %OR S. BLAIR'S THESIS, WHICH IS REFERENCED BY THIS THESIS.  nrods_8th= NUMBER OF RODS IN THE 1/8TH CORE,
      %flow_area_8th = TOTAL FLOW AREA OF 1/8TH CORE MODEL, rise_fraction = CORRECTION FACTOR USED BECAUSE RADIAL
      %POWER DISTRIBUTION DOESN'T INTEGRATE TO EXACTLY 1
      %make_core_wire IS THE SAME AS make_core, BUT WITH WIRE WRAP FLOW AREA, WETTED PERIMETER, AND EQUIVALENT DIAMETER
      %THE CONTROL ROD DIAMETER IS ALSO SET TO THE FUEL ROD DIAMETER, A NECESSITY FOR WIRE WRAPS TO WORK
      [geom1.nchanl geom1.nctyp rods1.nrod geom5 geom6 geom7 geom11 rods9_pre rods9 nrods_8th flow_area_8th...
         rise_fraction]= make_core_wire(pitch_range(l), diam_range(k));
%     [geom1.nchanl geom1.nctyp rods1.nrod geom5 geom6 geom7 geom11 rods9_pre rods9 nrods_8th flow_area_8th...
%        rise_fraction]= make_core(pitch_range(l), diam_range(k));
      %EVALUATE FRICTION AND LATERAL DRAG COEFFICIENTS. ANY P/D VALUE GREATER THAN 1.42 IS RESET TO 1.42 FOR WIRE WRAPS
      drag_pitch = hex_pdratio_range(l)*diam_range(k);
      drag_pitch = min(1.42,hex_pdratio_range(l))*diam_range(k);
      [drag2.atf drag2.alf drag5.ppitch] = change_drag_wire(drag_pitch, diam_range(k), sq_or_tri, axial_pitch, 1);
%     [drag2.atf drag2.alf drag5.ppitch] = change_drag(pitch_range(l), diam_range(k), sq_or_tri);
      %CALCULATE THE AXIAL VELOCITY LIMIT
      velocity_limit = connors_crossflow(hex_pdratio_range(l), diam_range(k), axial_pitch);
      %EVALUATE VARIABLES NEEDED FOR rods PORTION OF VIPRE INPUT DECK
      [rods62.drod rods62.dfuel rods62.tclad rods63.hgap oper2.fcool] = fuel_data_hydride(diam_range(k),...
         pitch_range(l),sq_or_tri);
      nrods_core(k,l) = 8*nrods_8th;%EVALUATE THE TOTAL NUMBER OF RODS IN THE CORE
      core_flow_area(k,l) = 8*flow_area_8th;%EVALUATE THE TOTAL CORE FLOW AREA (in^2)
      rods68.drod = rods62.drod;%EQUATE THE DUMMY ROD DIAMETER TO THE FUEL ROD DIAMETER
      area_in_m = 0.00064516*core_flow_area(k,l);%CHANGE TO SI UNITS (m)
```

```
85-        loopindex = loopindex+1
86-        power = 6250578.8969717;%INITIALIZE POWER
87-        lower_bound = 0;%INITIALIZE LOWER BOUND FOR POWER
88-        upper_bound = 6.262e6;%INITIALIZE UPPER BOUND FOR POWER
89-        error_v = 0;%INITIALIZE ERROR AND POWER VECTORS
90-        power_v = 0;
91-        error = 1;%INITIALIZE ERROR
92-        low_error = 1;%INITIALIZE LOW ERROR
93-        failed_interp = 0;%THIS TRACKS IF THE INTERPOLATION FAILS
94-        caution_interp = 0;%THIS TRACKS IF THE INTERPOLATION IS MOVING AWAY
    CONVERGANCE
95-        %BEGIN while LOOP THAT WILL CONTINUE UNTIL THE THE MAGNITUDE OF
    error(low_error) IS LESS THAN .01 AND ALL
96-        %VALUES OF THE ARRAY NAMED error ARE LESS THAN OR EQUAL TO 0
97-        count1 = 0;
98-        clear count;
99-        stop = 0;
100-       next_stop = 0;
101-       while ((abs(error(low_error))>.01) | (sum(error>0)~=0)) & count1 < 30 & stop
    == 0;
102-          %DETERMINE THE LINEAR HEAT RATE (kW/ft)
103- %         oper5.pwrinp =
    power*1.17267/(rise_fraction*nrods_core(k,1)*rods2.zzh/12);%FOR OVERPOWER
104-          oper5.pwrinp = power/(rise_fraction*nrods_core(k,1)*rods2.zzh/12);
105-          %DETERMINE THE MASS FLOW RATE FOR THE FULL CORE (kg/s)
106-          mdot = power/(enthalpy_rise);
107-          %DETERMINE THE MASS FLUX FOR THE FULL CORE
108-          oper5.gin = (mdot/area_in_m)*737.338117041e-6;
109-          %DETERMINE THE GRID SPACER PRESSURE LOSS COEFFICIENTS
110-          grid2 = grid_spacer2(pitch_range(1), diam_range(k), oper5.gin, oper5.pref,
    delta_p, sq_or_tri);
111-          %DETERMINE THE MIXXING COEFFICIENTS
112- %         [mixx3 int_channel_beta] = mixx(pitch_range(1), diam_range(k), oper5.gin,
    oper5.pref, delta_p,...
113- %             sq_or_tri,geom11);
114-          [mixx3 int_channel_beta] = mixx_tri(hex_pitch_range(1), diam_range(k),
    axial_pitch,geom11);
115-          %DEFINE VARIABLE NAMED output THAT ARCHIVES RELAVENT DATA;
116-          %HERE, THE PITCH, DIAMETER, AND FLOW AREA OF THE CURRENT ITERATION ARE
    ARCHIVED
117-          output(loopindex,2:4) = [pitch_range(1) diam_range(k) area_in_m];
118-          %SAVE THE VARIABLES WITHIN THE MATLAB REALM INTO THE FILE NAMED
    var_file_name

119-          %USING A PROGRAM CREATED BY S. BLAIR, CONSTRUCT A VIPRE INPUT DECK USING
    THE VARIABLES DEFINED
120-          %WITHIN THIS PROGRAM.  THEN EXECUTE VIPE AND SAVE THE VIPRE RESULTS TO
    ANOTHER MATLAB FILE CALLED
121-          %channel_data.mat
122-          count1 = count1 + 1;
123-          save(var_file_name);
124-          count = 0;
125-          max_count = 20;
126-          max_count = 5;
127-          save count count max_count;
128-          vipre_debug(input_file_name, var_file_name, power);
129-          %save count1 count1;
130-          load channel_data
131-          load count;
132-          %SEVERAL NEW VARIABLES THAT HAVE NOT BEEN DEFINED WITHIN THIS PROGRAM
133-          %DEFINE error USING THE VALUES OF THE CONSTRAINTS RETURNED BY VIPRE
134-          if count == max_count
135-             hot_channel = 1;
136-          else
```

```
137-            hot_channel = min(find(channel_enthalpy(:) ==
    max(channel_enthalpy(:))));
138-         end
139-         old_error = error;
140-         error(1) =(mdnbr_limit-w3l_mdnbr)/mdnbr_limit;
141-         error(2) =(max(max(rod_fuel_temp_cl))-temp_limit)/temp_limit;
142-         error(3) =(max(max(channel_delta_p_local))-dp_limit)/dp_limit;
143-         error(4) =(mean(channel_velocity_local(:,:,hot_channel))*.3048-
    velocity_limit)/velocity_limit;
144-         %DEFINE low_error AS THE POSITION IN THE ARRAY CALLED error HOLDING THE
    MINIMUM VALUE IN error
145-         low_error = find(abs(error) == min(abs(error)));
146-         if next_stop == 1 & max(error) < 0
147-            stop = 1;
148-         else
149-            next_stop = 0;
150-         end
151-         %IF THE MINIMUM OF error IS LESS THAN .01 AND NONE OF THE CONSTRAINED
    PARAMETERS EXCEED THE CONSTRAINT LIMITS
152-         %THEN THE MAXIMUM POWER IS ACHIEVED, RECORD THE VALUES; OTHERWISE CONTINUE
    ITERATING
153-         if (((abs(error(low_error))<.01) & (sum(error>0)==0)) | stop == 1) & count
    < max_count;
154-            %RECORD THE RESULTS IN VARIABLE NAMED OUTPUT
155-            delta_p = max(max(channel_delta_p_local));%PRESSURE DROP (psia)
156-            delta_T = max(max(channel_temp_local));%TEMPERATURE RISE (F)
157-            hotz = min(find(rod_fuel_temp_cl(1,:,1) ==
    max(max(rod_fuel_temp_cl(1,:,1)))));%AXIAL POSITION OF MAX FUEL
158-               %TEMP (in)
159-            hot_rod = min(find(rod_fuel_temp_cl(1,hotz,:) ==
    max(rod_fuel_temp_cl(1,hotz,:))));%HOTTEST ROD
160-            clad_temp_in = rod_clad_temp_in(1,hotz,hot_rod);%INSIDE CLAD TEMP OF
    hot_rod AT hotz (F)
161-            clad_temp_out = rod_clad_temp_out(1,hotz,hot_rod);%OUTSIDE CLAD TEMP
    hot_rod AT hotz (F)
162-            bulk_temp_hotz = channel_temp_local(1,hotz,1);%COOLANT TEMP IN CENTRAL
    CHANNEL AT hotz (F)
163-            channel_weight = channel_flow_rate./sum(channel_flow_rate);%FRACTION OF
    TOTAL FLOW RATE IN EACH CHANNEL
164-            average_enthalpy_rise = sum(channel_enthalpy.*channel_weight);%CORE
    AVERAGE ENTHALPY RISE (btu/kg)
165-            max_enthalpy_rise = max(channel_enthalpy);%HOT CHANNEL ENTHALPY RISE
    (btu/kg)
166-            output(loopindex,1) = power;%CORE POWER (kWt)
167-            output(loopindex,5) = oper5.pwrinp;% LINEAR HEAT RATE (kW/ft)
168-            output(loopindex,6) = oper5.gin;% MASS FLUX (Mlbm/ft^2-hr)
169-            output(loopindex,7) = max(max(max(channel_delta_p_local)));%PRESSURE
    DROP (psia)
170-            output(loopindex,8) = (max_enthalpy_rise-
    oper5.hin)/(average_enthalpy_rise-oper5.hin);%ENTHALPY PEAKING FACTOR
171-            output(loopindex,9) = w3l_mdnbr;%W3L PREDICTION OF MDNBR
172-            output(loopindex,10) = mdot;%MASS FLOW RATE (FOR FULL CORE THIS IS THE
    TOTAL MASS FLOW RATE)
173-            output(loopindex,11) =
    mean(channel_velocity_local(:,:,hot_channel));%HOT CHANNEL FLOW VELOCITY (ft/s)
174-            output(loopindex,12) = max(max(max(rod_fuel_temp_cl)));%HOT ROD MAX
    CENTERLINE TEMP (F)
175-            output(loopindex,13) = clad_temp_in;%%INSIDE CLAD TEMP OF hot_rod AT
    hotz (F)
176-            output(loopindex,14) = clad_temp_out;%OUTSIDE CLAD TEMP hot_rod AT hotz
    (F)
177-            output(loopindex,15) = bulk_temp_hotz;%COOLANT TEMP IN CENTRAL CHANNEL
    AT hotz (F)
178-            %output(loopindex,16) =
    mean(mean(mean(channel_void_fraction_local)));%CORE AVERAGE VOID FRACTION
```

```
179-            output(loopindex,16) = velocity_limit;%AXIAL VELOCITY LIMIT
180-            %output(loopindex,17) = mean(mean(mean(channel_quality_local)));%CORE
    AVERAGE QUALITY
181-            output(loopindex,17) = bowr_mdnbr;%bowr PREDICTION OF MDNBR
182-            output(loopindex,18) = mean(mean(mean(channel_density_local)));%CORE
    AVERAGE MIXTURE DENSITY
183-            output(loopindex,19) = nrods_core(k,l);%NUMBER OF RODS IN THE CORE
184-            output(loopindex,20) = int_channel_beta;%TURBULENT MIXING RATE
185-            %HOT CHANNEL MASS FLOWRATE OUT DIVIDED BY HOT CHANNLE MASS FLOWRATE OUT
186-            output(loopindex,21)
    =channel_flowrate_local(1,NUM_AXIAL_NODES,hot_channel)...
187-               /channel_flowrate_local(1,1,hot_channel);
188-            output(loopindex,22) = count;
189-            output(loopindex,23) = count1;
190-            output(loopindex,24) = ((max(max(max(rod_fuel_temp_cl)))) - 32) *
    (5/9);
191-            output(loopindex,25) = ((max(max(max(rod_fuel_temp_ave)))) - 32) *
    (5/9);
192-            %OTHERWISE, IF THE MINIMUM OF ERROR IS GREATER THAN .01 OR ONE OR MORE
    OF THE PARAMETERS EXEED THEIR CONSTRAINTS,
193-         else
194-            %THIS IS THE NEW METHOD OF CONVERGING ON THE MAX POWER, IT USES ABOUT
    HALF THE ITERATIONS OF THE OLD METHOD.
195-            %IF CONSTRAINTS HAVE NOT BEEN EXCEEDED THEN TRY TO INTERPOLATE, USING
    THE PREVIOUS POWER AND ERROR VECTORS TO
196-            %FIND THE NEW POWER.  THE INTERPOLATION GETS CAUTIONED IF THE ERROR
    STARTS TO INCREASE.  IF IT'S CAUTIONED SIX
197-            %TIMES, INTERPOLATION IS CANCELLED AND THE OLD METHOD IS USED.
198-            error_v(count1) = max(error);
199-            power_v(count1) = power;
200-            if count1 > 1 & abs(error_v(count1)) > abs(error_v(count1-1))
201-               caution_interp = caution_interp + 1
202-            end
203-            if max(error) < 0
204-               lower_bound = power;
205-            else
206-               upper_bound = power;
207-            end
208-            if count1 == 1 | caution_interp > 5;
209-               power = .5*(lower_bound + upper_bound);
210-            else
211-               try
212-                  power = interp1(error_v,power_v,-.005,'linear','extrap');
213-               catch
214-                  power = .5*(lower_bound + upper_bound);
215-               end
216-            end
217-            power = min(1.5e7,max(1e5,power));
218-            if power == 1.5e7
219-               next_stop = 1;
220-            end
221-         end
222-      end
223-      if count1 == 30 | count == max_count
224-         output(loopindex,1) = NaN;
225-         output(loopindex,2) = NaN;
226-         output(loopindex,3) = NaN;
227-         output(loopindex,4) = NaN;
228-         output(loopindex,5) = NaN;
229-         output(loopindex,6) = NaN;
230-         output(loopindex,7) = NaN;
231-         output(loopindex,8) = NaN;
232-         output(loopindex,9) = NaN;
233-         output(loopindex,10) = NaN;
234-         output(loopindex,11) = NaN;
```

```
235-          output(loopindex,12) = NaN;
236-          output(loopindex,13) = NaN;
237-          output(loopindex,14) = NaN;
238-          output(loopindex,15) = NaN;
239-          output(loopindex,16) = NaN;
240-          output(loopindex,17) = NaN;
241-          output(loopindex,18) = NaN;
242-          output(loopindex,19) = NaN;
243-          output(loopindex,20) = NaN;
244-          output(loopindex,21) = NaN;
245-          output(loopindex,22) = NaN;
246-          output(loopindex,23) = NaN;
247-          output(loopindex,24) = NaN;
248-          output(loopindex,25) = NaN;
249-       else
250-       end
251-    end
252- end
253- save(var_file_name);
```